

MARI LEHTI-POLOJÄRVI

# Electrical Impedance Tomography Integration with Optical Imaging for 3D *in vitro* Applications



MARI LEHTI-POLOJÄRVI

Electrical Impedance Tomography Integration with  
Optical Imaging for 3D *in vitro* Applications

ACADEMIC DISSERTATION

To be presented, with the permission of  
the Faculty of Medicine and Health Technology  
of Tampere University,  
for public discussion in the auditorium F114  
of the Arvo building, Arvo Ylpön katu 34, Tampere,  
on 3 November 2023, at 12 o'clock.

## ACADEMIC DISSERTATION

Tampere University, Faculty of Medicine and Health Technology  
Finland

<i>Responsible supervisor and Custos</i>	Professor Jari Hyttinen Tampere University Finland	
<i>Supervisor</i>	PhD Edite Figueiras Champalimaud Research Portugal	
<i>Pre-examiners</i>	Professor Richard Bayford Middlesex University London United Kingdom	Professor Manuchehr Soleimani University of Bath United Kingdom
<i>Opponent</i>	Professor Tanja Tarvainen University of Eastern Finland Finland	

The originality of this thesis has been checked using the Turnitin OriginalityCheck service.

Copyright ©2023 author

Cover design: Roihu Inc.

ISBN 978-952-03-3109-2 (print)

ISBN 978-952-03-3110-8 (pdf)

ISSN 2489-9860 (print)

ISSN 2490-0028 (pdf)

<http://urn.fi/URN:ISBN:978-952-03-3110-8>



ClimateCalc CC-000025FI  
PunaMusta Printing

Carbon dioxide emissions from printing Tampere University dissertations have been compensated.

PunaMusta Oy – Yliopistopaino  
Joensuu 2023

*To all who have contributed to this work*

“Do not go where the path may lead,  
go instead where there is no path and leave a trail.”

*—Ralph Waldo Emerson*



# ACKNOWLEDGEMENTS

This doctoral thesis work was conducted in the Computational Biophysics and Imaging Group (CBIG) of the Faculty of Medicine and Health Technology at the Tampere University (formerly Tampere University of Technology) during the years 2015–2022. The finalization of this thesis was accomplished as a side project during 2023 while already working in a Business Finland Research to Business project OrganAnalytics.

My research work and visits to conferences and collaborative laboratories have been made possible by several funders: Jane and Aatos Erkkö Foundation, Instrumentarium Science Foundation, Business Finland Human Spare Parts Project, Finnish Foundation for Technology Promotion, Emil Aaltonen Foundation, Academy of Finland Centre of Excellence in Body-on-Chip Research, Doctoral Programme at the Faculty of Medicine and Health Technology at Tampere University, and a travel grant from the National Institutes of Health (USA). In addition, a six-month (2018-2019) research exchange at Tallinn University of Technology was enabled by European Regional Development Fund's Doctoral Studies and Internationalisation Programme DoRa Plus.

The scientific content of this thesis has been enabled and initiated by my supervisor Professor Jari Hyttinen and cosupervisor PhD Edite Figueiras. They provided the wild and new idea of the integrated imaging system and trusted me to implement it in my own way. Thank you for your support and guidance throughout the project. I also appreciate that you encouraged me to reach out for collaboration regarding topics where we did not have sufficient internal expertise. Collaboration has been crucial since the topic of the thesis was cross-disciplinary.

A huge thank to my follow-up group member, collaborator, and coauthor Professor Aku Seppänen. You were the key advisor throughout the project, and you gave me confidence to continue in the times when I wasn't sure will this ever work out. I wish to thank the pre-examiners Professor Richard Bayford and Professor Manuchehr Soleimani for their constructive feedback that helped me to improve the quality of the thesis.

This work would not have been possible without all the great collaborators I have been privileged to work with. From the external collaborators I want to thank the

impedance group at Thomas Johann Seebeck Department of Electronics at Tallinn University of Technology (Estonia): Mart Min, Paul Annus, Raul Land, and Marek Rist. I am grateful for the collaborative development of the Spectro-EIT device, electrode fabrication, and all the practical expertise you shared with me regarding electronics and impedance measurements. Thank you for inviting me to write a chapter into the book that Paul and Mart edited. I am also grateful for the opportunity for a six-month research exchange in your group.

I would like to acknowledge Mikko Räsänen who conquered the task of creating computational methods for data fusion 3D reconstructions. It has been a pleasure to work with you and our cooperation went well even in remote working conditions during the pandemic. I wish to thank Tuomo Savolainen and Panu Kuusela for your help in the laboratory measurements that served as a kick-off for designing the integrated *in vitro* system.

All my colleagues and in-house collaboration created the soul of this whole process. First and foremost, I want to thank Olli Koskela for joining the ride with me to get the work started. Thank you for being a coauthor, a supportive friend, and a voice of rational reasoning that clarified my messy thoughts so many times. I am grateful to Markus Hannula for guidance in image segmentation and many other small issues along the way. I would like to thank Toni Montonen and Jarno Tanskanen for all the discussions and guidance that helped me move forward when facing an issue. Thanks to Antti Paldanius for the simulation collaboration and to Birhanu Belay for collaboration regarding OPT. I would like to acknowledge all colleagues in the CBIG group and other colleagues who shared the PhD student office on the second floor of Arvo.

I am grateful to my coauthors Leena Viiri, Hanna Vuorenpää, and Susanna Miettinen for helping me with stem cell and tissue samples. I wish to thank all other in-house collaborators who have helped me in many discussions and side projects: Matti Mäntysalo, Riikka Mikkonen, Tomi Rynänen, Minna Kellomäki, Janne Koivisto, Sampo Tuukkanen, and Juhani Virtanen. I would also like to acknowledge students who I have supervised and who have contributed to this thesis work: Qi Yuan, Simon Winkler, and Akseli Leino.

Last but not least, I want to express my gratitude to my family, friends, and relatives who have pulled me out of the scientific bubble and kept me busy in my free time. The support of my parents and help of parents-in-law has been invaluable over the years. I thank my friends who have kept me informed of real life and organized fun activities. I especially want to thank my children who have had to be the most patient when the working days have stretched into the evenings and



weekends. Thank you Ville, in good and bad times, your support and companionship has always been there.

Mari Lehti-Polojärvi  
Tampere, 25 July 2023



# ABSTRACT

The research on stem cell-derived cells and tissues is transitioning from traditional two-dimensional (2D) cultures into *in vivo* mimicking three-dimensional (3D) cell-biomaterial constructs. These 3D cultures enable novel solutions for disease models, toxicology studies, drug development, and precision medicine. However, assessing the state of the live 3D constructs requires advanced measurement and imaging techniques. Optical microscopy techniques are commonly used to image *in vitro* specimens, but imaging of the mesoscopic 3D constructs is challenging due to their thickness that causes the loss of optical signal. In addition, many optical imaging techniques are phototoxic or require staining/optical clearing of the specimens that renders them unusable for further culturing. Therefore, there is a need for novel 3D imaging techniques.

Multimodal imaging approaches produce multiphysical information of the specimen and enable to combine the strengths of different techniques. The approach of this doctoral thesis work was to develop a novel electrical impedance tomography (EIT) technique and integrate it with an optical projection tomography (OPT) system. EIT is an imaging technique where specimen's electrical conductivity is reconstructed based on several current injections and voltage measurements on the specimen surface. If these electrical measurements are conducted at different frequencies, the technique is called multifrequency EIT (mfEIT). In OPT, projection images are acquired from many view angles around the specimen and a morphological 3D image is reconstructed.

The aim of this dissertation was to create a novel method for 3D specimen investigation by developing an integrated OPT-mfEIT technique. First, the mfEIT was designed to be suitable for the integration: electrode configurations, imaging chambers, and rotational measurement protocols were developed. In addition, rotational reconstruction algorithms and data fusion techniques were developed to obtain multiphysical image reconstructions. Secondly, the functionality of a new mfEIT device was demonstrated with plant phantoms. The frequency dependent conductivities of the plants were well shown in the reconstructed images. Thirdly, the final developed 3D OPT-mfEIT was experimentally validated with a plant phantom, spheroids, and *ex vivo* tissues. The resulting images revealed both the

specimen's 3D morphology and conductivity at multiple frequencies. The derived conductivity spectra enabled the detection of stem cells in biomaterial spheroids and the analysis of cell membranes integrity in tissues.

In conclusion, this dissertation presents a new technique for the mesoscopic scale 3D imaging. The developed OPT-mfEIT technique can be used to image and assess various 3D specimens such as spheroids and organoids, that are challenging to image with traditional microscopy techniques. The obtained conductivity spectrum enables novel analysis of the biological specimens because electrical conductivity is not available with traditional microscopy techniques. Applications of *in vitro* EIT are relatively new in the field of biological specimen imaging, and more validation studies are needed on the correlation of biological phenomena and the resulting conductivity images. OPT-mfEIT provides a tool for such validation studies. Overall, this technique is expected to open new avenues in 3D tissue engineering research and contribute to advance the tissue engineering methods towards clinical applications.

# TIIVISTELMÄ

Kantasoluperäisten solujen ja kudosten tutkimus on siirtymässä kolmiulotteisia (3D) *in vivo* rakenteita jäljittelevään viljelyyn perinteisten kaksiulotteisten (2D) viljelmien sijaan. Nämä 3D-viljelmät mahdollistavat uusia ratkaisuja tautimalleihin, toksikologisiin tutkimuksiin, lääkekehitykseen ja tarkkuuslääketieteeseen. Elävien 3D-rakenteiden arvioiminen vaatii kuitenkin kehittyneitä mittaus- ja kuvantamistekniikoita. Optisia mikroskopiitekniikoita käytetään yleisesti *in vitro* näytteiden kuvaamiseen, mutta mesoskooppisten 3D-rakenteiden kuvantaminen on haastavaa niiden paksuuden vuoksi, joka aiheuttaa optisen signaalin heikkenemistä. Lisäksi monet optiset kuvantamistekniikat ovat fototoksisia tai vaativat näytteiden värjäämistä/optista puhdistamista, mikä tekee niistä käyttökelvottomia jatkoviljelyä varten. Näiden syiden vuoksi uusille 3D-kuvantamistekniikoille on tarve.

Multimodaaliset kuvantamismenetelmät tuottavat monifysikaalista tietoa näytteestä ja mahdollistavat hyötymisen eri tekniikoiden vahvuuksista. Tämän väitöstyön lähtökohtana oli kehittää uusi sähköinen impedanssitomografia (EIT) tekniikka ja integroida se optiseen projektiotomografia (OPT) järjestelmään. EIT on kuvantamistekniikka, jolla rekonstruoidaan näytteen sähkönjohtavuus useiden näytteen pinnalta tehtävien virtainjektioiden ja jännitemittausten perusteella. Jos nämä sähköiset mittaukset suoritetaan eri taajuuksilla, tekniikkaa kutsutaan monitaajuus-EIT:ksi (mfEIT). OPT kuvauksessa näytteestä otetaan projektiokuvia useista kuvakulmista, joiden perusteella rekonstruoidaan morfologinen 3D-kuva.

Tämän väitöskirjan tavoitteena oli luoda uusi menetelmä 3D-näytteiden tutkimukseen kehittämällä integroitu OPT-mfEIT-tekniikka. Ensin mfEIT kehitettiin integrointiin sopivaksi: elektrodikonfiguraatiot, kuvantamiskammiot ja rotaatiomittausprotokollat suunniteltiin ja testattiin. Lisäksi kehitettiin rekonstruktioalgoritmeja ja datafuusiotekniikoita monifysikaalisten kuvien rekonstruoimiseen. Toiseksi uuden mfEIT-laitteen toimivuus osoitettiin kasvifantomilla. Kasvien taajuudesta riippuvat johtavuudet näkyivät hyvin rekonstruoiduissa monitaajuuskuvissa. Kolmanneksi lopullinen kehitetty 3D OPT-mfEIT validoitiin kokeellisesti kasvifantomilla, sferoideilla ja *ex vivo* kudoksilla. Tuloksena saadut kuvat paljastivat sekä näytteen 3D-morfologian että johtavuuden useilla taajuuksilla. Rekonstruktioista johdetut johtavuusspektrit mahdollistivat

kantasolujen havaitsemisen biomateriaalisferoideissa ja solukalvojen eheyden analysoinnin kudoksissa.

Johtopäätöksenä voidaan todeta, että tämä väitöskirja esittelee uuden tekniikan mesoskooppisen mittakaavan 3D-kuvaukseen. Kehitetyllä OPT-mfEIT-tekniikalla voidaan kuvata ja arvioida erilaisia 3D-näytteitä, kuten sferoideja ja organoideja, joita on haastavaa kuvata perinteisillä mikroskopiakäyttötekniikoilla. Tuloksena saatu johtavuusspektri mahdollistaa uudenlaisen analyysin biologisista näytteistä koska perinteisillä mikroskopiakäyttötekniikoilla sähkön johtavuutta ei voida selvittää. *In vitro* EIT:n sovellukset ovat suhteellisen uusia biologisten näytteiden kuvantamisen alalla, joten biologisten ilmiöiden ja johtavuuskuvien korrelaatiosta tarvitaan lisää validointitutkimuksia. OPT-mfEIT tarjoaa työkalun tällaisiin validointitutkimuksiin. Kaiken kaikkiaan tämän tekniikan odotetaan avaavan uusia mahdollisuuksia 3D-kudosteknologian tutkimukseen ja edistävän kudosteknologisia menetelmiä kohti kliinisiä sovelluksia.

# CONTENTS

1	Introduction.....	21
2	Review of the literature .....	23
2.1	Biological background .....	23
2.1.1	Cells, tissues, and organs.....	23
2.1.2	Stem cells.....	24
2.1.3	3D cell and tissue cultures .....	24
2.2	Overview of 3D <i>in vitro</i> imaging.....	25
2.2.1	General features of <i>in vitro</i> imaging.....	25
2.2.2	Optical imaging methods.....	26
2.2.3	Optical projection tomography (OPT) .....	27
2.2.4	Other imaging methods .....	28
2.3	Electrical impedance .....	30
2.4	Impedance spectroscopy and measurement configurations.....	31
2.5	Electrical bioimpedance .....	33
2.6	Impedance spectroscopy <i>in vitro</i> applications .....	34
2.7	Lead field theory and impedance measurement patterns.....	35
2.8	Electrical impedance tomography (EIT).....	38
2.9	EIT image reconstruction .....	40
2.10	Multimodal EIT .....	42
2.11	Multimodal EIT applications.....	43
2.12	Rotational EIT.....	45
2.13	EIT <i>in vitro</i> hardware.....	46
2.13.1	Electrode configurations.....	46
2.13.2	Measurement patterns .....	47
2.13.3	Devices and mfEIT .....	48
2.14	EIT <i>in vitro</i> applications .....	49
3	Aims of the study .....	51
4	Methods.....	52
4.1	Overview of the multimodal system development.....	52
4.2	The developed OPT-mfEIT system.....	53
4.3	Electrode configurations .....	55
4.4	EIT patterns, OPT integration, and data acquisition .....	59

4.5	EIT devices .....	60
4.6	OPT image reconstruction and segmentation.....	61
4.7	EIT reconstruction methods .....	62
4.8	Statistical analysis.....	63
5	Materials .....	65
6	Summary of the results .....	67
6.1	Developing rotational mfEIT technique for multimodal setup(s).....	67
6.1.1	Numerical studies of electrode configurations.....	67
6.1.2	Effect of measurement patterns.....	67
6.1.3	Number of rotational measurement positions .....	68
6.1.4	Spectro-EIT device.....	69
6.2	Multimodal imaging of <i>in vitro</i> specimens .....	72
6.2.1	Developed imaging chambers .....	72
6.2.2	Integrated OPT-mfEIT system.....	74
6.2.3	OPT-mfEIT results using smoothness priors.....	74
6.2.4	MfEIT results using structural priors from OPT .....	76
6.2.5	Repeatability of OPT-mfEIT .....	81
7	Discussion .....	83
7.1	Development of the multimodal system .....	83
7.2	Multimodal imaging of <i>in vitro</i> specimens .....	85
7.3	Strengths and limitations of the developed system.....	87
8	Summary and conclusions.....	90
9	References .....	92

*List of Figures*

<b>Figure 1.</b>	Complex impedance $Z$ can be presented either by its modulus $ Z $ and phase angle ( $\theta$ ) or by its real ( $\text{Re}(Z) = R$ ) and imaginary ( $\text{Im}(Z) = X$ ) parts.....	31
<b>Figure 2.</b>	Simplified schematic of cell suspension in induced alternating current field between two electrodes. Arrows indicate the high and low frequency current paths and equivalent electrical circuit models the electrical properties of cells and extracellular medium: extracellular resistance ( $R_e$ ), cell membrane resistance ( $R_m$ ), cell membrane capacitance ( $C_m$ ), and intracellular resistance ( $R_i$ ).....	34



<b>Figure 3.</b>	Simulated lead fields and sensitivity distributions of two different tetrapolar measurement patterns applied to a phantom (conductivity 0.22 S/m) with a resistive inclusion (conductivity 0.02 S/m). Magenta arrows denote current lead field induced between electrodes I+ and I-, and blue arrows denote voltage sensing lead field induced between electrodes V+ and V-. Opposite pattern (a) lead fields and (b) sensitivity; edges pattern (c) lead fields and (d) sensitivity. The value of sensitivity (unit 1/m <sup>4</sup> ) depends on the magnitudes and directions of the lead fields.....	38
<b>Figure 4.</b>	Schematic of EIT measurement illustrating a 16-electrode scheme with an inclusion ( $\sigma_2$ ) and background ( $\sigma_1$ ) with differing conductivities. One possible current pattern (I) with sequential voltage measurements (V) is represented. The pattern needs to be repeated in other locations around the object.....	39
<b>Figure 5.</b>	Parts of the OPT-mfEIT system development and the related publications. a: (Koskela et al., 2019), b: (Winkler et al., 2021),c: (Yuan, 2020).....	53
<b>Figure 6.</b>	Flowchart of the final developed OPT-mfEIT system.....	54
<b>Figure 7.</b>	Schematic of the OPT-mfEIT system. MfEIT consisted of electrodes embedded on the opposing walls of the imaging chamber, wires, and the Spectro-EIT device. OPT consisted of LED illumination, rotation stage, optics, and a camera. The specimens were rotated in saline to enable electrical contact with the electrodes and refractive index matching path for OPT illumination. Adapted from (IV).....	55
<b>Figure 8.</b>	Trial 1 electrodes attached on the inner wall of a FEP tube to enable simultaneous OPT and mfEIT imaging.....	56
<b>Figure 9.</b>	Trial 2 electrodes. (a) Array with 16 electrodes and insulated conducting wires. (b) Electrodes rolled and placed into an OPT-mfEIT chamber. (c) Microscope image visualizing the cracking of the gold layer due to mechanical bending of the FEP sheet with electrodes.....	57
<b>Figure 10.</b>	Trial 3 electrode sheets (left) and their configuration in the imaging chamber (right) for 2D OPT-mfEIT imaging. Only the bottom layer of the electrodes was used in the measurements. ....	57
<b>Figure 11.</b>	Trial 4 electrode sheets (left) and their configuration in the imaging chamber (right) for 3D OPT-mfEIT imaging.....	58

**Figure 12.** Numbering of the electrodes in the trial 4 chamber. Novel EIT pattern was developed to obtain high sensitivity measurements of the whole volume with this configuration. Cylindrical shape represents the hydrogel-based rotated specimen. Adapted from (IV)..... 60

**Figure 13.** The opposite 4+4 electrode configuration was used in the experimental demonstration of the limited angle rotational EIT method. Plastic inclusions in different sizes and locations (cases (1)-(3)) were embedded in gelatin scaffold and rotated in the tank using 1-32 rotational measurement positions in 180° rotation. Conductivity changes along the dashed line of each reconstruction are shown in the graphs. The EIT domain was 28 cm in diameter. Reproduced from (I)..... 69

**Figure 14.** Examples of raw impedance data collected with the Spectro-EIT device and 16-electrode tank. (a) Measurements of a triangular yellow beetroot (plant) and reference data (saline) conducted with the opposite pattern. (b) Measurements of rectangular potato and reference data (saline) conducted with the all pattern. .... 70

**Figure 15.** Spectro-EIT device verification. Frequency-difference (top row) and time-difference EIT images (second and third row) of plant phantoms in saline. Triangular yellow beetroot measurements were conducted with the opposite pattern and the rectangular potato with the all pattern. The tank diameter was 22 cm. Conductivity changes along the dashed vertical line of each reconstruction are shown in the graphs. Top rows adapted from (II) and bottom row from (III)..... 71

**Figure 16.** First results of a combined OPT-mfEIT using the trial 1 electrodes. (a) Imaging chamber with a rotated plastic tube in saline. (b) OPT reconstruction of the tube (diameter 3.6 mm). (c) Time-difference EIT reconstruction of the same tube inside the 13 mm wide EIT domain..... 72

**Figure 17.** Trial 3 OPT-mfEIT chamber with a carrot rotated in saline. .... 73

**Figure 18.** Trial 4 electrodes built into the rectangular OPT-mfEIT chamber. Two pieces of tissues embedded in agarose hydrogel are rotated in saline. .... 73

**Figure 19.** Photograph of the OPT-mfEIT setup. 1: Spectro-EIT device, 2: LED and telecentric lens for OPT illumination, 3: electrode chamber, 4: stage for specimen placement, alignment, and rotation, 5: OPT camera..... 74

<b>Figure 20.</b>	OPT-mfEIT smoothness prior results. (a) OPT reconstruction and 2D time-difference mfEIT reconstructions of a rectangular carrot. The EIT domain was 6 mm x 9 mm in the xy-plane. Adapted from (III). (b) OPT reconstruction and absolute 3D mfEIT reconstructions of a potato. A plane at height 1.3 mm from the chamber bottom is visualized at each frequency. The dimensions of the EIT domain were $(x,y,z) = (6, 9, 4)$ mm. Adapted from (IV). .....	76
<b>Figure 21.</b>	OPT-mfEIT reconstructions of a tetrahedral piece of fresh potato. Left: OPT-mfEIT reconstruction at 7 kHz. Right: conductivity spectra derived from OPT-mfEIT reconstructions at 15 frequencies from 1 kHz to 349 kHz. Background consisted of saline and agarose hydrogel and is indicated as yellow color in both images. Adapted from (IV).....	77
<b>Figure 22.</b>	OPT-mfEIT reconstructions at 7 kHz of four specimens: (a) cells in biomaterial 1, (b) cells in biomaterial 2, (c) blank biomaterial 1, and (d) blank biomaterial 2. The conductivity of each segment is marked below each image and the rest of the volume is background.....	78
<b>Figure 23.</b>	Conductivity spectra derived from the OPT-mfEIT reconstructions of the spheroid specimens at 15 frequencies. Left: conductivity spectrum of each spheroid or specimen's background. Right: mean $\pm$ standard deviation of parallel segments. Adapted from (IV).....	78
<b>Figure 24.</b>	OPT-mfEIT reconstructions at 7 kHz of four specimens: (a) liver 1 (fresh), (b) liver 2 (treated), (c) liver 3 (fresh and treated), and (d) liver 4 (fresh and treated). The conductivity of each segment is marked below each image and the rest of the volume is background.....	80
<b>Figure 25.</b>	Conductivity spectra derived from the OPT-mfEIT reconstructions of the liver specimens at 15 frequencies. Left: conductivity spectrum of each liver tissue or specimen's background. Right: mean $\pm$ standard deviation of parallel segments. Adapted from (IV).....	80
<b>Figure 26.</b>	Mean and standard deviation of the background conductivities from nine specimens presented in the validation experiments in Figs. 21, 23, and 25.....	81

List of Tables

<b>Table 1.</b>	Properties of 3D imaging modalities in <i>in vitro</i> research. ....	29
<b>Table 2.</b>	Electrode systems, measurement patterns, and data collection schemes used in the experiments of each publication.....	59

# ABBREVIATIONS

2D	Two-dimensional
2P / MPM	Two- or multiphoton microscopy
3D	Three-dimensional
ECM	Extracellular matrix
EIDORS	Electrical Impedance Tomography and Diffuse Optical Tomography Reconstruction Software
EIT	Electrical impedance tomography
FEP	Fluorinated ethylene propylene
hiPS	Human induced pluripotent stem
iPS	Induced pluripotent stem
LED	Light-emitting diode
mfEIT	multifrequency electrical impedance tomography
OCT	Optical coherence tomography
OPT	Optical projection tomography
OPT-mfEIT	Integrated OPT and mfEIT
PAM	Photoacoustic microscopy
sCMOS	Scientific complementary metal-oxide-semiconductor
SEM	Scanning electron microscopy
SNR	Signal-to-noise ratio
SPIM	Selective plane illumination microscopy
TEM	Transmission electron microscopy
X-ray $\mu$ CT	X-ray micro computed tomography

# ORIGINAL PUBLICATIONS

This thesis is based on the following original publications, which are referred in the text by the Roman numerals **I-IV**. The original publications are reproduced at the end of this thesis with the permission of the copyright holders.

- I**        **Lehti-Polojärvi M\***, Koskela O\*, Seppänen A, Figueiras E, Hyttinen J. Rotational electrical impedance tomography using electrodes with limited surface coverage provides window for multimodal sensing. *Measurement Science and Technology*, vol. 29, issue 2, 02540, 2018. DOI: <http://dx.doi.org/10.1088/1361-6501/aa97f1>
- II**        Min M, **Lehti-Polojärvi M**, Hyttinen J, Rist M, Land R, Annus P. Bioimpedance spectro-tomography system using binary multifrequency excitation. *International journal of bioelectromagnetism*, vol 20, issue 1, 76-79, 2018. DOI: 10.18154/RWTH-CONV-224930
- III**       **Lehti-Polojärvi M**, Koskela O, Hyttinen J. Multifrequency electrical impedance tomography in biological applications: A multimodal perspective. In *Bioimpedance and Spectroscopy*, Annus P, Min M (eds.), Academic Press, 157-189, 2021. DOI: <https://doi.org/10.1016/B978-0-12-818614-5.00005-9>
- IV**        **Lehti-Polojärvi M\***, Räsänen MJ\*, Viiri LE, Vuorenpää H, Miettinen S, Seppänen A, Hyttinen J. Retrieval of the Conductivity Spectrum of Tissues *in-vitro* with Novel Multimodal Tomography. *Physics in Medicine and Biology*, 2021. DOI: <https://doi.org/10.1088/1361-6560/ac2b7f>

\* Authors contributed equally

# AUTHOR'S CONTRIBUTION

- I** M. Lehti-Polojärvi designed the study together with coauthors. The experimental parts of the study were performed by M. Lehti-Polojärvi, including setup design and measurements. Data analysis of experimental data was done by M. Lehti-Polojärvi using the reconstruction algorithm made by O. Koskela. The manuscript was written together by the shared first authors M. Lehti-Polojärvi and O. Koskela.
- II** M. Lehti-Polojärvi participated in the design of the measurement system. She made the reconstruction algorithm based on open source EIDORS package (Adler & Lionheart, 2006) and performed experimental data analysis. In writing tasks, her contribution included producing figures and writing the parts regarding experiments, as well as participating in the revision.
- III** M. Lehti-Polojärvi designed the book chapter and conducted experimental data analysis. She wrote and revised the manuscript as the first author.
- IV** M. Lehti-Polojärvi designed the study together with coauthors. She built the experimental setup and designed and performed the measurements. Data analysis and writing of the manuscript were done together with M. Räsänen.

# 1 INTRODUCTION

The research on stem cell-derived cells and tissues grown in biomaterials and microphysiological systems is rapidly developing to produce novel solutions for disease models, toxicology studies, drug development, and precision medicine (Fang & Eglen, 2017; Gomes et al., 2017). The great advantage in stem cell-based assays is the possibility to use cells of human origin that allows to avoid the cost-intensive and often ineffective animal testing (Edmondson et al., 2014; Fang & Eglen, 2017; Kim et al., 2020). Further, the ongoing transition from two-dimensional (2D) to three-dimensional (3D) cell cultures allows to obtain more realistic *in vivo* mimicking cultures instead of cells grown, for example, on chips or well plates. Although 3D constructs offer relevant environment for cells to grow and differentiate, they also pose challenges regarding monitoring and imaging.

Optical microscopy techniques are most used in the cell culture research, and they are well developed especially for 2D imaging. However, the thickness and possible nontransparent features of the 3D cultures hinders the use of optical microscopy. Non-harmful monitoring of 3D cultures is particularly challenging since many current methods require mechanical sectioning and/or staining of the specimen and are thus endpoint assessments. Therefore, new monitoring and imaging techniques are needed to assess 3D cultures in the mesoscopic scale. (Booij et al., 2019; De León et al., 2020; Fang & Eglen, 2017)

Tomography refers to methods that noninvasively visualize the insides of an object and is associated with 3D imaging techniques. Electrical impedance tomography (EIT) is a 3D visualization technique that has been used in many fields of science such as geology and medical imaging. For example, lung ventilation (Tomicic & Cornejo, 2019) and brain imaging (Ouypornkochagorn et al., 2022; Toivanen et al., 2021) EIT applications have been demonstrated for clinical use. Recently EIT applications have emerged also in *in vitro* research (Linderholm et al., 2008; Sun et al., 2010; Wu, Zhou, et al., 2018).

In EIT, electrical current is injected and voltages are measured at several locations around the specimen. The acquired data is reconstructed to visualize the conductivity or conductivity change in the specimen. If current injections are applied at different frequencies, the technique is called multifrequency EIT (mfEIT). Because the

electrical properties of the cell and tissue specimens change due to cell proliferation (Canali, Heiskanen, et al., 2015), differentiation (Bagnaninchi et al., 2018; Hildebrandt et al., 2010), and cell death (L. Gong et al., 2021; Halonen et al., 2022), EIT can provide a monitoring tool for such specimens. Despite the spatial resolution of EIT is limited, its advantages make it an attractive technique for *in vitro* studies: label-free imaging, high temporal resolution, and ability to visualize optically opaque specimens.

Optical projection tomography (OPT) is another solution for noninvasive 3D visualizations of the mesoscopic cell cultures (Belay et al., 2021; Sharpe et al., 2002). In OPT, projection images are collected of a rotated specimen. These projections are 3D reconstructed to visualize the specimen morphology.

Multimodal imaging aims to combine the strengths of different modalities to gain more information of the complex biological phenomena. For example, EIT has been integrated with ultrasound to create a noninvasive clinical diagnostic tool for muscle health evaluation (E. K. Murphy et al., 2019). EIT has also been integrated with optical microscopy to image *in vitro* specimens (Z. Liu et al., 2020, 2022). This thesis presents a novel multimodal approach where mfEIT was integrated with OPT to acquire both specimen morphology and electrical conductivity spectra of *in vitro* specimens in 3D. The novelty of this work is based on (1) integrating two inherently 3D imaging methods that enable 3D reconstructions of the specimen, and (2) data fusion that makes solving of accurate conductivity spectra possible that provides novel means for quantitative analysis.

The aim of this thesis was to develop a new tool for 3D *in vitro* imaging. The developed OPT-mfEIT was used to assess the integrity of *ex vivo* human and porcine tissues and to detect stem cells in biomaterial spheroids. This tool offers a new label-free and noninvasive solution for mesoscopic scale 3D imaging that provides the morphology and electrical conductivity spectra of even optically opaque samples. Conductivity information provides novel analysis possibilities for the research of cell and tissue culture growth.



## 2 REVIEW OF THE LITERATURE

### 2.1 Biological background

#### 2.1.1 Cells, tissues, and organs

The fundamental units of all living organisms are cells. In a simplified form, cells contain various internal organelles such as nucleus and endoplasmic reticulum embedded in aqueous cytosol and enclosed by cell membrane. Cell membrane is a thin lipid bilayer that separates cytoplasm from its surroundings and contains proteins for ion and molecule transportation and sensing. (Alberts et al., 2014)

Cells secrete extracellular matrix (ECM) around themselves, and together cell populations and ECM form cooperative assemblies called tissues. In plants, the ECM consists of tiny boxlike structures attached to each other creating a protecting cell wall around each cell. The cell wall composes mainly of cellulose and other polysaccharides and its task is to provide mechanical strength for the plant. In animal tissues, there are no such cell walls and ECM can have various forms and amounts depending on the tissue type. Animal cells can be attached to each other via ECM or directly via cell junctions. (Alberts et al., 2014)

Main tissue types in humans are epithelial, connective, muscle, and nervous tissues. For example, epithelial tissues are formed of single or multiple cell layers and their mechanical strength is based on the direct cell-cell junctions with scarce amount of ECM. Whereas connective tissues are composed of cells, ECM, and fibers (collagen, reticular, and elastin) and their properties depend on the composition of the ECM. For example, bones are dense connective tissues due of the high concentration of fibers in the ECM. Many tissue types together form organs, such as heart or liver, that act together to produce a specific function, such as pump blood or metabolize substances. (Alberts et al., 2014; Moreau et al., 2002)

## 2.1.2 Stem cells

The main features of stem cells are their ability to divide (proliferate) and differentiate – unlike many of the specialized cells that cannot divide themselves. The specialized terminally differentiated cells, such as red blood cells, need to be continuously replaced. The renewal of cells is taken care by adult stem cells that are preserved in the corresponding tissues. Adult stem cells are multipotent: they can only differentiate into specific cell types. Another stem cell type are embryonic stem cells that are derived from mammalian blastocysts. They are pluripotent, hence, they can differentiate into any cell type. (Alberts et al., 2014)

Due to ethical issues and poor availability of embryonic stem cells, Takahashi & Yamanaka (2006) developed a method to induce pluripotency in somatic cells (Takahashi & Yamanaka, 2006). These induced pluripotent stem (iPS) cells – or hiPS cells if they are of human origin – enable the use of patients own somatic cells in various stem cell-based treatments, drug testing, and disease models (Yamanaka, 2009). In theory, any adult cell type can be reprogrammed to iPS cells and then differentiated to form a desired tissue type.

## 2.1.3 3D cell and tissue cultures

Most of the *in vivo* tissues are naturally in 3D instead of planar 2D surfaces. It has been shown that chemical and mechanical microenvironments are very different in 2D and 3D cell cultures that affects the functionality and spatial organization of the cells, as reviewed in (Duval et al., 2017; Edmondson et al., 2014; Fang & Eglén, 2017). For example, cell-cell interaction and nutrient access differ in 2D and 3D environments. Therefore, *in vivo* mimicking 3D cell cultures have emerged in cell biology applications.

There are various forms of 3D cell cultures: biomaterial-based scaffolds and hydrogels, spheroids, organoids, bioprinted tissues, and organ-on-chip models. The 3D cultures can contain single or many different cell types (cocultures). Biomaterial-based scaffolds and hydrogels are used to generate a physiologically relevant microenvironment for cells to grow. They can be made of natural biological materials or synthetic materials, and fabricated with various techniques, such as electrospinning or 3D printing, depending on the desired geometry and mechanical and chemical properties. Spheroids are self-aggregated multicellular cultures that can be formed from various cell types. They have been traditionally used in tumor studies. Organoids are used to mimic *in vivo* organ functions and they consist of

various organ-specific cells grown in highly organized manner. They are grown from stem cells or cells derived from tissue. Bioprinted tissues are another form of 3D cultures that produce a desired microarchitecture. There are various fabrication techniques, such as layer-by-layer extrusion, but the main idea of bioprinting is to combine living cells, biological materials and biochemicals into a custom-made geometry. Organ-on-chip models are used to mimic a human organ grown on a microfluidic chip. Systems that connect multiple organs are called body-on-chip or multiorgan-on-chip models, where the organ-organ interactions can be studied. (Dellaquila et al., 2021; Fang & Eglén, 2017)

Building 3D cultures *in vitro* has many challenges, such as reproducibility, incorporation of different cell types, challenges in monitoring and imaging, and suitable scaffold design and its biocompatibility. Despite all the challenges, there is a wide consensus of the need to apply 3D assays in cell and tissue research. (Dellaquila et al., 2021; Duval et al., 2017; Edmondson et al., 2014; Gomes et al., 2017)

## 2.2 Overview of 3D *in vitro* imaging

### 2.2.1 General features of *in vitro* imaging

Imaging is needed for quality and quantity assessment of cell cultures and evaluation of the cell behavior and structure in cultures. 3D imaging techniques require data acquisitions from several planes, thus, the amount of collected data is large compared to 2D imaging. Large amount of data significantly increases the acquisition and postprocessing time and poses a challenge for high-throughput 3D systems. In addition, 3D specimens introduce challenges in the imaging preparation such as specimen placement, and they might require modifications to staining protocols due to specimen thickness. However, several 3D imaging techniques have been developed for *in vitro* imaging. A summary of the properties of the 3D imaging modalities used in *in vitro* research is presented in Table 1.

Imaging modalities in general are based on certain contrast mechanisms that result from the interactions of an induced energy – such as electromagnetic or electrical energy – with the specimen. The resulting images are created from the changes in the applied and detected energy after interaction events such as scattering, reflection, absorption, or luminescence. The type and frequency of the induced energy together with the imaging system and specimen characteristics determines the

possible imaging depth, spatial and temporal resolution, and contrast of the resulting images. (Appel et al., 2013; Booiij et al., 2019; Nam et al., 2015) The harmfulness of the modality depends on the intensity of the applied energy and the need of chemical specimen manipulation. Some imaging methods are endpoint methods that render the specimen unusable for further exploitation due to, for example, phototoxicity or clearing reagents. Other methods are less harmful and can be used to monitor the development of cell and tissue cultures.

Another important feature of 3D imaging modalities is how the images are generated from the raw data. Volume scanning techniques stack the raw data directly to produce images, whereas other methods need to reconstruct the raw data with inversion algorithms. Many optical imaging methods are scanning techniques where the specimen is imaged sequentially point-by-point of one plane at a time. This raw data can be stacked to a 3D matrix that represents the specimen volume. The reconstruction-based methods typically acquire data from the entire specimen volume collected from several view angles. In these cases, mathematical forward and inverse models, and possibly also priors are used to produce an image. (Ntziachristos, 2010)

## 2.2.2 Optical imaging methods

Optical imaging methods are the most used imaging techniques in *in vitro* research. They can provide high spatial accuracy for even subcellular features and molecular visualization. However, the imaging depth is often limited to couple hundred microns due to light scattering and disturbances from out-of-focus areas (Appel et al., 2013; Ntziachristos, 2010). Optical imaging methods can be divided into brightfield and fluorescence modes. Brightfield microscopes image the transmission of applied light through the specimen. Fluorescence microscopes excite fluorophores in the specimen with a specific wavelength and collect the emitted light at a different wavelength. Fluorescence can originate from biological molecules' intrinsic fluorescence or by label molecules with an extrinsic fluorophore.

Widefield microscopes are basic tools in most laboratories, and they provide relatively fast tool for specimen checkups. Widefield microscopes illuminate the whole specimen at once, thus out-of-focus signals disturb the image quality. To gain better spatial resolution, laser illumination techniques have been developed. Confocal microscopy is commonly used in 3D cell culture research: the specimen is scanned with a laser point source and a pinhole is used to reduce the collection of

light from out-of-focus areas. 3D images are obtained by scanning the specimen at different depths and stacking these image planes together. Limiting factors of confocal imaging are its limited throughput and photobleaching. (Appel et al., 2013; Ntziachristos, 2010)

Two- or multiphoton microscopies (2P/MPM) are fluorescence imaging methods that apply short laser pulses for exciting the fluorophores in the specimen. The excitation is spatially and temporally confined to the focus point, hence emitted photons arrive from a known location in the volume and a pinhole is not needed. Compared to confocal microscopy longer wavelengths are applied, thus, 2P/MPM can image thicker specimens with slightly lower spatial resolution. (Ntziachristos, 2010)

Selective plane illumination microscopy (SPIM) offers a practical 3D imaging technique where a thin light sheet illuminates one plane of the specimen at a time to excite exclusively the fluorophores in the illuminated plane. These imaged planes can be stacked to form a visualization of the specimen 3D volume. The spatial resolution is slightly poorer than in confocal microscopy but also, the use of light sheet reduces photobleaching and enables larger imaging depth and throughput. (Huisken et al., 2004)

Optical coherence tomography (OCT) detects reflected and scattered light from the specimen by matching the coherence of illuminated and collected light. It is an optical analogue to ultrasound imaging as echo time delay and magnitude of the reflected light are detected. OCT can image even couple of millimeters thick specimens. It only operates in brightfield mode and cannot be used for fluorescence imaging where excitation and emission light has differing wavelengths. (Appel et al., 2013; D. Huang et al., 1991; Ntziachristos, 2010)

Photoacoustic microscopy (PAM) combines optical illumination with ultrasound detection. Short light pulses transform to heat in the light absorbing structures such as hemoglobin. This creates sound waves that are detected with ultrasound transducers. Hence, the method combines spatial resolution of optical imaging and penetration depth of ultrasound imaging. (Appel et al., 2013; Ntziachristos, 2010)

### 2.2.3 Optical projection tomography (OPT)

Optical projection tomography (OPT) is an optical equivalent to X-ray imaging: specimens are prepared in transparent media to minimize scattering and images are formed mainly based on the absorbance of light transmitted through the specimen.

Thus, similar back-projection reconstruction algorithms can be applied as in X-ray computed tomography. OPT illumination is done with telecentric/nonfocused light beam through the whole specimen, so scattering and out-of-focus areas disturb the focus plane images. This causes the spatial resolution of OPT to be poorer than, for example, in confocal microscopy. In brightfield mode, a specimen attached to a rotational motor is illuminated with a white light beam. An image is acquired at each rotational position, and this raw data is postprocessed for 3D reconstruction of the specimen volume. In fluorescence mode, epi-illumination is typically used, and emitted light is collected from the rotated specimen. OPT offers a noninvasive 3D imaging method that is optimally suited for cleared or naturally transparent specimens, such as hydrogel-based cell cultures, that can be up to couple of millimeters thick. (Belay et al., 2021; Figueiras et al., 2014; Ntziachristos, 2010; Sharpe et al., 2002)

## 2.2.4 Other imaging methods

Other imaging methods are available for 3D *in vitro* imaging. One of them is X-ray micro computed tomography (X-ray  $\mu$ CT) where an ionizing X-ray beam is transmitted through the specimen and a 2D projection image is recorded by an X-ray detector. X-ray  $\mu$ CT provides an effective tool for 3D imaging since the penetration depth and spatial resolution are high, although the contrast in soft tissues is often low. (Appel et al., 2013) The application of contrast agents in X-ray  $\mu$ CT creates new possibilities for soft tissue and cell culture imaging (Tamminen et al., 2020).

Scanning electron microscopy (SEM) and transmission electron microscopy (TEM) techniques have probably the highest spatial resolutions available for *in vitro* imaging, enabling nanoscale images (Y. S. Zhang & Yao, 2018). The main disadvantages of these techniques are the limited specimen penetration depth, the imaging is limited to 2D, specimen preparation is challenging, and living cells are difficult to image.

EIT has emerged as an option for 3D *in vitro* imaging. In EIT, a low amplitude electrical current is applied through the specimen and induced voltages are measured. The method is sensitive for electrical conductivity variations in the specimen. The diffusive nature of the electrical current flow causes poor spatial resolution and, thus, effective inverse problem solutions are needed to obtain high-quality image reconstructions. However, EIT is label-free, has no known harmful effects, and it is

inherently a 3D method because electrical current flows throughout the whole volume of the specimen. Also, imaging of optically opaque specimens is feasible with EIT. (Wu, Zhou, et al., 2018)

**Table 1.** Properties of 3D imaging modalities in *in vitro* research<sup>a</sup>.

Modality	Contrast mechanism	Typical imaging depth	Spatial resolution	Inversion needed	Advantages	Limitations
Confocal	Fluorescent emission	350 $\mu\text{m}$	<1 $\mu\text{m}$	No	High spatial resolution	High phototoxicity
2P/MPM	Fluorescent emission, optical scattering	1 mm	1 $\mu\text{m}$	No	High spatial resolution and penetration depth	High phototoxicity
SPIM	Fluorescent emission	<500 $\mu\text{m}$	<10 $\mu\text{m}$	No	High spatial and temporal resolution	Complex specimen preparation and alignment
OCT	Optical back scattering	1–5 mm	1–10 $\mu\text{m}$	No	High temporal resolution	Only brightfield mode, low chemical sensitivity
PAM	Optical absorption	1–20 mm	50–150 $\mu\text{m}$	No	High functional and chemical sensitivity, deep penetration	Coupling medium needed
OPT	Optical absorption, fluorescent emission	0.5–2 mm	>1 $\mu\text{m}$	Yes	High spatial resolution and penetration depth	Complex specimen preparation and alignment
X-ray $\mu\text{CT}$	X-ray absorption	100 $\mu\text{m}$ –1 m	1–1000 $\mu\text{m}$	Yes	High spatial resolution and penetration depth	Ionizing radiation, low chemical sensitivity
SEM/TEM	Electron scattering or diffraction	0.1 $\mu\text{m}$	1 nm	No	Nanoscale spatial resolution	Complex and invasive specimen preparation, low penetration depth
EIT	Electrical conductivity	Extensive	Low	Yes	No known harmful effects, deep penetration, dimensions scalable	Low spatial resolution, lack of specificity

<sup>a</sup> Data adapted from (Appel et al., 2013; Nam et al., 2015; Ntziachristos, 2010; Y. S. Zhang & Yao, 2018)

All imaging techniques have strengths and limitations, and a suitable modality needs to be chosen for each application. This decision is often a trade-off between specimen thickness/field of view and spatial resolution. Furthermore, high spatial

resolution techniques are typically harmful for living specimens. Multimodal imaging techniques are an attempt to tackle these challenges since they combine the strengths of two modalities, as it is discussed in sections 2.10 and 2.11.

## 2.3 Electrical impedance

Electrical impedance is a specimens' passive property to oppose an induced electrical current. It is measured by injecting an electrical stimulus – either a known voltage or current – through the specimen, and the resulting voltage or current is sensed. Impedance ( $Z$ ) is a complex-valued quantity that is determined as a ratio of voltage ( $V$ ) and current ( $I$ ) based on the Ohm's law  $Z = V/I$ . Impedance is measured with alternating current injection that has a certain frequency. Therefore, currents and voltages are time-variant, and they can have a phase difference depending on the measured specimen.

The measured impedance composes of both magnitude ( $|Z|$ ) and phase ( $\theta$ ), as is illustrated in Fig. 1. Impedance can be expressed in cartesian form

$$Z = R + jX \quad [\Omega], \quad (1)$$

where resistance  $R$  is the real part and reactance ( $X$ ) is the imaginary part of the impedance, and imaginary unit  $j = (-1)^{1/2}$ . Resistance can be defined as

$$R = \rho \frac{x}{A} \quad [\Omega], \quad (2)$$

where  $\rho$  is resistivity,  $x$  is the distance between voltage measuring electrodes, and  $A$  is the cross-sectional area of the specimen. For example, the impedance of an ideal resistor is purely real, thus its impedance would be  $R$ . Reactance is composed of capacitance and inductance, that are present if charge carriers accumulate in the specimen due to alternating current injection. For biological specimens, inductance is not prevailing, but capacitance ( $C$ ) is a characteristic. Hence, impedance of biological specimens can be expressed as

$$Z = R + \frac{1}{j\omega C} \quad [\Omega], \quad (3)$$

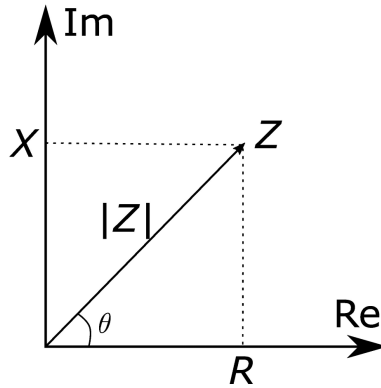
where  $\omega$  is angular frequency expressed in hertz (Hz). Capacitance of a plate capacitor is defined as



$$C = \varepsilon_0 \varepsilon_r \cdot \frac{A_c}{d} \quad [\text{F}], \quad (4)$$

where  $\varepsilon_0$  is the permittivity of vacuum,  $\varepsilon_r$  is relative permittivity,  $A_c$  is the area of the conductive plates, and  $d$  is the distance between the plates. Instead of this ideal capacitor, modified capacitances are often used to model cell membranes, for example, the constant phase element of the Cole model. (Klöggen et al., 2011; Simini & Bertemes-Filho, 2018)

**Figure 1.** Complex impedance  $Z$  can be presented either by its modulus  $|Z|$  and phase angle ( $\theta$ ) or by its real ( $\text{Re}(Z) = R$ ) and imaginary ( $\text{Im}(Z) = X$ ) parts.



According to equations (2)–(4), impedance value is dependent on the dimensions of the measured material and material specific properties: resistivity and permittivity. Conductivity ( $\sigma$ ) is the inverse of resistivity ( $\sigma = 1/\rho$ ) and is often used to describe materials' ability to conduct electrical current (unit siemens per meter (S/m)). Even though conductivity is a specific material property that is independent of the measurement dimensions, conductivity is dependent on the applied alternating current frequency and temperature of the material. (Grimnes & Martinsen, 2015; Simini & Bertemes-Filho, 2018)

## 2.4 Impedance spectroscopy and measurement configurations

Electrical impedance spectroscopy refers to impedance measurements where current injections are applied at several frequencies, typically in the range from 100 Hz to 10

MHz. The excitations are performed applying either a sinusoidal signal consecutively at different frequencies or a composite signal that includes several frequency components. The frequency components are then decomposed from the composite signal with signal processing methods, such as Fourier transform. In principle, the obtained information is the same with different waveforms if the excitation amplitude is low enough to assure linear conditions. One possibility is to use multifrequency binary excitation to obtain fast spectroscopic measurements at high signal-to-noise ratio (SNR). (Grimnes & Martinsen, 2015; Land et al., 2011; Min et al., 2012).

Typical impedance spectroscopy measurement setup consists of 2–4 electrodes that are galvanically coupled to the specimen and used to induce electrical current and measure voltages. Two-electrode (bipolar) systems use the same electrodes for both injection and voltage measurement. Four-electrode (tetrapolar) systems use one electrode pair for current injection and another electrode pair for voltage sensing. Three-electrode configuration is a mixture of these where voltage is measured between the current injection electrode and a third reference electrode.

The advantage of bipolar systems is that they are tolerant to movement errors that can be crucial when measuring, for example, humans. The drawback is that contact impedances of the electrode-specimen interface are merged in the sensed voltages that corrupt the impedance values in bipolar systems. The effect of contact impedances is minimized in tetrapolar systems where the voltage sensing circuit is separate from the current circuit. This is the main reason why tetrapolar configurations are preferred when feasible. The drawback of tetrapolar measurements is their sensitivity to movement errors if present.

Another important feature of electrode configurations is the induced sensitivity field that differ in bi- and tetrapolar systems, as is further discussed in section 2.7. Although tetrapolar systems are often preferred, both systems have been widely used. For example, impedance pneumography has been implemented both in bipolar (Luo et al., 1992) and tetrapolar (Seppä et al., 2010) schemes.

As mentioned in the previous section, impedance measurements depend on the setup geometry and electrode configuration. Therefore, impedance values are typically compared with reference data obtained with the same setup. This is especially important when measuring inhomogeneous specimens such as biological material. Reference data can be obtained, for example, from the same specimen measured at different time points or from blank saline or biomaterial.

## 2.5 Electrical bioimpedance

Electrical bioimpedance refers to impedance measurement of biological materials, such as tissues, either *in vivo* or *in vitro*. In contrast to electric circuits, the charge carriers inside biological specimens are ions instead of electrons. The measured bioimpedance produces information of the state and functionality of the specimen, such as cell viability.

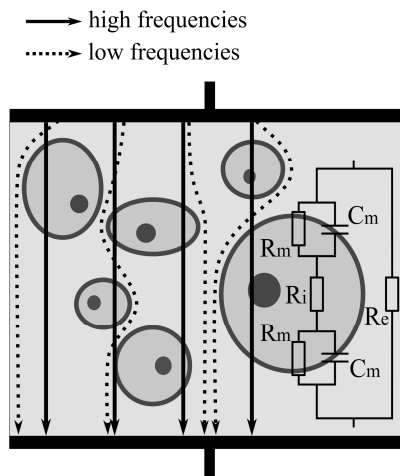
Impedance spectroscopy is the most frequent method used to measure bioimpedance. At low excitation frequencies, conductivity is dominant feature in biological specimens. As frequencies increase, ions become restricted to move and dielectric properties (i.e., capacitance) become dominant. In other words, conductivity increases and permittivity decreases along increasing frequency, and this typically leads to a decrease in the measured impedance as excitation frequencies increase. (Grimnes & Martinsen, 2015)

The frequency dependence of biological specimen's impedance has been described with three main dispersion mechanisms:  $\alpha$ ,  $\beta$ , and  $\gamma$  (Schwan, 1994). In principle, at each dispersion range specimen's permittivity decreases and conductivity increases. The  $\alpha$ -dispersion is difficult to measure since it arises below kHz frequencies where electrode polarization effects often corrupt the measurements. However,  $\alpha$ -dispersion has been shown to soon disappear as tissue dies. Commonly used frequency range in bioimpedance spectroscopy is from kHz to couple MHz, where the  $\beta$ -dispersion is dominating. At this range, the conductivity and permittivity changes are due to mechanisms of passive cell membrane capacitances, intracellular organelle membranes, and protein molecule responses. The  $\gamma$ -dispersion appears at GHz range and is associated with polarization of water molecules. (Grimnes & Martinsen, 2015)

Bioimpedance measurements can be modeled with various electrical equivalent circuits; one example is shown in Fig. 2 where a simplified schematic of cell suspension in alternating current electric field is shown. There are three main constituents that affect the measured bioimpedance in this case: cell membranes and intracellular (cytoplasm) and extracellular medium (ECM in case of tissues). The equivalent circuit forms two parallel current paths: one through the extracellular space, and another through the cells. Since capacitors conduct current poorly at low frequencies and the cell membrane resistance ( $R_m$ ) is typically high (in the range of  $M\Omega$ ), the low frequency current paths depend greatly on the extracellular resistance ( $R_e$ ). The value of resistance  $R_e$  depends on the ionic composition of extracellular medium and packing density of the cells. As discussed in section 2.1.1, ECM has

different compositions in different tissues, inducing distinct impedance values at low frequencies. At high frequencies, cell membrane capacitors ( $C_m$ ) start to conduct current, and intracellular resistance ( $R_i$ ) becomes involved in the current path. This leads to a decrease in impedance as current can flow through relatively well-conducting cytoplasm. (Klößen et al., 2011; Pethig & Kell, 1987)

**Figure 2.** Simplified schematic of cell suspension in induced alternating current field between two electrodes. Arrows indicate the high and low frequency current paths and equivalent electrical circuit models the electrical properties of cells and extracellular medium: extracellular resistance ( $R_e$ ), cell membrane resistance ( $R_m$ ), cell membrane capacitance ( $C_m$ ), and intracellular resistance ( $R_i$ ).



In practice, biological specimens are not as simple as is shown in Fig. 2 since varying cellular morphologies, cell-cell junctions, and cells intracellular organelles make the model more complex. In addition, tissues are not homogeneous and can be anisotropic with different conductivity in different directions, such as in muscle cells (Grimnes & Martinsen, 2015).

## 2.6 Impedance spectroscopy *in vitro* applications

The efficacy of impedance spectroscopy in cell and tissue culture studies has been established for many applications. The changes in cell morphology due to cell attachment, movement, proliferation and growth on a planar 2D electrode configuration have been well reported, for example in (Jaatinen et al., 2009; Keese & Giaever, 1994). The amount of biomass in a bioreactor has been monitored

(Justice et al., 2011), as well as proliferation of stem cells in 3D hydrogel scaffold (Canali, Heiskanen, et al., 2015). Stem cell differentiation (Bagnaninchi et al., 2018; Hildebrandt et al., 2010) and the maturation and integrity of stem cell derived epithelia (Onnela et al., 2012; Savolainen et al., 2011) produce significant changes in impedance. In addition, impedance spectroscopy of *in vivo* measurements have shown that tissue type can be identified (Halonen et al., 2019), and healthy liver tissue distinguished from tumor (Halonen et al., 2022) using a needle with embedded electrodes.

Cell and tissue viability is one of the most studied features in impedance spectroscopy applications, and it is often used as an indicator in drug testing and toxicity assays (L. Gong et al., 2021; Lei et al., 2014, 2018; Pan et al., 2020). Cell death – either necrosis or apoptosis – has a clear effect to cell membrane properties, which can be measured with impedance spectroscopy. In necrotic cell death, the cell membrane breaks and cytoplasm spreads uncontrollably to the surroundings. This decreases membrane resistance so that electrical current flows through the cytoplasm decreasing the measured impedance (Halonen et al., 2022). Necrosis is induced by external physical or chemical events, such as low/high temperature or lack of oxygen. Apoptotic cell death is a controlled process where the cell membrane remains intact, but cell size decreases, and cell-cell junctions disintegrate. This leads to changes in the measured impedance (Lei et al., 2014; Pan et al., 2020). Apoptosis is induced by the cell itself or by the signals from surrounding cells, for example due to DNA damage. (Alberts et al., 2014)

A single impedance spectroscopy measurement produces an average impedance of the measured volume. Spatial information of local differences in the specimen conductivity requires many measurements from different view angles. Couple of studies have used impedance spectroscopy to spatially map impedance values without image reconstruction and inversion methods: cardiac cells and brain tissue grown on a microelectrode array (Viswam et al., 2018), and human hepatoblastoma cells in 3D hydrogel scaffold with eight stick electrodes (Canali, Mazzoni, et al., 2015). To map the conductivities more accurately also from 3D specimens, EIT is an efficient method that is described in the next sections.

## 2.7 Lead field theory and impedance measurement patterns

Electrical current flows diffusively through the specimen volume. This makes the modeling of impedance measurements more complex than, for example, in X-ray

imaging where it is justified to assume that the detected photons traveled along a straight line. Lead field theory provides tools for modeling and assessing the effect of electrode locations and conductivity variations on the measured impedances. Originally, it was developed for electrocardiography (McFee & Johnston, 1953) and, further, for assessment of bioimpedance lead sensitivities (Geselowitz, 1971; Malmivuo & Plonsey, 1995). Applying the lead field theory in a finite element model (Hytinen et al., 1993) offered tools for simulating the sensitivity of, for example, various EIT measurement patterns (Kauppinen et al., 2006). EIT patterns are a collection of current injection and voltage sensing electrode pairs used in the measurements. Sensitivity simulations have been further used to design electrode configurations and measurement patterns, for example, for impedance spectroscopy setup applied to 3D tissue engineered specimens (Canali, Heiskanen, et al., 2015), single-cell microelectrode array measurements (Böttrich et al., 2017), and impedance measurements of epithelial tissues (Tervonen & Hytinen, 2018).

Injected current in impedance measurements forms a current density field in the specimen – called a lead field – that can be visualized with a vector field. According to the principle of reciprocity, the measured impedance value is the same if voltage sensing electrode pair and current injection electrode pair were interchanged. Possible deviations are due to nonidealities of the instrumentation that may lead to a reciprocity error. Also, the voltage sensing electrodes form a lead field that can be visualized with a vector field. The sensitivity  $S$  of a bioimpedance measurement can be calculated as a dot product of the current lead field  $J_{LI}$  and voltage lead field  $J_{LE}$  as

$$S = J_{LI} \cdot J_{LE}. \quad (5)$$

The direction and magnitude of the current density fields  $J_{LI}$  and  $J_{LE}$  depend on the electrode configuration and the specimen's shape and conductivity distribution, as is illustrated in Fig. 3 (a) and (c). It can be seen that current density fields are strong in well conducting regions and weak in poorly conducting regions. (Malmivuo & Plonsey, 1995)

The measured impedance  $Z$  depends on the conductivities  $\sigma$  in the volume  $V'$  and the sensitivity distribution  $S$  as follows

$$Z = \int_{V'} \frac{S}{\sigma} dV' = \int_{V'} \frac{1}{\sigma} J_{LI} \cdot J_{LE} dV'. \quad (6)$$

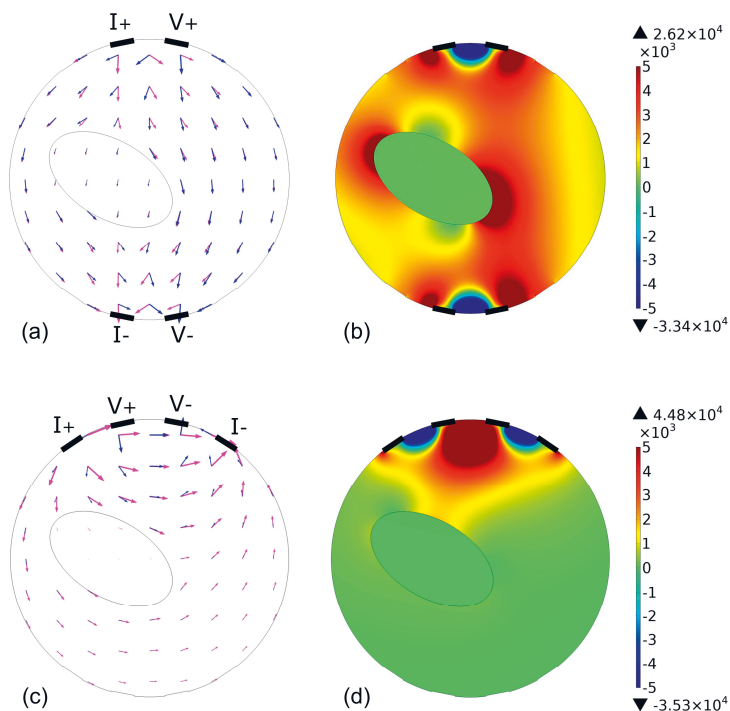
Sensitivity is a scalar field, and its value can be positive, negative, or zero depending on the angle and magnitude of the measurement and current feeding lead fields. In

the areas of positive sensitivity, a decrease of local conductivity leads to an increase in the measured impedance. In the areas of zero or close to zero sensitivity, conductivity changes are not detected. In the areas of negative sensitivity, a decrease of local conductivity leads to a decrease in the detected impedance. These are valid when the changes of the local conductivities are relatively small so that the lead fields are not drastically changed due to the change of conductivity. As an example, the lead fields and associated sensitivity distributions of two different tetrapolar measurement patterns are shown in Fig. 3 (b) and (d). (Kauppinen et al., 2006; Malmivuo & Plonsey, 1995)

The areas of negative or zero sensitivity complicate the analysis of the impedance results if sensitivity field is unknown. In bipolar configurations the  $J_{LI}$  and  $J_{LE}$  are parallel, thus, negative sensitivities are not present. However, in tetrapolar configurations the sensitivity field is more complex due to separate excitation and sensing electrode pairs. Despite this complexity, tetrapolar measurements enable to optimize the measurement pattern by focusing high sensitivity areas to the regions of interest.

EIT patterns typically consist of couple hundred impedance measurements that are used to reconstruct the conductivity image. Especially the areas of zero sensitivity should be considered when designing an EIT measurement pattern because conductivity variations in those regions would be undetected. Having different configurations of tetrapolar measurements in the pattern may be beneficial. For example, the opposite and edges pattern presented in Fig. 3 would complement each other.

**Figure 3.** Simulated lead fields and sensitivity distributions of two different tetrapolar measurement patterns applied to a phantom (conductivity 0.22 S/m) with a resistive inclusion (conductivity 0.02 S/m). Magenta arrows denote current lead field induced between electrodes I+ and I-, and blue arrows denote voltage sensing lead field induced between electrodes V+ and V-. Opposite pattern (a) lead fields and (b) sensitivity; edges pattern (c) lead fields and (d) sensitivity. The value of sensitivity (unit 1/m<sup>4</sup>) depends on the magnitudes and directions of the lead fields.

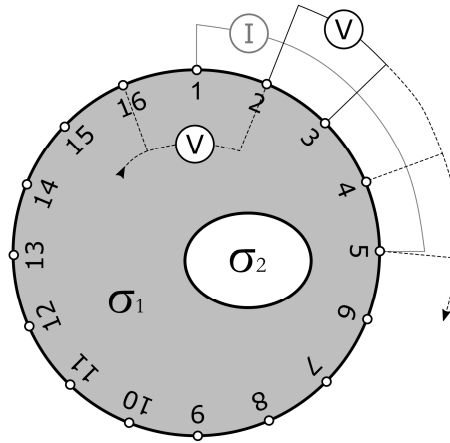


## 2.8 Electrical impedance tomography (EIT)

EIT is an imaging modality where several impedance measurements are obtained around the specimen and used to reconstruct a conductivity image. The main principles are the same as in impedance spectroscopy, but in addition, the measurement pattern needs to be designed for many electrodes and computational methods are applied to reconstruct the image. Also, most EIT setups apply only one frequency instead of a spectrum. A schematic in Fig. 4 represents a typical EIT scheme where one possible current injection pattern is illustrated with corresponding sequential or simultaneous voltage measurements.



**Figure 4.** Schematic of EIT measurement illustrating a 16-electrode scheme with an inclusion ( $\sigma_2$ ) and background ( $\sigma_1$ ) with differing conductivities. One possible current pattern (I) with sequential voltage measurements (V) is represented. The pattern needs to be repeated in other locations around the object.



EIT can be roughly divided into two modes: absolute (static) and difference imaging. In absolute mode, the conductivity of the specimen is reconstructed based on one measured data set, whereas in difference mode the conductivity change is reconstructed based on two measured data sets. The advantage of absolute imaging is that absolute conductivity values are obtained that enable quantitative analysis. The drawback is that absolute mode reconstruction is very sensitive to systematic and modeling errors. If these errors are not considered in the reconstruction, the resulting image quality is often poor (Nissinen et al., 2008, 2009, 2011). Difference mode EIT is more tolerant to such errors since the reconstructions are based on the difference between two data sets. Therefore, difference mode reconstructions typically represent the change in conductivity between two states: either as frequency-difference or time-difference images. Frequency-difference data are collected at the same time point from the same specimen, but the images are reconstructed using a certain frequency data as a reference. Thus, the frequency-difference images represent the conductivity change compared to conductivity at the reference frequency. Time-difference data are collected at different time points but with the same frequency, for example, reference data can be measured from blank saline without the inclusion. Therefore, time-difference images represent the conductivity change due to a change in the specimen over time. The drawback in difference images is that they are often qualitative in nature due to the linearization of the non-linear EIT model and cannot be used for quantitative analysis. (Brown, 2003; Hallaji et al., 2014; P. J. Vauhkonen et al., 1999)

The division of EIT to absolute and difference modes is somewhat flexible, as was shown, for example, in (Hallaji et al., 2014) where absolute images were reconstructed applying two data sets: reference data of a homogeneous specimen were used for estimating measurement noise and modeling errors. This method yielded high spatial resolution (in the context of EIT) and visualization of absolute conductivity values.

The contrast in EIT images is caused by the varying ability of local areas to conduct electrical current. There exist various applications where this property is inherent. For example, in geophysics sub-surface structures and water content can be detected with the direct current version of EIT – electrical resistance tomography (Daily et al., 2005). As an example in medical imaging, the conductivity of thorax changes according to the amount of air in the lungs, and EIT has been shown to be an efficient tool to monitor lung ventilation in intensive care (Tomicic & Cornejo, 2019). In microscopic scale, EIT has recently been reported as a tool for monitoring *in vitro* specimens, as is discussed in section 2.14.

## 2.9 EIT image reconstruction

Reconstructing the unknown conductivity inside a specimen based on measured electrode potentials on the surface is an inverse problem. The associated forward problem is to solve electrode potentials  $V$  when the conductivity distribution  $\sigma$  and injected currents are known, as follows

$$V = U(\sigma) + n, \tag{7}$$

where  $n$  is noise due to unideal instrumentation and  $U$  is the forward operator that includes the measurement pattern, dimensions of the specimen and electrode modeling. The forward operator  $U$  is nonlinear because electrical current flows diffusively in the specimen, depending on the conductivity distribution. Part of the inverse problem solution is to numerically solve the forward problem that links the boundary voltages with the injected currents and the conductivity of the specimen. (Holder, 2005; P. Vauhkonen, 2004)

To solve the forward problem, the electrical measurements need to be modeled. This is often implemented with the complete electrode model that maps the injected currents to electrode potentials (Cheng et al., 1989; Somersalo et al., 1992). The complete electrode model accounts for the effect of the conductivity and the so-

called shunt effect on electrodes, as well as the contact impedances between the electrodes and the object's surface. Another option is, for example, the point electrode model that is useful if electrode sizes are very small compared to the whole specimen surface (Hanke et al., 2011). The forward problem is numerically solved with, for example, finite element method (P. Vauhkonen, 2004).

Inverse problem in EIT is ill-posed which renders the inverse solution to be sensitive to noise and modeling errors. In ill-posed inverse problems, a unique solution may not exist and small errors in the measured data may lead to large errors in the solution. Therefore, accurate modeling of the measurements, that is, the forward solution, as well as customized inversion methods are needed to solve the inverse problem. The solution is often implemented with generalized Tikhonov regularization, and that can be expressed in absolute mode as a minimization problem

$$\sigma = \arg \min_{\sigma > 0} \{ \|L_n(V - U(\sigma))\|^2 + p_\sigma(\sigma) \}, \quad (8)$$

where  $L_n$  is a Cholesky factor of the noise precision matrix, thus,  $L_n^T L_n = \Gamma_n^{-1}$ , where  $\Gamma_n$  is the covariance of the Gaussian distributed noise. The regularization functional  $p_\sigma(\sigma)$  is used to penalize improbable features of  $\sigma$ , according to the prior information of the specimen's conductivity. (Hallaji et al., 2014; Seppänen et al., 2007; M. Vauhkonen et al., 1998)

In the case of difference EIT, the conductivity change  $\Delta\sigma$  is estimated based on the difference of voltage measurements  $\Delta V$  between the two states. Based on Eq. (7), the approximate observation model becomes

$$\Delta V \approx J\Delta\sigma + \Delta n, \quad (9)$$

where  $J$  is a Jacobian matrix of  $U(\sigma)$  and  $\Delta n$  represents the change in noise. The inverse solution in difference EIT becomes of the form

$$\Delta\sigma = \arg \min_{\Delta\sigma} \{ \|L_{\Delta n}(\Delta V - J\Delta\sigma)\|^2 + p_{\Delta\sigma}(\Delta\sigma) \} \quad (10)$$

where  $L_{\Delta n}$  is a Cholesky factor of the noise precision matrix regarding the change in noise, and  $p_{\Delta\sigma}(\Delta\sigma)$  is the regularization functional or prior potential. These inverse solutions can be computed with deterministic or Bayesian (statistical) approaches. Deterministic approaches assume the variables to have exact values, while in Bayesian inversion approach, both the measurements and the model unknowns are

modeled as random variables, and the solutions for equations (8) and (10) are the maximum a posteriori estimates for the conductivity. In both absolute and difference modes, the inverse problem is a minimization problem that is solved with, for example, finite element modeling and Gauss–Newton based line search methods. (Hallaji et al., 2014; P. Vauhkonen, 2004)

As the inverse problem in EIT is ill-posed, prior information is needed for good reconstruction accuracy. It is included in the functional  $p$  in equations (8) and (10) and can have various forms depending on what kind of information is available from the specimen. This can include, for example, the knowledge if the conductivity distribution has high or low values, is changing slowly, or has smooth or sharp edges. (M. Vauhkonen et al., 1998)

Structural priors have been studied especially for multimodal imaging approaches where the prior information would be available for EIT from another imaging modality, such as magnetic resonance imaging. This kind of spatial prior can be an efficient way to decrease the number of unknown parameters and possible solutions of the inverse problem and, thus, stabilize the EIT image reconstruction. (Kaipio et al., 1999; Kolehmainen et al., 2019)

## 2.10 Multimodal EIT

Multimodal imaging in medical scope typically aims to combine morphological and functional information to obtain more accurate diagnostic tools (Martí-Bonmatí et al., 2010). Multimodal EIT applications shares this aim and, in addition, aims to enhance the poor spatial resolution of EIT via embedding (structural) prior obtained from another imaging modality into EIT reconstruction (Crabb et al., 2014; Li et al., 2020; Soleimani, 2006). On the other hand, the advantages of EIT can be used to complement other imaging methods. No known harmful effects, high temporal resolution and compact or even portable instrumentation of EIT provide monitoring possibilities that are not easily available with, for example, magnetic resonance imaging or X-ray computed tomography.

Multimodality can be based on data fusion or coupled physics techniques. Data fusion techniques combine data acquired with separate modalities. In coupled physics systems, one modality alters the response of the other modality, such as in ultrasound-modulated EIT where focused ultrasound waves are used to change the conductivity of a certain region (H. Zhang & Wang, 2004). This thesis work focused

on fusing optical imaging data into EIT reconstruction, therefore, only data fusion techniques are considered further in this chapter.

Multimodal techniques can be roughly divided into asynchronous and synchronous systems according to the implementation of data acquisition and analysis. In asynchronous systems, image data from both modalities are acquired at different time points and combined afterwards. Synchronous systems again acquire data simultaneously and process data automatically. (Martí-Bonmatí et al., 2010) In practice, multimodal systems can be combinations of the asynchronous and synchronous systems: data can be acquired simultaneously but data processing can be done offline afterwards. The implementation depends on the feasibility of connecting all the sensors simultaneously, how fast changes in the specimen are expected, and how fast the results should be available.

## 2.11 Multimodal EIT applications

Many techniques have been presented on the integration of structural prior into EIT reconstruction to improve image quality via stabilizing the solution of the ill-posed inverse problem. The structural prior can be obtained from different modalities such as ultrasound, magnetic resonance imaging, or X-ray computed tomography. Kaipio et al. (1999) presented how prior information on the smoothness of the solution can be considered. They studied cases with exact data and approximate assumptions of the object as prior information (Kaipio et al., 1999). An approach where structural prior was used to build the finite element mesh in the forward solution, and divide it into clusters was presented in (B. Gong et al., 2016). They proposed structure-based regularization to eliminate image artifacts. A soft-regularization approach was proposed to distinguish breast tumors from healthy tissue according to its conductivity when the location of the possible tumor was known based on prior images (E. K. Murphy, Mahara, Wu, et al., 2017). EIT reconstruction accuracy was shown to improve when structural prior of internal edges was applied in the reconstruction, even in cases where the edge information was only partially known (Kolehmainen et al., 2019).

EIT has been combined with ultrasound imaging for various medical applications. One of the first systems was presented by Soleimani (2006) with the aim to obtain tissue monitoring during cryosurgery (Soleimani, 2006). The EIT results were more accurate when boundary information from ultrasound was used as a priori. To obtain enhanced methods for prostate cancer diagnostics, EIT

electrodes were incorporated on transrectal ultrasound probes (E. K. Murphy et al., 2018; Wan et al., 2010). This was an open-domain EIT system with limited sensitivity deep in the tissue. Therefore, they presented a data fusion approach to combine EIT measurements from various probe locations for enhanced image quality. Although data fusion with ultrasound was not applied, the multimodal probe could be used to image prostate with EIT and guide normal biopsy procedure if real time EIT reconstructions were developed. Another study presented EIT combined with ultrasound probe to develop noninvasive and accurate assessment of muscle health; ultrasound image was segmented and used to constrain EIT image reconstruction for enhanced image accuracy (E. K. Murphy et al., 2019).

Magnetic resonance imaging and X-ray computed tomography are commonly used in medicine as they produce anatomically accurate images. Using these images as prior information can be essential for medical EIT applications. For example, Paldanius et al. (2021) demonstrated the importance of anatomically accurate forward models based on structural prior images in the case of intracerebral hemorrhagic stroke EIT (Paldanius et al., 2022). Similar conclusion was presented in (Xu et al., 2011) where boundary information was extracted from computed tomography images and applied in EIT mesh generation. In lung imaging, EIT reconstructions were improved when shape correction was included according to prior images (Crabb et al., 2014; Schullcke et al., 2016). They also assessed EIT image quality by coregistering (geometrically aligning and integrating images) the results on the structural prior images.

Multimodal EIT systems for *in vitro* cell culture studies are currently emerging. Optical microscopy techniques are commonly used to image *in vitro* specimens, and they can be suitable for extracting prior information for EIT reconstruction. Liu et al. (2020) introduced impedance-optical dual-modal sensor where optical images were used to create a binary mask for prior information of the locations and morphology of the cell spheroids (Z. Liu et al., 2020). They presented high quality 2D difference EIT images of human breast cancer cell spheroids. Liu et al. (2022) have continued this work with embedded deep learning model for fusing dual modality information and image reconstruction (Z. Liu et al., 2022). These works have aimed to improve EIT image quality so that they could be used for quantitative analysis of 3D cell cultures.

## 2.12 Rotational EIT

In typical EIT systems the electrodes and the specimen are stationary, thus, the number of electrodes determines the maximum number of independent measurements. In stationary systems, the total number of independent current injection pairs  $N$  is

$$N = \frac{n_e(n_e-1)}{2}, \quad (11)$$

where  $n_e$  is the number of electrodes (Darnajou et al., 2019). Rotational EIT can be implemented either by turning the electrodes or the specimen and collecting data at several rotational positions. This enables a large number of independent measurements that are not limited by the number of electrodes as the measurement angle can be adjusted. Data collection at small increments can potentially enhance EIT image quality (Malmivuo, 2010).

Rotating either the specimen or the electrodes affect the setup design and image reconstruction. Instrumentation, specimen placement, and measurement pattern need to be suitable for rotational data collection. In the image reconstruction, the forward problem should be solved to all measured angles and the rotational scheme is modeled by the forward operator  $U$  in equation (7). Several approaches have been presented on how to create the mesh and map the rotational conductivity estimates into it (E. K. Murphy, Mahara, & Halter, 2017). If only few rotational positions were used, it is possible to embed virtual ('extra') electrodes in the mesh and choose which ones are used at each rotational position. Another option is to rotate the values inside the mesh that enables the use of multiple rotational positions, as it is discussed in section 4.7.

Rotational EIT has been experimentally shown to be effective. One of the first rotational EIT studies applied electrodes on a rotating impeller in the center of a saline-filled tank (S. C. Murphy & York, 2006). The results showed that rotational EIT could be useful tool in mixing process applications. Process monitoring with EIT was also shown to work even with rapidly changing specimens during rotational mixing (Seppänen et al., 2007). Huang et al. (2007, 2008) developed a device where electrodes were rotated near the boundary of saline-filled tanks to enhance image quality (C. N. Huang et al., 2007, 2008). To develop methods for medical imaging, rotational EIT was proven to produce better image contrast and inclusion distinguishability than stationary EIT for a breast shaped tank due to added number of measurements (E. K. Murphy, Mahara, & Halter, 2017).

## 2.13 EIT *in vitro* hardware

### 2.13.1 Electrode configurations

Electrode configurations are determined by the number, location, and size of the electrodes. The number of electrodes affect how many measurement combinations are available (see Eq. (11)), and their locations affect what measurement sensitivities are achievable (see section 2.7). The spacing between adjacent electrodes is also important; having many electrodes in a small *in vitro* chamber can enhance the spatial resolution, but SNR also decreases due to a decreased measured signal when electrode distance is small (Lee et al., 2014). Stray capacitances and the shunting effect also increase when many electrodes are near to each other (Canali et al., 2016; Q. Liu et al., 2011). In addition, electrode size affects the contact impedance: the smaller the electrodes the higher the contact impedances. In practice, electrode configuration design is limited by, for example, the available channels in the EIT device, and space available for electrodes in the imaging chamber.

Most present *in vitro* EIT systems consist of 8–32 equidistantly distributed electrodes often in a coplanar configuration at the bottom of the imaging chamber. The first *in vitro* EIT studies proposed that microelectrode arrays could be used to detect changes in cell cultures close to the electrodes (Chai et al., 2007; Daidi et al., 2007; Linderholm et al., 2008). Coplanar electrodes evenly distributed throughout the bottom of the chamber have shown to be effective in several other cell culture studies: 3D reconstructions were obtained from cancer cell aggregates (Yin et al., 2018) and cancer cells embedded in a 3D scaffold (Yang et al., 2019), as well as yeast growth monitoring (Farnham et al., 2019).

Another commonly used configuration applies electrodes at the edges of the chamber bottom. This configuration has been used to analyze the location and size of cells growing in hydrogel (Sun et al., 2010), image breast cancer cell spheroids and pellets (Yang et al., 2017), and the proliferation of yeast cells (Lemmens et al., 2018). Although coplanar electrodes have shown to be effective in many studies, their sensitivity is highest close to the electrodes and decreases in the vertical direction that limits the imaging of 3D cultures (Yang et al., 2017; Yin et al., 2018).

Other than coplanar electrode layouts have been developed for *in vitro* applications. A chamber containing hundreds of voltage sensing and few pairs for current injection electrodes in a cuboid chamber was built and demonstrated for 3D culture imaging (Ahn et al., 2014; Lee et al., 2014; Q. Liu et al., 2011). For microscopy



scale single cell EIT, electrodes were fabricated on the inner tube wall of a rolled-up thin film system (Weiz et al., 2017).

In multimodal EIT, the electrodes need to be positioned so that auxiliary sensors can be used preferably simultaneously and non-destructively. Liu et al. (2020) embedded 16 electrodes on the wall of a 1.6 mm high circular sensing chamber, thus allowing optical microscopy to be performed through the glass bottom (Z. Liu et al., 2020).

### 2.13.2 Measurement patterns

In EIT, impedance measurements are repeated a couple hundred times using various electrode combinations to gather enough spatial information of the specimen. Tetrapolar measurement configurations are often used due to the simplicity regarding hardware. In addition, tetrapolar configurations minimize the effect of contact impedances because voltage sensing electrodes are separate from current injection electrodes. Other configurations can also be used, such as adaptive methods where current or voltage sensing is done with several electrodes simultaneously (Cook et al., 1994; Kauppinen et al., 2006). Adaptive methods would require several channels in the hardware.

Commonly used tetrapolar patterns are adjacent (neighboring), opposite, and various cross (skip) patterns. The name of the pattern describes the current injection configuration and voltage measurements are obtained sequentially with the rest of the electrodes. In the adjacent pattern, both current injections and voltage measurements are obtained with adjacent electrode pairs sequentially around the specimen. In general, the sensitivity is high close to electrodes, but the center regions of the specimen are poorly detected if only adjacent pattern was used. This is due to zero or close to zero sensitivity areas in the center regions as is discussed in section 2.7. In the opposite pattern, current is injected with opposing electrodes and voltages are measured with the rest of the electrodes. This pattern creates high sensitivity to the center regions of the specimen. In the cross patterns, current is injected with more distant electrodes than in adjacent but not as distant as in opposite pattern. One possible cross pattern is illustrated in Fig. 4. Another possible tetrapolar pattern would be to include all current injection combinations and related voltage measurements. This all pattern could be beneficial since it produces maximum amount of data, but it also requires long data acquisition time and computing time in the reconstruction. (Kauppinen et al., 2006; Morcelles & Bertemes-Filho, 2021)

### 2.13.3 Devices and mfEIT

The main parts of EIT devices are current excitation, signal sensing, and switching (multiplexing) modules. Current excitation module can be implemented either with voltage or current source. In principle, if voltage excitation is used then currents should be measured or vice versa. Voltage sources are often used in commercial impedance analyzers and also in some EIT systems (Linderholm et al., 2008; Sun et al., 2010). The benefit of voltage sources is their straightforward design and higher bandwidth at frequencies above 1 MHz (in terms of accuracy and SNR) than in current sources (Mohamadou et al., 2012). However, current sources can precisely control the amplitudes of injected currents that is not feasible with voltage sources. The excitation signal amplitude should be low enough when *in vitro* specimens are measured not to cause damage to the living cells.

Signal sensing is implemented either as voltage or current measurements, depending on the used source type. The main tasks of the voltage sensing circuit are detection and amplification of the potential differences, filtering noise and direct current components, and digitizing the measurements. If voltage excitation was used, currents need to be measured either (1) from the sensing electrodes or (2) measure voltages from the sensing electrodes and currents from the voltage excitation circuit. In contrast to, for example, *in vivo* lung ventilation EIT, the changes in the detected signals can be very small when *in vitro* specimens are measured. This poses a challenge for *in vitro* EIT devices. (Morcelles & Bertemes-Filho, 2021)

Electrode switching is needed to conduct all the needed EIT measurements with several electrodes. Other option would be to use separate channels for each electrode pair, but that is often not a practical solution. Features of the switching circuit affect the frame rate of the EIT system, thus data acquisition time, and what measurement patterns are feasible. Switching circuits may also induce cross-talk noise and errors at high frequencies via stray capacitances. (Morcelles & Bertemes-Filho, 2021)

Commercial impedance analyzers are not usually optimized for EIT – especially regarding switching. Therefore, early *in vitro* EIT systems consisted of custom-built systems with an impedance analyzer, a multiplexer, and a control software, and they operated at single frequency (Linderholm et al., 2008; Sun et al., 2010). New systems have been introduced that have high temporal resolution, user friendly control software, and ability to use multiple frequencies. A device called Visual tomography is an example of a such device (Yang & Jia, 2017).

Multifrequency excitation can be implemented simply by successively applying one excitation frequency at a time. However, this approach is time consuming and

significantly increases the frame rate. Another approach is to combine two sine waves with differing frequencies in the same excitation signal (Yang & Jia, 2017). This approach is feasible with two frequencies, but to obtain many frequencies with a decent accuracy and frame rate, optimized broadband signals such as chirp or binary sequences, may be more effective (Morcelles & Bertemes-Filho, 2021; Sanchez et al., 2012).

The development of mfEIT devices could induce advancements in the cell culture applications via adding more specificity to the conductivity results based on the theory presented in section 2.5. For example, an EIT result indicating an increase in specimen's conductivity could have resulted from cell death or changes in the surrounding medium, and these effects might not be distinguishable with a single frequency measurement. Multifrequency data would enable more detailed analysis because cell membranes affect the measured impedance according to the applied frequency at the  $\beta$ -dispersion range, whereas the impedance of cell culture medium would be constant. (Morcelles & Bertemes-Filho, 2021)

Temporal resolution of EIT can be high but it depends on the measurement pattern, and signal excitation and sensing strategies. One solution to decrease data acquisition time and still obtain multifrequency data is to apply binary excitation, as presented in (Land et al., 2011; Min et al., 2012), or for example, split the voltage sensing into separate channels as was done in (Yang & Jia, 2017).

## 2.14 EIT *in vitro* applications

One of the first cell culture EIT studies monitored the growth of keratinocyte stem cells and evaluated cell membrane integrity using a microelectrode array with 16 planar line electrodes (Linderholm et al., 2008). They reported an increase of resistivity along cell culture growth and a decreased resistivity after permeabilizing substance (Triton-X) was added. The size and location of a single cellular organism (slime mold *Physarum Polycephalum*) growing on hydrogel was correctly detected with a 16-electrode circular chip (Sun et al., 2010). They reconstructed time-difference images showing that cellular organism was more conductive than agar gel.

EIT has been shown to be effective detecting an induced cell membrane breakage. Yin et al. (2018) used a planar 17-electrode chip to 3D reconstruct breast cancer cell aggregates and their response to permeabilizing substance (Triton X-100) at 10 kHz (Yin et al., 2018). The resulting time-difference images showed that cell aggregates were less conductive than cell culture medium and aggregates'

conductivity decreased after inserting the dissolving substance. Wu et al. (2018) examined the viability of breast cancer cell aggregates on a 17-electrode planar chip (Wu, Yang, et al., 2018). Their time-difference images at 10 kHz showed that the spheroids' conductivity increased after exposure to Triton X-100 solution.

Emerging mfEIT devices have enabled to visualize the frequency dependent conductivity of *in vitro* specimens. Breast cancer cells were embedded in 3D scaffolds and measured with a 16-electrode circular chip (Wu, Zhou, et al., 2018). The results showed that cell-loaded scaffolds were less conducting than blank scaffolds in time-difference mode at 10 kHz. In addition, frequency-difference images showed that the conductivity of the cell-loaded scaffolds increased along increasing frequencies from 10 kHz to 100 kHz, whereas blank scaffolds' conductivity remained unchanged. Similar setup and the frequency-difference mode were used in (Ogawa et al., 2021) to evaluate different cell concentrations embedded into 3D printed scaffolds. Both simulation and experimental results demonstrated that conductivity of the cell-loaded scaffolds decreased along increasing live cell concentration.

Recent study presented an 8-electrode setup with the aim for osteogenic differentiation monitoring (Cortesi et al., 2021). The experimental results showed that EIT could detect different calcium concentrations in hydrogel scaffolds and *in silico* simulations demonstrated the process of cell-induced mineralization. In addition, deep learning has been embedded with *in vitro* EIT to enhance image quality and computational efficiency (Chen et al., 2021; Chen & Yang, 2021; Z. Liu et al., 2022).

### 3 AIMS OF THE STUDY

The aim of this doctoral thesis work was to develop a novel multimodal imaging technique and demonstrate its functionality. The goal was to create a tool for assessing 3D *in vitro* specimens such as spheroids that are challenging to image with traditional microscopes. The approach was to combine mfEIT with OPT, abbreviated as OPT-mfEIT. This combination can reveal both specimens' morphology and conductivity spectra.

The specific aims of the work and the corresponding publications as described in section ORIGINAL PUBLICATIONS were:

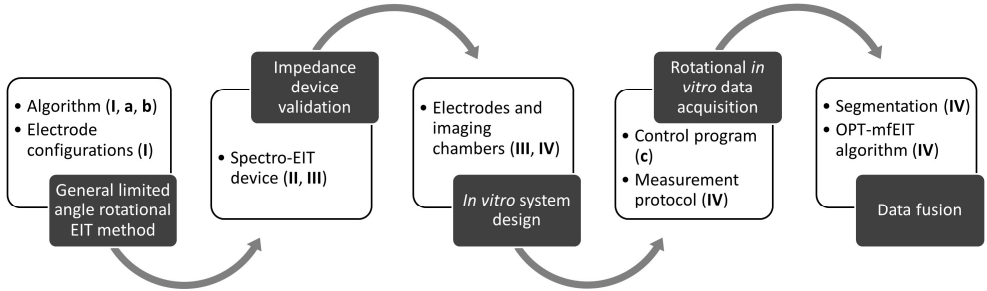
1. To **develop** a novel limited angle rotational EIT method suitable for multimodal imaging setups and a corresponding mathematical rotational image reconstruction algorithm (**I**). The limited angle EIT approach was needed to integrate EIT and OPT so that they would not block each other's field of view.
2. To **develop** a multimodal *in vitro* imaging system: design and produce imaging chambers with suitable electrode configurations and impedance measurement patterns (**III**, **IV**). In addition, data fusion techniques were developed in (**IV**).
3. To **demonstrate** the basic functionality of a fast mfEIT device called Spectro-EIT (**II**), and the feasibility of the 2D *in vitro* OPT-mfEIT setup (**III**) using plant phantoms.
4. To **validate** the technical functionality of the developed 3D *in vitro* OPT-mfEIT imaging technique in its intended use; first using a plant phantom and then with hiPS cell spheroids and *ex vivo* tissues (**IV**).

## 4 METHODS

### 4.1 Overview of the multimodal system development

The development process of the novel multimodal OPT-mfEIT system consisted of different parts that are depicted in Fig. 5. The first part consisted of developing a general rotational EIT method that would enable the use of auxiliary sensors via placing the electrodes on a limited angle configuration. This part included algorithm and electrode configuration development that were validated numerically and experimentally (**I**, (Koskela et al., 2019; Winkler et al., 2021)). In the second part, a novel fast mfEIT device called Spectro-EIT was developed based on Quadra technology (QUADRA technology, trademark of Tallinn University of Technology, Estonia). The feasibility of the Spectro-EIT device was experimentally demonstrated using plant phantoms in (**II**, **III**). The third part included designing, fabricating, and testing multimodal imaging chambers into which electrode arrays were embedded in a limited angle configuration to image *in vitro* specimens (**III**, **IV**). The fourth part of the work focused on rotational *in vitro* data acquisition implementation; a control program was coded to automate the data acquisition (Yuan, 2020), and a novel measurement protocol was designed in (**IV**). The measurement protocol included data acquisition scheme for simultaneous OPT and mfEIT, and an EIT measurement pattern suitable for a limited angle 3D electrode layout. The final part of the thesis work was to acquire multimodal data of *in vitro* specimens and fuse the morphological information from OPT into mfEIT reconstruction (**IV**).

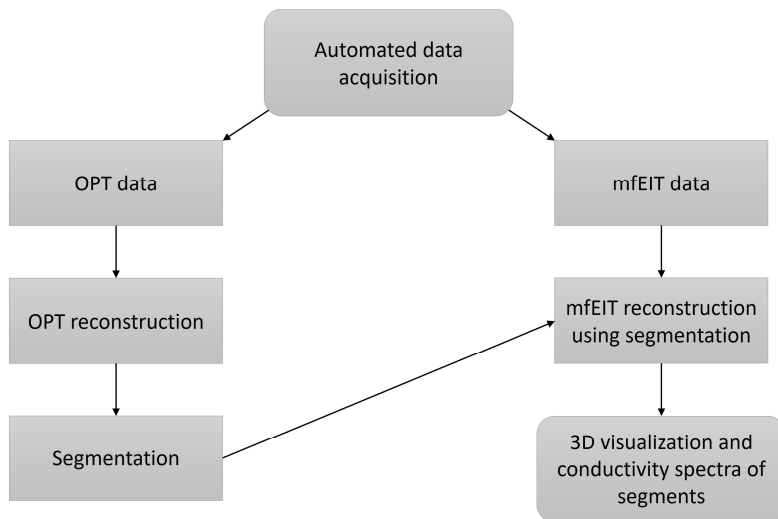
**Figure 5.** Parts of the OPT-mfEIT system development and the related publications. **a:** (Koskela et al., 2019), **b:** (Winkler et al., 2021), **c:** (Yuan, 2020).



## 4.2 The developed OPT-mfEIT system

This section presents the final OPT-mfEIT system, and the related intermediate stages of the development are presented in the following sections. A flowchart representing the final OPT-mfEIT image acquisition and image reconstruction is presented in Fig. 6. The automated data acquisition allowed simultaneous data collection of both OPT and mfEIT data. Brightfield OPT data was acquired and reconstructed to obtain morphological 3D images. These images were further segmented, and to enhance mfEIT image quality, the segmentation results were embedded in the mfEIT image reconstruction. The resulting OPT-mfEIT images revealed the 3D morphology and conductivity spectra of the segments. The specimen size of the final OPT-mfEIT system was approximately from 1 mm to 5 mm in diameter, which is suitable, for example, for small tissue pieces or large spheroids and organoids.

**Figure 6.** Flowchart of the final developed OPT-mfEIT system.



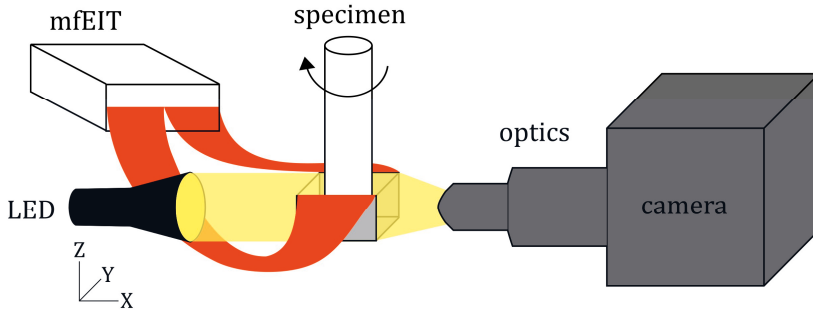
A simplified schematic of the final version of the integrated OPT-mfEIT system is shown in Fig. 7. MfEIT consists of the Spectro-EIT device, wires, electrodes, and the saline-filled chamber. The Spectro-EIT device was placed as close to the rotated specimen as possible but out of the way of OPT illumination. To connect the device with the electrodes, thin wires were soldered to zero insertion force connectors that were attached to electrode sheets. The limited angle rotational approach enabled to use relatively small number of electrodes because EIT data was collected from several angles from the rotated specimen. Electrodes were fabricated on flexible sheets and embedded on the two opposing walls of the imaging chamber.

The in-house-built OPT setup (Belay et al., 2021; Figueiras et al., 2014) consisted of three main parts: illumination, specimen rotation stage and light detection. Illumination was implemented with a white LED and a telecentric lens. The rotation stage included motorized x-y-z and rotational movements for specimen alignment. Main components in the light detection were a 2×objective lens, an iris diaphragm, a tube lens, and a sCMOS camera.

Imaging chamber was filled with saline to enable both electrical contact with the specimen in mfEIT and a refractive index matching path in OPT. Hydrogel based specimens were prepared into 5 mm inner diameter fluorinated ethylene propylene (FEP) tubes. The tubes were attached to a rotation stage and about 3 mm of the specimen containing the inclusion(s) was pushed out of the insulating tube to enable electrical contact with the electrodes.



**Figure 7.** Schematic of the OPT-mfEIT system. MfEIT consisted of electrodes embedded on the opposing walls of the imaging chamber, wires, and the Spectro-EIT device. OPT consisted of LED illumination, rotation stage, optics, and a camera. The specimens were rotated in saline to enable electrical contact with the electrodes and refractive index matching path for OPT illumination. Adapted from (IV).



### 4.3 Electrode configurations

The electrode systems used in this thesis work can be roughly divided into large tanks for initial EIT testing phase and the developed multimodal *in vitro* chambers. Two slightly different 16-electrode circular tanks were used. For the limited angle rotational EIT method development (I), a 16-electrode tank (diameter 28 cm) was modified so that eight electrodes were insulated and eight were in use. This electrode layout allowed to experimentally analyze an opposite 4+4 configuration where four electrodes were on two sides of the tank/chamber. The same EIT tank has previously been used for example in (D. Liu et al., 2015). The other large tank (diameter 22 cm) had equidistantly distributed 16-electrodes and it was built and used for Spectro-EIT device testing (II, III).

In addition to opposite 4+4 configuration, other limited angle electrode configurations were numerically studied in (I). The configurations included 4–8 electrodes placed either opposing to each other or next to each other. Their efficacy was evaluated based on the quality of the reconstructed images.

To design an *in vitro* imaging chamber for OPT-mfEIT, certain conditions had to be considered: (1) electrodes should be as close to the rotated specimen as possible to obtain high sensitivity impedance measurements (Lehti-Polojärvi, 2014), and (2) refractive index must be close to that of water throughout the field of view of OPT. To avoid optical scattering and reflections, the electrodes were placed out of the field of view of OPT. Based on the simulation results in (I) and the requirements for simultaneous OPT imaging, further *in vitro* chamber designs were based on the

opposite 4+4 configuration. The *in vitro* chamber development work consisted of four electrode fabrication trials.

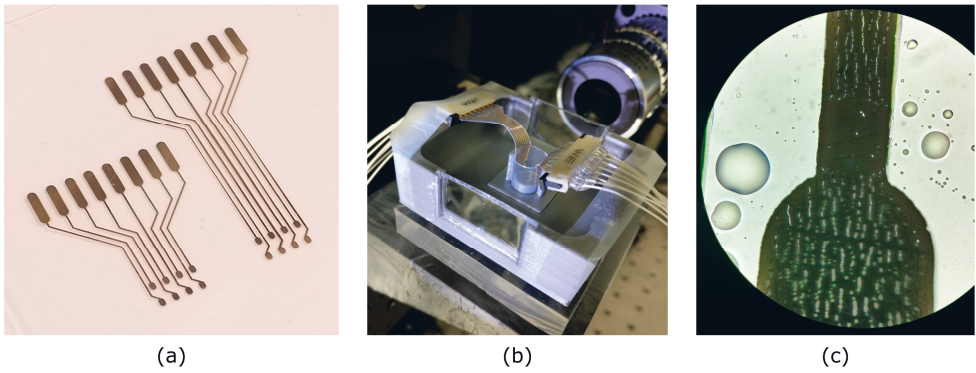
Trial 1: FEP has refractive index that is close to that of water, thus first trial was based on attaching electrodes on the inner surface of an etched FEP tube, as is shown in Fig. 8. Thin gold lines (50 nm thick) were metallized on a plastic (Polyethylene terephthalate) sheet (Associate professor Sampo Tuukkanen, Tampere University). These electrodes were then cut and glued on the FEP tube (inner diameter 13 mm), and a specimen could be rotated inside the tube when filled with saline. However, this configuration did not provide information of the impedance changes in the vertical direction and only enabled 2D mFEIT imaging. Also, the measured volume was relatively large, and the electrical measurements would not have been effective for small *in vitro* specimens.

**Figure 8.** Trial 1 electrodes attached on the inner wall of a FEP tube to enable simultaneous OPT and mFEIT imaging.



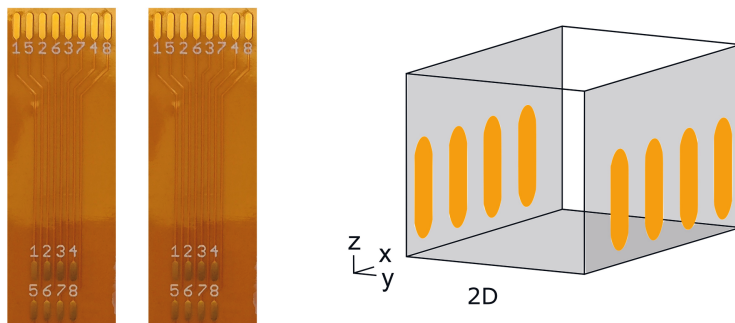
Trial 2: The second trial was an attempt to place 16 electrodes at two vertical layers close to the specimen to obtain 3D mFEIT. The electrode layout was designed for specimen size of 5 mm in diameter that would be covered by the field of view of the OPT when a 2×objective was in use. Electrodes (5 nm chrome for primer and 135 nm gold on top) were metallized on a FEP sheet (Adtech Polymer Engineering Ltd, UK) and the conducting wires were insulated with InkOrmo (micro resist technology GmbH, Germany) coating (PhD student Riikka Mikkonen, Tampere University), as is shown in Fig. 9 (a). The electrode sheets were rolled and placed on a 3D printed imaging chamber as is shown in Fig. 9 (b), and a specimen could be rotated inside this construct. However, the gold layer was cracked due to the mechanical bending of the FEP sheet which corrupted the electrical properties of the electrodes. An example of these cracks can be seen in a microscope image in Fig 9 (c).

**Figure 9.** Trial 2 electrodes. (a) Array with 16 electrodes and insulated conducting wires. (b) Electrodes rolled and placed into an OPT-mfEIT chamber. (c) Microscope image visualizing the cracking of the gold layer due to mechanical bending of the FEP sheet with electrodes.



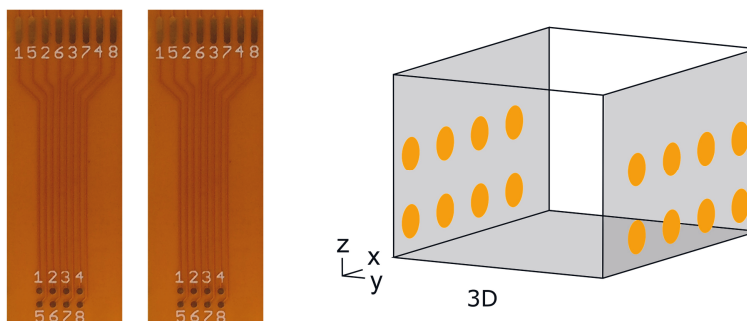
Trial 3: The chamber shape was evolved from circular to rectangular to achieve robust electrical measurements with the multimodal setup. The rectangular design was built with opposite 4+4 electrode configuration as is shown in Fig. 10. Electrodes ( $1\ \mu\text{m}$  copper with 50 nm gold coating) were fabricated on flexible Kapton-based sheets (PhD Marek Rist, Tallinn University of Technology, Estonia). Kapton was used as the substrate and insulation material due to its good electrical, thermal, and mechanical properties. The sheets were glued on two walls of a 3D printed chamber. Trial 3 configuration was used in (III). Nevertheless, the electrodes were in one vertical layer that would not be effective for 3D imaging.

**Figure 10.** Trial 3 electrode sheets (left) and their configuration in the imaging chamber (right) for 2D OPT-mfEIT imaging. Only the bottom layer of the electrodes was used in the measurements.



Trial 4: The electrode layout was slightly different in trial 4 compared to trial 3 but otherwise the electrodes were similarly fabricated. The main difference was the smaller size of the electrodes (1 mm in diameter), and that two vertical electrode layers were used to enable 3D mfEIT. The electrode sheets and the electrode locations in the OPT-mfEIT chamber are illustrated in Fig. 11. Trial 4 configuration was used in (IV).

**Figure 11.** Trial 4 electrode sheets (left) and their configuration in the imaging chamber (right) for 3D OPT-mfEIT imaging.



All the chosen electrode materials in the trials 1–4 were either gold or had gold coating on another metal due its inertness. Gold is commonly used in cell culture impedance studies since it is a non-toxic and stable material (Grimnes & Martinsen, 2015; Keese & Giaever, 1986). These properties are needed in the demanding cell culture conditions including various saline solutions and, for example, hydrogel compositions can be in contact or close to the electrodes for long periods of time.

The used experimental electrode layouts and the measurement patterns are collected in Table 2.

**Table 2.** Electrode systems, measurement patterns, and data collection schemes used in the experiments of each publication.

Publication	Electrode system	EIT pattern	Data collection
I	large tank with opposite 4+4 configuration	all	rotational
II	large tank with equidistant 16-electrodes	opposite	non-rotational
III	large tank with equidistant 16-electrodes and trial 3 <i>in vitro</i> chamber with opposite 4+4 configuration	adjacent, opposite, cross, and all	non-rotational and rotational
IV	trial 4 <i>in vitro</i> chamber with opposite 8+8 configuration	designed pattern with 390 measurements	rotational

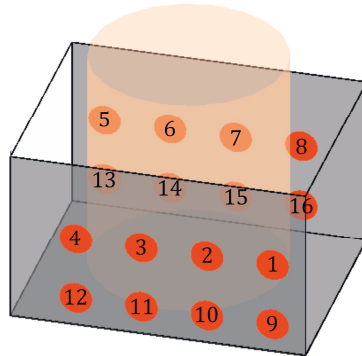
#### 4.4 EIT patterns, OPT integration, and data acquisition

Various EIT measurement patterns were used in the experiments as are presented in Table 2. In (II), the opposite pattern was applied to demonstrate the basic functionality of the Spectro-EIT device. To further study the effect of different measurement patterns on EIT image quality, four different patterns were compared in (III): adjacent, opposite, cross, and all. The all pattern was further applied to investigate the mfEIT with plant phantoms in (III).

In the rotational experiments, the measurement pattern was repeated at several rotational positions. This significantly increased the total acquisition time compared to non-rotational cases. With the 8 electrode cases, in (I) and (III), all current injection pattern was feasible, but with 16 electrodes in (IV), the amount of all possible current injection combinations would have induced long acquisition times that could cause errors when imaging time-variant live specimens.

The commonly used patterns, such as opposite or adjacent, would not have been optimal for the trial 4 configuration where electrodes were in a limited angle layout and in two vertical layers, as is illustrated in Fig. 12. For example, the adjacent pattern has poor sensitivity in the center of the volume. Therefore, novel measurement pattern was designed that gathered high sensitivity measurements especially at the location of the rotated specimen. The designed pattern consisted of 15 current injections sequentially applied between electrode 2 and all other electrodes, and 15 current injections between electrode 14 and all other electrodes. At each current injection, pairwise voltages were sequentially measured with the remaining electrodes. This pattern yielded  $30$  (injections)  $\times$   $13$  (measurements) =  $390$  tetrapolar measurements in total, as was presented in (IV).

**Figure 12.** Numbering of the electrodes in the trial 4 chamber. Novel EIT pattern was developed to obtain high sensitivity measurements of the whole volume with this configuration. Cylindrical shape represents the hydrogel-based rotated specimen. Adapted from (IV).



Integrating mfEIT measurements with OPT imaging required a protocol for the rotational data saving. Therefore, a LabVIEW program was implemented that controlled the Spectro-EIT device, OPT camera, and the rotation stage (Yuan, 2020). As OPT was acquired every  $0.9^\circ$ , the measurement angles for mfEIT were defined to be a multiple of the OPT angle. In addition, as one full rotation is  $360^\circ$  it should be divisible by both OPT and mfEIT angles. Data was saved at each rotational position either by saving only OPT image or both the OPT image and one mfEIT pattern. This protocol was used in (III) and (IV) for data collection.

## 4.5 EIT devices

Two different EIT devices were used in the experiments of this thesis work. First, a well-established device KIT4 (Kourunen, 2014) was used for the limited angle rotational EIT method development with large tank experiments in (I). The device operated at one alternating current frequency at a time and was connected to the circular tank where half of the equally distributed 16 electrodes were insulated to create an opposite 4+4 configuration.

To obtain mfEIT of *in vitro* specimens, we initiated novel design of the Spectro-EIT device (II). It was equipped with a multiplexer that contained 16 bi-directional input/output channels. The Spectro-EIT device generated binary multifrequency excitations that enabled fast data acquisition at multiple frequencies. The duration of one tetrapolar measurement was minimum 5 ms that included the average of three repeated measurements. In this work, the average of seven repeated measurements was used leading to 10 ms duration for each tetrapolar measurement. For example,

if a pattern consisting of 390 measurements was used, the duration of one cycle was 3,9 seconds. The operation range was from 1 kHz to 349 kHz and data was extracted with Fourier transform at 15 frequencies within this range. The resulting Spectro-EIT feasibility was first tested experimentally with a large 16-electrode tank and plant phantoms (**II**, **III**). Then it was connected to OPT-mfEIT chambers to measure *in vitro* specimens (**III**, **IV**).

To prevent damage to cells, the excitation signal of the Spectro-EIT device was adjusted as small as possible so that SNR remained adequate (approximately 40 dB as was calculated in (**IV**)). All OPT-mfEIT measurements of tissue or cell spheroid specimens were obtained with 600 mV<sub>pp</sub> excitation voltage that led to maximum 100 mA<sub>pp</sub> current. Current density field is strongest close to current feeding electrodes, as is demonstrated in Fig. 3 (a) and (c). In the developed OPT-mfEIT system, the inclusions were in the center parts of the imaging chamber and not close to the EIT electrodes that prevents possible damage to cells.

## 4.6 OPT image reconstruction and segmentation

OPT reconstructions in (**III**, **IV**) were computed using filtered back-projection algorithm (Natterer, 2001). Typically, the center-of-rotation needs to be corrected prior to reconstruction because perfect alignment of the specimen would be very difficult before image acquisition. Here, the center-of-rotation correction was made manually by choosing the visually best offset value from a set of reconstructions of the top and bottom parts of the specimen, as in (Koskela et al., 2021). These offset values were interpolated for the rest of the volume as in (Figueiras et al., 2014).

OPT reconstructions were segmented to obtain structural prior information for mfEIT reconstruction (**IV**). The OPT volume was segmented into 4 regions: inclusion(s), tube, marker, and the rest of the volume was assigned as background. The inclusion(s) was the main region of interest, and the aim was to obtain its 3D morphology and conductivity spectrum. The background conductivity was known beforehand, thus its reconstructed spectrum served as an indicator of data quality. The tube was electrically insulating hence it was cut out from the mfEIT mesh. Similarly, the marker was cut out from the finite element mesh after it was used as a tool for verifying correct orientation of the segmentation in the mesh. The use of OPT segmentation as a structural prior in mfEIT image reconstruction was expected to enhance image quality as is discussed in sections 2.9 and 2.10.

OPT reconstructions were computed in MATLAB (R2019a, The MathWorks, Inc., Natick, Massachusetts, USA) and segmentations were performed in Avizo (Thermo Scientific, v.2019.4).

## 4.7 EIT reconstruction methods

Rotational reconstruction approaches were used in **(I, III, IV)**, and nonrotational approaches in **(II, III)**. In the tank experiments, structural prior from OPT was not used, thus commonly used smoothness priors were applied in **(I-III)**. Studies in **(I-III)** were measured and reconstructed in 2D using deterministic reconstruction approach, and the reconstruction codes were based on EIDORS software package (Adler & Lionheart, 2006). In **(IV)**, Bayesian approach and structural prior from OPT were applied and the reconstructions were in 3D. Complete electrode model and finite element method were used in all reconstructions. EIT reconstructions were computed in MATLAB (The MathWorks, Inc., Natick, Massachusetts, USA) and 3D visualizations were done in Avizo (Thermo Scientific, v.2019.4) or open-source software Fiji.

To enable the use of multiple rotational positions, two different methods were developed for creating the rotational mesh and mapping the rotational conductivity estimates into it. The methods rotate the conductivity estimates inside the mesh in different ways: (1) rotating element values with a geometrically weighted mapping inside a fixed finite element mesh, called the weighted method **(I)**, or (2) by creating a set of nodes that are distributed to match the desired measurement angles on a boundary in the finite element mesh that divides the domain into a rotational and a static part, called the click method (Koskela et al., 2019). In the click method, the elements are mapped to new positions inside the rotational part and outside elements are static near the electrodes. Both methods enable the use of multiple rotational positions because electrodes are fixed and independent of the rotational measurement positions.

Rotational 3D EIT reconstruction is computationally demanding because of the large number of elements in the mesh, even more so in a 3D mesh compared to a 2D case. The click method provides a solution to this issue since the computationally heavy weighted mapping matrix is not needed as in the weighted method. Instead, the rotational mapping is computed during the reconstruction process only by translating the element indices according to desired rotational positions of the nodes. (Koskela et al., 2019)



The used reconstruction methods are listed below according to each publication.

- I** The novel weighted method was presented to achieve flexibility regarding the electrode configuration and number of rotational measurement positions in rotational EIT applications. Time-difference images were reconstructed with the regularized Tikhonov approach with smoothness promoting regularization matrix (Laplacian prior) and empirically chosen regularization parameter. One-step Gauss-Newton solver was used to compute the inverse problem.
- II** To test the Spectro-EIT device, time-difference and frequency-difference images were reconstructed with a non-rotational mesh. Laplacian smoothness prior with empirically chosen regularization parameter were used, and the inverse problem was computed with One-step Gauss-Newton solver.
- III** Time-difference EIT and mfEIT reconstructions were presented in rotational and non-rotational schemes. Rotational *in vitro* chamber was developed to a rectangular shape (trial 3 in Fig. 10) and the mesh updated accordingly using the click method. OPT and mfEIT were acquired from the same specimen, but the reconstructions were applied to both techniques independently. EIT images were reconstructed using Laplacian smoothness prior, empirically chosen regularization parameter, and One-step Gauss-Newton solver.
- IV** Absolute mfEIT images were reconstructed in 3D using structural prior from OPT. For comparison, one specimen was reconstructed using conventional Gaussian smoothness prior instead of the structural prior. Rotational 3D meshes were created based on the click method and segmentations. Images were reconstructed with Bayesian approaches using model error correction based on reference measurements, as is mentioned in section 2.8 (Hallaji et al., 2014). Iterative Gauss-Newton method was used to solve the inverse problem.

## 4.8 Statistical analysis

Normality of data was tested with one-sample Kolmogorov-Smirnov test before any further statistical tests. Mean and standard deviations were computed to evaluate the reconstructed conductivities of parallel segments. The similarity of median

conductivities of fresh and treated liver tissue segments was evaluated with Wilcoxon rank sum test. Cronbach's alpha test was used to evaluate the repeatability of the developed OPT-mfEIT technique using the reconstructed conductivities of the background segments. All statistical tests were carried out in MATLAB (R2019a, The MathWorks, Inc., Natick, Massachusetts, USA).

## 5 MATERIALS

Various specimens were used to test, demonstrate, and validate all the development phases of the OPT-mfEIT technique. Studies (I–III) focused on the development of the rotational method and device testing, thus simple inorganic objects or plant phantoms were used. In (IV), the aim was to validate the applicability of the integrated OPT-mfEIT technique for *in vitro* studies. Therefore, fresh tissues and hiPS cell spheroids were imaged in addition to a plant phantom. All specimens were immersed in saline to allow electrical contact with the electrodes. Most of the *in vitro* inclusions were embedded also in hydrogel scaffolds to allow proper placement during rotation. The imaged specimens according to each publication are listed below.

- I To test the feasibility of the limited angle rotational EIT approach, a rotation platform was 3D printed and hydrogel-based specimens were prepared on it. Cylindrical gelatin scaffolds were used, and plastic tubes of various sizes were inserted in the gelatin. These specimens were immersed in saline and manually rotated in the large 8-electrode EIT tank. The plastic inclusions were expected to be electrical insulators that should be seen as a decrease in conductivity in time-difference EIT images, as is shown in Fig. 13.
- II To evaluate the performance of the Spectro-EIT device, fresh plants were embedded in saline in the middle of the large 16-electrode tank. As the plants were fresh with intact cell walls, they were expected to express dielectric properties in the mfEIT images, as is shown in Figs. 14 and 15.
- III To evaluate the effect of different EIT patterns, a glass bottle was embedded in saline and measured in the 16-electrode tank with different tetrapolar patterns. The bottle was electrically insulating thus it was expected to show as a low conductivity region in the results. Another experiment with the 16-electrode tank was conducted using a fresh potato that was cut to a rectangular shape and embedded in saline. The potato was expected to show dielectric properties as is shown in Fig. 15. To demonstrate the feasibility of OPT-mfEIT integration, a rectangular

carrot was rotated in saline in the 2D *in vitro* chamber (trial 3). The fresh carrot was expected to show dielectric properties and its shape and location could be detected with OPT, as is shown in Fig. 20 (a).

#### IV

Four different specimen types were imaged to validate the technical functionality of the integrated OPT-mfEIT in 3D. All inclusions were embedded in agarose hydrogel scaffold and imaged in saline-filled 3D chamber (trial 4). Before hydrogel gelation, agarose solution was measured to be 37 °C before embedding the tissue pieces or spheroids in it to prevent damage due to high temperatures. (1) A tetrahedral piece of fresh potato was used to compare smoothness prior and structural prior mfEIT reconstructions, as is shown in Figs. 20 (b) and 21. (2) To evaluate the feasibility to image 3D cell cultures, hiPS cells were embedded into biomaterial spheroids of approximately 1 mm diameter. For comparison, blank biomaterial spheroids were also imaged. All spheroids were imaged within 7 h after spheroid formation. The presence of hiPS cells was expected to decrease the conductivity of the biomaterial spheroid. These results are shown in Figs. 22 and 23. (3) Experiment on *ex vivo* tissue viability was implemented with porcine liver tissue. Part of the pieces of the porcine liver was treated by Triton X-100 and part was imaged fresh. All measurements were acquired within 14 h of liver extraction. The treatment was expected to break the cell membranes, and this should increase the tissue conductivity, as is shown in Figs. 24 and 25. (4) The viability of *ex vivo* tissues were evaluated with human adipose tissue. A piece of human adipose tissue was killed by freezing and another piece was preserved as viable as possible. The conductivity was expected to increase due to tissue death.

## 6 SUMMARY OF THE RESULTS

### 6.1 Developing rotational mfEIT technique for multimodal setup(s)

#### 6.1.1 Numerical studies of electrode configurations

To build a novel limited angle EIT setup, various electrode configurations that would allow embedding of additional sensors on the specimen surface were numerically evaluated (**I**). Symmetrical and asymmetrical configurations consisting of 4, 6, or 8 electrodes were studied (Fig. 8 in (**I**)) and compared with a rotating 16-electrode ring (Fig. 9 in (**I**)). Numerical results indicated that increasing the number of electrodes from 4 to 8 electrodes enhances the quality of reconstructions in both symmetrical and asymmetrical configurations. Image quality with both symmetrical and asymmetrical limited angle 8-electrode configurations were comparable with the rotating full coverage 16-electrode case.

Due to the layout of OPT and the promising numerical and experimental (see Fig. 13) results of the opposite 4+4 configuration, further *in vitro* OPT-mfEIT development was based on that configuration.

#### 6.1.2 Effect of measurement patterns

Various measurement patterns were experimentally studied in Fig. 5 in (**III**). These results demonstrated that the reconstruction quality may be compromised if only one type of current injection is used. For example, the opposite pattern lacks latitudinal information that leads to slightly distorted inclusion shape. On the other hand, it is known that the adjacent pattern has poor sensitivity in the center of the volume (Kauppinen et al., 2006). The experimental results were in line with the lead field theory and the sensitivity simulations shown in Fig. 3 and Fig. 3 in (**I**). Therefore, patterns that contain both through-the-specimen injections and close-to-edge injections were used in (**I**), (**III**), and (**IV**).

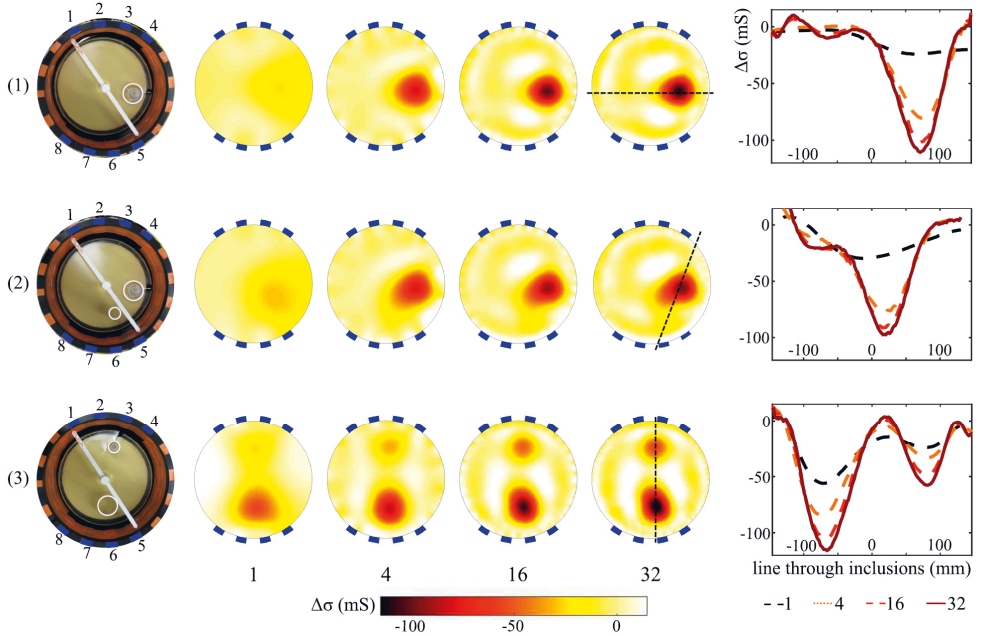
The opposite pattern was used in (II) since the aim of the study was to demonstrate the functionality of the Spectro-EIT device instead of optimizing the image quality. Part of these results are shown in the two top rows of Fig. 15. The effect of the opposite pattern can be compared with the potato results at the bottom row of Fig. 15 that are obtained with the all pattern. The edges of the top row results are noisier than at the bottom row, suggesting the opposite pattern provided good measurements in the center parts of the specimen but not as effectively at the edges.

### 6.1.3 Number of rotational measurement positions

The effect of increasing the number of rotational measurement positions was studied both numerically (I) and experimentally (I, IV). Numerical studies (Fig. 6 in (I)) showed that increasing the number of rotational positions did enhance reconstruction quality until the studied 256 measurement positions in  $180^\circ$  rotation (measurements every  $0.7^\circ$ ). 32 positions in  $180^\circ$  rotation produced adequate image quality and increments after 64 positions did not produce significant improvements. These numerical results were in line with the experimental results obtained with tank measurements as is shown in Fig. 13. Three different phantoms with insulating plastic inclusion(s) (1)–(3) were measured and images were reconstructed with 1, 4, 16, and 32 rotational measurement positions in  $180^\circ$  rotation. The image quality was enhanced as the number of measurement positions was increased.

Number of rotational positions was studied experimentally with the *in vitro* chamber in Fig. 5 in (IV). The results demonstrated that increasing the number of rotational positions enhanced image quality until the studied 40 measurement positions in  $180^\circ$  (measurements every  $4.5^\circ$ ). In addition, all these studies showed that several rotational measurement positions are needed when a limited angle electrode configuration is used. This can be seen, for example, in the second column in Fig. 13 where one rotational measurement position yielded very poor image quality.

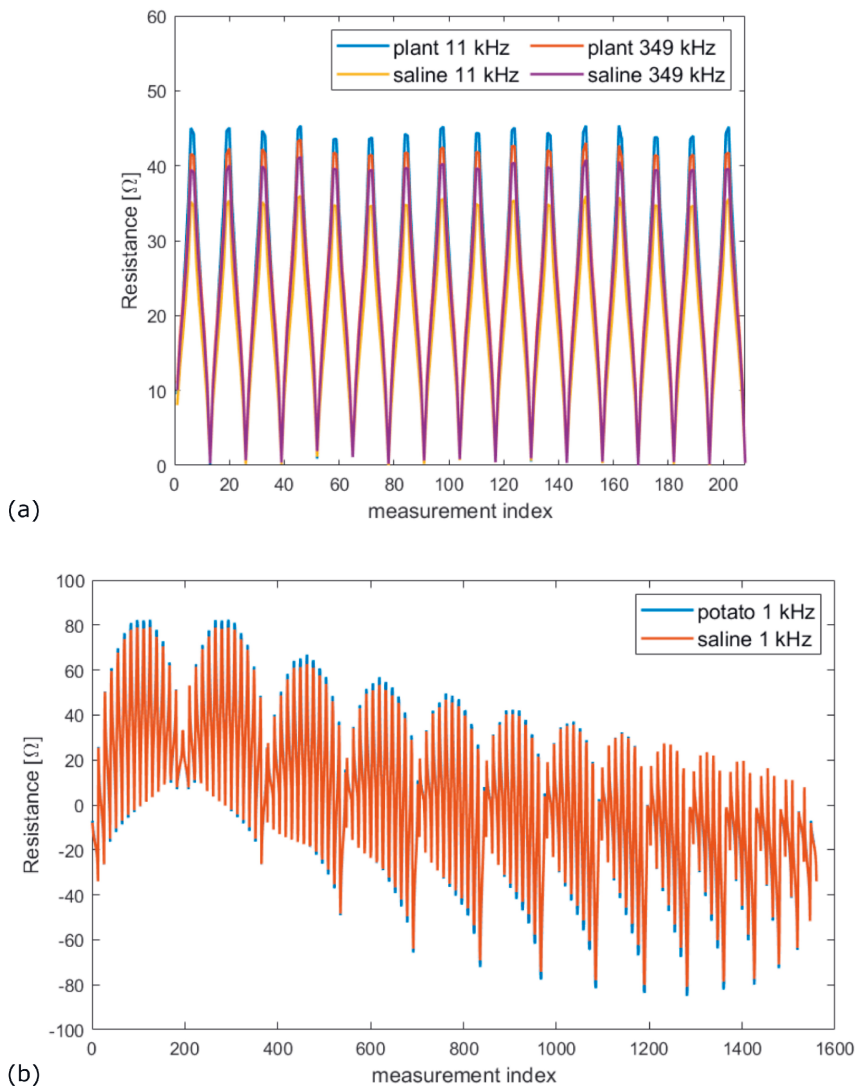
**Figure 13.** The opposite 4+4 electrode configuration was used in the experimental demonstration of the limited angle rotational EIT method. Plastic inclusions in different sizes and locations (cases (1)–(3)) were embedded in gelatin scaffold and rotated in the tank using 1–32 rotational measurement positions in 180° rotation. Conductivity changes along the dashed line of each reconstruction are shown in the graphs. The EIT domain was 28 cm in diameter. Reproduced from (I).



#### 6.1.4 Spectro-EIT device

The feasibility of the Quadra-based Spectro-EIT device was demonstrated in (II) and (III) and part of the results are shown in Figs. 14 and 15. Fig. 14 (a) illustrates raw measurement data of a plant in saline (corresponds to top rows in Fig. 15) and blank saline in the equidistant 16-electrode tank when the opposite pattern was used. The resistance values differed at 11 kHz and 349 kHz frequencies and the maximum values were higher if plant inclusion was present. Fig. 14 (b) shows data collected when a potato inclusion was present in the tank (corresponds to bottom row in Fig. 15) compared to blank saline acquired with the all pattern. Slight differences can be seen in the resistances at 1 kHz frequency.

**Figure 14.** Examples of raw impedance data collected with the Spectro-EIT device and 16-electrode tank. (a) Measurements of a triangular yellow beetroot (plant) and reference data (saline) conducted with the opposite pattern. (b) Measurements of rectangular potato and reference data (saline) conducted with the all pattern.

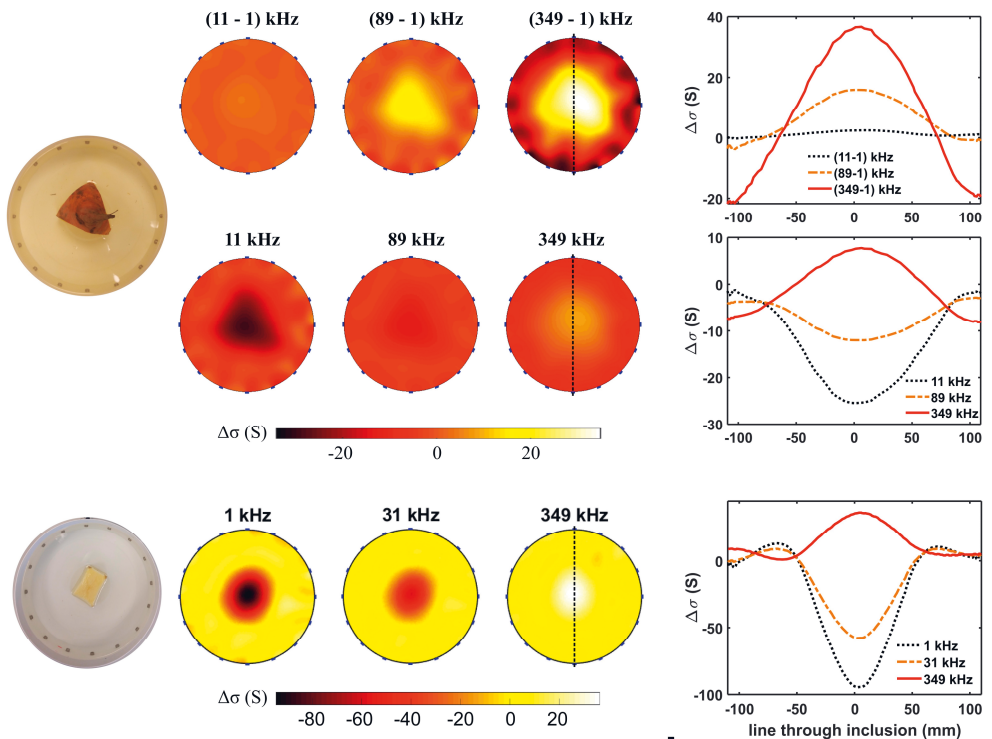


Frequency-difference and time-difference reconstructions from plant measurements are shown in Fig. 15. Difference mode reconstructions show the conductivity change relative to the used reference data. The frequency-difference reconstructions (top row in Fig. 15) applied reference data measured from the same specimen at 1 kHz. Thus, the images represent the change in conductivity due to



applying higher excitation frequency. Time-difference reconstructions applied reference data that is measured from blank saline at the same frequency (middle and bottom rows in Fig. 15). Therefore, the resulting images indicate the change in conductivity due to inserting the plant in the saline. Both the frequency-difference and the time-difference reconstructions showed clear conductivity changes according to applied frequency. Dielectric properties of the yellow beetroot and potato were clearly seen in the reconstructions as the conductivities increased with the increased frequency. This effect is presented in more detail in the graphs that visualize conductivity change along the vertical line of each reconstruction. The experimental results indicated that the Spectro-EIT device provided a fast mfEIT tool that could detect the  $\beta$ -dispersion of biological specimens. The Spectro-EIT device was further used in (IV).

**Figure 15.** Spectro-EIT device verification. Frequency-difference (top row) and time-difference EIT images (second and third row) of plant phantoms in saline. Triangular yellow beetroot measurements were conducted with the opposite pattern and the rectangular potato with the all pattern. The tank diameter was 22 cm. Conductivity changes along the dashed vertical line of each reconstruction are shown in the graphs. Top rows adapted from (II) and bottom row from (III).



## 6.2 Multimodal imaging of *in vitro* specimens

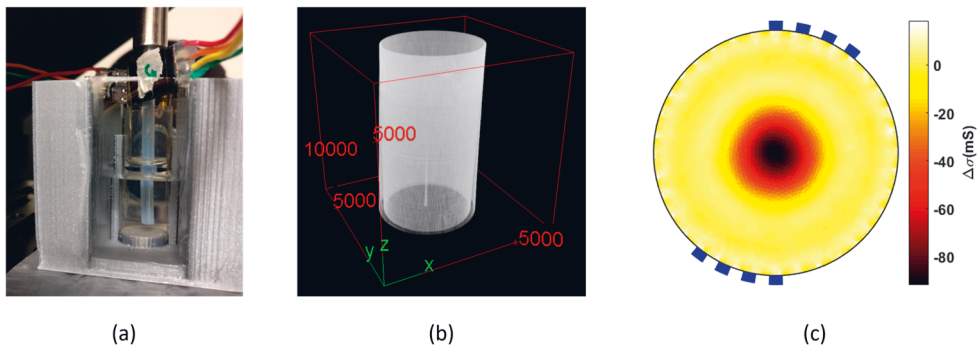
OPT-mfEIT technique was demonstrated with the trial 1, 3, and 4 electrodes and applying both smoothness (III, IV) and structural priors (IV) in the mfEIT reconstruction. In the smoothness prior cases, OPT and mfEIT were reconstructed separately. In the structural prior cases, OPT reconstruction was embedded in the mfEIT reconstruction.

### 6.2.1 Developed imaging chambers

Incorporating the trial 1–4 electrode configurations into the OPT-mfEIT chambers are presented below.

Trial 1: The preliminary results with the first combined OPT-mfEIT chamber were obtained with trial 1 electrode configuration as are shown in Fig. 16. The electrode-FEP tube construct was placed in a saline-filled chamber and a rotated semitransparent plastic tube was measured. OPT reconstruction of the plastic tube shows the cylindrical shape of the specimen. In the EIT reconstruction the plastic tube can be seen as a region of low conductivity in the center of the electrode-FEP tube construct. Trial 1 electrode configuration was feasible for the combined OPT-mfEIT but this configuration did not produce information of conductivity changes in the vertical direction. Therefore, further electrode configurations were developed to obtain 3D measurements for mfEIT.

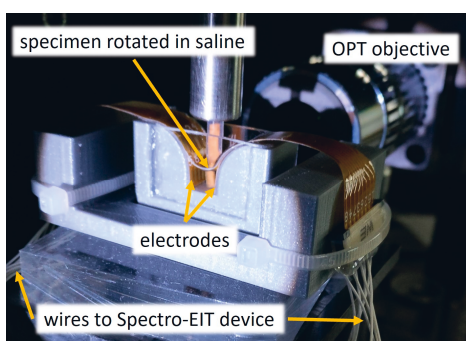
**Figure 16.** First results of a combined OPT-mfEIT using the trial 1 electrodes. (a) Imaging chamber with a rotated plastic tube in saline. (b) OPT reconstruction of the tube (diameter 3.6 mm). (c) Time-difference EIT reconstruction of the same tube inside the 13 mm wide EIT domain.



Trial 2: Due to issues explained in section 4.3, trial 2 electrode arrays could not be used to obtain OPT-mfEIT results.

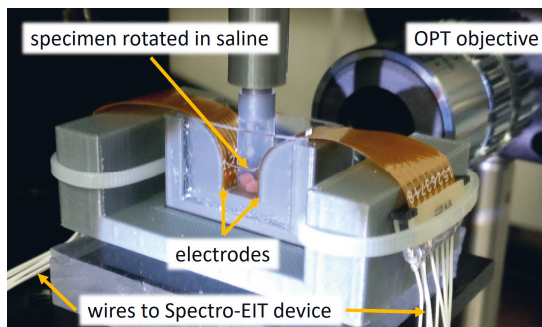
Trial 3: To attain robust electrodes and to have good sensitivity for small specimens (approximately diameter of 1 mm), a rectangular OPT-mfEIT chamber was developed using the electrodes as are shown in Fig. 17. The placement of the chamber in the imaging system is shown in Fig. 19. The feasibility of this configuration was proven with a plant phantom in (III), and the results are also shown in Fig. 20 (a). Trial 3 chamber contained eight electrodes in one vertical layer, thus it was suitable for 2D *in vitro* imaging.

**Figure 17.** Trial 3 OPT-mfEIT chamber with a carrot rotated in saline.



Trial 4: To attain 3D OPT-mfEIT results, trial 4 electrodes were attached to a chamber as is shown in Fig. 18. The placement of the chamber in the imaging system is shown in Fig. 19. Results using this chamber are shown in (IV) and in Figs. 20 (b) and 21-26.

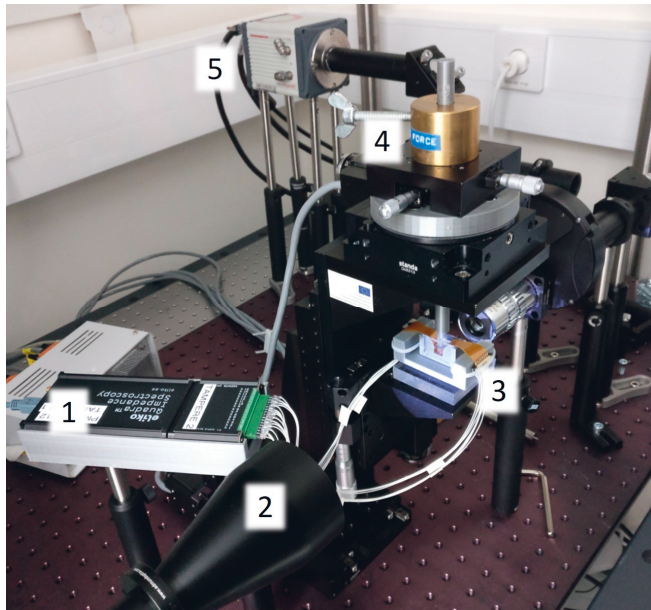
**Figure 18.** Trial 4 electrodes built into the rectangular OPT-mfEIT chamber. Two pieces of tissues embedded in agarose hydrogel are rotated in saline.



## 6.2.2 Integrated OPT-mfEIT system

The system presented in the Fig. 7 schematic is shown as a photograph in Fig. 19 with the trial 4 chamber. Specimens were attached to a long rotation stick and aligned in the saline-filled chamber. The upper part of the stick connected the specimen to the motorized rotational stage. After aligning the specimen in the center of the chamber, OPT and mfEIT were simultaneously acquired.

**Figure 19.** Photograph of the OPT-mfEIT setup. 1: Spectro-EIT device, 2: LED and telecentric lens for OPT illumination, 3: electrode chamber, 4: stage for specimen placement, alignment, and rotation, 5: OPT camera.



## 6.2.3 OPT-mfEIT results using smoothness priors

After the preliminary results with the trial 1 chamber, OPT-mfEIT was further used with the trial 3 (III) and trial 4 (IV) chambers. Smoothness promoting regularization functionals were used to test and demonstrate the novel technique. The smoothness assumption results in the smooth edges as is seen in the reconstructed images in Figs. 13, 15, 16 (c), and 20.

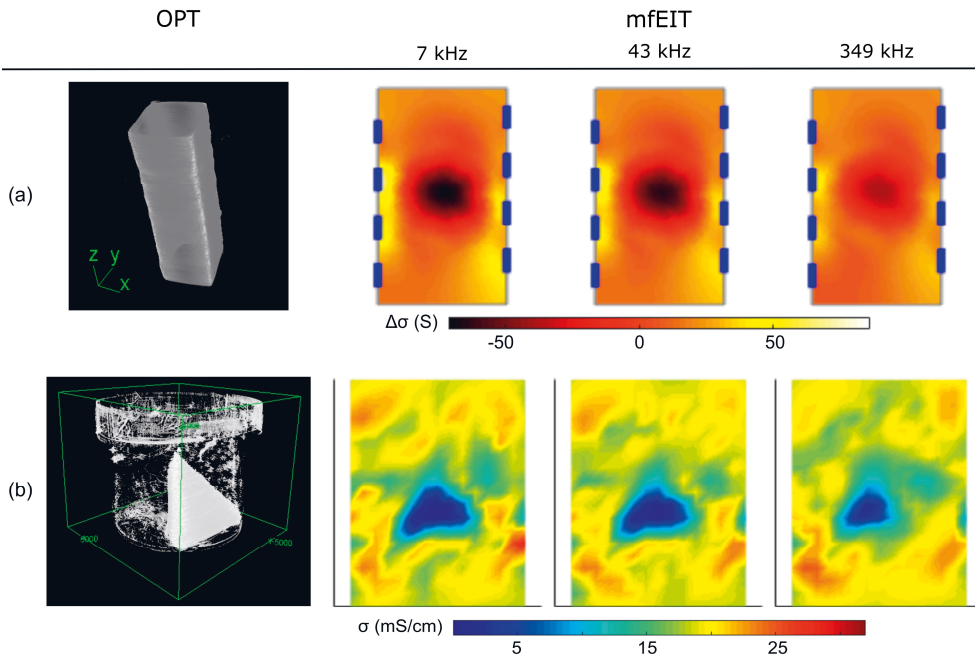
The main results with the trial 3 chamber are shown in Fig. 20 (a), where OPT reconstruction of the rectangular fresh carrot is visualized in the first column. Time-

difference mfEIT of the carrot is visualized with three different frequencies in the following columns. The mfEIT images show that the conductivity increased along increasing frequencies. This is in line with the theory of dielectric properties of biological specimens and experimental conductivity spectrum of a carrot in saline (Ahn et al., 2010).

Smoothness prior results with the trial 4 chamber are shown in Fig. 20 (b). A tetrahedral fresh potato was embedded in agarose hydrogel and rotated in saline. The tetrahedral shape of the potato can be seen in the OPT reconstruction. One plane of the absolute 3D mfEIT reconstruction is visualized at three different frequencies from 7 kHz to 349 kHz. The mfEIT results show that conductivity of the potato increased along increasing frequencies that is in line with the theory and experimental potato spectrum in (Ahn et al., 2010).

These 2D and 3D results indicated that rotational mfEIT method produces useful information of the conductivity distribution of the specimen. These results were promising since it can be assumed that the use of structural priors would further enhance the mfEIT image quality.

**Figure 20.** OPT-mfEIT smoothness prior results. (a) OPT reconstruction and 2D time-difference mfEIT reconstructions of a rectangular carrot. The EIT domain was 6 mm x 9 mm in the xy-plane. Adapted from (III). (b) OPT reconstruction and absolute 3D mfEIT reconstructions of a potato. A plane at height 1.3 mm from the chamber bottom is visualized at each frequency. The dimensions of the EIT domain were (x,y,z) = (6, 9, 4) mm. Adapted from (IV).



## 6.2.4 MfEIT results using structural priors from OPT

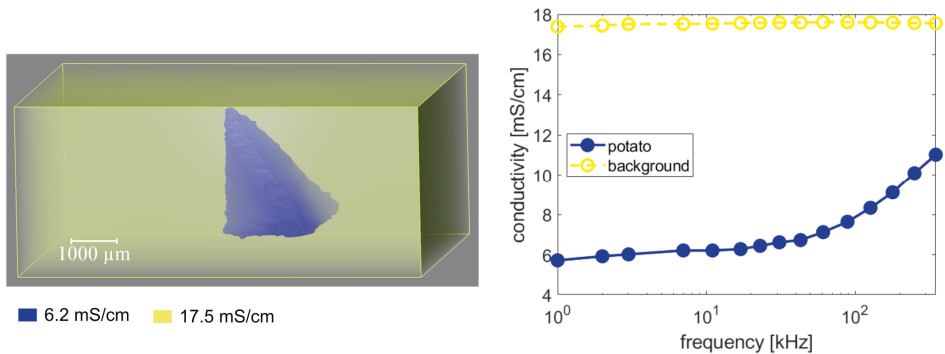
Validation experiments of the functionality of the 3D OPT-mfEIT were performed with the trial 4 chamber and various specimen types in (IV). 3D segmentations from OPT reconstructions were used as structural priors, thus, regularization was not needed in the mfEIT reconstruction. MfEIT results were reconstructed in the absolute mode that reveals absolute conductivity values of the specimen. The conductivities were reconstructed segmentally constant so that each segment, that is, the inclusion(s) and background, was assigned to have a homogenous conductivity at each frequency. Thus, OPT was used to detect segment shapes and locations and mfEIT was used to reconstruct segments conductivity spectra.

First validation experiment was made with a tetrahedral piece of fresh potato to demonstrate the difference of smoothness prior (Fig. 20 (b)) and structural prior results (Fig. 21) when the same data was used. OPT reconstruction shown in Fig. 20

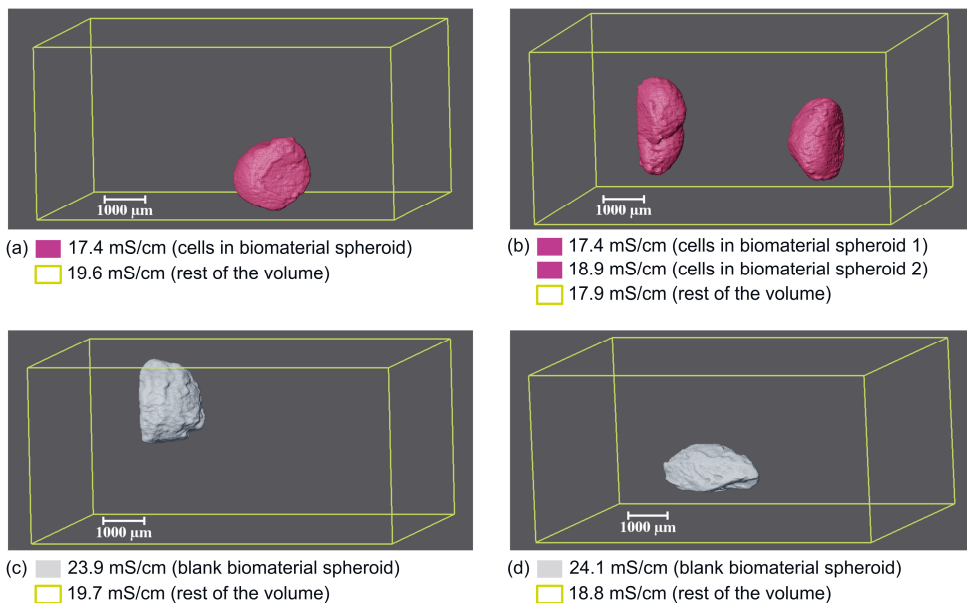
(b) was segmented and used as a structural prior. The results show that the potato was less conductive than the background, and the potato conductivity increased as the frequencies increased, as was expected (Ahn et al., 2010). In contrast, the background conductivity was rather constant along frequencies. This was expected since the background contained saline and agarose hydrogel that were not expected to show dielectric properties.

Second validation experiment was done with biomaterial spheroids: either blank or containing hiPS cells. OPT-mfEIT reconstructions of the spheroids and backgrounds are visualized in Fig. 22 at 7 kHz frequency. Three spheroids contained cells and two spheroids were blank. Rest of the measured volume was background containing saline and agarose hydrogel as in the previous potato experiment. The conductivity spectra derived from the OPT-mfEIT reconstructions are shown in Fig. 23. The hiPS cells -containing spheroids have lower conductivity than the blank biomaterial spheroids. This was expected due to the isolating intact cell membranes, as is explained in section 2.5. In addition, the background conductivities remained at approximately 19 mS/cm at all frequencies, as was expected.

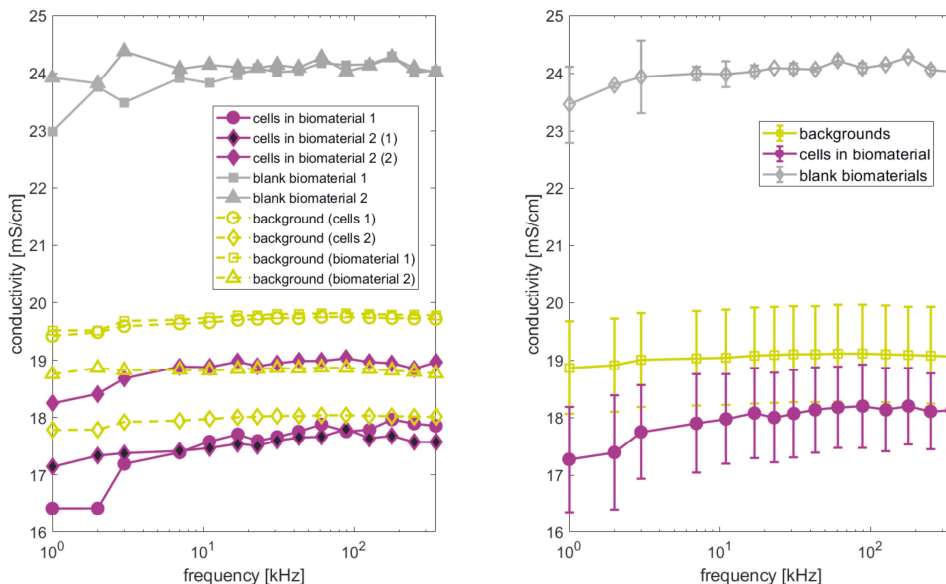
**Figure 21.** OPT-mfEIT reconstructions of a tetrahedral piece of fresh potato. Left: OPT-mfEIT reconstruction at 7 kHz. Right: conductivity spectra derived from OPT-mfEIT reconstructions at 15 frequencies from 1 kHz to 349 kHz. Background consisted of saline and agarose hydrogel and is indicated as yellow color in both images. Adapted from (IV).



**Figure 22.** OPT-mfEIT reconstructions at 7 kHz of four specimens: (a) cells in biomaterial 1, (b) cells in biomaterial 2, (c) blank biomaterial 1, and (d) blank biomaterial 2. The conductivity of each segment is marked below each image and the rest of the volume is background.



**Figure 23.** Conductivity spectra derived from the OPT-mfEIT reconstructions of the spheroid specimens at 15 frequencies. Left: conductivity spectrum of each spheroid or specimen's background. Right: mean  $\pm$  standard deviation of parallel segments. Adapted from (IV).





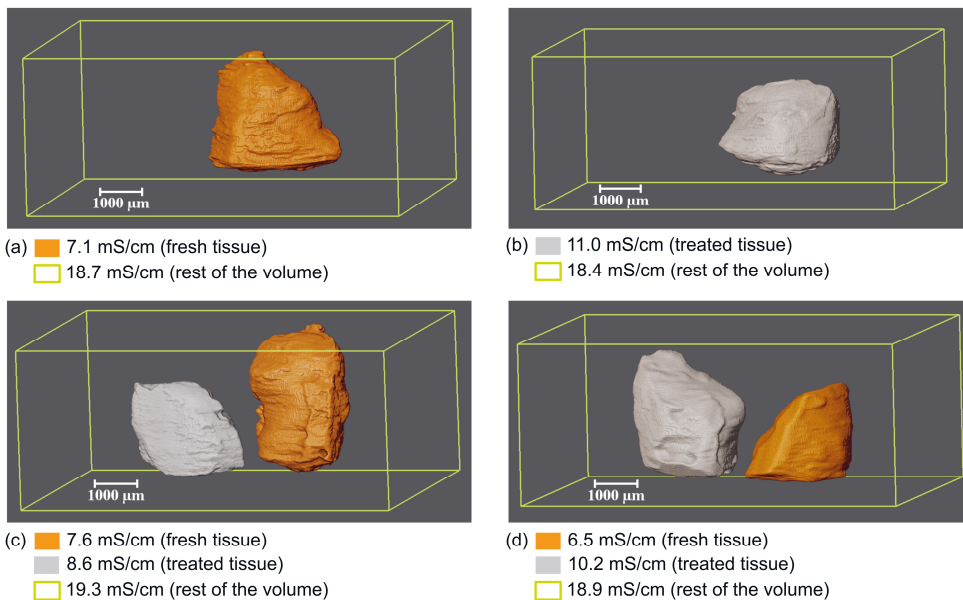
Third validation experiment was obtained with porcine liver tissues as are shown in Figs. 24 and 25. Fresh porcine liver tissue was cut to small pieces and half of them were dissolved in Triton X-100. Three tissue inclusions were fresh and three were treated. Two of the specimens contained one tissue piece and two specimens contained two tissue pieces. Background contained agarose hydrogel and saline as in the previous experiments.

The results in Fig. 25 show that the treated tissues were more conductive than the fresh ones. This is due to the breakage of the cell membranes that leads the current to flow through the well conducting cytoplasm. These results were in line with previously reported results on breast cancer spheroids (Wu, Yang, et al., 2018). The conductivities of fresh and treated tissues were proven to have different medians with Wilcoxon rank sum test ( $p$ -value  $3.2 \times 10^{-16}$ ). The means and standard deviations shown in Fig. 25 support the conductivity difference of the fresh and treated liver tissues. In addition, the background conductivities were close to 19 mS/cm in all specimens and all frequencies, as was expected.

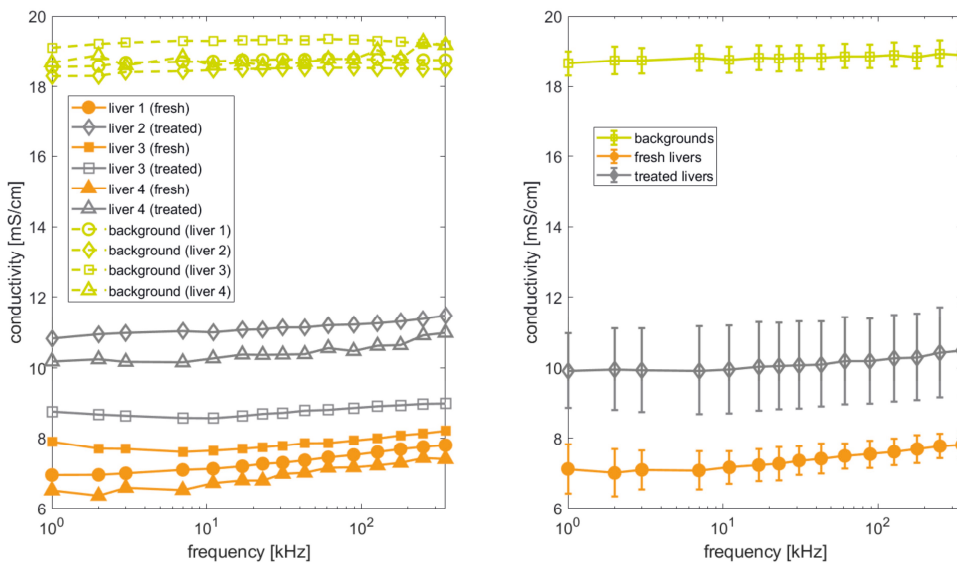
Distinguishability of OPT-mfEIT technique is high based on the results of the specimens: cells in biomaterial 2 (Fig. 22 (b)), liver 3 (Fig. 24 (c)), and liver 4 (Fig. 24 (d)). All the inclusions in these specimens resulted in separate conductivity spectra despite the short distance between them. Shortest distance between individual inclusions was 0.5 mm in liver 4 specimen.

Further validation results were obtained with viable and killed human adipose tissues (Fig. 7 in **(IV)**). The results on adipose tissue imply that the induced necrotic cell death could be detected using OPT-mfEIT. This is in line with the results reported in (Davalos & Rubinsky, 2004).

**Figure 24.** OPT-mfEIT reconstructions at 7 kHz of four specimens: (a) liver 1 (fresh), (b) liver 2 (treated), (c) liver 3 (fresh and treated), and (d) liver 4 (fresh and treated). The conductivity of each segment is marked below each image and the rest of the volume is background.



**Figure 25.** Conductivity spectra derived from the OPT-mfEIT reconstructions of the liver specimens at 15 frequencies. Left: conductivity spectrum of each liver tissue or specimen's background. Right: mean  $\pm$  standard deviation of parallel segments. Adapted from (IV).



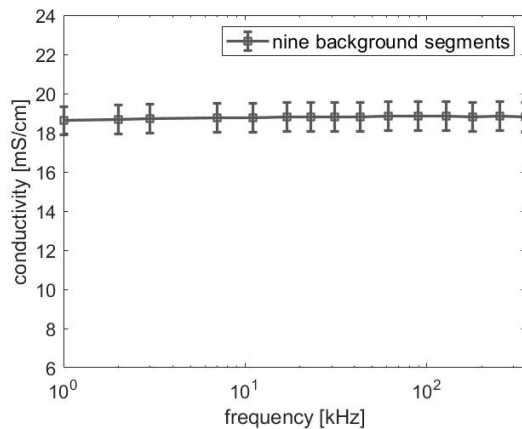
## 6.2.5 Repeatability of OPT-mfEIT

In all the specimens presented in the section 6.2.4, the background segment consisted of the same materials: agarose hydrogel and saline (phosphate buffered saline). All measurements were acquired with the trial 4 chamber and in room temperature. In addition, background materials were independent of biological variance that occurs in cell cultures and tissues. Therefore, the reconstructed conductivities of the background segments should be similar in each experiment presented in Figs. 21, 23, and 25.

Background data were tested to be normally distributed with one-sample Kolmogorov-Smirnov test. The mean and standard deviation of all nine backgrounds are shown in Fig. 26 where the average conductivity ranges between [18.61 18.85] mS/cm and standard deviation between [0.71 0.74] mS/cm at the studied frequency range.

The background materials were measured with conductivity meter (Hanna Instruments, HI-8733): saline solution was 12 mS/cm and agarose hydrogel 13 mS/cm at room temperature. As was stated in (IV), all resulting conductivity values reconstructed with OPT-mfEIT were slightly higher than comparable literature values due to approximate current injection value used in the image reconstruction. This is the case for background values too as they are close to 19 mS/cm.

**Figure 26.** Mean and standard deviation of the background conductivities from nine specimens presented in the validation experiments in Figs. 21, 23, and 25.



To further demonstrate the repeatability of the OPT-mfEIT technique, Cronbach's alpha statistical test was applied to the nine background values with a result of 0.85 (Leontitsis, 2023). Cronbach's alpha test is used to evaluate the reliability of measurement instruments. Values from 0.70 to 0.95 are typically considered acceptable, and high values indicate high repeatability whereas low values indicate low repeatability (Tavakol & Dennick, 2011). Both the low standard deviation and high value from the Cronbach's alpha test indicate high repeatability of the OPT-mfEIT technique.

Overall, the validation results of the OPT-mfEIT technique were in line with previous studies and the general theory. The results present that this technique provides a new label-free tool for the challenging mesoscopic scale imaging of 3D *in vitro* specimens.

## 7 DISCUSSION

Novel imaging methods are needed as cell culture research is evolving from 2D cultures to 3D constructs – and further to organ-/body-on-chip systems. Thickness of the constructs hinders the use of conventional imaging systems, especially if the specimen is wished to maintain viable during and after the imaging. EIT has emerged as one solution due to its ability to image optically opaque specimens in a label-free way. It has been shown to be efficient tool for cell viability detection for example in toxicity assays (Linderholm et al., 2008; Wu, Yang, et al., 2018; Yin et al., 2018).

Multimodal EIT applications have been presented in the field of medical imaging to obtain multiphysical information and to enhance the spatial resolution of EIT via structural priors (Crabb et al., 2014; Li et al., 2020; Soleimani, 2006). Multimodal *in vitro* systems have also emerged to improve EIT image quality and to enable quantitative analysis of 3D cell cultures (Z. Liu et al., 2020, 2022). This thesis work was the first to present 3D and rotational mfEIT that was combined with optical 3D imaging. The work focused on developing integrated OPT-mfEIT method to gain high spatial resolution combined with electrical conductivity images in a label-free way. In (I–III), the limited angle mfEIT technique was developed and demonstrated. In (III, IV), the use of OPT-mfEIT was validated with various 3D *in vitro* cases: plant phantoms, hiPS cell spheroids, and *ex vivo* tissues.

### 7.1 Development of the multimodal system

In the scope of OPT, the problem of acquiring full 3D data from *in vitro* specimens has been solved by rotating the specimen (Sharpe et al., 2002). Rotational EIT technique has also been shown to be feasible in different applications and provide many independent measurements (C. N. Huang et al., 2007; E. K. Murphy, Mahara, & Halter, 2017; S. C. Murphy & York, 2006). The approach in this work was to integrate EIT into already existing OPT system where the specimen was rotated during imaging. This setup enabled to gain plenty of independent EIT measurements and obtain structural prior from the OPT image. In (I), we showed that limited angle EIT is feasible if the specimen is rotated during data acquisition. Previously

presented rotational EIT applications have used full-coverage equidistantly placed electrodes where the benefit of rotation has been limited to few rotational angles. In the developed limited angle EIT, multiple rotational positions are beneficial. In **(III)** and **(IV)**, rotational EIT was demonstrated for the first time in the scope of *in vitro* imaging.

Previously presented *in vitro* EIT electrode configurations have been typically coplanar or in one vertical plane that are most suitable for 2D imaging (Farnham et al., 2019; Wu, 2020; Yang et al., 2017; Yin et al., 2018). Novel electrode configurations were needed to attain effective measurements in the OPT-mfEIT system. Therefore, numerical simulations were used to analyze the potential electrode configurations for the limited angle EIT **(I)**. Configurations that covered roughly half of the specimen boundary performed best. In **(IV)**, the opposite 4+4 electrode layout was modified into two vertical layers (opposite 8+8) to gain spatial 3D information. These configurations were demonstrated to be effective in the OPT-mfEIT imaging but are not limited to the developed system and could be potentially applied in other multimodal approaches.

There are couple of commonly used EIT measurement patterns, such as the adjacent or the cross pattern (Morcelles & Bertemes-Filho, 2021; E. K. Murphy, Mahara, & Halter, 2017; Wu, Zhou, et al., 2018). To obtain high sensitivity measurements with the new limited angle electrode configuration, various measurement patterns were designed and experimentally demonstrated **(I–IV)**. In **(IV)**, the *in vitro* OPT-mfEIT results were collected with a designed pattern that contained adjacent, cross, and opposite current injections to acquire high sensitivity data over the whole volume within a tolerable measurement time. The designs were based on the lead field theory that partly explains why EIT image quality is not linearly dependent solely on the amount of collected data; measurements with close to zero sensitivity do not provide useful information. This work has presented insight to the design of EIT measurement patterns in general.

It has been suggested that increasing the number of electrodes so that their distance would be extremely small would improve EIT accuracy as high as in X-ray tomography (Malmivuo, 2010). However, there are factors that limit the enhancement of EIT image quality via increasing the number of electrodes, or in the rotational case, the number of rotational measurement positions. One factor originates from the instrumentation noise. When the distance between adjacent voltage measurements is decreased, there will be a limit when no difference would be detected between adjacent measurements due to instrumentation noise (E. K. Murphy, Mahara, & Halter, 2017). Another limiting factor is the finite size of

elements in the inversion model. In case the element size is bigger than the shift between sequential rotational positions, one would create an overdetermined problem where the image quality would not enhance or could even deteriorate. In addition, increasing the number of electrodes or rotational measurement positions increases data acquisition and processing times. The numerical and experimental analysis presented in this thesis work showed that image quality was improved when rotational positions were increased that is in line with previous knowledge (J. Liu et al., 2015; E. K. Murphy, Mahara, & Halter, 2017; X. Zhang et al., 2015). However, the limit where the image quality improvement would stop was not published in the scope of this thesis work.

Multifrequency data acquisition has been an increasing trend in EIT applications because it opens new possibilities for biological research due to the dielectric properties of living cell and tissue cultures (Ogawa et al., 2021; Wu, Zhou, et al., 2018). However, the collection of mfEIT data increases the data acquisition time that can be problematic when imaging living *in vitro* specimens that are more or less time variant. This work presented and demonstrated the use of a fast Spectro-EIT device (II–IV). The applied binary multifrequency excitation offered fast data acquisition and simple instrumentation. The Spectro-EIT device enabled to collect a large amount of mfEIT data within reasonable imaging time even in the rotational 3D scheme.

## 7.2 Multimodal imaging of *in vitro* specimens

To obtain high quality 3D EIT reconstructions, a cuboid *in vitro* chamber with many electrodes on the walls has previously been presented (Ahn et al., 2014; Lee et al., 2014; Q. Liu et al., 2011). The cuboid chamber enabled extensive 3D data collection but was not effective for multimodal imaging. A multimodal *in vitro* system has been presented where the electrodes were in one vertical layer at the edges of the cell culture chamber to allow simultaneous optical imaging (Z. Liu et al., 2020, 2022). However, the used electrode and optical imaging layouts were optimal for 2D imaging. This thesis work introduced a novel *in vitro* imaging chamber (trial 4) that enabled both 3D and multimodal imaging. In addition, the imaging domain was relatively small and could be used to image inclusions of approximately 1 mm in diameter (IV).

MfEIT has been shown to detect cell density variations in scaffolds and it has the potential to indicate cell viability due to the frequency dependence of the specimen

conductivity (Ogawa et al., 2021; Wu, Zhou, et al., 2018). Plant phantoms are often used to develop and test novel EIT methods (Malone et al., 2015; Wi et al., 2014). The OPT-mfEIT smoothness prior results in **(III)** and **(IV)** (also in Fig. 20) presented mfEIT reconstructions of plant phantoms. The plants' conductivities increased along increasing frequencies that is in line with previous knowledge (Ahn et al., 2010). These smoothness prior results verified the functionality of the OPT-mfEIT system.

Quantitative analysis of the conductivity values is difficult from difference images and would be unreliable also from smoothness prior absolute images due to smoothness and image artifacts. Structural priors can be used in many ways in multimodal imaging. One of the most straightforward approach is to coregister the images to verify EIT results (Crabb et al., 2014). Another approach is to embed the structural info into the modelling of EIT, for example, in finite element mesh (B. Gong et al., 2016). The latter approach was applied in this thesis work for the first time in an *in vitro* application with detailed 3D segmentations embedded in the absolute mode mfEIT reconstructions **(IV)**. The resulting morphological images together with inclusions' conductivity spectra provide a novel tool for quantitative analysis in the field of *in vitro* mfEIT.

The presence of living stem cells in biomaterial spheroids decreased the spheroids' conductivity when compared to blank biomaterial spheroids **(IV)**. This is in agreement with previous studies where living cells and their growth and proliferation decreases the construct's conductivity (Canali, Heiskanen, et al., 2015; Linderholm et al., 2008).

The viability of cell cultures and tissues has been extensively studied with impedance methods (L. Gong et al., 2021; Lei et al., 2014; Pan et al., 2020; Wu, Yang, et al., 2018). The absolute mode OPT-mfEIT with structural priors was effective in detecting the tissue viability and cell membrane integrity in *ex vivo* tissues **(IV)**. The human adipose tissue, that had been killed by freezing, expressed higher conductivity than the living one. Similar results have previously been presented with rat liver (Davalos & Rubinsky, 2004). The porcine liver tissue pieces that were treated with the permeabilizing substance were more conductive than the fresh ones. These results were in agreement with previous studies that have shown an increase of conductivity after adding permeabilizing substance (Linderholm et al., 2008; Wu, Yang, et al., 2018). However, Yin et al. (2018) reported a decrease of cell aggregate conductivity after exposing it to permeabilizing substance (Yin et al., 2018). These conflicting results suggest there is a need for further validation studies on the biological phenomena in *in vitro* specimens and (mf)EIT results.



Repeatability of the developed OPT-mfEIT was proofed to be high based on Cronbach's alpha statistical test on the reconstructed conductivities of the background segments of nine different specimens.

### 7.3 Strengths and limitations of the developed system

The main strengths of the developed OPT-mfEIT technique are based on the (1) data fusion with OPT, (2) limited angle rotational data acquisition, and (3) fast Spectro-EIT device. The obvious benefit of data fusion was to obtain multiphysical information of the specimen: morphology and conductivity. OPT is inherently a 3D imaging technique that enabled the mfEIT to be developed into 3D mode as well. Absolute mode EIT is typically sensitive to noise and modeling errors that causes the resulting images to be noisy. However, the use of reference data to correct modeling errors and the OPT prior stabilized the inverse solution so well that the absolute mode OPT-mfEIT images were of high quality (**IV**). This thesis work is the first to present multimodal 3D mfEIT images.

The limited angle rotational EIT scheme and specifically designed measurement patterns allowed to collect large amount of data with high sensitivity measurements. For these reasons and the OPT data fusion, even 0.5% volume fraction inclusions were detected, and inclusions that were close to each other were distinguished (**IV**). In addition, the limited angle scheme allowed to use relatively small number of electrodes that decreased the complexity of the EIT instrument.

Important strength of this work was the developed fast Spectro-EIT device that enabled multifrequency data collection and, thus, the reconstruction of conductivity spectra of the inclusions. MfEIT is an emerging trend in the field of biological applications of EIT since it produces information of the dielectric properties of the specimen, thus, more detailed knowledge of, for example, cell concentration and viability (Ogawa et al., 2021; Wu, Zhou, et al., 2018). In addition, mfEIT increases the specificity of conductivity results since changes induced by cells and tissues can be distinguished from changes in the cell culture medium, which typically does not express capacitance.

The limitations of the developed technique are related to the novel rotational setup and the Spectro-EIT device. Typically, the temporal resolution is high in EIT systems but in OPT-mfEIT this feature was slightly compromised. Specimen alignment and rotational data acquisition induced longer specimen preparation and imaging time (10-15 min) than in typical non-rotational EIT setups. This duration

can be regarded suitable for many *in vitro* measurements such as viability assessment. Postprocessing of the data with the present system included manual work such as the segmentations and the 3D reconstructions that were computationally time-consuming: roughly 30 mins in OPT and 4–5 hours in mfEIT, depending on computer. However, this work focused on development and validation of the novel system with relatively small sample size, thus automatization of the specimen alignment and data postprocessing was not relevant.

The Spectro-EIT device used in this work did not provide the accurate excitation current values which led to inaccuracies in the absolute mfEIT images and in the derived conductivity spectra (IV). As was stated in (IV), the reconstructed conductivity values were systematically couple mS/cm higher than experimental or literature reference values. This was likely because the reconstructions used a current value that was approximately the maximum value of all tetrapolar measurements in the mfEIT pattern.

The frequency range of the used Spectro-EIT device was from 1 kHz to 349 kHz. This range is in the  $\beta$ -dispersion range for many biological specimens, and it was seen in the plant specimen results as an increase in conductivity along increasing frequency. Wider frequency range could provide better frequency difference contrast or more information of, for example,  $\alpha$ -dispersion. In future, the operating frequencies of the Spectro-EIT device could be better targeted for a specific specimen type.

The developed reconstruction algorithm in (IV) computed inclusion-wise constant conductivity. In future, computational methods could be developed to account for conductivity variations inside the inclusion.

All reconstructions in this thesis describe the conductivity change or conductivity that were computed from real part of the data and imaginary part was not applied. In future, imaginary part of the measured data could be applied in image reconstruction.

There are other challenges that are common in many *in vitro* EIT applications. One of them is how to control the factors affecting the specimen conductivity, such as temperature or changes in the ionic composition of the cell culture medium. For example, evaporation or cell metabolism may change the ionic composition of the culture medium. This should be considered especially in long-term EIT applications. The same issue applies for chemical manipulation studies where the concentration of the chemicals should be the same in the reference measurement/control specimens as in the actual specimen. Another challenge has to do with the electrode arrays material stability in moist and chemically complex environments. For example,

Kapton-based electrode insulation and substrate material would not be optimal for long-term studies since Kapton properties are affected in the presence of water.

The novelty of this dissertation was to integrate two independent 3D imaging methods for *in vitro* imaging. This offers new possibilities in the mesoscopic scale imaging. The developed technique can be used to image various 3D specimens such as spheroids and organoids that are increasingly in use in *in vitro* research but also in clinical work such as in cancer treatment. In addition, OPT-mfEIT provides a tool for validation studies of biological phenomena and their effect on the conductivity that are needed in the field of *in vitro* EIT.

## 8 SUMMARY AND CONCLUSIONS

The aim of this doctoral thesis work was to develop and validate a novel multimodal imaging technique for 3D *in vitro* studies. MfEIT was designed, built, and integrated with already existing OPT imaging system. Various plant phantoms were imaged during the development process and the final OPT-mfEIT was validated with hiPS cell constructs and *ex vivo* tissues. The results of this work can be summarized as follows:

1. The developed limited angle rotational EIT method was shown to be effective in the circular and rectangular electrode setups used in this work. Numerical and experimental studies showed that different electrode configurations are applicable in rotational limited angle systems in general, and they enable the attachment of additional sensors simultaneously with EIT. Two different mathematical algorithms were developed to model the specimen rotation in the EIT reconstruction. The weighted method was proven to produce high quality 2D results, but due to its computational load, the click method was developed for rotational 3D reconstructions. The developed limited angle electrode configurations and the click and weighted algorithms are scalable and independent of OPT, thus, applicable for other multimodal EIT approaches as well.
2. The developed *in vitro* chambers enabled simultaneous optical and electrical 3D imaging. The chambers were based on the rectangular limited angle layout where electrodes were attached on two opposing straight chamber walls. Electrode fabrication on a cylindrical and optically transparent material (FEP) was not successful. Rotational EIT measurement patterns were designed so that high sensitivity measurements were collected within suitable data acquisition time. Automated and simultaneous OPT-mfEIT acquisition minimized errors during rotational data acquisition and enabled smooth data fusion of the two imaging modalities. Reconstructions of the brightfield OPT were

successfully segmented and the segments were integrated into the finite element mesh generation in the mfEIT reconstruction.

3. The Spectro-EIT device enabled fast multifrequency data acquisition and its functionality was demonstrated by imaging plant phantoms. The  $\beta$ -dispersion of the plant phantoms was well visible in the reconstructed mfEIT images in both large tank and *in vitro* chamber experiments. The fast data acquisition enabled the collection of a large number of mfEIT measurements also with the rotational scheme, which improved the quality of the mfEIT images.
4. Validation experiments showed that multimodal imaging of hiPS cell spheroids and *ex vivo* tissue pieces was feasible and repeatable with the developed OPT-mfEIT technique. Biomaterial spheroids with embedded living hiPS cells were distinguished from biomaterial spheroids without cells. The cell membrane integrity and viability were well detected as was shown by imaging porcine liver tissue and human adipose tissue. Even low volume fraction inclusions were successfully imaged when structural prior from OPT was used, as well as inclusions that were close to each other.

## 9 REFERENCES

- Adler, A., & Lionheart, W. R. B. (2006). Uses and abuses of EIDORS: An extensible software base for EIT. *Physiological Measurement*, 27(5).
- Ahn, S., Jun, S. C., Seo, J. K., Lee, J., Woo, E. J., & Holder, D. (2010). Frequency-difference electrical impedance tomography: Phantom imaging experiments. *Journal of Physics: Conference Series*, 224(1), 012152. <https://doi.org/10.1088/1742-6596/224/1/012152>
- Ahn, S., Wi, H., Oh, T. I., McEwan, A. L., Jun, S. C., & Woo, E. J. (2014). Continuous nondestructive monitoring method using the reconstructed three-dimensional conductivity images via GREIT for tissue engineering. *Journal of Applied Mathematics*, 2014. <https://doi.org/10.1155/2014/562176>
- Alberts, B., Bray, D., Hopkin, K., Johnson, A., Lewis, J., Raff, M., Roberts, K., & Walter, P. (2014). *Essential Cell Biology*. Garland Science.
- Appel, A. A., Anastasio, M. A., Larson, J. C., & Brey, E. M. (2013). Imaging challenges in biomaterials and tissue engineering. *Biomaterials*, 34, 6615–6630. <https://doi.org/10.1016/j.biomaterials.2013.05.033>
- Bagnaninchi, P., Hay, D. C., & Zhou, W. (2018). Real-time monitoring of hepatocyte differentiation and impedimetric activity using impedance sensing. *Proceedings - 2017 10th International Congress on Image and Signal Processing, BioMedical Engineering and Informatics, CISP-BMEI 2017, 2018-Janua*, 1–2. <https://doi.org/10.1109/CISP-BMEI.2017.8302254>
- Belay, B., Koivisto, J. T., Parraga, J., Koskela, O., Montonen, T., Kellomäki, M., Figueiras, E., & Hyttinen, J. (2021). Optical projection tomography as a quantitative tool for analysis of cell morphology and density in 3D hydrogels. *Scientific Reports*, 11(1), 1–10. <https://doi.org/10.1038/s41598-021-85996-8>
- Booij, T. H., Price, L. S., & Danen, E. H. J. (2019). 3D Cell-Based Assays for Drug Screens: Challenges in Imaging, Image Analysis, and High-Content Analysis. *SLAS Discovery*, 24(6), 615–627. <https://doi.org/10.1177/2472555219830087>
- Böttrich, M., Tanskanen, J. M. A., & Hyttinen, J. A. K. (2017). Lead field theory provides a powerful tool for designing microelectrode array impedance measurements for biological cell detection and observation. *BioMedical Engineering Online*, 16(85), 1–17. <https://doi.org/10.1186/s12938-017-0372-5>
- Brown, B. H. (2003). Electrical impedance tomography (EIT): A review. *Journal of Medical Engineering and Technology*, 27(3), 97–108. <https://doi.org/10.1080/0309190021000059687>
- Canali, C., Aristovich, K., Ceccarelli, L., Larsen, L. B., Martinsen, G., Wolff, A., Dufva, M., Emnéus, J., & Heiskanen, A. (2016). Electrical impedance tomography methods for miniaturised 3D systems. *Journal of Electrical Bioimpedance*, 7(1), 59–67. <https://doi.org/10.5617/jeb.4084>
- Canali, C., Heiskanen, A., Muhammad, H. B., Høyum, P., Pettersen, F.-J., Hemmingsen, M., Wolff, A., Dufva, M., Martinsen, O. G., & Emnéus, J. (2015). Bioimpedance monitoring of 3D cell culturing-Complementary electrode configurations for

- enhanced spatial sensitivity. *Biosensors & Bioelectronics*, 63, 72–79. <https://doi.org/10.1016/j.bios.2014.07.020>
- Canali, C., Mazzoni, C., Larsen, L. B., Heiskanen, A., Martinsen, O. G., Wolff, A., Dufva, M., & Emneus, J. (2015). An impedance method for spatial sensing of 3D cell constructs—Towards applications in tissue engineering. *Analyst*, 140(17), 6079–6088. <https://doi.org/10.1039/c5an00987a>
- Chai, K. T. C., Davies, J. H., & Cumming, D. R. S. (2007). Electrical impedance tomography for sensing with integrated microelectrodes on a CMOS microchip. *Sensors and Actuators, B: Chemical*, 127(1), 97–101. <https://doi.org/10.1016/j.snb.2007.07.009>
- Chen, Z., & Yang, Y. (2021). Structure-Aware Dual-Branch Network for Electrical Impedance Tomography in Cell Culture Imaging. *IEEE Transactions on Instrumentation and Measurement*, 70, 1–9. <https://doi.org/10.1109/TIM.2021.3092524>
- Chen, Z., Yang, Y., & Bagnaninchi, P. O. (2021). Hybrid Learning-Based Cell Aggregate Imaging with Miniature Electrical Impedance Tomography. *IEEE Transactions on Instrumentation and Measurement*, 70. <https://doi.org/10.1109/TIM.2020.3035384>
- Cheng, K.-S., Isaacson, D., Newell, J., & Gisser, D. G. (1989). Electrode Models for Electric Current Computed Tomography. *IEEE Transactions on Biomedical Engineering*, 36(9), 918–924. <https://doi.org/10.1109/10.35300>
- Cook, R. D., Saulnier, G. J., Gisser, D. G., Goble, J. C., Newell, J. C., & Isaacson, D. (1994). ACT3: A High-Speed, High-Precision Electrical Impedance Tomograph. *IEEE Transactions on Biomedical Engineering*, 41(8), 713–722. <https://doi.org/10.1109/10.310086>
- Cortesi, M., Samoré, A., Lovecchio, J., Ramilli, R., Tartagni, M., Giordano, E., & Crescentini, M. (2021). Development of an electrical impedance tomography set-up for the quantification of mineralization in biopolymer scaffolds. *Physiological Measurement*, 42, 064001. <https://doi.org/10.1088/1361-6579/ac023b>
- Crabb, M. G., Davidson, J. L., Little, R., Wright, P., Morgan, A. R., Miller, C. A., Naish, J. H., Parker, G. J. M., Kikinis, R., McCann, H., & Lionheart, W. R. B. (2014). Mutual information as a measure of image quality for 3D dynamic lung imaging with EIT. *Physiological Measurement*, 35(5), 863–879. <https://doi.org/10.1088/0967-3334/35/5/863>
- Daidi, Z., Siltanen, S., Tanskanen, J., & Hyttinen, J. (2007). Using Micro Electrode Array For On-line EIT Measurement. In H. Scharfetter & R. Merva (Eds.), *13th International Conference on Electrical Bioimpedance and the 8th Conference on Electrical Impedance Tomography. IFMBE Proceedings, vol 17*. (pp. 444–447). Springer-Verlag. [https://doi.org/10.1007/978-3-540-73841-1\\_115](https://doi.org/10.1007/978-3-540-73841-1_115)
- Daily, W., Ramirez, A., Binley, A., & LaBrecque, D. (2005). Electrical Resistance Tomography—Theory and Practice. In D. K. Butler (Ed.), *Near-Surface Geophysics* (pp. 525–550). Society of Exploration Geophysicists (SEG).
- Darnajou, M., Dupré, A., Dang, C., Ricciardi, G., Bourennane, S., & Bellis, C. (2019). On the implementation of simultaneous multi-frequency excitations and measurements for electrical impedance tomography. *Sensors (Switzerland)*, 19(17), 1–19. <https://doi.org/10.3390/s19173679>
- Davalos, R., & Rubinsky, B. (2004). Electrical Impedance Tomography of Cell Viability in Tissue With Application to Cryosurgery. *Journal of Biomechanical Engineering*, 126, 305–309. <https://doi.org/10.1115/1.1695577>

- De León, S. E., Pupovac, A., & McArthur, S. L. (2020). Three-Dimensional (3D) cell culture monitoring: Opportunities and challenges for impedance spectroscopy. *Biotechnology and Bioengineering*, *117*(4), 1230–1240. <https://doi.org/10.1002/bit.27270>
- Dellaquila, A., Le Bao, C., Letourneur, D., & Simon-Yarza, T. (2021). In Vitro Strategies to Vascularize 3D Physiologically Relevant Models. *Advanced Science*, *8*(19). <https://doi.org/10.1002/advs.202100798>
- Duval, K., Grover, H., Han, L. H., Mou, Y., Pegoraro, A. F., Fredberg, J., & Chen, Z. (2017). Modeling physiological events in 2D vs. 3D cell culture. *Physiology*, *32*(4), 266–277. <https://doi.org/10.1152/physiol.00036.2016>
- Edmondson, R., Broglie, J. J., Adcock, A. F., & Yang, L. (2014). Three-dimensional cell culture systems and their applications in drug discovery and cell-based biosensors. *Assay and Drug Development Technologies*, *12*(4), 207–218. <https://doi.org/10.1089/adt.2014.573>
- Fang, Y., & Eglén, R. M. (2017). Three-Dimensional Cell Cultures in Drug Discovery and Development. *SLAS Discovery*, *22*(5), 456–472. <https://doi.org/10.1177/1087057117696795>
- Farnham, K. R., Murphy, E. K., & Halter, R. J. (2019). EIT tissue growth monitor for 3D imaging of tissue viability. In A. Boyle, K. Aristovich, A. Witkowska-Wrobel, & D. Holder (Eds.), *Proceedings of the 20th International Conference on Biomedical Applications of Electrical Impedance Tomography*. <https://doi.org/10.5281/zenodo.2691705>
- Figueiras, E., Soto, A. M., Jesus, D., Lehti, M., Koivisto, J., Parraga, J. E., Silva-Correia, J., Oliveira, J. M., Reis, R. L., Kellomäki, M., & Hyttinen, J. (2014). Optical Projection Tomography as a tool for 3D imaging of hydrogels. *Biomedical Optics Express*, *5*(10), 3443–3449.
- Geselowitz, D. B. (1971). An Application of Electrocardiographic Lead Theory to Impedance Plethysmography. *IEEE Transactions on Biomedical Engineering*, *BME-18*(1), 38–41. <https://doi.org/10.1109/TBME.1971.4502787>
- Gomes, M. E., Rodrigues, M. T., Domingues, R. M. A., & Reis, R. L. (2017). Tissue engineering and regenerative medicine: New trends and directions—A year in review. *Tissue Engineering - Part B: Reviews*, *23*(3), 211–224. <https://doi.org/10.1089/ten.teb.2017.0081>
- Gong, B., Schullcke, B., Krueger-Ziolek, S., Mueller-Lisse, U., & Moeller, K. (2016). Sparse regularization for EIT reconstruction incorporating structural information derived from medical imaging. *Physiological Measurement*, *37*(6), 843–862. <https://doi.org/10.1088/0967-3334/37/6/843>
- Gong, L., Petchakup, C., Shi, P., Tan, P. L., Tan, L. P., Tay, C. Y., & Hou, H. W. (2021). Direct and Label-Free Cell Status Monitoring of Spheroids and Microcarriers Using Microfluidic Impedance Cytometry. *Small*, *17*(21), 1–11. <https://doi.org/10.1002/sml.202007500>
- Grimnes, S., & Martinsen, Ø. G. (2015). *Bioimpedance and Bioelectricity Basics*. London, England: Academic Press.
- Hallaji, M., Seppänen, A., & Pour-Ghaz, M. (2014). Electrical impedance tomography-based sensing skin for quantitative imaging of damage in concrete. *Smart Materials and Structures*, *23*(8), 085001. <https://doi.org/10.1088/0964-1726/23/8/085001>
- Halonen, S., Kari, J., Ahonen, P., Kronström, K., & Hyttinen, J. (2019). Real-Time Bioimpedance-Based Biopsy Needle Can Identify Tissue Type with High Spatial Accuracy. *Annals of Biomedical Engineering*, *47*(3), 836–851. <https://doi.org/10.1007/s10439-018-02187-9>



- Halonen, S., Ovissi, A., Boyd, S., Kari, J., Kronström, K., Kosunen, J., Laurén, H., Numminen, K., Sievänen, H., & Hyttinen, J. (2022). Human in vivo liver and tumor bioimpedance measured with biopsy needle. *Physiological Measurement*, *43*(1). <https://doi.org/10.1088/1361-6579/ac4d38>
- Hanke, M., Harrach, B., & Hyvönen, N. (2011). Justification of point electrode models in electrical impedance tomography. *Mathematical Models and Methods in Applied Sciences*, *21*(06), 1395–1413. <https://doi.org/10.1142/S0218202511005362>
- Hildebrandt, C., Büth, H., Cho, S., Impidjati, & Thielecke, H. (2010). Detection of the osteogenic differentiation of mesenchymal stem cells in 2D and 3D cultures by electrochemical impedance spectroscopy. *Journal of Biotechnology*, *148*, 83–90. <https://doi.org/10.1016/j.jbiotec.2010.01.007>
- Holder, D. S. (Ed.). (2005). *Electrical impedance tomography: Methods, history and applications*. IOP Publishing Ltd.
- Huang, C. N., Yu, F. M., & Chung, H. Y. (2007). Rotational electrical impedance tomography. *Measurement Science and Technology*, *18*(9), 2958–2966. <https://doi.org/10.1088/0957-0233/18/9/028>
- Huang, C. N., Yu, F. M., & Chung, H. Y. (2008). The scanning data collection strategy for enhancing the quality of electrical impedance tomography. *IEEE Transactions on Instrumentation and Measurement*, *57*(6), 1193–1198. <https://doi.org/10.1109/TIM.2007.915149>
- Huang, D., Swanson, E. A., Lin, C. P., Schuman, J. S., Stinson, W. G., Chang, W., Hee, M. R., Flotte, T., Gregory, K., Puliafito, C. A., & Fujimoto, J. G. (1991). Optical coherence tomography. *Science*, *254*(5035), 1178–1181. <https://doi.org/10.1126/science.1957169>
- Huisken, J., Swoger, J., Bene, F. D., Wittbrodt, J., & Stelzer, E. H. K. (2004). Optical Sectioning Deep Inside Live Embryos by Selective Plane Illumination Microscopy. *Science*, *305*, 1007–1009. <https://doi.org/10.1126/science.1100035>
- Hyttinen, J. A. K., Malmivuo, J. A., & Walker, S. J. (1993). Lead field of ECG leads calculated by a computer thorax model—an application of reciprocity. *Proceedings of Computers in Cardiology Conference*, 241–244. <https://doi.org/10.1109/CIC.1993.378459>
- Jaatinen, L., Sippola, L., Kellomäki, M., Miettinen, S., Suuronen, R., & Hyttinen, J. (2009). Bioimpedance Measurement Setup for the Assessment of Viability and Number of Human Adipose Stem Cells Cultured as Monolayers. In O. Dössel & W. C. Schlegel (Eds.), *World Congress on Medical Physics and Biomedical Engineering* (pp. 286–288). Springer, Berlin, Heidelberg. [https://doi.org/10.1007/978-3-642-03900-3\\_83](https://doi.org/10.1007/978-3-642-03900-3_83)
- Justice, C., Brix, A., Freimark, D., Kraume, M., Pfromm, P., Eichenmueller, B., & Czermak, P. (2011). Process control in cell culture technology using dielectric spectroscopy. *Biotechnology Advances*, *29*(4), 391–401. <https://doi.org/10.1016/j.biotechadv.2011.03.002>
- Kaipio, J. P., Kolehmainen, V., Vauhkonen, M., & Somersalo, E. (1999). Inverse problems with structural prior information. *Inverse Problems*, *15*(3), 713–729. <https://doi.org/10.1088/0266-5611/15/3/306>
- Kauppinen, P., Hyttinen, J., & Malmivuo, J. (2006). Sensitivity Distribution Visualizations of Impedance Tomography Measurement Strategies. *International Journal of Bioelectromagnetism*, *8*, 63–71.
- Keese, C. R., & Giaever, I. (1986). Electric to Monitor the Dynamical Behavior in Tissue Culture. *Transactions on Biomedical Engineering, BME-3*(2), 242–247.

- Keese, C. R., & Giaever, I. (1994). A Biosensor that Monitors Cell Morphology with Electrical Fields. *IEEE Engineering in Medicine and Biology Magazine*, 13(3), 402–408. <https://doi.org/10.1109/51.294012>
- Kim, J., Koo, B. K., & Knoblich, J. A. (2020). Human organoids: Model systems for human biology and medicine. *Nature Reviews Molecular Cell Biology*, 21(10), 571–584. <https://doi.org/10.1038/s41580-020-0259-3>
- Klößgen, B., Rümenapp, C., & Gleich, B. (2011). Bioimpedance Spectroscopy. In B. Booß-Bavnbek, B. Klößgen, J. Larsen, F. Pociot, & E. Renström (Eds.), *BetaSys Systems Biology of Regulated Exocytosis in Pancreatic  $\beta$ -Cells* (pp. 241–271). Springer Science+Business Media.
- Kolehmainen, V., Ehrhardt, M. J., & Arridge, S. R. (2019). Incorporating structural prior information and sparsity into EIT using parallel level sets. *Inverse Problems and Imaging*, 13(2), 285–307. <https://doi.org/10.3934/ipi.2019015>
- Koskela, O., Chowdhury, M. T. K., Montonen, T., Belay, B., Pursiainen, S., & Hyttinen, J. (2021). Optical Projection Tomography for Particle Counting and Morphology Analysis. *IFMBE Proceedings*, 80, 944–951. [https://doi.org/10.1007/978-3-030-64610-3\\_105](https://doi.org/10.1007/978-3-030-64610-3_105)
- Koskela, O., Lehti-Polojärvi, M., Seppänen, A., Figueiras, E., & Hyttinen, J. (2019). Finite Element Mapping for Efficient Image Reconstruction in Rotational Electrical Impedance Tomography. In L. Lhotska, L. Sukupova, I. Lacković, & G. Ibbott (Eds.), *World Congress on Medical Physics and Biomedical Engineering 2018* (pp. 901–904). IFMBE Proceedings. [https://doi.org/10.1007/978-981-10-9038-7\\_166](https://doi.org/10.1007/978-981-10-9038-7_166)
- Kourunen, J. (2014). *Imaging of Mixing in Selected Industrial Processes Using Electrical Resistance Tomography*. University of Eastern Finland. <https://erepo.uef.fi/handle/123456789/14521>
- Land, R., Cahill, B. P., Parve, T., Annus, P., & Min, M. (2011). Improvements in design of spectra of multisine and binary excitation signals for multi-frequency bioimpedance measurement. *Proceedings of the Annual International Conference of the IEEE Engineering in Medicine and Biology Society, EMBS*, 4038–4041. <https://doi.org/10.1109/IEMBS.2011.6091003>
- Lee, E. J., Wi, H., McEwan, A. L., Farooq, A., Sohal, H., Woo, E. J., Seo, J. K., & Oh, T. I. (2014). Design of a microscopic electrical impedance tomography system for 3D continuous non-destructive monitoring of tissue culture. *BioMedical Engineering Online*, 13(1), 1–15. <https://doi.org/10.1186/1475-925X-13-142>
- Lehti-Polojärvi, M. (2014). *Electrical impedance tomography applied to stem cells in hydrogel scaffold* [Tampere University of Technology]. <https://urn.fi/URN:NBN:fi:tty-201412051588>
- Lei, K. F., Liu, T. K., & Tsang, N. M. (2018). Towards a high throughput impedimetric screening of chemosensitivity of cancer cells suspended in hydrogel and cultured in a paper substrate. *Biosensors and Bioelectronics*, 100(259), 355–360. <https://doi.org/10.1016/j.bios.2017.09.029>
- Lei, K. F., Wu, M. H., Hsu, C. W., & Chen, Y. D. (2014). Real-time and non-invasive impedimetric monitoring of cell proliferation and chemosensitivity in a perfusion 3D cell culture microfluidic chip. *Biosensors and Bioelectronics*, 51, 16–21. <https://doi.org/10.1016/j.bios.2013.07.031>
- Lemmens, M., Biesmans, H., Bormans, S., Vandenryt, T., & Thoelen, R. (2018). Electrical Impedance Tomography With a Lab-on-Chip for Imaging Cells in Culture. *Physica Status Solidi (A) Applications and Materials Science*, 215(15), 1–8. <https://doi.org/10.1002/pssa.201700868>

- Leontitsis, A. (2023). *Cronbach's Alpha* [Computer software]. MATLAB Central File Exchange. <https://www.mathworks.com/matlabcentral/fileexchange/7829-cronbach-s-alpha>
- Li, Z., Zhang, J., Liu, D., & Du, J. (2020). CT Image-Guided Electrical Impedance Tomography for Medical Imaging. *IEEE Transactions on Medical Imaging*, *39*(6), 1822–1832. <https://doi.org/10.1109/TMI.2019.2958670>
- Linderholm, P., Marescot, L., Loke, M. H., & Renaud, P. (2008). Cell Culture Imaging Using Microimpedance Tomography. *IEEE Transactions on Biomedical Engineering*, *55*(1), 138–146. <https://doi.org/10.1109/TBME.2007.910649>
- Liu, D., Kolehmainen, V., Siltanen, S., Laukkanen, A.-M., & Seppänen, A. (2015). Estimation of conductivity changes in a region of interest with electrical impedance tomography. *Inverse Problems and Imaging*, *9*(1), 211–229. <https://doi.org/10.3934/ipi.2015.9.211>
- Liu, J., Xiong, H., Lin, L., & Li, G. (2015). Evaluation of measurement and stimulation patterns in open electrical impedance tomography with scanning electrode. *Medical & Biological Engineering & Computing*, *53*(7), 589–597. <https://doi.org/10.1007/s11517-015-1274-y>
- Liu, Q., Oh, T. I., Wi, H., Lee, E. J., Seo, J. K., & Woo, E. J. (2011). Design of a microscopic electrical impedance tomography system using two current injections. *Physiological Measurement*, *32*(9), 1505–1516. <https://doi.org/10.1088/0967-3334/32/9/011>
- Liu, Z., Bagnaninchi, P., & Yang, Y. (2022). Impedance-Optical Dual-Modal Cell Culture Imaging with Learning-Based Information Fusion. *IEEE Transactions on Medical Imaging*, *41*(4), 983–996. <https://doi.org/10.1109/TMI.2021.3129739>
- Liu, Z., Kang, X., Bagnaninchi, P., & Yang, Y. (2020). Impedance-optical Dual-modal Sensor and Image Reconstruction for Cell Spheroids Imaging. *Proceedings of IEEE Sensors, 2020-Octob*(2), 7–10. <https://doi.org/10.1109/SENSORS47125.2020.9278662>
- Luo, S., Afonso, V. X., Webster, J. G., & Tompkins, W. J. (1992). The electrode system in impedance-based ventilation measurement. *IEEE Transactions on Biomedical Engineering*, *39*(11), 1130–1141. <https://doi.org/10.1109/10.168692>
- Malmivuo, J. (2010). Principle of reciprocity solves the most important problems in bioimpedance and in general in bioelectromagnetism. *Journal of Physics: Conference Series*, *224*(012001), 1–4. <https://doi.org/10.1088/1742-6596/224/1/012001>
- Malmivuo, J., & Plonsey, R. (1995). *Bioelectromagnetism: Principles and Application of Bioelectric and Biomagnetic Fields*. Oxford University Press, New York. <http://www.bem.fi/book/>
- Malone, E., Dos Santos, G. S., Holder, D., & Arridge, S. (2015). A Reconstruction-Classification Method for Multifrequency Electrical Impedance Tomography. *IEEE Transactions on Medical Imaging*, *34*(7), 1486–1497. <https://doi.org/10.1109/TMI.2015.2402661>
- Martí-Bonmatí, L., Sopena, R., Bartumeus, P., & Sopena, P. (2010). Multimodality imaging techniques. *Contrast Media and Molecular Imaging*, *5*(4), 180–189. <https://doi.org/10.1002/cmml.393>
- McFee, R., & Johnston, F. D. (1953). Electrocardiographic Leads: I. Introduction. *Circulation*, *8*(4), 554–568.
- Min, M., Ojarand, J., Martens, O., Paavle, T., Land, R., Annus, P., Rist, M., Reidla, M., & Parve, T. (2012). Binary signals in impedance spectroscopy. *Proceedings of the Annual International Conference of the IEEE Engineering in Medicine and Biology Society, EMBS*, 134–137. <https://doi.org/10.1109/EMBC.2012.6345889>
- Mohamadou, Y., Oh, T. I., Wi, H., Sohal, H., Farooq, A., Woo, E. J., & Lee McEwan, A. (2012). Performance evaluation of wideband bio-impedance spectroscopy using

- constant voltage source and constant current source. *Measurement Science and Technology*, 23(10). <https://doi.org/10.1088/0957-0233/23/10/105703>
- Morcelles, K. F., & Bertemes-Filho, P. (2021). Hardware for cell culture electrical impedance tomography: A critical review. *Review of Scientific Instruments*, 92(10). <https://doi.org/10.1063/5.0053707>
- Moreau, D., Stockslager, J. L., Cheli, R., & Haworth, K. (2002). *Lippincott professional guides: Anatomy & physiology*. Wolters Kluwer Health.
- Murphy, E. K., Mahara, A., & Halter, R. J. (2017). Absolute Reconstructions Using Rotational Electrical Impedance Tomography for Breast Cancer Imaging. *IEEE Transactions on Medical Imaging*, 36(4), 892–903. <https://doi.org/10.1109/TMI.2016.2640944>
- Murphy, E. K., Mahara, A., Wu, X., & Halter, R. J. (2017). Phantom experiments using soft-prior regularization EIT for breast cancer imaging. *Physiological Measurement*, 38(6), 1262–1277. <https://doi.org/10.1088/1361-6579/aa691b>
- Murphy, E. K., Skinner, J., Martucci, M., Rutkove, S. B., & Halter, R. J. (2019). Toward Electrical Impedance Tomography Coupled Ultrasound Imaging for Assessing Muscle Health. *IEEE Transactions on Medical Imaging*, 38(6), 1409–1419. <https://doi.org/10.1109/TMI.2018.2886152>
- Murphy, E. K., Wu, X., & Halter, R. J. (2018). Fused-data transrectal EIT for prostate cancer imaging. *Physiological Measurement*, 39(5). <https://doi.org/10.1088/1361-6579/aabf22>
- Murphy, S. C., & York, T. A. (2006). Electrical impedance tomography with non-stationary electrodes. *Measurement Science and Technology*, 17(11), 3042–3052. <https://doi.org/10.1088/0957-0233/17/11/025>
- Nam, S. Y., Ricles, L. M., Suggs, L. J., & Emelianov, S. Y. (2015). Imaging strategies for tissue engineering applications. *Tissue Engineering - Part B: Reviews*, 21(1), 88–102. <https://doi.org/10.1089/ten.teb.2014.0180>
- Natterer, F. (2001). *The mathematics of computerized tomography*. Society for Industrial and Applied Mathematics.
- Nissinen, A., Heikkinen, L. M., & Kaipio, J. P. (2008). The Bayesian approximation error approach for electrical impedance tomography—Experimental results. *Measurement Science and Technology*, 19(1). <https://doi.org/10.1088/0957-0233/19/1/015501>
- Nissinen, A., Heikkinen, L. M., Kolehmainen, V., & Kaipio, J. P. (2009). Compensation of errors due to discretization, domain truncation and unknown contact impedances in electrical impedance tomography. *Measurement Science and Technology*, 20(10). <https://doi.org/10.1088/0957-0233/20/10/105504>
- Nissinen, A., Kolehmainen, V. P., & Kaipio, J. P. (2011). Compensation of modelling errors due to unknown domain boundary in electrical impedance tomography. *IEEE Transactions on Medical Imaging*, 30(2), 231–242. <https://doi.org/10.1109/TMI.2010.2073716>
- Ntziachristos, V. (2010). Going deeper than microscopy: The optical imaging frontier in biology. *Nature Methods*, 7(8), 603–614. <https://doi.org/10.1038/nmeth.1483>
- Ogawa, R., Hallas-Potts, A., Wu, H., Jia, J., & Bagnaninchi, P. O. (2021). Measuring 3D Cell Culture Viability in Multiple 3D Printed Scaffolds Within a Single Miniature Electrical Impedance Tomography Sensor. *Advanced Engineering Materials*, 23, 2100338. <https://doi.org/10.1002/adem.202100338>
- Onnela, N., Savolainen, V., Juuti-Uusitalo, K., Vaajasaari, H., Skottman, H., & Hyttinen, J. (2012). Electric impedance of human embryonic stem cell-derived retinal pigment

- epithelium. *Medical & Biological Engineering & Computing*, 50, 107–116. <https://doi.org/10.1007/s11517-011-0850-z>
- Ouypornkochagorn, T., Terzija, N., Wright, P., Davidson, J. L., Polydorides, N., & McCann, H. (2022). Scalp-Mounted Electrical Impedance Tomography of Cerebral Hemodynamics. *IEEE Sensors Journal*, 22(5), 4569–4580. <https://doi.org/10.1109/JSEN.2022.3145587>
- Paldanius, A., Dekdouk, B., Toivanen, J., Kolehmainen, V., & Hyttinen, J. (2022). Sensitivity Analysis Highlights the Importance of Accurate Head Models for Electrical Impedance Tomography Monitoring of Intracerebral Hemorrhagic Stroke. *IEEE Transactions on Biomedical Engineering*, 69(4), 1491–1501. <https://doi.org/10.1109/TBME.2021.3120929>
- Pan, Y., Jiang, D., Gu, C., Qiu, Y., Wan, H., & Wang, P. (2020). 3D microgroove electrical impedance sensing to examine 3D cell cultures for antineoplastic drug assessment. *Microsystems and Nanoengineering*, 6(1). <https://doi.org/10.1038/s41378-020-0130-x>
- Pethig, R., & Kell, D. B. (1987). The passive electrical properties of biological systems: Their significance in physiology, biophysics and biotechnology. *Physics in Medicine and Biology*, 32(8), 933–970. <https://doi.org/10.1088/0031-9155/32/8/001>
- Sanchez, B., Vandersteen, G., Bragos, R., & Schoukens, J. (2012). Basics of broadband impedance spectroscopy measurements using periodic excitations. *Measurement Science and Technology*, 23(10). <https://doi.org/10.1088/0957-0233/23/10/105501>
- Savolainen, V., Juuti-Uusitalo, K., Onnela, N., Vaajasaari, H., Narkilahti, S., Suuronen, R., Skottman, H., & Hyttinen, J. (2011). Impedance spectroscopy in monitoring the maturation of stem cell-derived retinal pigment epithelium. *Annals of Biomedical Engineering*, 39(12), 3055–3069. <https://doi.org/10.1007/s10439-011-0387-1>
- Schullcke, B., Gong, B., Krueger-Ziolek, S., Soleimani, M., Mueller-Lisse, U., & Moeller, K. (2016). Structural-functional lung imaging using a combined CT-EIT and a Discrete Cosine Transformation reconstruction method. *Scientific Reports*, 6(May), 1–12. <https://doi.org/10.1038/srep25951>
- Schwan, H. P. (1994). Electrical properties of tissues and cell suspensions: Mechanisms and models. *Proceedings of 16th Annual International Conference of the IEEE Engineering in Medicine and Biology Society*, A70–A71. <https://doi.org/10.1109/IEMBS.1994.412155>
- Seppä, V. P., Viik, J., & Hyttinen, J. (2010). Assessment of pulmonary flow using impedance pneumography. *IEEE Transactions on Biomedical Engineering*, 57(9), 2277–2285. <https://doi.org/10.1109/TBME.2010.2051668>
- Seppänen, A., Heikkinen, L., Savolainen, T., Voutilainen, A., Somersalo, E., & Kaipio, J. P. (2007). An experimental evaluation of state estimation with fluid dynamical models in process tomography. *Chemical Engineering Journal*, 127(1–3), 23–30. <https://doi.org/10.1016/j.cej.2006.09.025>
- Sharpe, J., Ahlgren, U., Perry, P., Hill, B., Ross, A., Hecksher-Sørensen, J., Baldock, R., & Davidson, D. (2002). Optical projection tomography as a tool for 3D microscopy and gene expression studies. *Science (New York, N.Y.)*, 296(5567), 541–545. <https://doi.org/10.1126/science.1068206>
- Simini, F., & Bertemes-Filho, P. (Eds.). (2018). *Bioimpedance in Biomedical Applications and Research*. Springer International Publishing AG part of Springer Nature.
- Soleimani, M. (2006). Electrical impedance tomography imaging using a priori ultrasound data. *BioMedical Engineering Online*, 5, 1–8. <https://doi.org/10.1186/1475-925X-5-8>

- Somersalo, E., Cheney, M., & Isaacson, D. (1992). Existence and Uniqueness for Electrode Models for Electric Current Computed Tomography. *Society for Industrial and Applied Mathematics*, 52(4), 1023–1040.
- Sun, T., Tsuda, S., Zauner, K. P., & Morgan, H. (2010). On-chip electrical impedance tomography for imaging biological cells. *Biosensors and Bioelectronics*, 25(5), 1109–1115. <https://doi.org/10.1016/j.bios.2009.09.036>
- Takahashi, K., & Yamanaka, S. (2006). Induction of Pluripotent Stem Cells from Mouse Embryonic and Adult Fibroblast Cultures by Defined Factors. *Cell*, 126(4), 663–676. <https://doi.org/10.1016/j.cell.2006.07.024>
- Tamminen, I., Lehto, K., Hannula, M., Ojansivu, M., Johansson, L., Kellomäki, M., Miettinen, S., Aula, A., Ihalainen, T., & Hyttinen, J. (2020). A tube-source X-ray microtomography approach for quantitative 3D microscopy of optically challenging cell-cultured samples. *Communications Biology*, 3(1), 1–13. <https://doi.org/10.1038/s42003-020-01273-w>
- Tavakol, M., & Dennick, R. (2011). Making sense of Cronbach’s alpha. *International Journal of Medical Education*, 2, 53–55. <https://doi.org/10.5116/ijme.4dfb.8dfd>
- Tervonen, A., & Hyttinen, J. (2018). Sensitivity distribution of electrical impedance epithelial measurement systems. In H. Eskola, O. Väisänen, J. Viik, & J. Hyttinen (Eds.), *EMBEC & NBC 2017, IFMBE Proceedings* (Vol. 65, pp. 623–626). <https://doi.org/10.1007/978-981-10-5122-7>
- Toivanen, J., Hänninen, A., Savolainen, T., Forss, N., & Kolehmainen, V. (2021). Monitoring hemorrhagic strokes using EIT. In P. Annus & M. Min (Eds.), *Bioimpedance and Spectroscopy* (pp. 271–298). Academic Press. <https://doi.org/10.1016/B978-0-12-818614-5.00007-2>
- Tomicic, V., & Cornejo, R. (2019). Lung monitoring with electrical impedance tomography: Technical considerations and clinical applications. *Journal of Thoracic Disease*, 11(7), 3122–3135. <https://doi.org/10.21037/jtd.2019.06.27>
- Vauhkonen, M., Vadász, D., Karjalainen, P. A., Somersalo, E., & Kaipio, J. P. (1998). Tikhonov regularization and prior information in electrical impedance tomography. *IEEE Transactions on Medical Imaging*, 17(2), 285–293. <https://doi.org/10.1109/42.700740>
- Vauhkonen, P. (2004). *Image Reconstruction in Three-Dimensional Electrical Impedance Tomography*. University of Kuopio.
- Vauhkonen, P. J., Vauhkonen, M., Savolainen, T., & Kaipio, J. P. (1999). Static three-dimensional electrical impedance tomography. *Annals of the New York Academy of Science*, 873, 472–481. <https://doi.org/10.1111/j.1749-6632.1999.tb09496.x>
- Viswam, V., Bounik, R., Shadmani, A., Dragas, J., Urwyler, C., Boos, J. A., Obien, M. E. J., Müller, J., Chen, Y., & Hierlemann, A. (2018). Impedance Spectroscopy and Electrophysiological Imaging of Cells with a High-Density CMOS Microelectrode Array System. *IEEE Transactions on Biomedical Circuits and Systems*, 12(6), 1356–1368. <https://doi.org/10.1109/TBCAS.2018.2881044>
- Wan, Y., Halter, R., Borsic, A., Manwaring, P., Hartov, A., & Paulsen, K. (2010). Sensitivity study of an ultrasound coupled transrectal electrical impedance tomography system for prostate imaging. *Physiological Measurement*, 31(8). <https://doi.org/10.1088/0967-3334/31/8/S02>
- Weiz, S. M., Medina-Sanchez, M., Lee, K., & Schmidt, O. G. (2017). Electrical impedance tomography in on-chip integrated microtubular fluidic channels. In A. Boyle, R. Halter, E. Murphy, & A. Adler (Eds.), *Proceedings of the 18th International Conference on*

- Biomedical Applications of Electrical Impedance Tomography* (p. 23). <https://doi.org/10.5281/zenodo.892679>
- Wi, H., Sohal, H., McEwan, A. L., Woo, E. J., & Oh, T. I. (2014). Multi-frequency electrical impedance tomography system with automatic self-calibration for long-term monitoring. *IEEE Transactions on Biomedical Circuits and Systems*, *8*(1), 119–128. <https://doi.org/10.1109/TBCAS.2013.2256785>
- Winkler, S., Lehti-Polojärvi, M., & Hyttinen, J. (2021). Hyperparameter Algorithms in Electrical Impedance Tomography for Rotational Data. *IFMBE Proceedings*, *80*, 631–643. [https://doi.org/10.1007/978-3-030-64610-3\\_71](https://doi.org/10.1007/978-3-030-64610-3_71)
- Wu, H. (2020). *Electrical impedance tomography for real-time 3D tissue culture monitoring*. The University of Edinburgh. <https://hdl.handle.net/1842/36813>
- Wu, H., Yang, Y., Bagnaninchi, P. O., & Jia, J. (2018). Electrical impedance tomography for real-time and label-free cellular viability assays of 3D tumour spheroids. *Analyst*, *143*(17), 4189–4198. <https://doi.org/10.1039/c8an00729b>
- Wu, H., Zhou, W., Yang, Y., Jia, J., & Bagnaninchi, P. (2018). Exploring the potential of electrical impedance tomography for tissue engineering applications. *Materials*, *11*(6), 930. <https://doi.org/10.3390/ma11060930>
- Xu, C., Dai, M., You, F., Shi, X., Fu, F., Liu, R., & Dong, X. (2011). An optimized strategy for real-time hemorrhage monitoring with electrical impedance tomography. *Physiological Measurement*, *32*(5), 585–598. <https://doi.org/10.1088/0967-3334/32/5/007>
- Yamanaka, S. (2009). A Fresh Look at iPS Cells. *Cell*, *137*(1), 13–17. <https://doi.org/10.1016/j.cell.2009.03.034>
- Yang, Y., & Jia, J. (2017). A multi-frequency electrical impedance tomography system for real-time 2D and 3D imaging. *Review of Scientific Instruments*, *88*(8), 085110. <https://doi.org/10.1063/1.4999359>
- Yang, Y., Jia, J., Smith, S., Jamil, N., Gamal, W., & Bagnaninchi, P. O. (2017). A miniature electrical impedance tomography sensor and 3-D Image Reconstruction for Cell Imaging. *IEEE Sensors Journal*, *17*(2), 514–523. <https://doi.org/10.1109/JSEN.2016.2631263>
- Yang, Y., Wu, H., Jia, J., & Bagnaninchi, P. O. (2019). Scaffold-Based 3-D Cell Culture Imaging Using a Miniature Electrical Impedance Tomography Sensor. *IEEE Sensors Journal*, *19*(20), 9071–9080. <https://doi.org/10.1109/JSEN.2019.2924154>
- Yin, X., Wu, H., Jia, J., & Yang, Y. (2018). A micro EIT sensor for real-time and non-destructive 3-d cultivated cell imaging. *IEEE Sensors Journal*, *18*(13), 5402–5412. <https://doi.org/10.1109/JSEN.2018.2834509>
- Yuan, Q. (2020). *A Modular LabVIEW Program for Controlling Multimodal Micro- scope Imaging Platform* [Tampere University, Finland]. <https://trepo.tuni.fi/handle/10024/121143>
- Zhang, H., & Wang, L. V. (2004). Acousto-electric tomography. *Proc. SPIE 5320, Photons Plus Ultrasound: Imaging and Sensing*. <https://doi.org/10.1117/12.532610>
- Zhang, X., Chatwin, C., & Barber, D. C. (2015). A feasibility study of a rotary planar electrode array for electrical impedance mammography using a digital breast phantom. *Physiological Measurement*, *36*(6), 1311–1335. <https://doi.org/10.1088/0967-3334/36/6/1311>
- Zhang, Y. S., & Yao, J. (2018). Imaging Biomaterial–Tissue Interactions. *Trends in Biotechnology*, *36*(4), 403–414. <https://doi.org/10.1016/j.tibtech.2017.09.004>





# ORIGINAL PUBLICATIONS



# PUBLICATION

I

## **Rotational electrical impedance tomography using electrodes with limited surface coverage provides window for multimodal sensing**

Mari Lehti-Polojärvi, Olli Koskela, Aku Seppänen, Edite Figueiras, Jari Hyttinen

Measurement Science and Technology 29 (2018) 025401

<https://doi.org/10.1088/1361-6501/aa97f1>

**Publication is licensed under a Creative Commons Attribution 3.0 Unported (CC BY 3.0)**



# Rotational electrical impedance tomography using electrodes with limited surface coverage provides window for multimodal sensing

Mari Lehti-Polojärvi<sup>1,4</sup>, Olli Koskela<sup>1,4</sup>, Aku Seppänen<sup>2</sup>,  
Edite Figueiras<sup>3</sup> and Jari Hyttinen<sup>1</sup>

<sup>1</sup> BioMediTech Institute and Faculty of Biomedical Sciences and Engineering, Tampere University of Technology, Tampere, Finland

<sup>2</sup> Department of Applied Physics, University of Eastern Finland, Kuopio, Finland

<sup>3</sup> International Iberian Nanotechnology Laboratory, Braga, Portugal

E-mail: [mari.lehti@tut.fi](mailto:mari.lehti@tut.fi) and [olli.koskela@tut.fi](mailto:olli.koskela@tut.fi)

Received 11 October 2017

Accepted for publication 3 November 2017

Published 17 January 2018




CrossMark

## Abstract

Electrical impedance tomography (EIT) is an imaging method that could become a valuable tool in multimodal applications. One challenge in simultaneous multimodal imaging is that typically the EIT electrodes cover a large portion of the object surface. This paper investigates the feasibility of rotational EIT (rEIT) in applications where electrodes cover only a limited angle of the surface of the object. In the studied rEIT, the object is rotated a full 360° during a set of measurements to increase the information content of the data. We call this approach limited angle full revolution rEIT (LAFR-rEIT). We test LAFR-rEIT setups in two-dimensional geometries with computational and experimental data. We use up to 256 rotational measurement positions, which requires a new way to solve the forward and inverse problem of rEIT. For this, we provide a modification, available for EIDORS, in the supplementary material. The computational results demonstrate that LAFR-rEIT with eight electrodes produce the same image quality as conventional 16-electrode rEIT, when data from an adequate number of rotational measurement positions are used. Both computational and experimental results indicate that the novel LAFR-rEIT provides good EIT with setups with limited surface coverage and a small number of electrodes.

Keywords: electrical impedance tomography, limited angle surface detection, rotational finite element method, multimodal imaging

 Supplementary material for this article is available online

(Some figures may appear in colour only in the online journal)



Original content from this work may be used under the terms of the Creative Commons Attribution 3.0 licence. Any further distribution of this work must maintain attribution to the author(s) and the title of the work, journal citation and DOI.

<sup>4</sup> Authors contributed equally to this work.

## 1. Introduction

Electrical impedance tomography (EIT) is a high-speed, non-destructive and non-invasive imaging technique that has applications in several fields that include medical imaging, industrial process tomography and geophysical surveying. Traditionally in EIT, current stimulations and voltage measurements are carried out using equally spaced electrodes on the surface of the object (i.e. sample with inclusions of interest) [1, 2]. Based on these measurements, an image is reconstructed that represents the conductivity distribution of the object. The major advantages of EIT are high temporal resolution and that no ionizing radiation is applied as, for example, in x-ray computed tomography. The main drawback of EIT is its relatively poor spatial resolution. One approach to enhance spatial resolution is to use rotational EIT (rEIT), a method that increases the number of independent measurements [3–7].

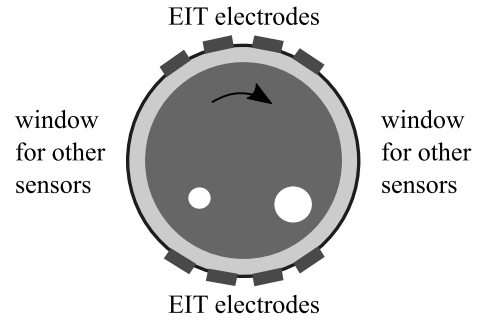
EIT is a functional imaging method that could become a valuable tool in multimodal applications [8–11]. The combination of EIT and a structural imaging method, such as ultrasonic imaging, could provide robust diagnostic or research tools. One challenge in simultaneous multimodal imaging is that in typical settings the EIT electrodes cover a large portion of the object surface, and therefore the area left for other sensors is very limited.

To attain new applications for multimodal EIT with good spatial resolution, we propose a rEIT setup where stationary electrodes span a limited angle near to the object surface and measurements are acquired along  $360^\circ$  (asymmetric electrode configurations) or  $180^\circ$  (symmetric electrode configurations) rotation of the object. We call this approach limited angle full revolution rotational EIT (LAFR-rEIT).

Figure 1 illustrates one scheme of a LAFR-rEIT setup, where electrodes cover less than half of the object surface and additional measurements are possible at the sides that are free from EIT electrodes. This particular configuration will allow multimodal measurements as, for example, the combination of other tomographic methods with rEIT.

Previously presented rEIT setups have applied electrode arrays that are evenly distributed around the circumference of the object. Rotating this kind of electrode array only increases the acquired independent data within rotation angles smaller than the distance between the centres of the neighbouring electrodes. For example, in a conventional 16-electrode setup, rEIT measurements are obtained within  $22.5^\circ$  rotation. LAFR-rEIT, on the other hand, is expected to benefit from measurements within full  $360^\circ$  or  $180^\circ$  rotation. In addition, LAFR-rEIT enables relatively simple instrumentation due to the small number of electrodes.

LAFR-rEIT could be used to image objects that can be rotated while the electrodes remain at rest, or vice versa. We present a case where the object is rotated in conductive aqueous solution, as is shown in figure 1. Such setups are relevant in applications where EIT is used for imaging specimens of materials and/or structures, e.g. for non-destructive testing of concrete [12] and biological samples [13].



**Figure 1.** Schematic of the rotational measurement setup comprising a rotating object (dark grey) with inclusions (white circles), aqueous solution (light grey) and electrodes used for EIT. Additional modality can be measuring either backscattering or transmission and has possible contact sites on the left and right sides of the object.

The purpose of this paper is to introduce LAFR-rEIT approach and to study whether it could provide image quality comparable with 16-electrode rEIT. The efficacy of LAFR-rEIT is evaluated in both computational models (sections 2.3 and 3) and experimental measurements on two-dimensional (2D) phantoms (sections 2.4 and 4). We anticipate this work will open new possibilities for high-quality multimodal imaging of material specimens.

## 2. Methods

### 2.1. Image reconstruction

This section presents the mathematical model for a rEIT setup. Using the model, the number and placement of the electrodes and the number of rotational measurement positions can be chosen arbitrarily.

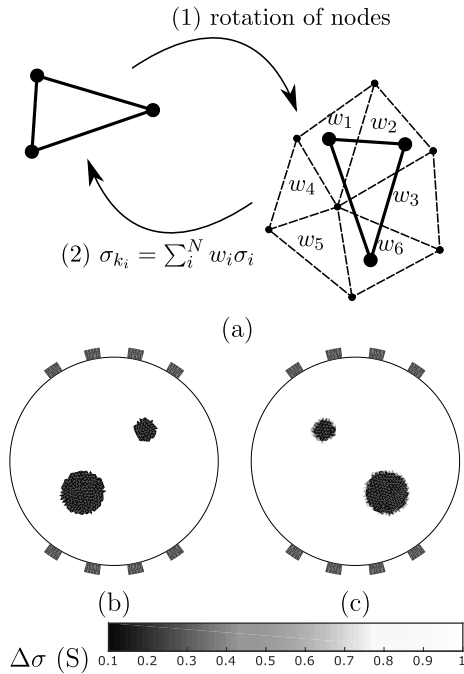
Let  $\sigma \in \Omega$  mark the conductivity distribution inside a given object  $\Omega$ . For each measurement position  $k$  and rotated object  $\Omega_k$ , we have a conductivity distribution  $\sigma_k \in \Omega_k$  in the rotated coordinates. The model used for measurement  $V_k$  using the complete electrode model is given in [14] and is of the form:

$$V_k = U(\sigma_k) + n_k, \quad (1)$$

where  $U$  is the forward model and  $n_k$  is a noise term.

We modelled the rotation of the coordinates in  $k$ th position using a linear mapping  $M_k$  so that for conductivity distribution  $\sigma \in \Omega$  in initial position, the rotated coordinates are given by  $\Omega_k = M_k \Omega$  and  $\sigma_k = M_k \sigma$ . We assume that  $\sigma$  does not change during the rotation. For a finite element approximation  $\Omega = (e_i)$ , mapping  $M_k = (w_{i,j})_k$  is a weight matrix. Each weight  $w_{i,j}$  is the area of intersection of  $e_j$  and  $e_i$ , where  $e_i$  is rotated for the measurement angle  $\alpha_k$ . Rotation is illustrated in figure 2.

For a set of  $m$  measurements  $V_k (k \in [1, m] \subset \mathbf{N})$  with rotational measurement positions within  $\alpha_k \in [0, 2\pi]$ , the forward EIT model was written in stacked form as follows:



**Figure 2.** (a) For each element and each rotational position, weights of the mapping  $M$  are computed by (1) first rotating element coordinates around the centre of the mesh in the opposite direction and then calculating the areas of intersection  $w_i$  with underlying elements. (2) The element data value  $\sigma_k$  of the rotational position is assigned using these weights. (b) Phantom and (c) its rotation for 90 degrees.

$$\begin{bmatrix} V_1 \\ V_2 \\ \vdots \\ V_m \end{bmatrix} = \begin{bmatrix} U(M_1\sigma) \\ U(M_2\sigma) \\ \vdots \\ U(M_m\sigma) \end{bmatrix} + \begin{bmatrix} n_1 \\ n_2 \\ \vdots \\ n_m \end{bmatrix} \quad (2)$$

or

$$V_r = U_r(\sigma) + n_r. \quad (3)$$

We adapted the rEIT to the framework of linearised difference imaging. In difference imaging, EIT measurements (here, corresponding to  $m$  rotational measurement positions) of a temporally varying object are performed before and after the change in two stages. It should be noted that here this change is expected to be slow. Therefore the above assumption/approximation of the conductivity being non-varying during each set of rEIT measurements is valid. The conductivity distribution of the object is denoted before and after the change by  $\sigma^{(1)}$  and  $\sigma^{(2)}$ , respectively, and the corresponding EIT measurements by  $V_r^{(1)}$  and  $V_r^{(2)}$ .

To reconstruct the change of the conductivity  $\Delta\sigma = \sigma^{(2)} - \sigma^{(1)}$  on the basis of difference data  $\Delta V_r = V_r^{(2)} - V_r^{(1)}$ , the mapping  $U_r(\sigma)$  was linearized by writing the first order Taylor approximation:

$$U_r(\sigma) \approx U_r(\sigma_0) + J_r(\sigma - \sigma_0). \quad (4)$$

Here,  $\sigma_0$  is a linearization point and  $J_r$  denotes the Jacobian matrix of  $U_r(\sigma)$  at  $\sigma_0$ .

$$J_r = \begin{bmatrix} JM_1 \\ \vdots \\ JM_m \end{bmatrix}, \quad (5)$$

where  $J_r$  and  $J$ , respectively, denote the Jacobian matrices of  $U_r(\sigma)$  and  $U(\sigma)$  at  $\sigma_0$ .

Using the approximation (4) for both measurement sets  $V_r^{(1)}$  and  $V_r^{(2)}$ , the observation model (3) can be expressed in terms of differences as in the following:

$$\Delta V_r = J_r \Delta\sigma + \Delta n_r, \quad (6)$$

where  $\Delta n_r = n_r^{(2)} - n_r^{(1)}$  is the difference between the noise realisations  $n_r^{(1)}$  and  $n_r^{(2)}$ .

Due to the ill-posedness of the EIT inverse problem, the reconstruction of  $\Delta\sigma$  requires regularisation. Here, we used the Tikhonov regularised solution:

$$\widehat{\Delta\sigma} = \arg \min_{\Delta\sigma} \{ \|\Delta V_r - J_r \Delta\sigma\|^2 + \alpha \|L \Delta\sigma\|^2 \} \quad (7)$$

$$= (J_r^T J_r + \alpha L^T L)^{-1} J_r^T \Delta V_r, \quad (8)$$

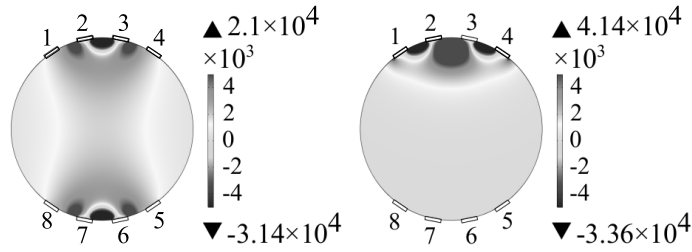
where  $L$  is a smoothness promoting regularisation matrix defined as a discrete second order differential operator, and  $\alpha$  is a regularisation parameter [15].

## 2.2. Stimulation and measurement patterns

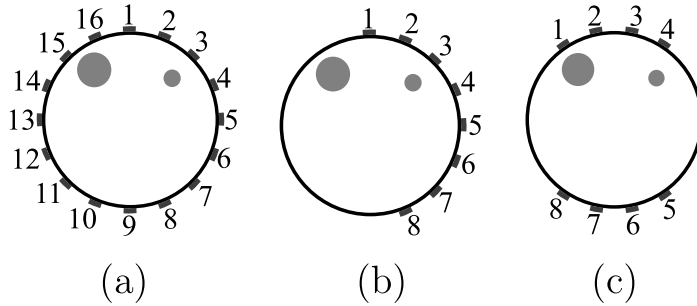
In EIT, it is preferable to have measurements both through the object (opposite electrodes) and near the surface of the object (adjacent electrodes). Based on the lead field theory [16], the sensitivity of a tetrapolar measurement can be calculated as a dot product of two current density vector fields. These fields are formed by feeding current to the current feeding electrodes, and reciprocally to the voltage measurement electrodes. This theory has been applied to design novel impedance measurement patterns for whole body EIT, tissue engineered systems and single cell measurements [17–20].

Figure 3 illustrates the sensitivity fields calculated for two different tetrapolar measurements in a LAFR-rEIT setup. These finite element simulations were carried out in Comsol Multiphysics v5.2a. The object was assumed to be homogeneous with conductivity of  $0.22 \text{ S m}^{-1}$  and relative permittivity of 80. A current of 3 mA was consecutively applied between electrode pairs. The pattern using opposing electrodes had high sensitivity close to the electrodes and in the centre of the object. The pattern using four adjacent electrodes had high sensitivity close to the electrodes, but low sensitivity elsewhere.

To maximise the information obtained by the limited number of electrodes in LAFR-rEIT, we chose to use all the available tetrapolar combinations for each electrode configuration. In this way, we were able to obtain patterns that were



**Figure 3.** Sensitivity field distributions ( $1/m^{-4}$ ) of two different measurement patterns. Current is injected between electrodes 2 and 7 (left) or 1 and 4 (right). Voltage is measured with electrodes 3 and 6 (left) or 2 and 3 (right).



**Figure 4.** (a) The standard 16-electrode configuration and (b), (c) two possible LAFR-rEIT configurations along with the phantom used in the numerical analysis. (b) Configuration HALF8 includes electrodes 1 to 8 and (c) OPP4 electrodes 1–4 and 9–12. Low conductivity inclusions are shown in grey.

both sensitive in the centre of the object and also sensitive at the edges. The rotation of the object allowed it to be measured from different angles, and thus the whole object was covered.

2.3. Numerical analysis

A numerical comparison of LAFR-rEIT using electrodes with limited angular coverage but full rotation, and a rotational 16-electrode model with full angular coverage electrodes but limited rotation was carried out. Full rotation is considered here to be  $180^\circ$  for LAFR-rEIT electrode configurations that are symmetrical to rotation after  $180^\circ$  and  $360^\circ$  for non-symmetrical electrode configurations. The 16-electrode model followed previous publications, for example [4], and shown in figure 4(a).

LAFR-rEIT electrode configurations followed two different approaches: the electrodes were placed either in two sets on opposite halves of the object, or in one set covering about half of the object surface. Both approaches allow measurements that are sensitive close to surface and through the object. Figures 4(b) and (c) shows the configurations with eight electrodes called HALF8 and OPP4, respectively. The angular difference between the centres of the stationary electrodes was  $22.5^\circ$  in all cases, and hence eight electrodes were distributed in the range of  $[0^\circ, 157.5^\circ]$  (HALF8), or  $[-33.75^\circ, 33.75^\circ] \cup [146.25^\circ, 213.85^\circ]$  (OPP4).

LAFR-rEIT was additionally tested with four and six electrode configurations called OPP2, OPP3, OPP4 + 2, HALF4 and HALF6, shown in figure 8. In HALF4, four electrodes

were positioned in an angular span of  $[0^\circ, 135^\circ]$  and in HALF6 six electrodes were positioned in a span of  $[0^\circ, 150^\circ]$

The phantom used in the simulations was circular with radius of 1 units and had 0.14 units size electrodes in all configurations. The electrode size equalled 18% object surface coverage with 16 electrodes. All inclusions in the phantoms had conductivity of 0.1 S while the background and aqueous solution had conductivity of 1 S. The inclusion diameters were 0.4 units and 0.2 units. The phantom is shown in figure 4. Input current in simulations is 1 ‘Amps’ (EIDORS unit in 2D).

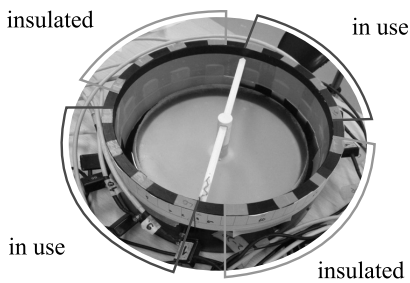
For the 16-electrode model, data were simulated by rotating the object in an angular range of  $[0^\circ, 22.5^\circ - \frac{22.5^\circ}{N+1}]$ , where  $N$  is the number of rotational measurement positions. Outside this range the measurements become repeated due to symmetry. We studied the conventional single measurement position without rotation, and then rotational cases with 2, 3 and 6 measurement positions equally distributed within the mentioned range.

With the electrode configuration OPP4, data was simulated up to 256 measurement positions within  $180^\circ$  rotation. The other symmetric configurations, OPP2 and OPP3, were simulated with 32 rotational measurement positions in the same range. For asymmetric electrode configurations HALF4, HALF6, HALF8 and OPP4 + 2, data was simulated with 64 measurement positions in  $360^\circ$  rotation.

In all of the simulated data points  $V \in \mathbf{R}^n$ , the additive noise of two components was included yielding noisy data  $V_{\text{noisy}} \in \mathbf{R}^n$ :

$$V_{\text{noisy}} = V + p_1 \max(|V|) \cdot 10^{-4} + |V| p_2^T \cdot 10^{-3}.$$





**Figure 5.** Measurement tank where eight of the 16 electrodes were insulated and eight electrodes were in use. A transparent cylindrical shaped gelatine phantom was placed on top of a rotation platform (white). A thin aqueous layer was between the object and the electrodes.

The first component is proportional to the maximum measured amplitude and the second component is proportional to each measurement. The vectors  $p_1, p_2 \in [-1, 1]^n$  were random numbers with uniform distribution.

#### 2.4. Experimental analysis

An experimental setup was used to test the feasibility of the LAFR-rEIT approach. The setup included a rotated object and OPP4 electrode configuration that was also numerically simulated as described above. An overview of the experimental setup is shown in figure 5. We used cylindrical shaped phantoms made of gelatine as a scaffold into which resistive inclusions were inserted. The phantoms were placed on a 3D printed platform (Polylactic acid) that was manually rotated. The phantoms and the platform were surrounded by an aqueous solution to preserve the structure of the object during its rotation and to ensure good electrical contact.

The gelatine scaffold for the phantoms was prepared from uncoloured 9.1% w/w Gelatine Powder (Dr.Oetker), 90.8% w/w tap water and 0.1% w/w sodium chloride (Maldon Sea Salt Flakes, Maldon Crystal Salt Co.). First, the gelatine powder was hydrated in cold tap water for 10 min. The mixture was then heated up to 74 °C and sodium chloride was added. The solution was then poured into a silicon mould (25 cm in diameter) and cooled in a refrigerator for 7 h for gelation. Prior to the measurements, the gelatine was stabilised at room temperature for about 9 h.

The tank was first filled with an aqueous solution (0.1% w/w sodium chloride and tap water) with a conductivity of 2.2 mS cm<sup>-1</sup>. The gelatine, with a conductivity of 2.4 mS cm<sup>-1</sup>, was placed on the rotation platform. The gelatine and platform were positioned in the middle of the tank (28 cm in diameter) and the height of the aqueous solution was adjusted to a height of 1 mm above the electrodes. After 30 min of stabilising the gelatine in the aqueous solution, the measurements were started.

Eight thin rectangular electrodes (25 mm × 45 mm) were attached to the inner surface of the tank. The measurements were conducted with the well-established KIT4 device presented in [21]. A sinusoidal 10 kHz 3.2 mA electrical current was used.

Three experimental phantoms were studied. In the first experimental case, we inserted a 50 mm diameter plastic tube into the gelatine. In the second case, we added a 29 mm diameter tube next to the tube in the case (1). In the third case, we replaced gelatine with one of the same composition and inserted two inclusions (50 mm and 29 mm in diameter) into opposite sides of it. The three cases are shown in photographs in figure 10. Prior to adding any tubes, both gelatine scaffolds (as in figure 5) were measured to obtain reference data for difference reconstruction.

The outer part of the measurement tank was marked with 32 equal length sectors over 180°. The sectors were used in combination with the stick in the rotation platform to allow correct rotation angles during the measurements. The data for all cases were acquired every 5.625° throughout the 180° rotation, leading to a total of 32 rotational measurement positions. The data were used to reconstruct the images with 1, 4, 16 and 32 positions by choosing only the first, every eighth, every second or all rotational measurement positions, respectively. In the reconstructions, we assumed the electrodes to be so thin that they can be modelled to be on the circumference of the region.

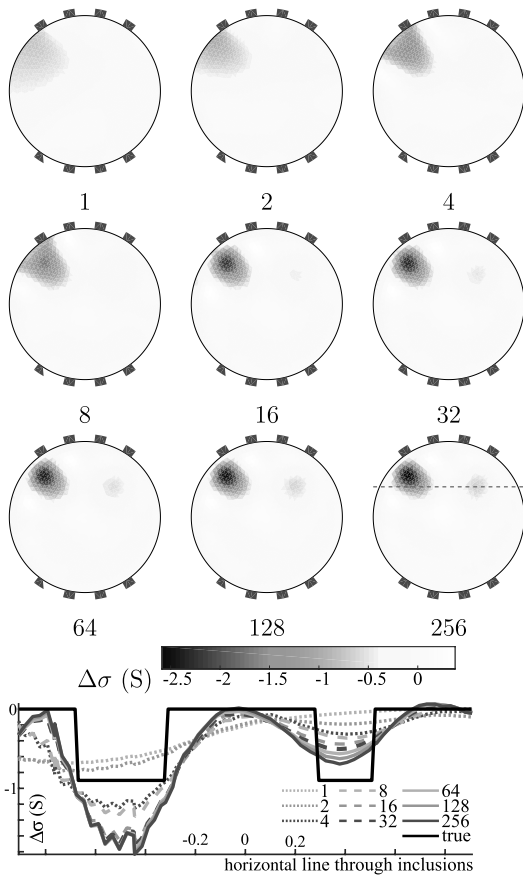
#### 2.5. EIDORS implementation of forward and inverse solver

We implemented the required modifications into EIDORS [22] functions to solve the forward and inverse problem of the rotational setting. These functions are provided in the supplementary material ([stacks.iop.org/MST/29/025401/mmedia](https://stacks.iop.org/MST/29/025401/mmedia)). All computations were performed using MATLAB R2014a or newer (The MathWorks, Inc.).

A Laplacian prior was used in the regularisation with a hyperparameter value of 0.08. The hyperparameter was empirically chosen. In the simulation studies, the reconstructions were computed using meshes that were coarser than those used for simulating the data to avoid inverse crime. In all simulations and experimental reconstructions, we used the EIDORS complete electrode model with an electrode impedance of  $z = 0.01$ .

### 3. Results of the numerical analysis

The LAFR-rEIT electrode configurations (presented in section 2.3) were numerically analysed with the phantom with two inclusions. To show the performance of LAFR-rEIT as a function of number of rotational measurement positions, we present reconstructions using OPP4 configuration from single (no rotation) up to 256 rotational measurement positions in 180° rotation, presented in figure 6. As was expected, when the object was not rotated, the quality of the reconstruction was very poor: only the larger inclusion was seen and the reconstruction resolution was inadequate. However, when the number of rotational measurement positions was increased, the shape and location of the larger inclusion was improved. Moreover, when the number of measurement positions was increased to 32, the smaller inclusion was also detected by LAFR-rEIT. Increasing the number of positions from 32

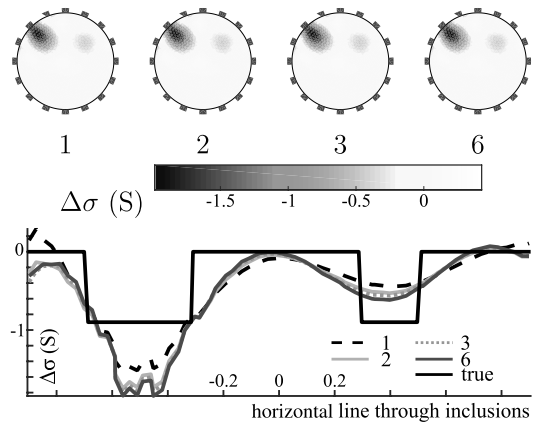


**Figure 6.** Development of reconstructions with respect to number of measurement positions 1–256 with electrode configuration OPP4. Conductivity profiles along a horizontal line through both inclusions are shown in the lower graph. The location of the horizontal lines is shown on top of the reconstruction with 256 measurement positions.

further improved the reconstruction. Although, this improvement was rather small after 64 positions, as seen in the reconstruction conductivity profiles along the inclusions in figure 6.

A 16-electrode configuration was analysed from 1 to 6 rotational measurement positions, as is shown in figure 7, for comparison to previous rEIT approaches. Small improvements in accuracy were also achieved in the 16-electrode model by increasing the amount of data through rotation.

The feasibility of additional LAFR-rEIT electrode configurations OPP2, OPP3, OPP4 + 2, HALF4, HALF6 and HALF8 are shown in figure 8. Symmetrical configurations OPP2 and OPP3 were reconstructed from simulated data with 32 rotational measurement positions in 180° rotation and asymmetrical OPP4 + 2, HALF4, HALF6 and HALF8 from data with 64 rotational measurement positions in 360° rotation. Thus, angular difference between rotational measurement positions



**Figure 7.** Reconstructions of the phantom using FULL16 electrode stepping model with 1, 2, 3, and 6 rotational measurement positions and respective conductivity profiles along a horizontal line passing through the centres of the inclusions, as shown in figure 6.

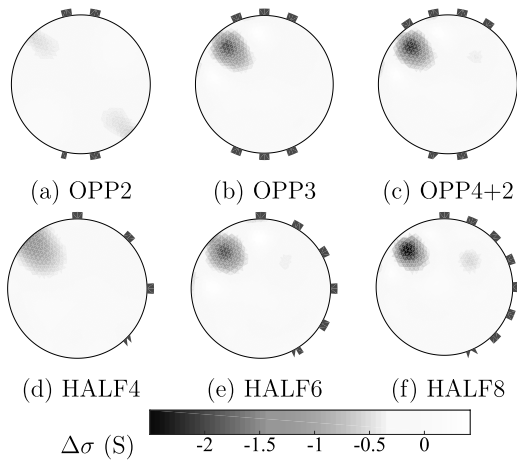
was the same in all cases. It is obvious from the reconstructions that accuracy was increased as the number of electrodes was increased. Configurations OPP4 + 2 and HALF8 found both inclusions, whereas in others the smaller is totally or almost invisible.

Visually, reconstructions with the 16-electrode model in figure 7 compared with the eight electrode LAFR-rEIT setups OPP4 (figure 6) and HALF8 (figure 8(f)) are very close to each other, when at least 32 (OPP4) or 64 (HALF8) rotational measurement positions were used. The plotted conductivity profiles through both inclusions in figure 9 support this observation, as the profiles differed only slightly in the conductivity of the larger inclusion and followed each other closely elsewhere.

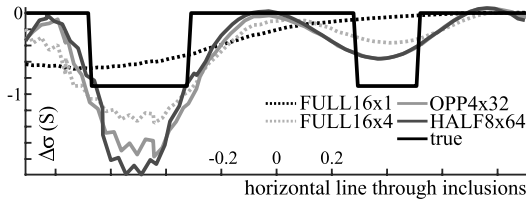
#### 4. Results of the experimental analysis

We studied LAFR-rEIT experimentally using the OPP4 electrode configuration and three phantoms. The reconstructions were obtained using data from 1, 4, 16 and 32 rotational measurement positions in 180° rotation. The pictures and corresponding reconstructions in difference mode are shown in figure 10. In addition, the conductivity profiles along a line through the centres of the inclusions are shown for each case.

As was expected, and already seen in the simulated studies, a single measurement (without rotation) with OPP4 configuration did not provide enough information for good quality reconstruction. Then inclusions were only visible if they were close to the electrodes, as in case (3). By increasing the amount of data through rotation, most of the inclusions were detected by LAFR-rEIT already with 4 rotational measurement positions. Image accuracy and contrast were further improved as rotational measurement positions were increased, as can be seen visually and in the conductivity profiles.



**Figure 8.** Reconstructions of additional LAFR-rEIT electrode configurations using (a), (b) 32 rotational measurement positions in 180° rotation and (c)–(f) 64 rotational measurement positions in 360° rotation.



**Figure 9.** Comparison between 16- and 8-electrode models, the former with 1 and 6 rotational measurement positions (denoted FULL16 × 1 and FULL16 × 6) and the latter with the models OPP4 and HALF8 with 32 or 64 rotational measurement positions, respectively (denoted OPP4 × 32 and HALF8 × 64). The location of the horizontal lines is represented in figure 6.

## 5. Discussion

In this work, we have presented a new approach to rEIT where the angular span of the electrodes over the surface of the object is limited. The main motivation for the development of limited angle full revolution rotational EIT (LAFR-rEIT) was to enable multimodal imaging. Traditionally electrodes span over the object surface completely, and therefore the attachment of other measurement devices simultaneously is difficult. The simulated and experimental analysis results prove the potential of the approach in solving this problem.

In addition to demonstrating the LAFR-rEIT, we have developed functionality for the open source EIDORS package that solves the forward and inverse problems of EIT in the presented rotational setting. The developed functions are applicable to any feasible electrode configuration. In previous approaches on rEIT [4], additional electrodes have been added to model the rotation of the object. Another option is to rotate the nodes of the finite element mesh and change the nodes of the electrodes to correspond with the rotation. This approach has been noted to work well [7]. However, in the worst case when using several rotational measurement positions, amount

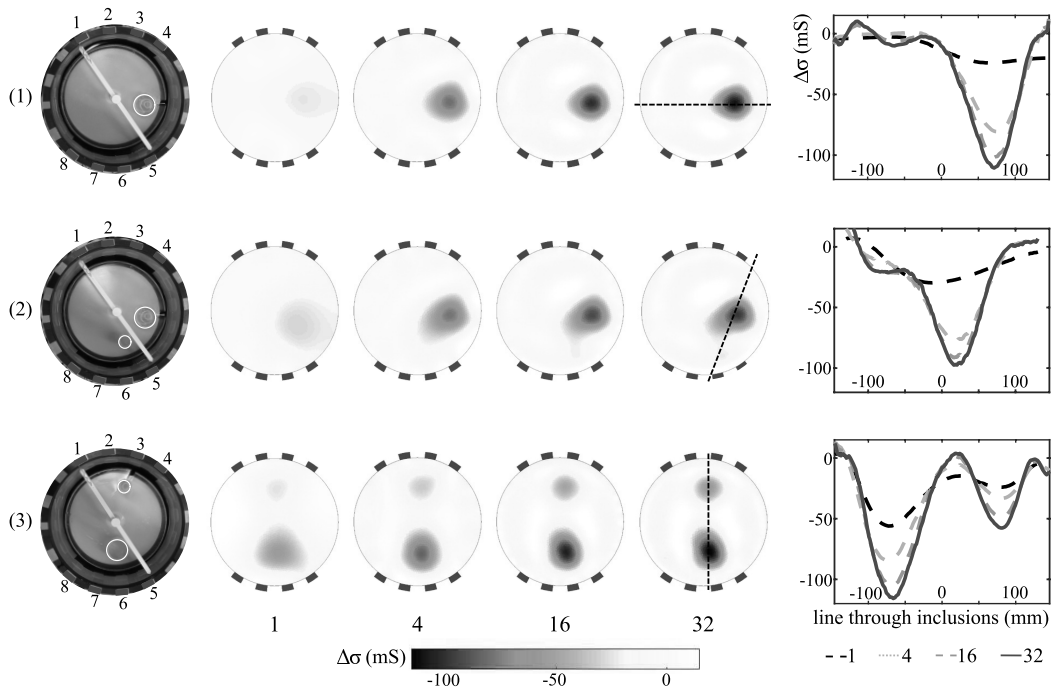
of boundary nodes explodes if each electrode requires separate nodes for each rotational coordinate. In this study, rotation was taken into account using a mapping matrix that describes rotation in a more realistic manner and models only the actual electrodes with controlled amount of boundary nodes. Also, rotation inside an already constructed finite element mesh preserves the electrode structure. Our EIDORS codes are provided in the supplementary material.

According to 2D numerical analysis, the eight electrode configurations OPP4 and HALF8 are the most promising ones in LAFR-rEIT. However, we note that the optimal setup depends on a variety of factors, including the geometry of the measured specimen. With the presented inversion model, using measurement data from 32 (OPP4) or 64 (HALF8) rotational measurement positions, reconstructions of conductivity change distributions are very similar compared to the reconstructions based on the 16-electrode rEIT with full surface coverage.

We found that rotational data from 32 to 64 measurement positions is a ‘sweet spot’ in terms of accuracy and computing time for eight electrode LAFR-rEIT using configurations OPP4 and HALF8. Reconstruction quality still benefits significantly from the additional data and computing time is in the order of minutes. LAFR-rEIT reconstruction from 128 and 256 rotational measurement positions was impossible to compute using a 8 Gb RAM computer. If memory is available, computing times are in the order of one to a few hours and the increase in accuracy achieved is relatively small. The issue with memory is due to full matrix operations in current implementation of the rotation. The eventual saturation of reconstruction quality is in accordance with previous 16-electrode rEIT studies [4, 7].

The feasibility of LAFR-rEIT was also verified with experimental measurements using OPP4 configuration. Resistive inclusions in the gelatine phantoms were detected using only 4 rotational measurement positions, but accuracy and contrast were significantly enhanced when measurement positions were increased up to 32 that was a feasible amount of rotations when done manually.

The amount of data acquired depends on the used stimulation and measurement pattern, the number of electrodes and the rotational measurement positions used. Using all tetrapolar combinations possible with eight electrodes and 64 measurement positions, results in  $64 \cdot 28 \cdot 15 = 26880$  independent measurements (28 different current injections and 15 measuring electrode pairs). Using all tetrapolar combinations possible with 16 electrodes and 6 measurement positions, results in  $6 \cdot 120 \cdot 91 = 65520$  independent measurements (120 injections and 91 measuring pairs). However, many of the tetrapolar measurements have low sensitivity. For example, in a conventional 16-electrode configuration, when current is injected between electrodes 1 and 2, most of the pairwise voltage measurements have low sensitivity. Hence, the amount of significant data is of the same order between 8-electrode LAFR-rEIT and 16-electrode rEIT, which justifies the comparable quality of the reconstructions in line with the lead field theory.



**Figure 10.** Experimental cases (1)–(3) and corresponding reconstructions using 1–32 rotational measurement positions in 180° rotation. Resistive inclusions are highlighted with white circles in the photographs. Conductivity profiles along a line passing through the centres of the inclusions are shown on the right. The locations of the lines are shown on top of the reconstructions with 32 measurement positions.

Rotational mapping  $M$  produces small local variations between neighbouring elements of the finite element mesh, as can be seen in figure 2. This is one limiting factor on the resolution of our method with a high number of rotational measurement positions. The advantage of the method is, however, the flexibility in accepting any configuration of electrodes and number of rotational measurement positions. By restricting these flexibilities, optimisation of the mapping may be possible for that specific application.

Other than numerical improvements, further interesting research includes whether other limited angle electrode configurations are feasible. This choice depends heavily on the needs of the multimodal instrumentation. Configurations can be studied in terms of the number and placement of the electrodes [23] as well as in terms of their size compared with the object size.

## 6. Conclusion

In this paper we introduced a novel approach to rEIT, where eight electrodes were distributed unevenly covering only half the surface of the object. In LAFR-rEIT, the object is rotated for 180° or 360°, depending on the electrode configuration, in aqueous solution, and several measurements are taken in different rotational positions to acquire information from all

parts the object. The conductivity change distribution is then reconstructed using novel finite element mesh modification that is available for EIDORS package.

We show here that LAFR-rEIT works using both simulated and experimental measurements and that LAFR-rEIT reconstructions are of the same quality as in previously published results of 16-electrode rEIT. The LAFR-rEIT approach offers new possibilities for multimodal imaging as it enables attaching other sensors simultaneously with EIT. The method is promising for biomedical imaging but also in other fields, such as non-destructive industrial process imaging.


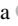


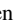
## Acknowledgments

This work is funded by Jane and Aatos Erkko Foundation, Instrumentarium Science Foundation, TEKES Human Spare Parts project and Academy of Finland (projects 270174 and 303801). The authors would like to thank Tuomo Savolainen and Panu Kuusela (University of Eastern Finland) for the help in the laboratory measurements.

## Conflicts of interest

The authors declare that they have no conflicts of interest.

## ORCID iDs

Mari Lehti-Polojärvi  <https://orcid.org/0000-0001-9826-5741>  
 Olli Koskela  <https://orcid.org/0000-0002-3424-9969>  
 Aku Seppänen  <https://orcid.org/0000-0002-4042-2254>  
 Edite Figueiras  <https://orcid.org/0000-0002-9824-3507>  
 Jari Hyttinen  <https://orcid.org/0000-0003-1850-3055>

## References

- [1] Webster J G 1990 *Electrical Impedance Tomography* (London: Taylor and Francis)
- [2] Holder D S 2004 *Electrical Impedance Tomography: Methods, History and Applications* (Boca Raton, FL: CRC Press)
- [3] Murphy S and York T 2006 Electrical impedance tomography with non-stationary electrodes *Meas. Sci. Technol.* **17** 3042
- [4] Huang C-N, Yu F-M and Chung H-Y 2007 Rotational electrical impedance tomography *Meas. Sci. Technol.* **18** 2958
- [5] Huang C-N, Yu F-M and Chung H-Y 2008 The scanning data collection strategy for enhancing the quality of electrical impedance tomography *IEEE Trans. Instrum. Meas.* **57** 1193–8
- [6] Zhang X, Chatwin C and Barber D 2015 A feasibility study of a rotary planar electrode array for electrical impedance mammography using a digital breast phantom *Physiol. Meas.* **36** 1311
- [7] Murphy E K, Mahara A and Halter R J 2017 Absolute reconstructions using rotational electrical impedance tomography for breast cancer imaging *IEEE Trans. Med. Imaging* **36** 892–903
- [8] Soleimani M 2006 Electrical impedance tomography imaging using *a priori* ultrasound data *Biomed. Eng. online* **5** 8
- [9] Grychtol B, Lionheart W, Wolf G, Bodenstern M and Adler A 2011 The importance of shape: thorax models for GREIT *Conf. EIT*
- [10] Borsic A, Syed H, Halter R and Hartov A 2011 Using ultrasound information in EIT reconstruction of the electrical properties of the prostate *Conf. EIT*
- [11] Crabb M G *et al* 2014 Mutual information as a measure of image quality for 3d dynamic lung imaging with EIT *Physiol. Meas.* **35** 863
- [12] Karhunen K, Seppänen A, Lehtikoinen A, Monteiro P J and Kaipio J P 2010 Electrical resistance tomography imaging of concrete *Cement Concr. Res.* **40** 137–45
- [13] Sun T, Tsuda S, Zauner K-P and Morgan H 2010 On-chip electrical impedance tomography for imaging biological cells *Biosens. Bioelectron.* **25** 1109–15
- [14] Somersalo E, Cheney M and Isaacson D 1992 Existence and uniqueness for electrode models for electric current computed tomography *SIAM J. Appl. Math.* **52** 1023–40
- [15] Vauhkonen M 1997 Electrical impedance tomography and prior information *PhD Thesis* University of Kuopio
- [16] Geselowitz D B 1971 An application of electrocardiographic lead theory to impedance plethysmography *IEEE Trans. Biomed. Eng.* **18** 38–41
- [17] Kauppinen P K, Hyttinen J A, Kööbi T and Malmivuo J 1999 Lead field theoretical approach in bioimpedance measurements: towards more controlled measurement sensitivity *Ann. New York Acad. Sci.* **873** 135–42
- [18] Kauppinen P, Hyttinen J and Malmivuo J 2006 Sensitivity distribution visualizations of impedance tomography measurement strategies *Int. J. Bioelectromagn.* **8** 1–9
- [19] Canali C, Mazzoni C, Larsen L B, Heiskanen A, Martinsen Ø G, Wolff A, Dufva M and Emnéus J 2015 An impedance method for spatial sensing of 3d cell constructs—towards applications in tissue engineering *Analyst* **140** 6079–88
- [20] Böttrich M, Tanskanen J M A and Hyttinen J A K 2017 Lead field theory provides a powerful tool for designing microelectrode array impedance measurements for biological cell detection and observation *Biomed. Eng. Online* **16** 85
- [21] Kourunen J 2014 Imaging of mixing in selected industrial processes using electrical resistance tomography *PhD Thesis* University of Eastern Finland ([http://epublications.uef.fi/pub/urn\\_isbn\\_978-952-61-1638-9/urn\\_isbn\\_978-952-61-1638-9.pdf](http://epublications.uef.fi/pub/urn_isbn_978-952-61-1638-9/urn_isbn_978-952-61-1638-9.pdf))
- [22] Adler A and Lionheart W R 2006 Uses and abuses of EIDORS: an extensible software base for EIT *Physiol. Meas.* **27** S25
- [23] Hyvonen N, Seppänen A and Staboulis S 2014 Optimizing electrode positions in electrical impedance tomography *SIAM J. Appl. Math.* **74** 1831–51



# PUBLICATION II

## **Bioimpedance spectro-tomography system using binary multifrequency excitation**

Mart Min, Mari Lehti-Polojärvi, Jari Hyttinen, Marek Rist, Raul Land, Paul Annus

International Journal of Bioelectromagnetism 20(1) (2018) pp.76–79  
<https://doi.org/10.18154/RWTH-CONV-224930>

**Publication reprinted with the permission of the copyright holders.**





# Bioimpedance spectro-tomography system using binary multifrequency excitation

M. Min<sup>1</sup>, M. Lehti-Polojärvi<sup>2</sup>, J. Hyttinen<sup>2</sup>, M. Rist<sup>3</sup>, R. Land<sup>1,3</sup>, P. Annus<sup>1</sup>

<sup>1</sup>Tallinn University of Technology, Ehitajate tee 5, Tallinn, Estonia  
<sup>2</sup>BioMediTech Institute and Faculty of Biomedical Sciences and Engineering, Tampere University of Technology, Arvo Ylpön katu 34, Tampere, Finland  
<sup>3</sup>Competence Center ELIKO, Mäealuse 2/1, Estonia  
 Contact: mart.min@ttu.ee

## Introduction

While both, the impedance spectroscopy and the impedance tomography, have already become well-established methods for exploring biological objects, their combination - bioimpedance spectro-tomography - offers a number of unresolved problems [1]. An important problem is ensuring the required measurement speed in the wide-band spectrometry of dynamic (time-varying) objects [2].

In this paper, we propose a way to adapt the fast impedance spectroscopy method [2, 3] (proprietary Quadra technology) for the tomography of time-varying bioimpedances. First, we present the instrumentation of the new spectro-tomography device. Then, we evaluate its function in experimental measurements with complex impedance phantom. We reconstruct spectro-tomographic images both in time-difference and frequency-difference mode. The method is also known as electrical impedance tomography.

## Materials and Methods

### Development of the Spectroscopy system

The Quadra main spectroscopy unit in fig.1 is built-up on the bases of digital signal processor (DSP) type TMS320F28069 from Texas Instruments, USA [4]. Besides the standard digital computing part, it contains a dual 16x16 bit multiply-and-accumulate (MAC) processing unit for performing the discrete Fourier transform (DFT). Especially important is the inclusion of a high-resolution (200 ps) pulse width modulator (PWM) for

generating the binary excitation voltage  $V_{EXC}$  at 80 MHz clock (fig. 2). As a result, real time spectral analysis becomes available after every 1 ms time interval at 15 frequencies: 1, 2, 3, 7, 11, 17, 23, 31, 43, 61, 89, 127, 179, 251, and 349 kHz, (fig. 3).

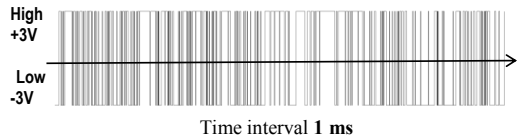


Figure 2: A full 1 ms cycle of the binary excitation

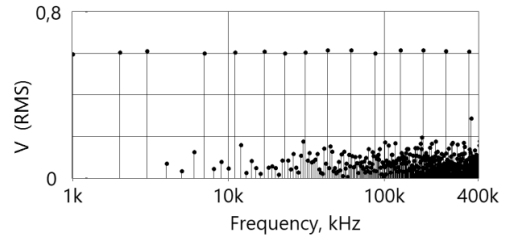


Figure 3: Spectrum of the binary excitation signal

To operate also as a tomography device, a versatile multiplexer (unit B in fig.1) was developed on the bases of a cross-point switch CD22M3494 from Intersil [4]. The cross-point switch allows switch over analog signals from any of its input pins to any of its output pins. All the 16 inputs/output pins are bi-directional for passing through both excitation and response signals. The order of

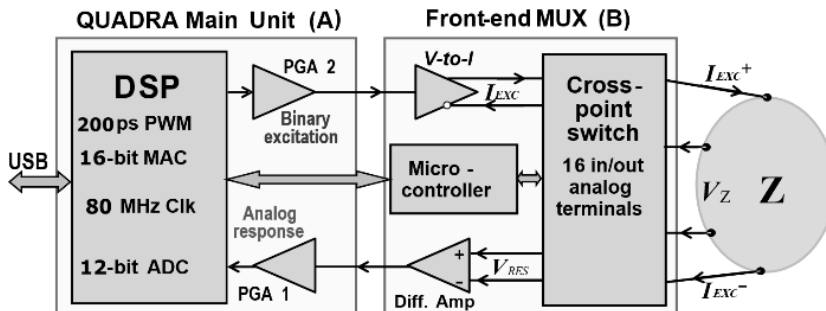
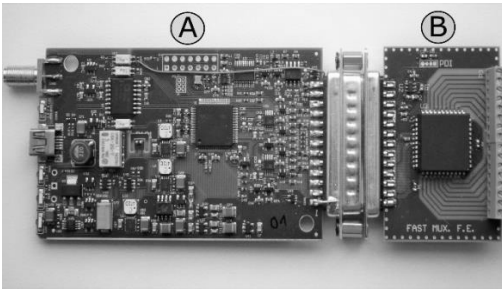


Figure 1: Structure of the spectro-tomography device – the base unit (A), and the developed multiplexing front-end (B)

switching goes on under control of the microcontroller in the front-end unit B, see fig. 1. A photo in fig. 4 shows the spectro-tomography device developed in accordance with the structure in fig.1.

### Commutation Procedure

Switching of excitation and response pick-up nodes is synchronized with applied excitation signal cycles after every 1 ms. Both, the excitation current  $I_{EXC}$  and response voltage  $V_{RES}$  are switched over hundreds of times during one tomography round, according to the used excitation and measurement pattern and the number of electrodes. See different patterns for example in [5, 6]. The total measurement time may reach several seconds or minutes. Therefore, minimizing of the switch over time is exceptionally important in the tomography of time-variant impedances.



**Figure 4:** A photo of the prototyped spectro-tomography device containing the main digital processing unit (A), and a multiplexing front-end (B)

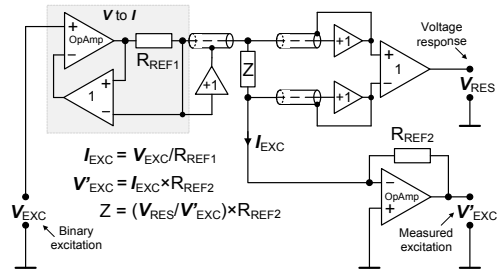
Shortening of the switching time is limited by at least two instrumentation factors: 1) ability of electronics to accomplish the switching process fast, and 2) capability to process the response signals at the highest possible speed. More important is the dependence on the inertia of bioimpedance to analyze. When switching over the excitation current, we cannot measure before the settling of voltage response. The main time constant of tissues can vary greatly. Our primary interest are cell suspensions that expresses characteristic  $\alpha$ - and  $\beta$ -dispersions. The characteristic frequency of cell suspensions in  $\alpha$ -region lies between 150 Hz to 1.5 kHz [7]. At this region, the time constant can reach 1 ms, at which the transient response takes 5 to 10 ms for the detecting of tiny changes

The electronics and signal processing algorithms of the developed spectroscopy device Quadra enables the signal processing in real time during the 1 ms excitation cycle. Because the switching moment corrupts the response during only a very short interval (takes a single or pair of microseconds), acquisition of the new response voltage takes 2 ms instead of 1 ms, ideally. Let us repeat here that the time interval, which is required for voltage acquisition after subsequent sampling of response can be short and is

not dependent on inertia of the bioimpedance. On the other hand, the time for settling of voltage after the switching of excitation current depends directly on the inertia of bioimpedance and takes significantly more time than the sampling of voltage response. By our practice, the transfer processes can take more than 1 ms and one current commutation step can last several milliseconds, for example, even 4 ms in our experiments.

### Analog Circuitry for Measurement Signals

Fig. 5 depicts the analog part of the developed device [4]. The digital signal processor DSP (fig. 1) generates the binary sequence of pulses  $V_{EXC}$  (fig. 2) with the predetermined spectrum of 15 spectral lines (fig. 3) at the required frequencies. A voltage-to-current converter ( $V$ -to- $I$ ) converts the voltage to excitation current  $I_{EXC}$  with 1 mA amplitude (fig. 1) using a resistor  $R_{REF1}$  in the current feedback chain of operational amplifier (OpAmp), see fig. 5. Every single spectral component of the synthesized ones (fig. 3) has the RMS value of 0.25 mA.



**Figure 5:** Analog part with a voltage to current converter ( $V$ -to- $I$ ), a circuit for pick-up the response voltage  $V_{RES}$ , and an excitation measurement circuit

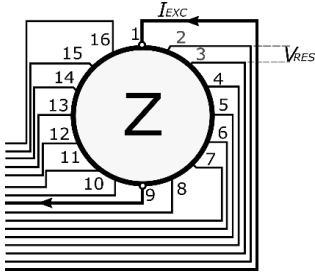
Although the current converter operates with high quality at lower frequencies, its output impedance goes down to 10 k $\Omega$  at 1 MHz. The degradation takes place due to parasitic capacitances, mostly, but also from the lowering of amplification of the feed backed operational amplifier (OpAmp) in the  $V$ -to- $I$ .

Due to this degradation, the excitation current  $I_{EXC}$  through the impedance  $Z$  is measured by the aid of current-to-voltage converter, containing an inverting operational amplifier (OpAmp) with feedback resistor  $R_{REF2}$  (fig. 5). The  $I_{EXC}$  measurement results in voltage  $V'_{EXC}$ . The response voltage  $V_{RES}$  comes from the impedance  $Z$  as a voltage drop caused by the excitation current  $I_{EXC}$ . The response  $V_{RES}$  is picked up by the aid of a unity gain differential amplifier with guarded inputs.

### Bioimpedance spectro-tomographic measurements

In order to evaluate the performance of the new spectro-tomography device, we used 16 equally distributed electrodes in a tank to image a phantom (schematic in fig. 6). Each of the 16 pins of the multiplexer was

connected to one of the 16 electrodes in the tank and several tetrapolar impedance measurements were conducted through them. For the tetrapolar measurements, we applied an opposite excitation pattern and measured voltages serially between other electrodes. For example, when excitation was applied between electrodes 1-9, voltages were measured between electrodes 2-3, 2-4, ... 2-16. In total, we obtained 16 excitation patterns and 13 voltage measurements for each, leading to 208 tetrapolar impedance measurements.



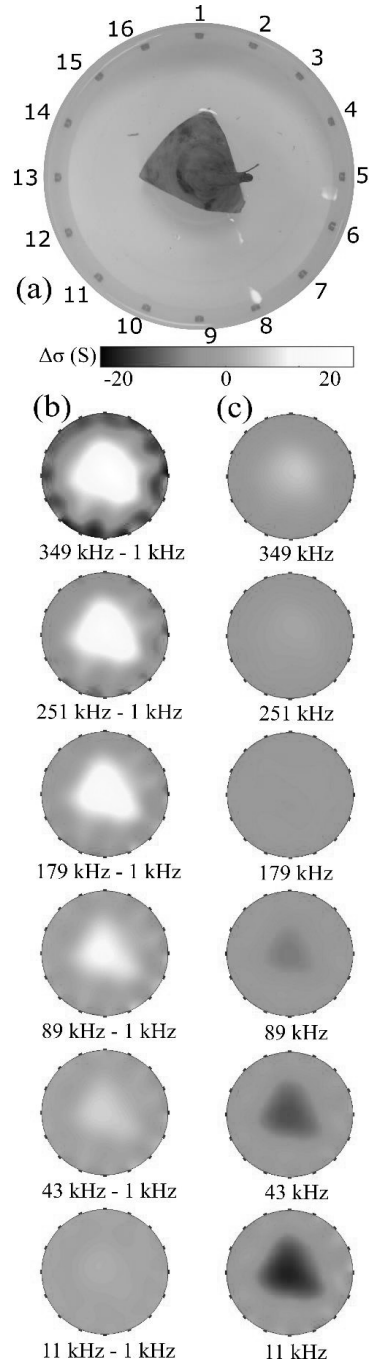
**Figure 6:** Connections of the measurement tank with impedance  $Z$  to multiplexing front-end

The tank (220 mm in diameter) was filled with saline solution with a concentration of 1ppt (a part per thousand). A vegetable (yellow beetroot) was cut into a triangular shape and placed in the middle of the tank (fig. 7(a)). The electrodes were bolt heads made of stainless steel and 6.6 mm in diameter. Before adding the vegetable into the saline solution, the tank was measured with only saline solution in it to obtain reference data for time-difference images.

#### Reconstruction of spectro-tomographic images

Images representing the conductivity change were reconstructed using an open source software EIDORS v3.9 (Electrical Impedance Tomography and Diffuse Optical Tomography Reconstruction Software) [8] in MATLAB R2016a (The MathWorks, Inc.). In addition to the measured impedance values, the minimum information one needs in the image reconstruction are the dimensions of the measured setup and the excitation and measurement pattern used. For computing the conductivity values in a finite element mesh approach, we applied a one step Gauss-Newton solver and a Laplacian smoothness prior with hyperparameter value of 0.005. A complete electrode model with contact impedance value  $0.01 \Omega$  was used.

In difference mode electrical impedance tomography, the conductivity values are computed from two sets of data. Thus, they represent the change of the conductivities rather than the absolute conductivity values. In this paper, the images were reconstructed both in time-difference and frequency-difference mode. In time-difference, the data at certain frequency is compared to a reference data from a different time point but equal frequency. In frequency-



**Figure 7:** Reconstructed images of an experimental phantom measurement in a 16-electrode tank; a photograph of the measured tank with triangular vegetable in saline solution (a), frequency-difference (b) and time-difference (c) reconstructions. The conductivity change depends on the applied frequency.

difference, the data at certain frequency is compared with the same time point but with different frequency.

## Results

The frequency-difference and time-difference reconstructions of the triangular vegetable are shown in fig. 7 (b, c). The frequency of the data ranged from 11 kHz to 349 kHz in both reconstruction modes. The reference data was chosen to be 1 kHz in the frequency-difference images. Thus, these images represent the change of conductivity compared to the conductivity at 1 kHz (fig. 7 (b)). On the other hand, time-difference images represent the change of conductivity due to inserting the vegetable into saline solution.

Both reconstruction modes indicate that the conductivity of the vegetable increased as the applied frequency increased. This change becomes visible at 43 kHz and above in the frequency-difference images. According to time-difference images, the vegetable was more resistive than the saline solution until 89 kHz. At 179 kHz, the vegetable was as conductive as saline solution (no change was detected), but above this, the vegetable became more conductive than the saline solution. These results are in accordance with [9], for example.

## Discussion

The new bioimpedance spectro-tomography device has been presented and demonstrated to work at frequencies from 1 kHz to 349 kHz. Reconstructed images met expectations: conductivity of the vegetable increased as the applied frequency increased, and both the shape and location of the phantom were correct. The excitation pattern and the relatively small number of electrodes used limit the resolution of the results. For enhanced image resolution, excitation patterns including, for example, skip-3 pattern could provide more accuracy to the results. For including the 3D spectro-tomography of time varying impedances, different methods for further minimization of measuring time will become actual.

## Conclusions

The presented spectro-tomography device provides a fast and effective tool for bioimpedance applications. Binary excitation enables to make instrumentation part simple and power efficient. In perspective, both, battery based power supply and wireless communication make possible to isolate the device electrically and minimize accompanying interference.

## References

- [1] Y. Yang and J. Jia. A multi-frequency electrical impedance tomography system for real-time 2D and 3D imaging. *Rev. Sci. Instr.* 88, 085110, 2017, DOI: 10.1063/1.4999359.
- [2] M. Rist *et al.* Modular System for Spectral Analysis of Time-Variant Impedances. In I. Laskovic, D. Vasic (eds.), *IFMBE Proc.* 45, pp 858-861. Springer Switzerland, 2015.
- [3] M. Min, J. Ojarand *et al.* Binary signals in impedance spectroscopy. In *IEEE EMBS Soc. EMB Conf.* 2012, pp 134-137. IEEE, Hoboken, NJ, 2012.
- [4] M. Rist. Principles for the Design of Impedance Spectroscopy Devices for Identification of Dynamic Bio-Systems. PhD thesis, Tallinn University of Technology, Tallinn, Estonia, 2018.
- [5] P. Kauppinen *et al.* Sensitivity distribution visualizations of impedance tomography measurement strategies. *Int. J. Bioelectromagn.* 8, 1-9, 2006.
- [6] M. Lehti-Polojärvi and O. Koskela *et al.* Rotational electrical impedance tomography using electrodes with limited surface coverage provides window for multimodal sensing. *Meas. Sci. Technol.* 29 025401, 2018, DOI: 10.1088/1361-6501/aa97f1.
- [7] S. Grimnes and O. G. Martinsen, Ch. 4 Passive Tissue Electrical Properties (p. 93-95), in: *Bioimpedance and Bioelectricity Basics*, 3rd ed., Academic Press (Elsevier), 2015.
- [8] A. Adler and WRB Lionheart. Uses and abuses of EIDORS: an extensible software base for EIT. *Physiol. Meas.* 27(5): 25-42, 2006.
- [9] S. Ahn *et al.* Frequency-difference electrical impedance tomography: Phantom imaging experiments. *J. Phys.: Conf. Ser.* 224(1), 012152, 2010, DOI: 10.1088/1742-6596/224/1/012152.

## Acknowledgements

Image reconstruction part was supported by Jane and Aatos Erkko Foundation (Finland) and by Business Finland Human Spare Part Program. The authors would like to thank Olli Koskela (Tampere University of Technology) and Aku Seppänen (University of Eastern Finland) for their advice in the image reconstruction. The institutional grant IUT1911 of Estonian Research Council and Estonian IT Center of Excellence EXCITE supported the development of instrumentation part.

# PUBLICATION III

## **Multifrequency electrical impedance tomography in biological applications: A multimodal perspective**

Mari Lehti-Polojärvi, Olli Koskela, Jari Hyttinen

In *Bioimpedance and Spectroscopy*, Annus P, Min M (eds.), Academic Press (2021), pp. 157–189

<https://doi.org/10.1016/B978-0-12-818614-5.00005-9>

**Publication reprinted with the permission of the copyright holders.**



# Multifrequency electrical impedance tomography in biological applications: A multimodal perspective

Mari Lehti-Polojärvi<sup>a</sup>, Olli Koskela<sup>a,b</sup>, and Jari Hyttinen<sup>a</sup>

<sup>a</sup>Tampere University, Faculty of Medicine and Health Technology, Tampere, Finland. <sup>b</sup>HAMK Smart Research Unit, Häme University of Applied Sciences, Hämeenlinna, Finland

## Chapter outline

- 1 Impedance tomography in biology 157**
  - 1.1 Multifrequency EIT 158
  - 1.2 EIT modes and mathematical rationale 161
  - 1.3 Rotational EIT reconstruction 163
  - 1.4 Rotational EIT applications 165
  - 1.5 Multimodal applications of EIT 166
- 2 Instrumentation and data acquisition 166**
  - 2.1 Electrode placement 166
  - 2.2 Excitation and measurement pattern design 169
  - 2.3 MfEIT devices available for cell and tissue cultures 172
- 3 Examples of mfEIT of biological samples 175**
  - 3.1 Traditional mfEIT 175
  - 3.2 LAFR-rEIT imaging 178
- 4 Conclusions 182**
- References 183**

## 1 Impedance tomography in biology

In tomographic imaging, task is to see the inside of an object and visualize it through noninvasive means. In electrical impedance tomography (EIT), current excitations are applied, and voltage is measured on electrodes around the sample. This arrangement

allows to estimate (i.e., to reconstruct) the conductivity distribution within the target or sample (Cheney et al., 1999).

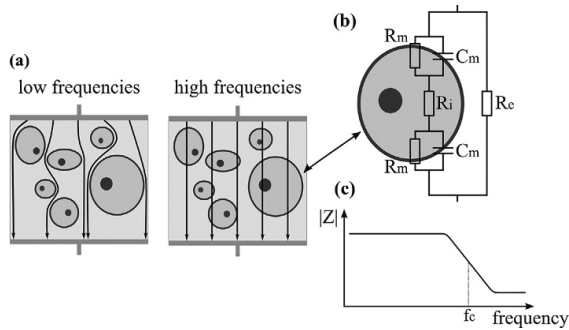
EIT has been used in various fields of science, such as geology, civil engineering, medical imaging, and biotechnology. Recently, several studies have reported the use of EIT for in vitro cell and tissue culture imaging due to its nonharmfulness to living organisms, flexibility in sample requirements (in principle, applicable to any electrically conducting sample), and label-free properties (Linderholm et al., 2008; Sun et al., 2010; Wu et al., 2018a). Technologies including cells and tissues cultured in biomaterials or scaffolds, that is, tissue-engineered samples, are fast emerging and provide novel solutions for disease models, toxicology studies, drug development, and precision medicine (Gomes et al., 2017). A growing trend in cell culture research is to transit from two-dimensional (2D) cultures to three-dimensional (3D) constructs that offer more realistic in vivo mimicking environment for cells to grow and differentiate. In particular, stem cell-derived cells combined with biomaterials in a 3D construct are a potential source for new therapies and innovations (Fang and Eglén, 2017). Because the electric impedance of the cultures changes with cell proliferation, cell death (Lei et al., 2012; Lei et al., 2014; Canali et al., 2015), and differentiation (Hildebrandt et al., 2010), EIT can provide a novel monitoring tool for such samples.

This chapter reviews rationale and current solutions for monitoring cell and tissue cultures by EIT. We focus especially on multifrequency EIT (mfEIT), also known as electrical impedance spectro-tomography, technologies and present a novel rotational multimodal solution based on limited angle full revolution rotational EIT (LAFR-rEIT). We go through the computational principles and models of rotational mfEIT and later show examples of its use.

## 1.1 Multifrequency EIT

Biological tissues, composed of cells in complex arrangements, behave differently when different frequencies of alternating electric current (AC) is applied to them. This difference depends on the composition of the tissue, its structure and health, functional status, and, most importantly, the frequency of the applied signal. This phenomenon is described in Fig. 1, where the electrical properties of biological cell cultures are depicted. Simplifying, cells consist of a nucleus, well-conducting cytoplasm ( $R_i$ ), and thin insulating cell membrane ( $R_m, C_m$ ) surrounding them. The cell membrane electric properties can be modeled as an equivalent resistor-capacitor circuit of cell membrane resistance and a capacitor that mimics the cell membrane property to keep ionic charges separated. This prevents the direct current and





**Fig. 1** (A) A schematic of electrical current paths at high- and low-excitation frequencies in a cell culture. (B) Example of an equivalent circuit of a cell in extracellular medium with resistance ( $R_e$ ) based on the study by Klösgen et al. (2011). Main electrical components of the cell are intracellular resistance ( $R_i$ ), membrane resistance ( $R_m$ ), and membrane capacitance ( $C_m$ ). (C) Typical impedance spectrum of a cell culture. Cell culture-specific capacitance ( $C_m$ ) causes the impedance  $|Z|$  to decrease at a specific frequency range described by cutoff frequency ( $f_c$ ). Cell membrane properties are essential in cell culture analysis.

low-frequency currents of AC electric field to enter the cell but passes high-frequency currents. Extracellular space is typically fluidic cell culture medium or, for example, hydrogel scaffold. This space can typically be modeled with a simple resistor ( $R_e$ ). At low frequencies, the shape and number of cells and the resistance of extracellular space have the most effect on the impedance measurements, as can be seen in Fig. 1. As again, at high frequencies, also the internal properties, as cytoplasmic resistance  $R_i$ , can be probed.

Both EIT and electrical impedance spectroscopy (EIS) apply AC impedance measurements and, thus, share the same physical rationale. Main difference is that EIT uses several impedance measurements around the sample, in contrast to EIS, which typically only uses one bi- or tetrapolar measurement. Hence, EIT considers the conductivity distribution spatially, whereas EIS provides an impedance spectrum graph of the sample average.

EIS has proven to be an effective method for cell and tissue culture studies. Intact cell membrane expresses both resistive and capacitive effects. However, cell death opens the cell membrane, and thus these properties are changed, suggesting that the impedance can be an effective tool for viability monitoring. EIS has been proven to provide meaningful results in various applications such as sorting of dead cells from living cells and counting them (Mernier et al., 2011), tissue and cell type determination

(Gabriel et al., 1996; Halonen et al., 2019; Cheung et al., 2005), stem cell differentiation detection (Hildebrandt et al., 2010), epithelial maturity and integrity monitoring (Savolainen et al., 2011; Onnela et al., 2012), and drug testing and toxicity assays (Zhou et al., 2019; Jahnke et al., 2013). Furthermore, several proofs of case studies have been published regarding cell cultures in hydrogel or other 3D scaffold material, providing information about the cell amount, proliferation, and viability (Lei et al., 2012; Lei et al., 2014; Canali et al., 2015; Wu et al., 2018b). However, mfEIT has not yet been widely used in biological research; even these results promise good capabilities of EIT in 3D cell culture monitoring.

First publications on spatial sensing and monitoring of cell cultures using EIT were done with planar microelectrode arrays (MEAs) that are also commercially available by many commercial vendors to study cellular electric signaling. Daidi et al. (2007) showed in a simulation study that the planar EIT can detect changes on cell culture close to the well bottom. Later, the same principle was applied in the first experimental cell studies (Linderholm et al., 2008; Sun et al., 2010). Linderholm et al. (2008) was able to localize and monitor cell growth and detect cell membrane changes due to permeabilizing substance. Sun et al. (2010) showed that the location and size of the cells can be visualized with EIT. Planar electrode arrays have been successfully used further, for example, cell-drug response analysis and 3D reconstruction of breast cancer cell aggregates (Yin et al., 2018), multifrequency analysis of breast cancer cells in 3D scaffolds (Wu et al., 2018a), viability assessment of breast cancer cell spheroids (Wu et al., 2018b), and real-time detection of cancer cells in a 3D scaffold (Yang et al., 2019).

Other than planar EIT, sensors have been proposed for cell and tissue culture studies. To image 3D cultures, a system with 360 voltage-sensing electrodes on the walls of a rectangular tank has been built (Liu et al., 2011; Lee et al., 2014; Ahn et al., 2014). In addition, flexible nanomaterials rolled to a cylindrical shape with electrodes fabricated into the material have been developed toward microscopy scale EIT of single cells (Weiz et al., 2017a, b). A third sensor type has been designed for LAFR-rEIT setups. Lehti-Polojärvi et al. (2019) attached flexible electrode sheets on two opposing walls of a rectangular EIT chamber to enable multimodal imaging. Overall, the present mfEIT results in the field of biological studies are mainly at proof of concept stage and intensive analyses of biological cell cultures are still needed. Studies of EIT in multimodal imaging setups could provide novel tools for this development. It would be especially feasible to integrate EIT into optical microscopy, which in most cases is also available in the culture setups.

## 1.2 EIT modes and mathematical rationale

In EIT reconstruction, task is to solve the internal conductivity distribution based on boundary measurements. This reconstruction task is called an inverse problem, and the corresponding forward, or direct problem, would be to estimate the measurement data with the given measurement model and internal structure. Computing EIT reconstruction is highly ill-posed: the solution is very sensitive to noise and modeling errors. In this section, we will shortly describe the mathematical principles behind EIT and present some recent works on the inverse problem.

To be able to consider the inverse problem, the forward model has to be formulated and is in basic form

$$V = U(\sigma) + n, \quad (1)$$

where  $\sigma$  is the conductivity distribution of the sample;  $V$  is the voltage measurements on the sample boundary;  $n$  is additive noise term due to unideal instrumentation; and  $U$  is the forward operator, including the electrode modeling and information of measurement pattern and spatial domain dimensions (Somersalo et al., 1992). EIT operator  $U$  is nonlinear because the measurement is diffusive in nature. Electrical current applied in EIT propagates in the material depending on the conductivity distribution.

Two questions can be asked of the conductivity distribution depending on the measurements available. First, what is the conductivity distribution that explains the measurement. This is called absolute (static) EIT and requires only one measurement from the sample. The second question is what change in conductivity distribution between two samples or states explains the difference between two measurements. This is called difference EIT and it can be used to detect change between two different samples, frequency response difference within the same sample, or the change over time of a sample.

The nonlinear forward operator  $U$  is often linearized by writing its first-order Taylor approximation

$$U(\sigma) \approx U(\sigma_0) + J(\sigma - \sigma_0) \quad (2)$$

to compute the inverse solution, that is, the conductivity distribution  $\sigma$  with known measurement  $V$ . Here, the  $\sigma_0$  is the linearization point, and  $J$  is the Jacobian matrix of  $U(\sigma_0)$ . Now, given two measurements  $V_1$  and  $V_2$  of background object and the varied object, respectively, the difference model can be defined as follows:

$$\Delta V = V_1 - V_2 = J\Delta\sigma + \Delta n, \quad (3)$$

that is, the difference in the measurements is due to difference in the conductivity distributions.

In practice, the ill-posedness of EIT inverse problems requires to use regularization to compute the conductivity distribution change  $\Delta\sigma$ . Regularization enforces the solution toward known a priori information of the sample. For example, with widely used Tikhonov regularization, a solution with smaller norms or smoothness is preferred and Tikhonov regularization allows the solution to be computed as a minimization problem (Vauhkonen, 1997; Mueller and Siltanen, 2012)

$$\widehat{\Delta\sigma} = \arg \min_{\Delta\sigma} \left\{ \|\Delta V - J\Delta\sigma\|^2 + \alpha \|L\Delta\sigma\|^2 \right\} = (J^T J + \alpha L^T L)^{-1} J^T \Delta V, \quad (4)$$

which is balancing with weight  $\alpha$  between data fidelity (first term) and regularization (latter term with, where  $L$  is a suitable regularizer). Often, the computation is performed in finite element mesh (FEM) model, which includes the information about the sample and measurement domain, as well as the placements of the electrodes (Dehghani and Soleimani, 2007).

Recently, several other approaches to compute the inverse problem have been reported, including deterministic (e.g., Vauhkonen, 1997) and statistical (e.g., Calvetti et al., 2012; Ren et al., 2019; Kaipio et al., 2000), genetic optimization (e.g., Olmi et al., 2000; Leskinen et al., 2009), level set methods (Liu et al., 2018), deep learning and artificial intelligence (e.g., Khan and Ling, 2019; Wei et al., 2019; Fan and Ying, 2020), nonlinear Fourier transform (e.g., Knudsen et al., 2009; Alsaker et al., 2017; Hamilton and Hauptmann, 2018), and Graz consensus reconstruction (e.g., Grychtol et al., 2016).

Difference EIT is commonly used if reference data are available, because of its robustness to modeling errors; small inaccuracies in modeling of electrode locations, boundary shape, and electrode contact impedances may lead to drastic differences when using absolute reconstruction methods. In addition, difference EIT is typically computationally fast to reconstruct. However, in difference imaging, the nonlinear observation model of EIT is linearized, which causes the results to be only qualitative in nature. Thus the results only indicate the trend of conductivity change and not the actual conductivity value. In absolute imaging, the conductivity distribution is estimated from a single measurement data. It does not require linearization of the nonlinear EIT model. However, its sensitivity to modeling errors may cause poor image resolution (Liu et al., 2016).

In recent years, some research studies have introduced methods that combine the benefits of absolute and difference

imaging modes. Hallaji et al. (2014) incorporated a discrepancy term to the nonlinear observation model of EIT to eliminate the modeling errors but solving the conductivity distribution in absolute, quantitative sense. This discrepancy term was based on estimating the background conductivity of a homogenous sample. The approach provided both high spatial resolution and quantitative information, that is, absolute conductivity values were visualized. The resolution was further improved by refining the discretization level, resulting in probably the highest spatial resolution seen in EIT thus far (Seppänen et al., 2014). Another slightly more advanced approach for using reference measurements in EIT is using the so-called nonlinear difference imaging (Liu et al., 2015a), where a nonhomogeneous background conductivity is reconstructed simultaneously with the conductivity change based on measurements before and after the change. This approach was shown to be particularly tolerant to modeling errors (Liu et al., 2015b) and has also been applied to high-resolution crack detection (Smyl et al., 2018). The success of these methods in the cited works is based on two factors: (1) the availability of reference data and (2) application-specific earlier information encoded in the reconstruction. These computational methods could potentially help improving the resolution also in cell and tissue culture studies, where reference data can usually be measured and which may also enable acquiring application-specific (structural) earlier information, for example, by using an additional imaging modality.

A well-established software package to solve EIT problems is EIDORS (Adler and Lionheart, 2006), which has been developed since 1999. More recent alternatives include works such as a fast parallel forward solver (Jehl et al., 2014), zedhat (Boyle, 2019) and Zeffiro (He et al., 2019). MATLAB code package for D-bar method is available through (FIPS Computational Blog, n.d.).

### 1.3 Rotational EIT reconstruction

To reconstruct difference mode conductivity distribution from rotational EIT data  $V_1, V_2, \dots, V_m$  acquired in  $m$  measurement positions, we formulated the EIT forward model in Eq. (1) into stacked format

$$\begin{bmatrix} V_1 \\ V_2 \\ \vdots \\ V_m \end{bmatrix} = \begin{bmatrix} U(M_1\sigma) \\ U(M_2\sigma) \\ \vdots \\ U(M_m\sigma) \end{bmatrix} + \begin{bmatrix} n_1 \\ n_2 \\ \vdots \\ n_m \end{bmatrix}, \quad (5)$$

where  $M_i$  is a mapping function of the FEM model from initial position to rotated measurement position, and  $n_i$  are the individual noise realizations of respective measurement positions. In short, we use subscript  $r$  for this rotational mapping and denote

$$V_r = U_r(\sigma) + n_r \quad (6)$$

for the rotational forward model.

Now, the linearization is similar to that of the static case in Eq. (2):

$$U_r(\sigma) \approx U_r(\sigma_0) + J_r(\sigma - \sigma_0) \quad (7)$$

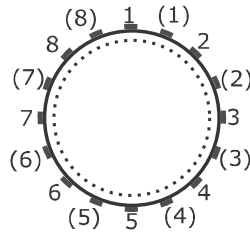
with linearization point  $\sigma_0$  and Jacobian

$$J_r = \begin{bmatrix} JM_1 \\ JM_2 \\ \vdots \\ JM_m \end{bmatrix}, \quad (8)$$

where  $J$  is the Jacobian matrix of  $U(\sigma_0)$ . The inverse solution is computed just as in the nonrotational case in Eq. (4):

$$\widehat{\Delta\sigma} = \arg \min_{\Delta\sigma} \left\{ \|\Delta V_r - J_r \Delta\sigma\|^2 + \alpha \|L \Delta\sigma\|^2 \right\} = (J_r^T J_r + \alpha L^T L)^{-1} J_r^T \Delta V. \quad (9)$$

Several approaches exist to the rotational mapping  $M$ , that is, the mapping of the FEM element positions to correspond to rotated position of electrodes or sample. Different approaches are illustrated in Fig. 2. For a small number of rotated positions, a common approach has been to include “virtual” electrodes into the model so that the rotated positions can be estimated by choosing a suitable combination of these. An excellent review of the reconstruction approaches in rotational EIT has been included into the study by Murphy et al. (2017), where they also considered the poorer performing option of computing inverse solution from each rotated position individually and then postprocessing the final reconstruction from these. Another approach is to rotate the values inside the FEM model, which provides flexibility due to the electrode positioning being detached from the rotational measurement position design. Two such methods of rotational mapping  $M$  have been implemented: first, with fixed FEM, where the element values are rotated through weighted geometric mapping (Lehti-Polojärvi et al., 2018); and second, with FEM model, including rotationally invariant node design within the domain, such that the elements can be mapped rotational positions without blurring due to the mapping (Koskela et al., 2019).



**Fig. 2** Different types of rotations are illustrated. Rotation of an eight-electrode setup can be modeled through computing reconstructions with virtual electrodes in rotated positions, depicted with actual electrodes numbered from one to eight and their rotated virtual electrodes in parenthesis. Another option is to use only the actual electrodes in the computations but rotate the values of the FEM model inside the domain, either by interpolating the rotated values or by constructing a boundary that is invariant to rotation (marked with the dashed line), and elements are mapped to new positions inside this rotational boundary while keeping the exterior domain static.

## 1.4 Rotational EIT applications

In rotational EIT, either the electrodes or the sample is rotated. Even if this may cause challenges in instrumentation, sample placement, and image reconstruction, in some cases, it is worth the effort. The main idea behind rotational EIT is to enhance spatial resolution by increasing the amount of independent measurements because the same electrodes are used to measure the targets from various angles. The first work on rotational EIT was presented by Murphy and York (2006) who applied electrodes on a rotating impeller inside an EIT chamber to enhance image resolution for industrial mixing applications. Huang et al. (2007, 2008) continued rotational EIT method development with rotating 16-electrode and 8-electrode rings in EIT chamber filled with saline solution. Regarding medical applications, rotational EIT has been studied for breast cancer detection systems applying movable planar electrode array (Zhang et al., 2015) and rotated 16-electrode cylindrical and breast-shaped chambers (Murphy et al., 2017). First rotational EIT setup for cell and tissue culture studies was presented by Lehti-Polojärvi et al. (2019). In this setup, the sample was rotated, and electrodes were fixed on two opposing EIT chamber walls. In general, rotational EIT may be especially useful in systems where electrodes can only cover part of the sample surface area, that is, limited angle (LAFR-rEIT) cases (Lehti-Polojärvi et al., 2018).

## 1.5 Multimodal applications of EIT

Relevant to multimodal setting, the structural a priori information incorporated into EIT reconstruction has been studied in several works, for example, the works done by Kaipio et al. (1999) and Kang et al. (2016), and applied in the scope of medical imaging. Ultrasonic imaging used as a priori with EIT was suggested by Soleimani (2006) and Steiner et al. (2008) for enhanced image accuracy and resolution. EIT combined with ultrasonic imaging has been further studied for prostate cancer detection (Wan et al., 2010; Murphy et al., 2018) and muscle health inspection (Murphy et al., 2019). Ultrasound reflection tomography has been considered alongside impedance measurements (Steiner et al., 2008; Liang et al., 2020). Furthermore, ultrasound can be used to induce conductivity changes within the sample and is used in the context of frequency difference imaging (Harrach et al., 2015; Jensen et al., 2019). Anatomical information obtained from CT has been merged with EIT for accurate diagnosis of hemorrhage location (Canhua et al., 2011). Combining EIT with MRI imaging has been shown to be effective in phantoms (Davidson et al., 2012) and in lung imaging (Crabb et al., 2014). However, there are still very few effective solutions for multimodal in vitro cell culture studies. Such applications could provide methods for validating the EIT results regarding cellular phenomena through coregistration of the microscopy images. In addition, a priori information could improve the typically poor spatial resolution of EIT images.

## 2 Instrumentation and data acquisition

### 2.1 Electrode placement

Electrode placement depends on the application and the desired simplicity of the instrumentation. Main aspect regarding EIT is to collect sufficient data from the whole sample. Another aspect to consider is whether 2D or 3D images are desired. The further the region of interest is from the current excitation electrodes, the weaker the current density field is, as can be seen, for example, in Fig. 6 (black arrows on the rightmost image). Here, we review EIT electrode configurations designed for cell and tissue culture studies.

Most EIT setups in cell culture applications consist of 8–32 equidistantly distributed electrodes at the bottom of the chamber (Sun et al., 2010, Yin et al., 2018, Yang et al., 2017, York et al., 2004, Lemmens et al., 2018, Farnham et al., 2019). In addition,

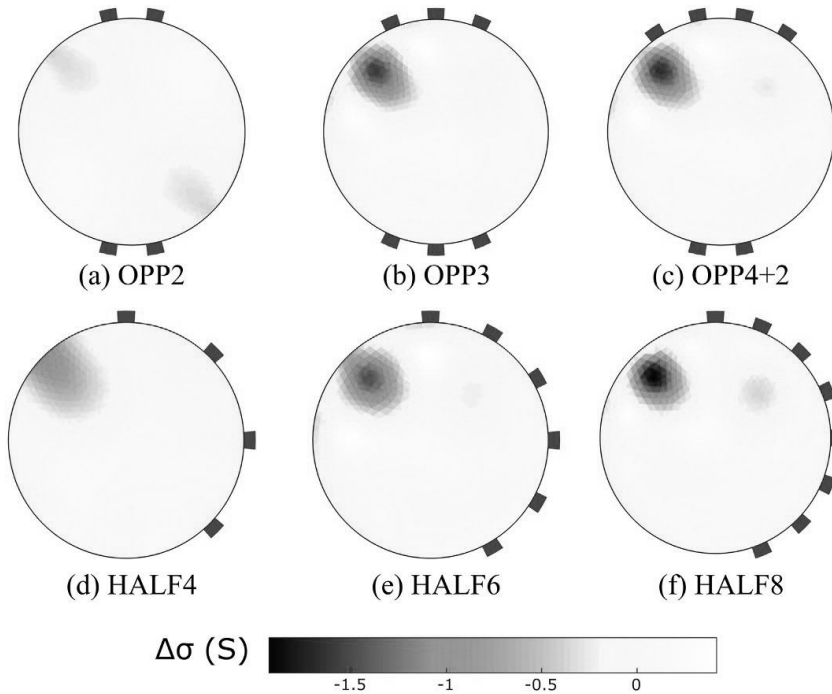


commercial MEAs, which are commonly used for *in vitro* neuronal activity monitoring, have been proposed to be used in EIT (Daidi et al., 2007). Linderholm et al. (2008) used a custom-built MEA with electrodes placed according to the needs of the planar EIT for human epithelial stem cell imaging. One example of a planar electrode configuration for EIT is shown in Fig. 9 where 16 working electrodes are distributed at the bottom of the chamber.

Microscale rolled-up EIT sensor made of strain-engineered thin films has been proposed for single-cell studies (Weiz et al., 2017a). Eight electrodes were fabricated on the inner tube circumference of a 35- $\mu\text{m}$  diameter tube, and  $\text{SiO}_2$  particles were successfully imaged (Weiz et al., 2017a). In addition, necrotic cell death of a single HeLa cell was detected with 12 electrodes on a 30- $\mu\text{m}$  diameter tube (Weiz et al., 2017b). Another approach is to use hundreds of electrodes in a rectangular cuboid chamber, as has been presented for tissue engineering studies (Liu et al., 2011; Ahn et al., 2014; Lee et al., 2014). Two pairs of current injection and 360 voltage-measurement electrodes were fabricated on the chamber walls, and the setup was shown to provide reasonable 3D reconstructions of phantom data.

For applications where the number or space available for the electrodes is limited, LAFR-rEIT method could be a solution. It is based on placing the electrodes at a suitable angle around the sample, and either the electrodes or the sample is rotated to obtain enough data (Lehti-Polojärvi et al., 2018). This method is especially useful if there is another modality that needs a sensor space or optical window into the sample, as is illustrated in Fig. 10. Several electrode configurations have been studied for this setup (Lehti-Polojärvi et al., 2018), and part of the results is shown in Fig. 3. Designing suitable electrode configuration is important for sensor and hardware design to avoid using excessive amount or ineffective placement of electrodes. It is also especially useful before extending a LAFR-rEIT setup to 3D imaging that requires more electrodes and measurements around the sample than 2D setup.

Results in Fig. 3 show EIT images reconstructed from simulated data of a two-inclusion phantom (phantom as in Fig. 10). The used configurations can be divided into symmetrical and asymmetrical according to the electrode placement. In symmetrical configuration, the same numbers of electrodes are placed opposite each other (here, OPP2 and OPP3). Asymmetrical configuration (OPP4 + 2, HALF4, HALF6, and HALF8) include both opposite and so-called half configuration electrodes. The term HALF refers to electrodes that are left if half of the equidistantly placed



**Fig. 3** LAFR-rEIT reconstructions visualizing conductivity change of a two-inclusion phantom with different electrode positions. (A–B) 32 rotational measurement positions in 180 degrees rotation and (C–F) 64 rotational measurement positions in 360 degrees rotation. Two inclusions are well visible only with HALF8 configuration. Source: Lehti-Polojärvi, M., Koskela O., Seppänen A., Figueiras E., Hyttinen J., 2018. Rotational electrical impedance tomography using electrodes with limited surface coverage provides window for multimodal sensing. *Meas. Sci. Technol.* 29, 025401. <https://doi.org/10.1088/1361-6501/aa97f1>.

electrodes, often used in traditional EIT systems, were removed. For example, HALF8 configuration results from electrodes 1–8 of the conventional 16 equidistantly placed electrodes, shown, for example, in Fig. 4.

To obtain comparable results, the same angular difference between rotational measurement positions was used for all cases, as shown in Fig. 3, so that symmetrical configurations were reconstructed with 32 rotational measurement positions in 180 degrees rotation and asymmetrical with 64 rotational measurement positions in 360 degrees rotation. Results show that both the number of electrodes and the electrode configuration affects the image

accuracy. HALF configurations were more effective in image accuracy compared with OPP configurations with the same number of electrodes. However, increasing the number of electrodes enhances image accuracy in both configurations. Both inclusions were found only with OPP4 + 2 and HALF8 configurations, whereas in others, the smaller inclusion is totally or almost invisible. In addition, a symmetrical electrode configuration with four electrodes on opposing sides (OPP4 + 4), shown in Fig. 10, has been experimentally studied both in a circular setup (Fig. 11) and in a rectangular setup (Fig. 12).

Electrode configuration is crucial for the resulting image quality because it specifies the amount of collectible data, but it is not the only factor affecting the results. Furthermore, electrode configuration is often determined by various needs and limitations of the application, for example, possible probes of other modalities or device limitation for the number of electrodes. Other important factors for the resulting image quality are the chosen excitation and measurement patterns, electrode contact impedances, instrumentation parasitics, and image artifacts due to computational deficiencies.

## 2.2 Excitation and measurement pattern design

It is important to apply EIT measurements that obtain information from the regions of interest. Lead field theory was originally introduced for electrocardiographic measurements (McFee and Johnston, 1953) and later modified for bioimpedance lead sensitivity assessment (Geselowitz, 1971; Malmivuo and Plonsey, 1995). It offers a useful tool for designing optimal excitation and measurement patterns for EIT applications and enables a way to visualize impedance measurement sensitivity. The theory was first applied in an FEM model (Hytinen et al., 1993) and further developed for simulations of impedance measurements and impedance tomography (Kauppinen et al., 1996; Kauppinen et al., 2005). This method has been used, for example, to design electrode configuration and excitation and measurement patterns for LAFR-rEIT approach (Lehti-Polojärvi et al., 2018), EIS of tissue-engineered systems (Canali et al., 2015), impedance measurements of epithelial tissues (Tervonen and Hytinen, 2018), and single-cell MEA measurements (Böttrich et al., 2017).

Measured impedance  $Z$ , or its change, depends on the conductivities  $\sigma$ , or conductivity change, of all objects located in the generated current field in the volume  $V$  and the sensitivity distribution  $S$  associated with the excitation and measurement pattern as follows:

$$\Delta Z = \int_V \frac{S}{\Delta\sigma} dV \quad (10)$$

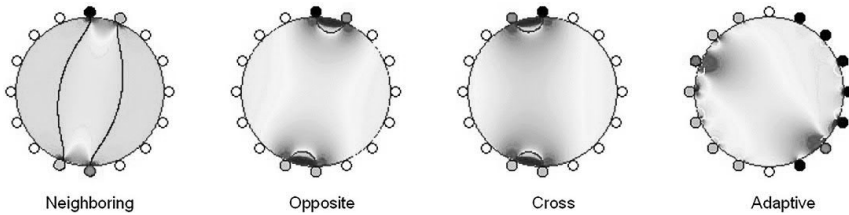
According to the lead field theory, the sensitivity of an impedance measurement can be determined as a dot product of two current density fields as follows:

$$S = \mathbf{J}_{LE} \cdot \mathbf{J}_{LI}, \quad (11)$$

where the vector field  $\mathbf{J}_{LE}$  is formed by feeding current to the measurement electrodes and the other vector field  $\mathbf{J}_{LI}$  reciprocally to the excitation electrodes. The sensitivity distribution describes the effect of each region to the measured impedance value. Sensitivity values can be positive, negative, or zero depending on the angle of the two vector fields (examples shown in Figs. 4 and 6). In the regions of positive sensitivity, an increase of local conductivity leads to a decrease in the measured impedance. If sensitivity is negative, an increase in conductivity causes increase in measured impedance. Regarding EIT, most problematic regions are those that have zero or close to zero sensitivity because the measured impedance value is then unaffected by the conductivity in that region. This causes instability to the reconstruction because even high conductivity values in these regions are not detected in the measurements or in the forward solution.

Excitation and measurement pattern for EIT consists of several impedance measurements to obtain enough spatial information from the object. It is preferable to have measurement pattern that contains high local sensitivity measurements from all areas in the object, for example, center and edges. Here, we consider mainly tetrapolar measurement schemes, but the lead field concept can be applied to design and analyze various types of impedance measurements patterns (Kauppinen et al., 2006).

In traditional EIT systems, where electrodes are placed equidistantly around the object, commonly used patterns include neighboring (adjacent), opposite, and skip patterns. The name of the pattern describes the current excitation pattern, and voltage measurements are typically done sequentially with all remaining electrodes. In neighboring pattern, current is excited through two neighboring electrodes and voltage measured successively from all other neighboring electrode pairs. Generally, not using the current-driving electrodes in voltage measurements makes the measurement less sensitive to the electrode contact impedances. A comparison of four different patterns is shown in Fig. 4 where

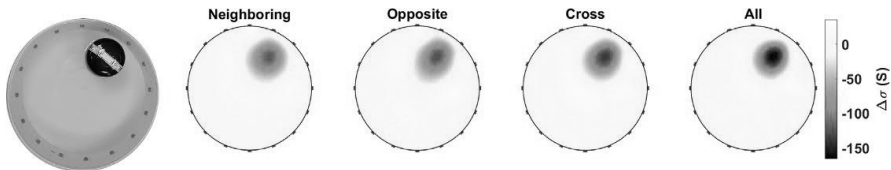


**Fig. 4** Comparison of excitation and measurement patterns sensitivity. The most sensitive tetrapolar pattern to detect the center of the sample is visualized for each pattern. Black electrodes are used for current excitation and red for voltage measurement. Source: Kauppinen P., Hyttinen J., Malmivuo J., 2006. Sensitivity distribution visualizations of impedance tomography measurement strategies. *Int. J. Bioelectromagn.* 8 (1), 63–71.

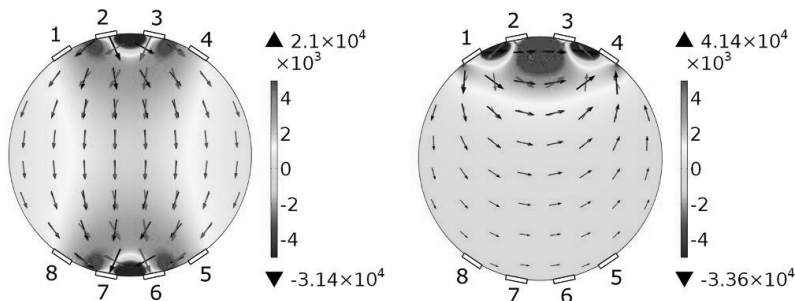
one measurement that is most sensitive in the center region is visualized for each pattern (Kauppinen et al., 2006). Animations of these patterns are available in the online version of the publication (Kauppinen et al., 2006).

Fig. 4 shows significant differences in sensitivity to central regions of the object. Opposite, cross, and adaptive patterns include measurements with high sensitivity in the center, but neighboring pattern is clearly limited to the surface regions. Reconstructed examples applying neighboring, opposite, cross, and all combinations patterns using experimental data can be seen in Fig. 5. Differences in image quality can be seen, although in each method there are measurements with high sensitivity at the region of the inclusion, that is, close to the electrodes. The shape and contrast of the inclusion is most clear if all current excitations pattern (All) is used. If current is only applied on opposing electrodes (opposite), the shape of the resistive inclusion becomes distorted.

A suitable pattern for each application depends mainly on the required temporal and spatial resolutions and possibly on setup



**Fig. 5** Effect of measurement pattern to reconstructions using excitation patterns: neighboring, opposite, cross, and all. Resistive inclusion in saline is shown as a decrease in conductivity. Images reconstructed at 11 kHz excitation frequency.



**Fig. 6** Sensitivity field distributions ( $1/m_4$ ) and current density arrows visualized for two tetrapolar measurements used in a LAFR-rEIT setup. Black arrows show the current density field induced by current excitation electrodes 2–7 (left) and 1–4 (right). Green arrows show the current density field induced by voltage measurement electrodes 3–6 (left) and 2–3 (right). Source: Modified from Lehti-Polojärvi, M., Koskela O., Seppänen A., Figueiras E., Hyttinen J., 2018. Rotational electrical impedance tomography using electrodes with limited surface coverage provides window for multimodal sensing. *Meas. Sci. Technol.* 29, 025401. <https://doi.org/10.1088/1361-6501/aa97f1>.

specific features, such as rotating object. Careful measurement pattern design is especially needed for applications where the electrode surface coverage is limited, as in the LAFR-rEIT case. Two tetrapolar examples included in a pattern designed for eight-electrode LAFR-rEIT case are shown in Fig. 6. The one using opposing electrodes (on the left) has high sensitivity in a large region, including the center of the object. The other on the right has high sensitivity at the edge of the object. These measurements complement well the excitation and measurement pattern used in this case. The sensitivity distribution, shown as background colour in Fig. 6, is computed as a dot product of the green and black current density field arrows that visualize the direction and magnitude of the reciprocal fields, respectively.

In a LAFR-rEIT setup, the object is rotated that allows it to be measured from different angles. Rotation combined with well-designed tetrapolar measurement pattern provides high sensitivity measurements covering the whole object. Example reconstructions are shown in Figs. 11 and 12.

### 2.3 MfEIT devices available for cell and tissue cultures

There are plenty of developed EIT systems for process tomography and medical EIT. Multifrequency systems developed to

identify biological tissues in medical applications are, for example, the UCLH Mark 1b (Yerworth et al., 2002) and the KHU Mark 1 (Oh et al., 2007). However, these are not optimal for cell and tissue culture studies that need to operate in suitable frequency range, that is, typically,  $\beta$ -dispersion range where conductivity changes are associated with cell membrane integrity and also work with sufficiently low-excitation amplitudes not to cause damage to the small living samples. Early systems for cell studies were mainly custom-built from an impedance analyzer, a multiplexing board, and a custom control software applying single frequency (Linderholm et al., 2008; Sun et al., 2010). Recently introduced systems have significantly better temporal resolution, programs for data acquisition, and easy use of multiple frequencies. These systems are tabulated in Table 1.

Spectro-EIT device (Min et al., 2018) was developed in collaboration of Eliko (Estonia), Technical University of Tallinn (Estonia), and Tampere University (Finland). It is based on fast impedance spectroscopy platform using chirp multifrequency pulse excitation (QUADRA technology, trademark of Tallinn University of Technology, Estonia) with embedded multiplexer. Currently, there are 16 input/output pins to enable maximum of 16 electrodes to be connected. The system applies binary excitation voltage and performs discrete Fourier transform to extract

**Table 1 MfEIT systems for cell and tissue cultures.**

System	Electrodes	Excitation	Pattern switching	Operating frequencies
Spectro-EIT	16	Binary, voltage-controlled current source	Flexible	1 kHz–349 kHz, 15 simultaneously
Visual tomography	32	Sinusoidal, voltage-controlled current source	Flexible	10 kHz–1 MHz, 2 simultaneously
Sciospec EIT	128	Sinusoidal current excitation	Flexible	100 Hz–1 MHz
MUSEIC V2.0	16	differential square wave current excitation	Flexible	1 kHz–1 MHz
Dartmouth EIT tissue growth monitor	64	sinusoidal current excitation	Flexible	100 Hz–1 MHz

frequency domain data from the measured voltages generated by the pulsed current feed. The device provides impedance data simultaneously at 15 frequencies: 1, 2, 3, 7, 11, 17, 23, 31, 43, 61, 89, 127, 179, 251, and 349 kHz. Excitation and measurement patterns switching is flexible and easily changed by the user. Temporal resolution is very high with this device because one tetrapolar measurement, including data with 15 frequencies, could be obtained in 1 ms. Owing to time constant of the sample and need for averaging, manufacturer recommends using 5 ms for each tetrapolar measurement. This includes average from three repeated measurements. Averaging can be easily increased by the user in the LabVIEW-based user interface. The great strength of this device is its temporal resolution in gathering multiple frequencies simultaneously. Example results using this device are shown in Figs. 5, 7, and 12.

Another suitable mfEIT system (Yang and Jia, 2017), named as Visual Tomography, has been developed by Agile Tomography Group (University of Edinburgh, Scotland). The system has interface for 32 electrodes, and adjustable multifrequency current source applies sinusoidal current excitation at one or two frequencies simultaneously. The frequency selection ranges from 10 kHz to 1 MHz. This system has high-speed data acquisition, and the frame rate depends on the applied frequency and data acquisition mode. For example, the system can record 1014 frames per second at 625 kHz and 89 frames per second at 10 kHz in semiparallel mode, where each frame includes 104 measurements. Excitation and measurement patterns are flexible, and system incorporates Visual Tomography software for real-time 2D and 3D image reconstruction. Example results using this device are shown in Fig. 9.

Sciospec EIT system (Sciospec Scientific Instruments GmbH, n.d.) offers up to 128 channels for electrode connections. It operates from 100 Hz to 1 MHz with a sinusoidal current excitation. Image reconstruction for difference EIT is embedded in the control software. Sciospec EIT device has been used, for example, for single-cell studies in microtubular fluidic channels (Weiz et al., 2017a).

MUSEIC V2.0 system was presented in the study by Ha et al. (2017) and applied in yeast cell studies by Lemmens et al. (2018). The system can be used with 16 electrodes, and excitation frequency ranges from 1 kHz to 1 MHz. Temporal resolution is somewhat limited because it takes 0.5 s both for switching and each measurement, for example, 56 s in total for 56 potential measurements.



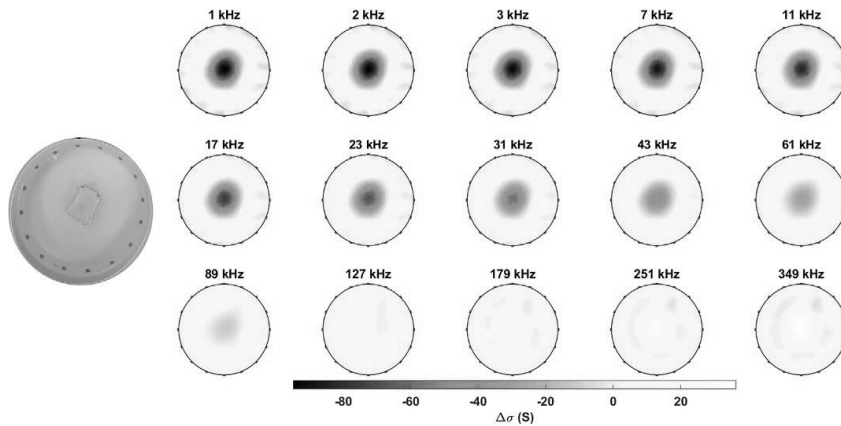
A 64-channel Dartmouth EIT Tissue Growth Monitor based on HP impedance analyzer has been developed for tissue culture studies (Farnham et al., 2019). The system allows flexible design of tetrapolar measurements and operates from 100 Hz to 1 MHz. Farnham et al. (2019) connected the device with a flexible planar printed circuit board-based electrode array at the bottom of a 6-well cell culture dish. Studies with yeast cells have been performed to verify the tissue growth monitoring tool.

From the presented mfEIT devices in Table 1, Spectro-EIT and Visual tomography can measure different frequencies simultaneously. Other devices record multifrequency data sequentially one frequency at a time. Most of these devices are novel and currently under development. There is a great variance in measurement duration provided by different systems, which can be crucial for time-variant samples. In general, temporal resolution is dependent on the instrumentation switching time, measurement pattern, data acquisition software, and acceptable noise level. In addition, the time constant of tissues at the used frequencies should be considered (Min et al., 2018).

### 3 Examples of mfEIT of biological samples

#### 3.1 Traditional mfEIT

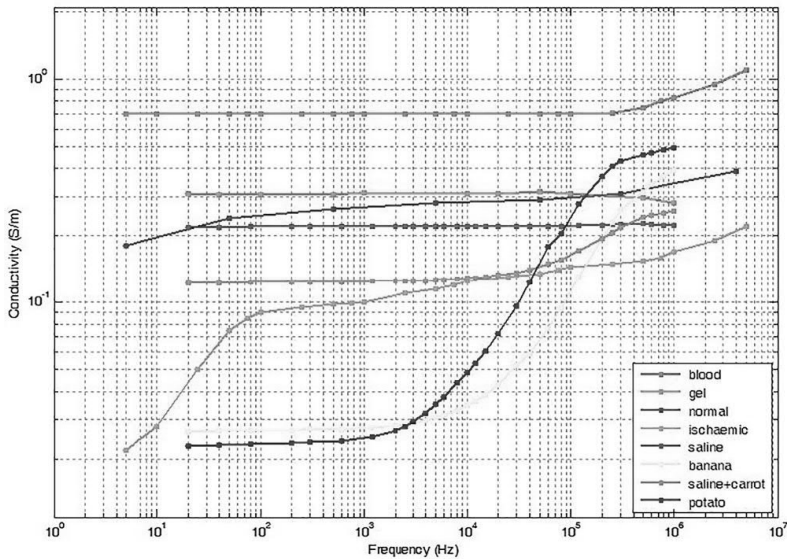
To demonstrate the features of mfEIT of a biological specimen, reconstructed images of a potato inclusion in saline solution are shown in Fig. 7. Measurements were obtained with Spectro-EIT device (Table 1), and the applied pattern contained all current excitation combinations and 1560 sequential voltage measurements (“All” in Fig. 5). The device provides 15 frequencies in the range from 1 kHz to 349 kHz at a single measurement. The excitation voltage was 2.0 V, and each measured value was an average of seven measurements. A rectangular potato was placed in the center of a 16-electrode 22-cm diameter chamber filled with saline solution. Reference data were measured from blank saline solution applying the same settings. According to the analysis in Section 2.2, the sensitivity of these measurements is expected to be high also in the center of the chamber. Difference mfEIT images were reconstructed in EIDORS visualizing the effect of the potato compared with blank saline at the same frequency, that is, time difference EIT.



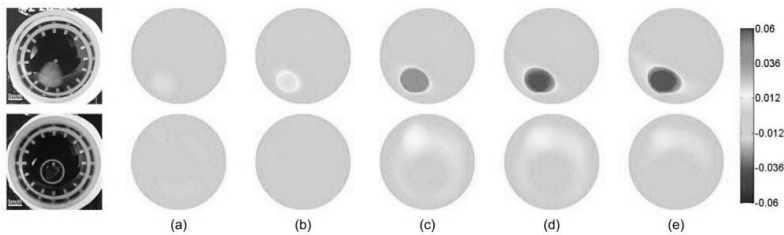
**Fig. 7** MfEIT of potato in saline solution. Conductivity of the potato increases as the applied frequency increases.

Each reconstruction in Fig. 7 visualizes the conductivity change caused by the potato inclusion compared with blank saline at each frequency in question. The results demonstrate how effectively mfEIT detects and localizes the frequency-dependent properties of biological samples. At low frequencies until 89 kHz, the potato is less conductive than the saline solution. At 127 kHz, their conductivity is similar, and above 179 kHz, potato becomes more conductive than saline solution. This phenomenon is in accordance with the theory (Fig. 1) and spectral impedance measurements presented by Ahn et al. (2010) in Fig. 8.

MfEIT of blank hydrogel and cells in hydrogel are shown in Fig. 9 (Wu et al., 2018a). The chamber diameter was 15 mm and height 10 mm. Sixteen working electrodes were at the edge of the chamber bottom. Measurements were conducted with the Visual Tomography multifrequency EIT system (Yang and Jia, 2017) described in Section 2.3 by applying the neighboring (adjacent) excitation and measurement patterns. They applied 1 mA excitation current with frequencies from 10 kHz to 100 kHz. Breast cancer cells (MCF-7) were seeded in HyStem-HP hydrogel scaffold, and the cell-loaded hydrogel and blank hydrogel were measured in cell culture medium. The electrodes were located at the bottom of the chamber, causing the sensitivity to be highest near the bottom. According to Fig. 4, the sensitivity of neighboring pattern is low in the center of the chamber. Thus the inclusions were located at the highest possible sensitivity field in this case. The reconstructed difference mfEIT images visualize the effect of the applied frequency on the same sample, that is, frequency difference EIT.



**Fig. 8** Conductivity spectra of blood, ischemic and normal brain tissue, various plants, and gel. The steep conductivity increase of potato between 1 kHz and 400 kHz is visualized with mEIT in Fig. 7. Source: Ahn, S., Jun, S.C., Seo, J.K., Lee, J., Woo, E.J., Holder, D., 2010. Frequency-difference electrical impedance tomography: phantom imaging experiments. *J. Phys. Conf. Ser.* 224, 012152. <https://doi.org/10.1088/1742-6596/224/1/012152>.



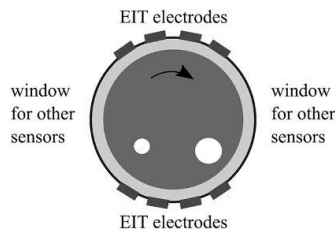
**Fig. 9** MfEIT reconstructions of blank hydrogel (bottom row) and cell-loaded hydrogel (top row), (A) 20 kHz, (B) 40 kHz, (C) 60 kHz, (D) 80 kHz, and (E) 100 kHz with 10 kHz reference. Source: Wu, H., Zhou, W., Yang, Y., Jia, J., Bagnaninchi, P., 2018a. Exploring the potential of electrical impedance tomography for tissue engineering applications. *Materials (Basel)* 11 (6), 930. <https://doi.org/10.3390/ma11060930>.

The results in Fig. 9 show frequency difference reconstructions with cell-loaded hydrogel and blank hydrogel at 20, 40, 60, 80, and 100 kHz using data from the same sample but at different frequency (10 kHz) as a reference. These images demonstrate the feasibility of mfEIT to monitor the frequency-dependent properties,  $\beta$ -dispersion in this case, of cell samples. The conductivity of cell-loaded samples increased as the applied frequency increased, which is an indication of the capacitive effects at the intact cell membranes, as is presented in Fig. 1. As a comparison, the blank hydrogel did not show significant conductivity changes depending on the frequency. Wu et al. (2018a) obtained similar results with blank and cell-loaded AlgiMatrix scaffold.

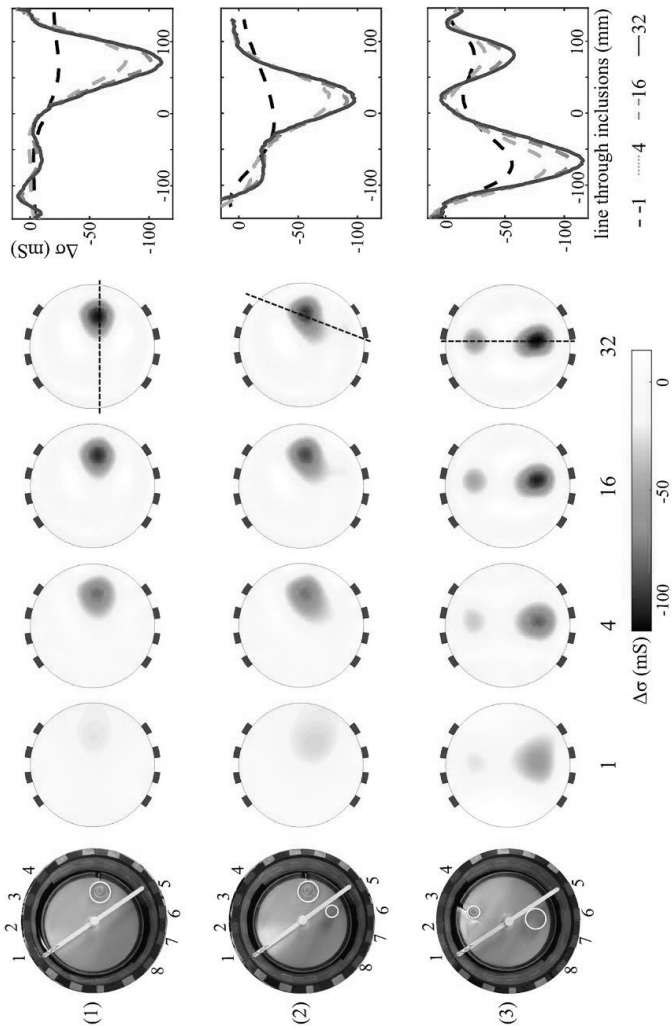
### 3.2 LAFR-rEIT imaging

To obtain novel and unique solution for multimodal imaging of cell and tissue cultures, the LAFR-rEIT approach has been studied both in a circular (Lehti-Polojärvi et al., 2018; Koskela et al., 2019) and a rectangular (Lehti-Polojärvi et al., 2019) EIT setup. The schematic in Fig. 10 shows the top view of an OPP4 + 4 electrode configuration. There are eight fixed electrodes placed around a rotated sample that is embedded in saline solution.

Time difference EIT was used to study the circular configuration with OPP4 + 4 electrodes, as is shown in Fig. 11 (Lehti-Polojärvi et al., 2018). This proof of concept study of the rotational EIT method was conducted in a 28-cm diameter EIT chamber with one excitation frequency (10 kHz) to demonstrate the feasibility of the LAFR-rEIT method. Measurements were conducted with KIT4 EIT device (Kourunen, 2014) applying all tetrapolar measurement combinations that included 28 excitations and 15 voltage measurements (420 in total) at each rotational position.



**Fig. 10** Rotational EIT built for multimodal systems; LAFR-rEIT schematic. Source: Lehti-Polojärvi, M., Koskela O., Seppänen A., Figueiras E., Hyttinen J., 2018. Rotational electrical impedance tomography using electrodes with limited surface coverage provides window for multimodal sensing. *Meas. Sci. Technol.* 29, 025401. <https://doi.org/10.1088/1361-6501/aa97f1>.



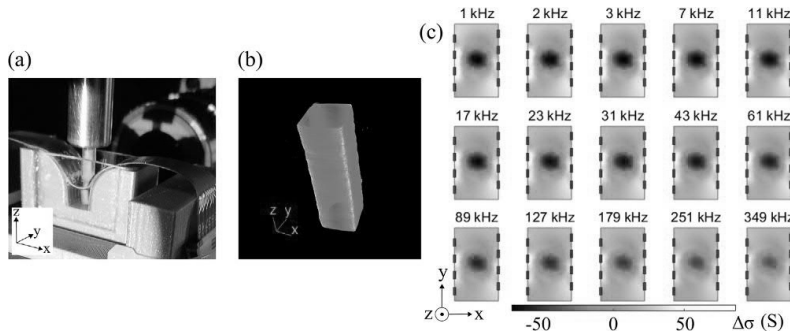
**Fig. 11** Experimental evaluation of a LAFR-rEIT setup with OPP4 + 4 electrode configuration and four different number of rotational positions: 1, 4, 16, and 32. Inclusions of interest are highlighted with white circles on the photographs. The dotted lines on the rightmost reconstructions show the location where the conductivity profiles are drawn from. Source: Lehti-Polojärvi, M., Koskela O., Seppänen A., Figueiras E., Hyttinen J., 2018. Rotational electrical impedance tomography using electrodes with limited surface coverage provides window for multimodal sensing. *Meas. Sci. Technol.* 29, 025401. <https://doi.org/10.1088/1361-6501/aa97f1>.

Four different amounts of rotational positions were evaluated with experimental data, as is shown in Fig. 11. According to Fig. 6, these measurements include high-sensitivity measurements both from the center and the edges of the sample. The imaged inclusions were insulating plastic tubes of different sizes that were pushed in the gelatin hydrogel. This gelatin phantom was manually rotated in saline solution for rotational EIT.

Fig. 11 shows experimental LAFR-rEIT results using data from 1, 4, 16, and 32 rotational measurement positions in 180 degrees rotation. Thus measurements were obtained with 0 degrees, 45 degrees, 11.25 degrees, and 5.625 degrees angular increments, respectively. The conductivity profiles along a line through the inclusion centers are shown for each experimental case. These evaluations show how beneficial the increment of rotational positions is when LAFR-rEIT setup is used. Most of the inclusions were already detected with four rotational measurement positions, but the image accuracy and contrast are enhanced as more rotational data are acquired. It can also be seen that rotations are needed in a limited angle setup because single-measurement position did not provide reasonable image quality.

LAFR-rEIT approach has been further integrated with optical projection tomography (OPT) (Sharpe et al., 2002; Figueiras et al., 2014), as is shown in Fig. 12 (Lehti-Polojärvi et al., 2019). OPT is commonly referred to as the optical version of X-ray computed tomography, and its working principle is indeed close. In OPT, several shadowgrams of light transmitted through the sample are recorded while rotating the sample. The attenuation coefficient distribution is then reconstructed similar to the conductivity distribution reconstruction in EIT. The attenuation coefficients are physically closely related to the mass of the sample, and, thus, the reconstruction can be interpreted as mass distribution of the sample. The golden standard of reconstruction methods in both X-ray computed tomography and OPT is filtered back-projection (Kak et al., 2002). OPT provides high spatial resolution in reconstruction of mesoscopic samples whose diameters are from 1 to 10 mm, and it has low impact on living tissues during image acquisition.

Integrating LAFR-rEIT with OPT is feasible with, for example, OPP4 + 4 electrode configuration (see Fig. 10). In practice, this was built to a rectangular chamber that was  $6 \times 9$  mm in XY-plane. The chamber had four electrodes on two opposing walls, and the other two walls were optically transparent glass walls, as is shown in Fig. 12A. This setup enables simultaneous electrical and optical imaging of a rotated sample. EIT measurements were acquired with Spectro-EIT device (Table 1), which obtained 15 frequencies simultaneously from each tetrapolar



**Fig. 12** Multifrequency LAFR-rEIT method integrated with optical imaging. (A) A rectangular carrot phantom rotated in saline solution in the center of a multimodal chamber (6 mm in  $x$ -direction and 9 mm in  $y$ -direction). OPT illumination is done through the glass walls and EIT measurements with electrodes on the other two chamber walls. (B) 3D OPT reconstruction and (C) time difference mFEIT reconstruction with 15 frequencies. Source: Lehti-Polojärvi, M., Koskela, O., Seppänen, A., Rist, M., Land, R., Annus, P., Min, M., Figueiras, E., Hyttinen, J., 2019. EIT in hybrid imaging setup for tissue engineering applications. In: Boyle, A., Aristovich, K., Witkowska-Wrobel, A., Holder, D. (Eds.), *Proceedings of the 20th International Conference on Biomedical Applications of Electrical Impedance Tomography. EIT2019*, 1–3 July 2019, London, UK. <https://doi.org/10.5281/zenodo.2691705>.

measurement. The excitation and measurement patterns were similar as the one with circular LAFR-rEIT results, including 420 measurements at each rotational position. Measurements were acquired every 10 degrees in full 360 degrees rotation; thus 36 rotational measurement positions were used in total. Optical bright-field transmission image was acquired every 0.9 degrees in 360 degrees rotation providing 400 projection images in total. Filtered back-projection algorithm was used to reconstruct the 3D volume. This simultaneous multimodal data acquisition was controlled by a modular Labview program (Yuan, 2020). The program synchronizes the data capture of OPT and EIT modalities according to a motorized rotation stage where the sample is attached to. A rectangular carrot ( $1.8 \times 1.6$  mm in  $XY$ -plane) was rotated in saline solution, and 3D OPT (Fig. 12B) and 2D time difference EIT (Fig. 12C) were reconstructed.

Spectral time difference EIT images in Fig. 12 visualized the conductivity spectrum of the carrot phantom and localized it correctly. OPT reconstruction provides structural information, such as size and shape of the phantom. The conductivity changes of the carrot phantom are in accordance with the spectrum in Fig. 8 (saline + carrot). This novel multimodal mFEIT-OPT approach is expected to be useful in cell and tissue culture studies, but it could be applied to various fields of science.

## 4 Conclusions

In this chapter, we have reviewed the mfEIT with application for in vitro cell and tissue culture applications that include the growing field of tissue engineering and organ-on-chip as well as body-on-chip studies. Its applications include monitoring of the cell proliferation or tissue growth, monitoring the well-being or contamination of the culture, cell movements, or migration and cell differentiation. We have also presented a novel solution for multimodal mfEIT for such samples. MfEIT and its use, especially for tissue-engineered 3D grafts or organ-on-chip systems is relatively new research field. Owing to this, there remain several technical challenges to be solved. In addition, cell biology and scaffold material research evolve rapidly causing new requirements for, for instance, sensor design.

The great advantages of EIT are its nonharmfulness to living organisms and flexibility regarding sample properties and electrode designs, although not all these benefits have yet been efficiently employed. Nonharmful property of EIT would make it a perfect tool for long-term in vitro assay monitoring, and few studies have reported monitoring of the samples for several days or weeks. EIT would be optimal for 3D monitoring solutions because of its diffusive nature and, as discussed in this chapter, the applied current density field can be optimized with electrode and lead selection to contain the whole volume. This is essential because commonly used planar electrode arrays have rather shallow detection areas and do not provide optimal measurements for 3D reconstruction. As demonstrated using the LAFR-rEIT method, EIT could be easily integrated with other measurement modalities to complement the obtained information of a sample.

In addition to complementing multimodal imaging, long-term monitoring of samples with EIT requires development of embedded incubation systems and sophisticated sensor fabrication. Open questions in development of such setups include the cytocompatibility and material corrosion requirements, which are high for a long-term cell and tissue culture EIT. Furthermore, electrodes and insulation materials need to be made nontoxic and stable with biomaterials and various mediums and chemicals for a long period of time. In addition, the application-specific needs may limit the range of suitable materials. For example, flexible sensors or optical transparency might be required. In addition to instrumentation development, computational methods, for example, the ones presented in Section 1.2, could be more efficiently applied for better image quality.



Overall, promising solutions have emerged for cell and tissue culture EIT that enable both conductivity imaging and fast imaging of frequency spectrum. Current research studies have shown that mEIT is able to detect and localize cellular effects, such as viability. Nevertheless, most studies are still in proof of concept stage, and rigorous studies showing the true benefits in monitoring cellular phenomena or long-term culture monitoring are lacking. This would require more validation studies involving other modalities, for example, optical imaging, for result verification. We expect the presented LAFR-rEIT method will provide novel tools for combining other imaging or measurement methods with the EIT. On the grounds of current research studies, we can state that mEIT shows great potential as a monitoring tool for toxicity and disease model studies and even for viability monitoring before tissue implantation.

## References

- Adler, A., Lionheart, W.R., 2006. Uses and abuses of EIDORS: an extensible software base for EIT. *Physiol. Measur.* 27 (5), S25. <https://doi.org/10.1088/0967-3334/27/5/S03>.
- Ahn, S., Jun, S.C., Seo, J.K., Lee, J., Woo, E.J., Holder, D., 2010. Frequency-difference electrical impedance tomography: phantom imaging experiments. *J. Phys. Conf. Ser.* 224. <https://doi.org/10.1088/1742-6596/224/1/012152>, 012152.
- Ahn, S., Wi, H., Oh, T.I., McEwan, A.L., Jun, S.C., Woo, E.J., 2014. Continuous non-destructive monitoring method using the reconstructed three-dimensional conductivity images via GREIT for tissue engineering. *J. Appl. Math.* <https://doi.org/10.1155/2014/562176>. Article ID 562176.
- Alsaker, M., Hamilton, S.J., Hauptmann, A., 2017. A direct D-bar method for partial boundary data electrical impedance tomography with a priori information. *Inverse Probl. Imaging* 11 (3), 427–454. <https://doi.org/10.3934/ipi.2017020>.
- Böttlich, M., Tanskanen, J.M., Hyttinen, J.A., 2017. Lead field theory provides a powerful tool for designing microelectrode array impedance measurements for biological cell detection and observation. *Biomed. Eng. Online* 16 (1), 85. <https://doi.org/10.1186/s12938-017-0372-5>.
- Boyle, A., 2019. Zedhat: an EIT tool library. In: Boyle, A., Aristovich, K., Witkowska-Wrobel, A., Holder, D. (Eds.), *Proceedings of the 20th International Conference on Biomedical Applications of Electrical Impedance Tomography. EIT2019*, 1–3 July 2019, London, UK., <https://doi.org/10.5281/zenodo.2691705>.
- Calvetti, D., McGivney, D., Somersalo, E., 2012. Left and right preconditioning for electrical impedance tomography with structural information. *Inverse Probl.* 28, 055015. <https://doi.org/10.1088/0266-5611/28/5/055015>.
- Canali, C., Heiskanen, A., Muhammad, H.B., Høyum, P., Pettersen, E.-J., Hemmingsen, M., Wolff, A., Dufva, M., Martinsen, Ø.G., Emnéus, J., 2015. Bioimpedance monitoring of 3D cell culturing—complementary electrode configurations for enhanced spatial sensitivity. *Biosens. Bioelectron.* 63, 72–79. <https://doi.org/10.1016/j.bios.2014.07.020>.
- Canhua, X., Dai, M., You, F., Shi, X., Fu, F., Liu, R., Dong, X., 2011. An optimized strategy for real-time hemorrhage monitoring with electrical impedance

- tomography. *Physiol. Meas.* 32 (5), 585–598. <https://doi.org/10.1088/0967-3334/32/5/007>.
- Cheney, M., Isaacson, D., Newel, J.C., 1999. Electrical impedance tomography. *SIAM Rev.* 41 (1), 85–101. <https://doi.org/10.1137/S0036144598333613>.
- Cheung, K., Gawad, S., Renaud, P., 2005. Impedance spectroscopy flow cytometry: on-chip label-free cell differentiation. *Cytometry* 65A, 124–132. <https://doi.org/10.1002/cyto.a.20141>.
- Crabb, M.G., Davidson, J.L., Little, R., Wright, P., Morgan, A.R., Miller, C.A., Naish, J.-H., Parker, G.J., Kikinis, R., McCann, H., Lionheart, W.R., 2014. Mutual information as a measure of image quality for 3D dynamic lung imaging with EIT. *Physiol. Meas.* 35 (5), 863–879. <https://doi.org/10.1088/0967-3334/35/5/863>.
- Daidi, Z., Siltanen, S., Tanskanen, J., Hyttinen, J., 2007. Using micro electrode array for on-line EIT measurement. In: Scharfetter, H., Merwa, R. (Eds.), *IFMBE Proceedings, 13th International Conference on Electrical Bioimpedance, and the 8th Conference on Electrical Impedance Tomography*, pp. 444–447. [https://doi.org/10.1007/978-3-540-73841-1\\_115](https://doi.org/10.1007/978-3-540-73841-1_115).
- Davidson, J.L., Little, R.A., Wright, P., Naish, J., Kikinis, R., Parker, G.J.M., McCann, H., 2012. Fusion of images obtained from EIT and MRI. *Electron. Lett.* 48 (11), 617–618. <https://doi.org/10.1049/el.2012.0327>.
- Dehghani, H., Soleimani, M., 2007. Numerical modelling errors in electrical impedance tomography. *Physiol. Meas.* 28 (7), S45.
- Fan, Y., Ying, L., 2020. Solving electrical impedance tomography with deep learning. *J. Comput. Phys.* 404. <https://doi.org/10.1016/j.jcp.2019.109119>, 09119.
- Fang, Y., Eglen, R.M., 2017. Three-dimensional cell cultures in drug discovery and development. *SLAS Discov.* 22 (5), 456–472. <https://doi.org/10.1177/1087057117696795>.
- Farnham, K.R., Murphy, E.K., Halter, R.J., 2019. EIT tissue growth monitor for 3D imaging of tissue viability. In: Boyle, A., Aristovich, K., Witkowska-Wrobel, A., Holder, D. (Eds.), *Proceedings of the 20th International Conference on Biomedical Applications of Electrical Impedance Tomography. EIT2019, 1–3 July 2019, London, UK*, <https://doi.org/10.5281/zenodo.2691705>.
- Figueiras, E., Soto, A.M., Jesus, D., Lehti, M., Koivisto, J., Parraga, J.E., Silva-Correia, J., Oliveira, J.M., Reis, R.L., Kellomäki, M., Hyttinen, J., 2014. Optical projection tomography as a tool for 3D imaging of hydrogels. *Biomed. Opt. Express* 5 (10), 3443–3449. <https://doi.org/10.1364/BOE.5.003443>.
- FIPS Computational Blog, Finnish Inverse Problems Society. Available from: <https://blog.fips.fi/tomography/eit/the-d-bar-method-for-electrical-impedance-tomography-simulated-data/>.
- Gabriel, S., Lau, R.W., Gabriel, C., 1996. The dielectric properties of biological tissues: II. Measurements in the frequency range 10 Hz to 20 GHz. *Phys. Med. Biol.* 41 (11), 2251–2269. <https://doi.org/10.1088/0031-9155/41/11/002>.
- Geselowitz, D.B., 1971. An application of electrocardiographic lead theory to impedance plethysmography. *IEEE Trans. Biomed. Eng.* 18 (1), 38–41. <https://doi.org/10.1109/tbme.1971.4502787>.
- Gomes, M.E., Rodrigues, M.T., Domingues, R.M.A., Reis, R.L., 2017. Tissue engineering and regenerative medicine: new trends and directions—a year in review. *Tissue Eng. Part B Rev.* 23 (3), 211–224. <https://doi.org/10.1089/ten.TEB.2017.0081>.
- Grychtol, B., Müller, B., Adler, A., 2016. 3D EIT image reconstruction with GREIT. *Physiol. Measur.* 37 (6), 785.
- Ha, H., Konijnenburg, M., Lukita, B., Wegberg, R., Xu, J., Hoven, R., Lemmens, M., Thoelen, R., Hoof, C., Helleputte, N., 2017. A bio-impedance readout IC with frequency sweeping from 1k-to-1MHz for electrical impedance tomography.

- In: 2017 Symposium on VLSI Circuits, Kyoto, pp. C174–C175, <https://doi.org/10.23919/VLSIC.2017.8008471>.
- Hallaji, M., Seppänen, A., Pour-Ghaz, M., 2014. Electrical impedance tomography-based sensing skin for quantitative imaging of damage in concrete. *Smart Mater. Struct.* 23, 085001. 13 pp. <https://doi.org/10.1088/0964-1726/23/8/085001>.
- Halonen, S., Kari, J., Ahonen, P., Kronström, K., Hyttinen, J., 2019. Real-time bioimpedance-based biopsy needle can identify tissue type with high spatial accuracy. *Ann. Biomed. Eng.* 47 (3), 836–851. <https://doi.org/10.1007/s10439-018-02187-9>.
- Hamilton, S.J., Hauptmann, A., 2018. Deep D-bar: real-time electrical impedance tomography imaging with deep neural networks. *IEEE Trans. Med. Imaging* 37 (10), 2367–2377.
- Harrach, B., Lee, E., Ullrich, M., 2015. Combining frequency-difference and ultrasound modulated electrical impedance tomography. *Inverse Probl.* 31. <https://doi.org/10.1088/0266-5611/31/9/095003>, 095003.
- He, Q., Rezaei, A., Pursiainen, S., 2019. Zeffiro user interface for electromagnetic brain imaging: a GPU accelerated FEM tool for forward and inverse computations in Matlab. *Neuroinformatics*, 1–14.
- Hildebrandt, C., Büth, H., Cho, S., Impidjati, Thielecke, H., 2010. Detection of the osteogenic differentiation of mesenchymal stem cells in 2D and 3D cultures by electrochemical impedance spectroscopy. *J. Biotechnol.* 148, 83–90. <https://doi.org/10.1016/j.jbiotec.2010.01.007>.
- Huang, C.-N., Yu, F.-M., Chung, H.-Y., 2007. Rotational electrical impedance tomography. *Meas. Sci. Technol.* 18, 2958. <https://doi.org/10.1088/0957-0233/18/9/028>.
- Huang, C.-N., Yu, F.-M., Chung, H.-Y., 2008. The scanning data collection strategy for enhancing the quality of electrical impedance tomography. *IEEE Trans. Instrum. Meas.* 57 (6), 1193–1198. <https://doi.org/10.1109/TIM.2008.915149>.
- Hyttinen, J.A.K., Malmivuo, J.A., Walker, S.J., 1993. Lead field of ECG leads calculated by a computer thorax model—an application of reciprocity. In: *Proceedings of Computers in Cardiology Conference*, London, UK, 1993, pp. 241–244, <https://doi.org/10.1109/CIC.1993.378459>.
- Jahnke, H.-G., Steel, D., Fleischer, S., Seidel, D., Kurz, R., Vinz, S., Dahlenborg, K., Sartipy, P., Robitzki, A.A., 2013. A novel 3D label-free monitoring system of hES-derived cardiomyocyte clusters: a step forward to in vitro cardiotoxicity testing. *PLoS ONE* 8 (7), e68971. <https://doi.org/10.1371/journal.pone.0068971>.
- Jehl, M., Dedner, A., Betcke, T., Aristovich, K., Klöfkom, R., Holder, D., 2014. A fast parallel solver for the forward problem in electrical impedance tomography. *IEEE Trans. Biomed. Eng.* 62 (1), 126–137.
- Jensen, B., Kirkeby, A., Knudsen, K., 2019. Feasibility of Acousto-Electric Tomography. *arXiv preprint arXiv: 1908.04215*.
- Kaipio, J.P., Kolehmainen, V., Vauhkonen, M., Somersalo, E., 1999. Inverse problems with structural prior information. *Inverse Probl.* 15, 713–729. <https://doi.org/10.1088/0266-5611/15/3/306>.
- Kaipio, J.P., Kolehmainen, V., Somersalo, E., Vauhkonen, M., 2000. Statistical inversion and Monte Carlo sampling methods in electrical impedance tomography. *Inverse Probl.* 16 (5), 1487. <https://doi.org/10.1088/0266-5611/16/5/321>.
- Kak, A.C., Slaney, M., Wang, G., 2002. Principles of computerized tomographic imaging. *Med. Phys.* 29, 107. <https://doi.org/10.1118/1.1455742>.
- Kang, S.I., Khambampati, A.K., Jeon, M.H., Kim, B.S., Kim, K.Y., 2016. A sub-domain based regularization method with prior information for human thorax imaging

- using electrical impedance tomography. *Meas. Sci. Technol.* 27. <https://doi.org/10.1088/0957-0233/27/2/025703>, 025703.
- Kauppinen, P., Hyttinen, J., Malmivuo, J., 1996. Calculation of impedance cardiography measurement sensitivity-application of reciprocity. *Med. Biol. Eng. Comput.* 34 (Suppl 1), 153–154.
- Kauppinen, P., Hyttinen, J., Malmivuo, J., 2005. Sensitivity distribution simulations of impedance tomography electrode combinations. *Int. J. Bioelectromagn. 7* (1), 344–347.
- Kauppinen, P., Hyttinen, J., Malmivuo, J., 2006. Sensitivity distribution visualizations of impedance tomography measurement strategies. *Int. J. Bioelectromagn. 8* (1), 63–71.
- Khan, T.A., Ling, S.H., 2019. Review on electrical impedance tomography: artificial intelligence methods and its applications. *Algorithms* 12 (5), 88.
- Klösgen, B., Rümenapp, C., Gleich, B., 2011. Bioimpedance spectroscopy. In: Boof-Bavnbeek, B., Klösgen, B., Larsen, J., Pociot, F., Renström, E. (Eds.), *BetaSys, Systems Biology 2*, second ed. Springer Science+Business Media, pp. 241–271, [https://doi.org/10.1007/978-1-4419-6956-9\\_11](https://doi.org/10.1007/978-1-4419-6956-9_11).
- Knudsen, K., Lassas, M., Mueller, J.L., Siltanen, S., 2009. Regularized D-bar method for the inverse conductivity problem. *Inverse Probl. Imaging* 3 (4), 599.
- Koskela, O., Lehti-Polojärvi, M., Seppänen, A., Figueiras, E., Hyttinen, J., 2019. Finite element mapping for efficient image reconstruction in rotational electrical impedance tomography. In: Lhotska, L., Sukupova, L., Lacković, I., Ibbott, G. (Eds.), *World Congress on Medical Physics and Biomedical Engineering 2018. IFMBE Proceedings 68/2*. Springer, Singapore, pp. 901–904, [https://doi.org/10.1007/978-981-10-9038-7\\_166](https://doi.org/10.1007/978-981-10-9038-7_166).
- Kourunen, J., 2014. Imaging of Mixing in Selected Industrial Processes Using Electrical Resistance Tomography. PhD thesis, University of Eastern Finland.
- Lee, E.J., Wi, H., McEwan, A.L., Farooq, A., Sohal, H., Woo, E.J., Seo, J.K., Oh, T.I., 2014. Design of a microscopic electrical impedance tomography system for 3D continuous non-destructive monitoring of tissue culture. *Biomed. Eng. Online* 13 (142). <https://doi.org/10.1186/1475-925X-13-142>.
- Lehti-Polojärvi, M., Koskela, O., Seppänen, A., Figueiras, E., Hyttinen, J., 2018. Rotational electrical impedance tomography using electrodes with limited surface coverage provides window for multimodal sensing. *Meas. Sci. Technol.* 29. <https://doi.org/10.1088/1361-6501/aa97f1>, 025401.
- Lehti-Polojärvi, M., Koskela, O., Seppänen, A., Rist, M., Land, R., Annus, P., Min, M., Figueiras, E., Hyttinen, J., 2019. EIT in hybrid imaging setup for tissue engineering applications. In: Boyle, A., Aristovich, K., Witkowska-Wrobel, A., Holder, D. (Eds.), *Proceedings of the 20th International Conference on Biomedical Applications of Electrical Impedance Tomography. EIT2019*, 1–3 July 2019, London, UK, <https://doi.org/10.5281/zenodo.2691705>.
- Lei, K.F., Wu, M.H., Hsu, C.W., Chen, Y.D., 2012. Electrical impedance determination of cancer cell viability in a 3-dimensional cell culture microfluidic chip. *Int. J. Electrochem. Sci.* 7, 12817–12828.
- Lei, K.F., Wu, M.H., Hsu, C.W., Chen, Y.D., 2014. Real-time and non-invasive impedance monitoring of cell proliferation and chemosensitivity in a perfusion 3D cell culture microfluidic chip. *Biosens. Bioelectron.* 51, 16–21. <https://doi.org/10.1016/j.bios.2013.07.031>.
- Lemmens, M., Biesmans, H., Bormans, S., Vandenryt, T., Thoelen, R., 2018. Electrical impedance tomography with a lab-on-chip for imaging cells in culture. *Phys. Status Solidi A* 215, 1700868. <https://doi.org/10.1002/pssa.201700868>.
- Leskinen, J., Neri, E., Neittaanmäki, P., 2009. Memetic variation local search vs. lifetime learning in electrical impedance tomography. In: Giacobini, M., et al.

- (Eds.), *Applications of Evolutionary Computing*. EvoWorkshops 2009. Lecture Notes in Computer Science. vol. 5484. Springer, Berlin, Heidelberg, [https://doi.org/10.1007/978-3-642-01129-0\\_71](https://doi.org/10.1007/978-3-642-01129-0_71).
- Liang, G., Ren, S., Dong, F., 2020. A shape-based statistical inversion method for EIT/URT dual-modality imaging. *IEEE Trans. Image Process.* 29, 4099–4113. <https://doi.org/10.1109/TIP.2020.2969077>.
- Linderholm, P., Marescot, L., Loke, M.H., Renaud, P., 2008. Cell culture imaging using microimpedance tomography. *IEEE Trans. Biomed. Eng.* 55 (1), 138–146. <https://doi.org/10.1109/TBME.2007.910649>.
- Liu, Q., Oh, T.I., Wi, H., Lee, E.J., Seo, J.K., Woo, E.J., 2011. Design of a microscopic electrical impedance tomography system using two current injections. *Physiol. Meas.* 32, 1505–1516. <https://doi.org/10.1088/0967-3334/32/9/011>.
- Liu, D., Kolehmainen, V., Siltanen, S., Laukkanen, A.-M., Seppänen, A., 2015a. Estimation of conductivity changes in a region of interest with electrical impedance tomography. *Inverse Probl. Imaging* 9 (1), 211–229. <https://doi.org/10.3934/ipi.2015.9.211>.
- Liu, D., Kolehmainen, V., Siltanen, S., Seppänen, A., 2015b. A nonlinear approach to difference imaging in EIT; assessment of the robustness in the presence of modelling errors. *Inverse Probl.* 31 (3), 035012. <https://doi.org/10.1088/0266-5611/31/3/035012>.
- Liu, D., Kolehmainen, V., Siltanen, S., Laukkanen, A., Seppänen, A., 2016. Nonlinear difference imaging approach to three-dimensional electrical impedance tomography in the presence of geometric modeling errors. *IEEE Trans. Biomed. Eng.* 63 (9), 1956–1965. <https://doi.org/10.1109/TBME.2015.2509508>.
- Liu, D., Zhao, Y., Khambampati, A.K., Seppänen, A., Du, J., 2018. A parametric level set method for imaging multiphase conductivity using electrical impedance tomography. *IEEE Trans. Comput. Imaging* 4 (4), 552–561. <https://ieeexplore.ieee.org/document/8425727>.
- Malmivuo, J., Plonsey, R., 1995. *Bioelectromagnetism: Principles and Application of Bioelectric and Biomagnetic Fields*. Oxford University Press, New York. Available from: [www.bem.fi/book/](http://www.bem.fi/book/).
- McFee, R., Johnston, F.D., 1953. Electrocardiographic leads: I. introduction. *Circulation* 8 (4), 554–568.
- Mernier, G., Piacentini, N., Tornay, R., Buffi, B., Renaud, P., 2011. Cell viability assessment by flow cytometry using yeast as cell model. *Sensors Actuators B Chem.* 154 (2), 160–163. <https://doi.org/10.1016/j.snb.2009.11.066>.
- Min, M., Lehti-Polojärvi, M., Hyttinen, J., Rist, M., Land, R., Annus, P., 2018. Bioimpedance spectro-tomography system using binary multifrequency excitation. *Int. J. Bioelectromagn.* 20 (1), 76–79. <https://doi.org/10.18154/RWTH-CONV-224930>.
- Mueller, J.L., Siltanen, S. (Eds.), 2012. *Linear and Nonlinear Inverse Problems with Practical Applications*. Society for Industrial and Applied Mathematics.
- Murphy, S., York, T., 2006. Electrical impedance tomography with non-stationary electrodes. *Meas. Sci. Technol.* 17, 3042. <https://doi.org/10.1088/0957-0233/17/11/025>.
- Murphy, E.K., Mahara, A., Halter, R.J., 2017. Absolute reconstructions using rotational electrical impedance tomography for breast cancer imaging. *IEEE Trans. Med. Imaging* 36 (4), 892–903. <https://doi.org/10.1109/TMI.2016.2640944>.
- Murphy, E.K., Wu, X., Halter, R.J., 2018. Fused-data transrectal EIT for prostate cancer imaging. *Physiol. Meas.* 39 (5). <https://doi.org/10.1088/1361-6579/aaaf22,054005>.
- Murphy, E.K., Skinner, J., Martucci, M., Rutkove, S.B., Halter, R.J., 2019. Toward electrical impedance tomography coupled ultrasound imaging for assessing muscle

- health. *IEEE Trans. Med. Imaging* 38 (6), 1409–1419. <https://doi.org/10.1109/TMI.2018.2886152>.
- Oh, T.I., Woo, E.J., Holder, D., 2007. Multi-frequency EIT system with radially symmetric architecture: KHU Mark1. *Physiol. Meas.* 28, S183.
- Olmi, R., Bini, M., Priori, S., 2000. A genetic algorithm approach to image reconstruction in electrical impedance tomography. *IEEE Trans. Evol. Comput.* 4 (1), 83–88. <https://doi.org/10.1109/4235.843497>.
- Onnela, N., Savolainen, V., Juuti-Uusitalo, K., Vaajasaari, H., Skottman, H., Hyttinen, J., 2012. Electric impedance of human embryonic stem cell-derived retinal pigment epithelium. *Med. Biol. Eng. Comput.* 50 (2), 107–116. <https://doi.org/10.1007/s11517-011-0850-z>.
- Ren, S., Sun, K., Liu, D., Dong, E., 2019. A statistical shape-constrained reconstruction framework for electrical impedance tomography. *IEEE Trans. Med. Imaging* 38 (10), 2400–2410. <https://doi.org/10.1109/TMI.2019.2900031>.
- Savolainen, V., Juuti-Uusitalo, K., Onnela, N., Vaajasaari, H., Narkilahti, S., Suuronen, R., Skottman, H., Hyttinen, J., 2011. Impedance spectroscopy in monitoring the maturation of stem cell-derived retinal pigment epithelium. *Ann. Biomed. Eng.* 39 (12), 3055–3069. <https://doi.org/10.1007/s10439-011-0387-1>.
- Sciospec Scientific Instruments GmbH, Sciospec Solutions for Electrical Impedance Tomography. Available from: <https://www.sciospec.de/product/eit-8-16/>.
- Seppänen, A., Hallaji, M., Pour-Ghaz, M., 2014. Electrical impedance tomography-based sensing skin for detection of damage in concrete. In: *Proceedings of the 11th European Conference on Non-Destructive Testing (ECNDT 2014)*, Prague, Czech Republic, pp. 6–10.
- Sharpe, J., Ahlgren, U., Perry, P., Hill, B., Ross, A., Hecksher-Sørensen, J., Baldock, R., Davidson, D., 2002. Optical projection tomography as a tool for 3D microscopy and gene expression studies. *Science* 296 (5567), 541–545. <https://doi.org/10.1126/science.1068206>.
- Smyl, D., Pour-Ghaz, M., Seppänen, A., 2018. Detection and reconstruction of complex structural cracking patterns with electrical imaging. *NDT & E Int.* 99, 123–133. <https://doi.org/10.1016/j.ndteint.2018.06.004>.
- Soleimani, M., 2006. Electrical impedance tomography imaging using a priori ultrasound data. *Biomed. Eng. Online* 5 (8). <https://doi.org/10.1186/1475-925X-5-8>.
- Somersalo, E., Cheney, M., Isaacson, D., 1992. Existence and uniqueness for electrode models for electric current computed tomography. *SIAM J. Appl. Math.* 52 (4), 1023–1040.
- Steiner, G., Soleimani, M., Watzneg, D., 2008. A bio-electromechanical imaging technique with combined electrical impedance and ultrasound tomography. *Physiol. Meas.* 29 (6), S63. <https://doi.org/10.1088/0967-3334/29/6/S06>.
- Sun, T., Tsuda, S., Zauner, K.-P., Morgan, H., 2010. On-chip electrical impedance tomography for imaging biological cells. *Biosens. Bioelectron.* 25, 1109–1115. <https://doi.org/10.1016/j.bios.2009.09.036>.
- Tervonen, A., Hyttinen, J., 2018. Sensitivity distribution of electrical impedance epithelial measurement systems. In: Eskola, H., Väisänen, O., Viik, J., Hyttinen, J. (Eds.), *EMBEC & NBC 2017*. EMBEC 2017, NBC 2017. IFMBE Proceedings, vol. 65. Springer, Singapore, [https://doi.org/10.1007/978-981-10-5122-7\\_156](https://doi.org/10.1007/978-981-10-5122-7_156).
- Vauhkonen, M., 1997. *Electrical Impedance Tomography and Prior Information*. PhD thesis, Kuopio University, Finland.
- Wan, Y., Halter, R., Borsic, A., Manwaring, P., Hartov, A., Paulsen, K., 2010. Sensitivity study of an ultrasound coupled transrectal electrical impedance tomography

- system for prostate imaging. *Physiol. Meas.* 31 (8), S17–S29. <https://doi.org/10.1088/0967-3334/31/8/S02>.
- Wei, Z., Liu, D., Chen, X., 2019. Dominant-current deep learning scheme for electrical impedance tomography. *IEEE Trans. Biomed. Eng.* 66 (9), 2546–2555. <https://doi.org/10.1109/TBME.2019.2891676>.
- Weiz, S.M., Medina-Sánchez, M., Lee, K., Schmidt, O.G., 2017a. Electrical impedance tomography in on-chip integrated microtubular fluidic channels. In: Boyle, A., Halter, R., Murphy, E., Adler, A. (Eds.), *Proceedings of the 18th International Conference on Biomedical Applications of Electrical Impedance Tomography. EIT2017*, 21–24 June, 2017, Dartmouth, USA., <https://doi.org/10.5281/zenodo.892679>.
- Weiz, S.M., Medina-Sánchez, M., Schmidt, O.G., 2017b. Single-cell analysis with rolled-up tomography devices. In: *NanoBioSensors Conference*, 4–5 September, 2017, Dresden, Germany. Available from: <https://cfaed.tu-dresden.de/nanobiosensors-program>. (Accessed 31 August 2020).
- Wu, H., Zhou, W., Yang, Y., Jia, J., Bagnaninchi, P., 2018a. Exploring the potential of electrical impedance tomography for tissue engineering applications. *Materials (Basel)* 11 (6), 930. <https://doi.org/10.3390/ma11060930>.
- Wu, H., Yang, Y., Bagnaninchi, P.O., Jia, J., 2018b. Electrical impedance tomography for real-time and label-free cellular viability assays of 3D tumour spheroids. *Analyst* 143 (17), 4189–4198. <https://doi.org/10.1039/c8an00729b>.
- Yang, Y., Jia, J., 2017. A multi-frequency electrical impedance tomography system for real-time 2D and 3D imaging. *Rev. Sci. Instrum.* 88 (8). <https://doi.org/10.1063/1.4999359>, 085110.
- Yang, Y., Jia, J., Smith, S., Jamil, N., Gamal, W., Bagnaninchi, p., 2017. A miniature electrical impedance tomography sensor and 3-D image reconstruction for cell imaging. *IEEE Sensors J.* 17 (2), 514–523. <https://doi.org/10.1109/JSEN.2016.2631263>.
- Yang, Y., Wu, H., Jia, J., Bagnaninchi, P., 2019. Scaffold-based 3-D cell culture imaging using a miniature electrical impedance tomography sensor. *IEEE Sensors J.* 19 (20), 9071–9080. <https://doi.org/10.1109/JSEN.2019.2924154>.
- Yerworth, R.J., Bayford, R.H., Cusick, G., Conway, M., Holder, D.S., 2002. Design and performance of the UCLH mark 1b 64 channel electrical impedance tomography (EIT) system, optimized for imaging brain function. *Physiol. Meas.* 23 (1), 149–158. <https://doi.org/10.1088/0967-3334/23/1/314>.
- Yin, X., Wu, H., Jia, J., Yang, Y., 2018. A micro EIT sensor for real-time and non-destructive 3-D cultivated cell imaging. *IEEE Sensors J.* 18 (13), 5402–5412. <https://doi.org/10.1109/JSEN.2018.2834509>.
- York, T., Sun, L., Gregory, C., Hatfield, J., 2004. Silicon-based miniature sensor for electrical tomography. *Sensors Actuators A Phys.* 110 (1–3), 213–218. <https://doi.org/10.1016/j.sna.2003.08.012>.
- Yuan, Q., 2020. A Modular LabVIEW Program for Controlling Multimodal Microscope Imaging Platform. MSc thesis, Tampere University, Finland. Available from: <http://urn.fi/URN:NBN:fi:tuni-202004284176>.
- Zhang, X., Chatwin, C., Barber, D.C., 2015. A feasibility study of a rotary planar electrode array for electrical impedance mammography using a digital breast phantom. *Physiol. Meas.* 36, 1311–1335. <https://doi.org/10.1088/0967-3334/36/6/1311>.
- Zhou, W., Graham, K., Lucendo-Villarín, B., Flint, O., Hay, D.C., Bagnaninchi, P., 2019. Combining stem cell-derived hepatocytes with impedance sensing to better predict human drug toxicity. *Expert Opin. Drug Metab. Toxicol.* 15 (1), 77–83. <https://doi.org/10.1080/17425255.2019.1558208>.





# PUBLICATION IV

## **Retrieval of the conductivity spectrum of tissues *in vitro* with novel multimodal tomography**

Mari Lehti-Polojärvi, Mikko J Räsänen, Leena E Viiri, Hanna Vuorenpää, Susanna Miettinen, Aku Seppänen, Jari Hyttinen

Physics in Medicine & Biology 66 (2021) 205016  
<https://doi.org/10.1088/1361-6560/ac2b7f>

**Publication is licensed under a Creative Commons Attribution 4.0 International (CC BY 4.0)**





## PAPER

Retrieval of the conductivity spectrum of tissues *in vitro* with novel multimodal tomography

## OPEN ACCESS

## RECEIVED

11 May 2021

## REVISED

22 September 2021

## ACCEPTED FOR PUBLICATION

29 September 2021

## PUBLISHED

14 October 2021

M Lehti-Polojärvi<sup>1,3,\*</sup>, M J Räsänen<sup>2,3</sup>, L E Viiri<sup>1</sup>, H Vuorenpää<sup>1</sup>, S Miettinen<sup>1</sup>, A Seppänen<sup>2</sup> and J Hyttinen<sup>1</sup><sup>1</sup> Faculty of Medicine and Health Technology, Tampere University, Tampere, Finland<sup>2</sup> Department of Applied Physics, University of Eastern Finland, Kuopio, Finland<sup>3</sup> Authors contributed equally.

\* Author to whom any correspondence should be addressed.

E-mail: [mari.lehti-polojarvi@tuni.fi](mailto:mari.lehti-polojarvi@tuni.fi) and [mikko.rasanen@uef.fi](mailto:mikko.rasanen@uef.fi)**Keywords:** electrical impedance tomography (EIT), hybrid imaging, limited angle tomography, optical projection tomography (OPT), rotational multifrequency electrical impedance tomography (R-mfEIT), tissue engineering

Supplementary material for this article is available online

Original content from this work may be used under the terms of the Creative Commons Attribution 4.0 licence.

Any further distribution of this work must maintain attribution to the author(s) and the title of the work, journal citation and DOI.

**Abstract**

**Objective:** Imaging of tissue engineered three-dimensional (3D) specimens is challenging due to their thickness. We propose a novel multimodal imaging technique to obtain multi-physical 3D images and the electrical conductivity spectrum of tissue engineered specimens *in vitro*. **Approach:** We combine simultaneous recording of rotational multifrequency electrical impedance tomography (R-mfEIT) with optical projection tomography (OPT). Structural details of the specimen provided by OPT are used here as geometrical priors for R-mfEIT. **Main results:** This data fusion enables accurate retrieval of the conductivity spectrum of the specimen. We demonstrate experimentally the feasibility of the proposed technique using a potato phantom, adipose and liver tissues, and stem cells in biomaterial spheroids. The results indicate that the proposed technique can distinguish between viable and dead tissues and detect the presence of stem cells. **Significance:** This technique is expected to become a valuable tool for monitoring tissue engineered specimens' growth and viability *in vitro*.

**1. Introduction**

Multifrequency electrical impedance tomography (mfEIT) is an imaging technique that reconstructs electrical conductivity images based on surface current excitations and voltage measurements acquired at several frequencies. This imaging technique could find significant applications in the field of tissue engineering, where three-dimensional (3D) biomaterial constructs are combined with stem cell-derived cells. These constructs show great potential in *in vitro* disease models, toxicology studies, drug development, and precision medicine (Fang and Eglén 2017, Gomes *et al* 2017). The imaging of mesoscopic scale (1 mm to 10 mm) 3D specimens is challenging using conventional optical microscopy techniques due to limited penetration depth. Additionally, many of these techniques require staining or clearing the specimens, which eventually kills the cells and renders the biological specimens unusable for further study. For example, an x-ray microtomography method to image the subcellular structures of 3D specimens has been proposed, but the method is only available for fixed specimens (Tamminen *et al* 2020). In order to create novel technologies for non-harmful live 3D imaging, we propose a multimodal tool in which mfEIT is integrated with optical projection tomography (OPT).

In OPT (Sharpe *et al* 2002), multiple projection images are acquired from a rotating specimen to enable full 3D image reconstruction. OPT has been applied to, for example, the characterization of hydrogels (Figueiras *et al* 2014) and the imaging of cells in 3D hydrogels (Belay *et al* 2021). OPT operates in either brightfield or fluorescence mode. Since fluorescence imaging requires autofluorescent or stained specimens, we focus on applying brightfield, i.e. transmission OPT.

Electrical impedance measurements, either spectroscopic or tomographic, do not require staining to obtain information on, for example, cell membrane integrity (Klösgen *et al* 2011), cell–cell contact maturation (Savolainen *et al* 2011), or cell aggregate localization (Wu *et al* 2018). EIT, or in case several frequencies are applied, mFEIT, images the electrical conductivity distribution (absolute mode) or its temporal changes (difference mode). EIT is a non-harmful and fast 3D imaging technique that has been used for the viability detection of cell cultures (Wu *et al* 2018).

The limitation of EIT is typically poor spatial resolution due to its diffusive nature and the associated mathematical ill-posedness of the image reconstruction problem. To tackle this, multimodal imaging techniques have been proposed, where *a priori* information provided by another imaging modality is incorporated into the EIT image reconstruction (Kaipio *et al* 1999). In medical imaging, ultrasound images have been successfully used as a structural prior, for example in Borsic *et al* (2010), Soleimani (2006). A dual-modal sensor that combines EIT and optical microscopy has been presented for *in vitro* applications (Liu *et al* 2020).

We aim to provide multi-physical images and enhanced mFEIT image quality via prior information provided by OPT. We are unaware of previous studies that would have attempted to combine microscopy-scale, optical-based 3D imaging, such as OPT, with mFEIT to perform *in vitro* specimen conductivity analysis. In our system, mFEIT and OPT data are collected simultaneously. The electrode array used for mFEIT covers only a limited portion of the imaging chamber's surface to allow access for OPT acquisition. The problem associated with having only limited angle access to the boundary—both in OPT and mFEIT—is resolved by rotating the specimen step-wise and carrying out the measurements sequentially at multiple rotational positions.

The feasibility of the rotational EIT setup with limited electrode coverage has previously been demonstrated in a two-dimensional (2D) circular setup (Lehti-Polojärvi *et al* 2018) and a 2D rectangular setup (Lehti-Polojärvi *et al* 2019, Winkler *et al* 2020, Lehti-Polojärvi *et al* 2021) using phantoms. In these studies, however, the structural information provided by OPT had not been fused into the mFEIT reconstruction. Further, mFEIT was based on 2D modeling and linearized difference imaging and yielded only qualitative reconstructions of the conductivity. Nevertheless, these studies have demonstrated that the rotational limited angle data acquisition scheme enables the EIT/mFEIT reconstruction while also providing space for OPT. In addition to multimodality, the benefits of this EIT scheme are that it enables a large number of independent measurements and reduces the complexity of the electronics, as a relatively small number of electrodes are needed.

In this study, we extend the rotational mFEIT (R-mFEIT) impedance measurement setup and image reconstruction methods to 3D and, above all, combine data from two imaging modalities by utilizing the structural information from OPT to enhance the conductivity reconstruction in R-mFEIT. This data fusion is achieved by extracting 3D segmentation from OPT reconstructions and incorporating this information into 3D R-mFEIT image reconstruction using rotational meshing and Bayesian inversion methods, finally yielding estimates for the electrical conductivity spectra of the segments.

We test the feasibility of the proposed multimodal technique experimentally. First, the imaging technique is evaluated with a potato inclusion with a controlled shape and known frequency response. Next, the ability of OPT-mFEIT to differentiate the conditions of tissues (especially their viability) is tested by imaging specimens of adipose and liver tissues before and after chemical or thermal treatment. Finally, we carry out a preliminary experiment on human induced pluripotent stem cells (iPSCs) in biomaterial spheroids—an application that will in future be the main target of the developed multimodal imaging system.

## 2. Methods and materials

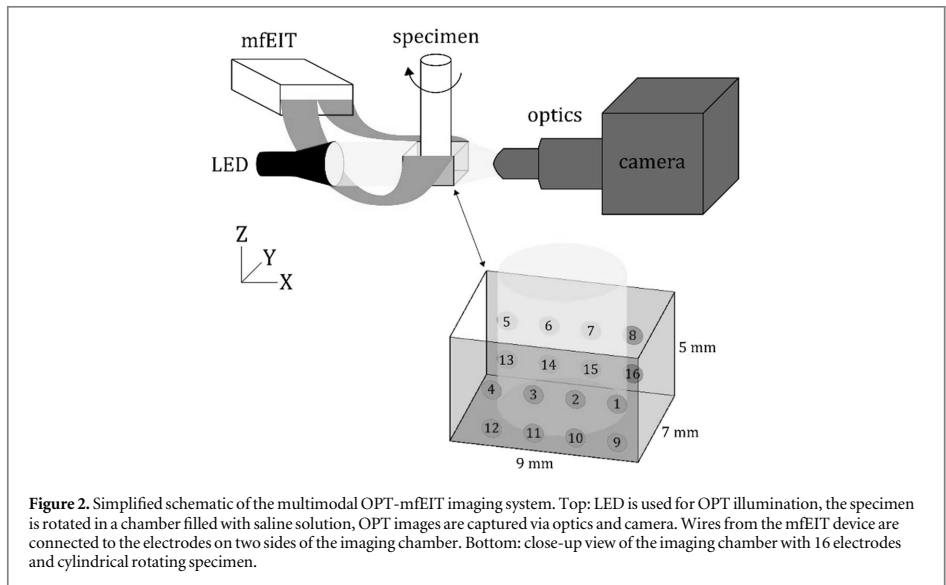
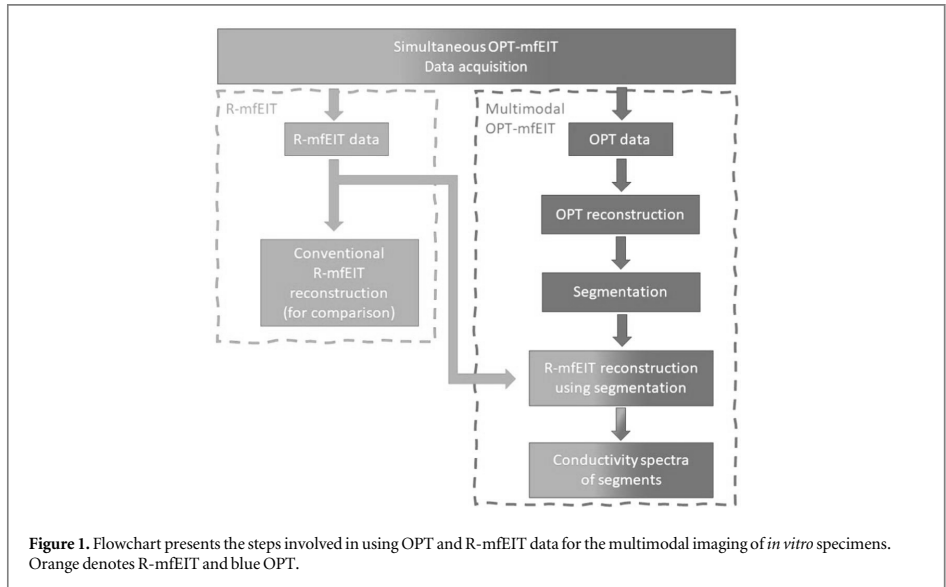
### 2.1. Overview of the multimodal imaging

Figure 1 summarizes the steps used in multimodal OPT-mFEIT imaging. The raw R-mFEIT data consist of electrical impedance values and OPT data consist of 2D projection images acquired from several rotational positions. The R-mFEIT data was used both for conventional R-mFEIT reconstruction and for multimodal OPT-mFEIT reconstruction. The conventional R-mFEIT reconstruction served as a comparison to the integrated OPT-mFEIT reconstruction approach, and as a check of the quality of the measured R-mFEIT data.

OPT data were used for reconstructing the light absorption distribution within the imaging domain. The 3D OPT reconstruction was segmented to extract the morphology and location of the specimen. The segmentation was then integrated into the R-mFEIT reconstruction process in order to directly estimate the conductivity spectra of the segmented regions from the R-mFEIT data.

### 2.2. Multimodal system design

Our R-mFEIT technique was designed to be combined with an in-house-built OPT system (Figueiras *et al* 2014, Belay *et al* 2021). A schematic of the OPT-mFEIT system is shown in figure 2.



The main parts of OPT are illumination, specimen rotation stage, and light detection. We used a white LED (irradiance maximum  $2.8 \text{ mW cm}^{-2}$ ) for brightfield parallel beam illumination. The specimens were attached from the top to a motorized stage (Standa Ltd, Lithuania) with rotational and  $x$ - $y$ - $z$  movements for proper specimen alignment. The imaging chamber had two transparent glass walls for OPT, and it was filled with saline solution. Saline was used to enable both a refractive index matching path for illumination and suitable electrical conductivity between the electrodes and the specimen. The optical detection system consisted mainly of a  $2\times$  objective lens (Edmund Optics, USA), an iris diaphragm (Thorlabs, USA), a tube lens (Mitutoyo, USA), and an sCMOS camera (ORCA-Flash 4.0, Hamamatsu, Japan).

Fluorinated ethylene propylene (FEP) tubes (5 mm inner diameter, 6 mm outer diameter, Adtech Polymer Engineering Ltd, UK) were used to attach the hydrogel-based specimen to the rotational stage. To allow electrical contact, approximately 3 mm of the hydrogel with the embedded inclusion(s) was pushed out of the insulating tube during imaging.

An mfEIT device that generates binary multifrequency excitation (Min *et al* 2018) was used for impedance measurements. The current excitations were carried out using 15 frequencies ranging from 1 to 349 kHz, which is typically in the  $\beta$ -dispersion region of biological samples (Klösgen *et al* 2011). The device had a multiplexer with 16 bi-directional input/output channels for tetrapolar impedance measurements.

mEIT electrodes were fabricated on two flexible Kapton-based sheets and attached to two opposing walls of the rectangular imaging chamber. These 16 electrodes (1  $\mu\text{m}$  copper coated with 50 nm gold layer), shown in figure 2, were connected to the mfEIT device via zero insertion force connectors (Würth Elektronik, Germany) and wires that were as short as possible to reduce noise.

### 2.3. Rotational data acquisition

Simultaneous OPT-mfEIT data acquisitions were performed with a custom-made LabVIEW program (Yuan 2020). OPT images were acquired every  $0.9^\circ$  over  $360^\circ$  rotation, and the R-mfEIT measurements were saved at  $4.5^\circ$  intervals.

The measurement pattern applied at every R-mfEIT rotational position was designed for our limited angle electrode layout (see figure 2). The pattern contained 30 pairwise current excitation configurations and 13 pairwise voltage measurements for each excitation, providing 390 tetrapolar measurements. The first 15 excitations were applied sequentially between electrode 2 and each of the other 15 electrodes. Correspondingly, in the second set of excitations, currents were injected between electrode 14 and the other 15 electrodes. Voltage measurements were obtained sequentially between the electrode adjacent to the current excitation electrode and the rest of the electrodes. Current excitation electrodes were not included in the voltage sensing. The measurement pattern is visualized in supplementary materials (available online at [stacks.iop.org/PMB/66/205016/mmedia](https://stacks.iop.org/PMB/66/205016/mmedia)). The design of the current excitation and voltage measurement configurations was based on the lead field theory (Geselowitz 1971) to obtain measurement patterns with high sensitivity in the entire volume of the specimen.

Total data acquisition time depended on several factors, such as camera exposure time, the number of measurement angles, and the number of repeated impedance measurements for averaging. We used an exposure time of approximately 1.2 ms, and the number of projection images taken for OPT was 400. For R-mfEIT, measurements were collected from 80 rotational positions, resulting in  $80 \times 390 = 31\,200$  measurements. Each tetrapolar measurement was taken as the average of seven repeated measurements, resulting in a measuring time of 10 ms for each measurement. With these settings, the total imaging time was approximately 15 min. We note, however, that the amount of data acquired here was excessive and was only measured to ensure that no relevant information was lost in the experiment. Only the R-mfEIT data corresponding to the latter half of the full rotation were used in the image reconstruction.

For each R-mfEIT data acquisition, a reference measurement with only saline present in the imaging chamber was taken. The OPT projections and measured R-mfEIT data are visualized for each specimen type in supplementary materials. The real part of the measured impedance values  $Z$  was converted to voltages  $U$  with 1 mA current  $I$ , as  $U = \text{Re}(Z)I$ . The videos show the difference between the angular data and the initial position data to clarify the changes due to rotation.

### 2.4. Estimation of noise statistics

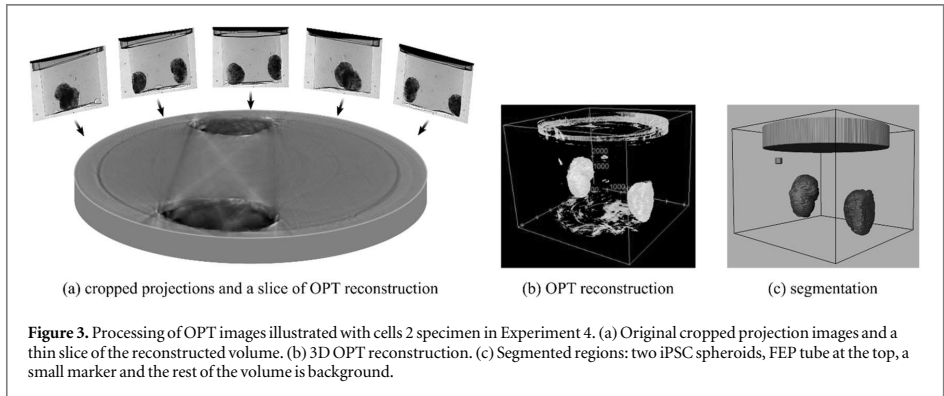
An estimate for the level of the overall noise introduced by the electrodes, wiring, and the mfEIT device was obtained from 1000 repeated blank saline solution measurements in the imaging chamber. The signal-to-noise ratio (SNR) of the R-mfEIT imaging system was calculated as follows:

$$\text{SNR} = 10 \log \frac{\sum_{n=1}^N [y(n)]^2}{\sum_{n=1}^N [y(n) - \bar{y}]^2}, \quad (1)$$

where  $N = 1000$  is the number of repeated measurements,  $y(n)$  the  $n$ th measured voltage value, and  $\bar{y}$  the average of  $N$  repeated voltage data. The SNR value depends on the measurement configuration, that is, the relative positions of the excitation and measurement electrodes and the applied frequency. For a low sensitivity configuration, the minimum SNR was  $(5 \pm 2)$  dB, and for a high sensitivity configuration, the maximum SNR was  $(55 \pm 3)$  dB. According to the applied frequency, the minimum SNR was  $(32 \pm 9)$  dB at 1 kHz and the maximum was  $(40 \pm 9)$  dB at 251 kHz.

The reciprocity error is another commonly used metric to evaluate the accuracy of EIT systems. It was calculated from two tetrapolar measurements that applied the same electrodes but interchanged current excitation and voltage measurement pairs. The repeated measurements' percentage error was between 0.1% and 0.7%, depending on the applied frequency.

The covariance of the measurement noise was also estimated for each frequency based on the same repeated measurements. The sample covariance for measurements at given frequency  $f$  was the following:



**Figure 3.** Processing of OPT images illustrated with cells 2 specimen in Experiment 4. (a) Original cropped projection images and a thin slice of the reconstructed volume. (b) 3D OPT reconstruction. (c) Segmented regions: two iPSC spheroids, FEP tube at the top, a small marker and the rest of the volume is background.

$$\Gamma_e^f = \frac{1}{N-1} \sum_{i=1}^N (V_i^f - V_*^f)(V_i^f - V_*^f)^T, \quad (2)$$

where the superscript  $f$  refers to the frequency, vector  $V_i^f$  is the  $i$ th realization of the complete set of voltage measurements corresponding to all injected currents at frequency  $f$ , and vector  $V_*^f$  is the mean of the repeated voltage measurements. The noise covariance matrix was used when computing the R-mfEIT reconstructions.

### 2.5. OPT image reconstruction and segmentation

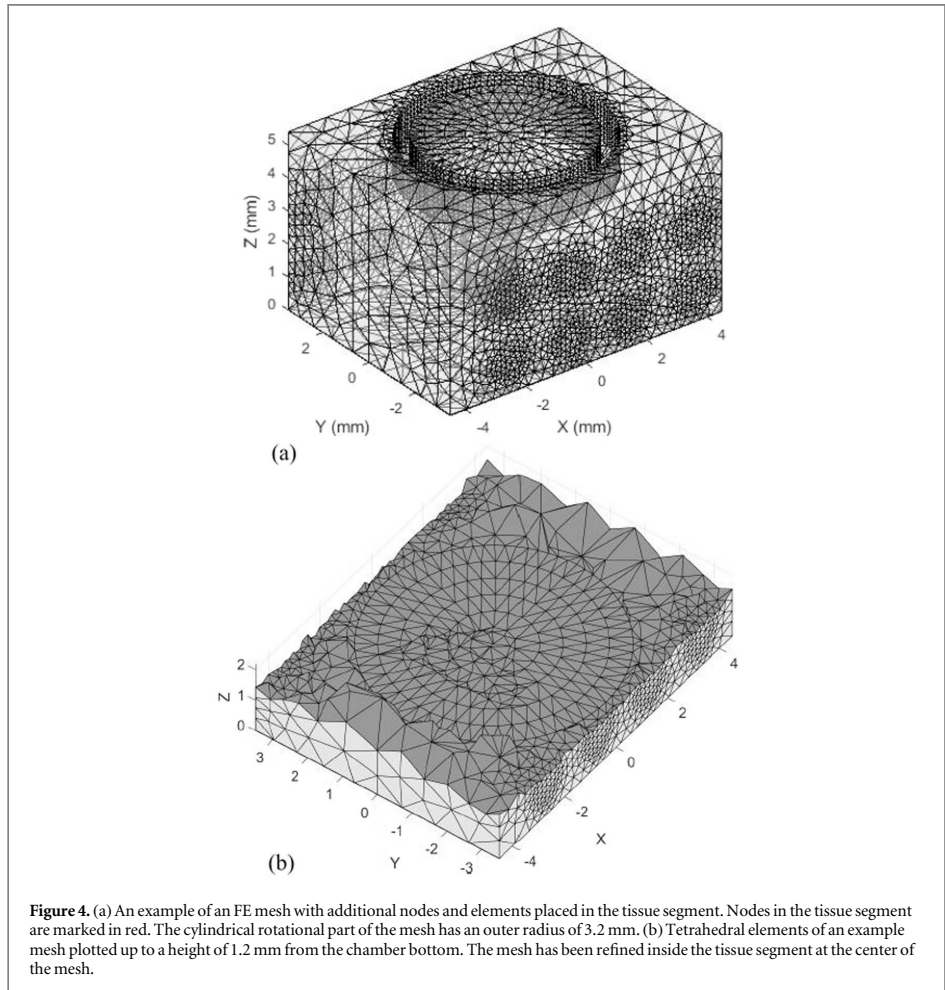
Before computing OPT reconstructions, the R-mfEIT chamber walls were cropped from the sides and bottom of the projection images to save memory. Possible offsets in the specimen's center-of-rotation were manually corrected. This was achieved by reconstructing the top and bottom slices of the specimen with different offset values and visually choosing the best values for each specimen, as in Koskela *et al* (2021). The center-of-rotation was corrected for the rest of the volume by interpolating the top and bottom offsets, as is explained in Figueiras *et al* (2014). OPT reconstructions were computed using a filtered back-projection algorithm (Natterer 2001) implemented in the built-in function `iradon` of MATLAB R2019a (The MathWorks, Inc.). The principle of back-projection from projection images is visualized in figure 3(a). The applicable codes are available at [<https://github.com/lkkskl/fbp-cor>]. OPT reconstructions were visualized with the open-source software Fiji.

The grayscale 3D OPT reconstructions, as the one shown in figure 3(b), were segmented into four regions shown in figure 3(c): inclusion(s), background, FEP tube, and a manually applied marker. The inclusions were the main regions of interest, namely, pieces of tissue or iPSC spheroids. The background was composed of the cylindrical hydrogel scaffold and saline solution. The tube, from which the hydrogel was emerging, is seen as an annular-shaped piece on top of the 3D images in figures 3, 4 and 6. A small cut was made in the tube before specimen preparation to verify the correct orientation of the segmentation during R-mfEIT mesh creation. The marker was added below this cut in the segmentation. After the mesh creation, the marker was removed from further computations.

Segmentations were performed and visualized in Avizo (Thermo Scientific, v.2019.4). First, the OPT reconstructions were resampled from the original  $3.25 \mu\text{m}$  voxel size to  $13 \mu\text{m}$  voxel size to lighten the image processing. Then, the image stacks were 3D median filtered with a neighborhood of six voxels to slightly smooth the image volume while preserving the edge information. Many of the image stacks were slightly challenging to segment, as some of the inclusion(s) grayscale values were close to the background values. Thus, we mainly used manual thresholding (Magic Wand tool) for the inclusion segments and made corrections with morphological operations and the Lasso tool. The tube and the marker were segmented by generating two ellipses and interpolating a cylinder between them. The rest of the volume was labeled as background. Finally, the segments were 3D smoothed and exported to Matlab to include them in the R-mfEIT finite element (FE) model.

### 2.6. R-mfEIT modeling and image reconstruction

This section discusses the mathematical models and computational methods used in the R-mfEIT and OPT-mfEIT image reconstruction. We start by briefly reviewing the complete electrode model (CEM), which mathematically describes the dependence of the electrode potentials on the injected currents and electrical conductivity within the volume. This model (or its numerical approximation) is referred to as the forward model of EIT. Next, we review an image reconstruction method that combines the R-mfEIT measurements, CEM, and a smoothness promoting prior model for the electrical conductivity. This method, which does not utilize the structural information given by OPT, is referred to as the conventional reconstruction method. In this study, the



conventional reconstruction method is only used in the first experimental study (1) as a reference for the multimodal OPT-mfEIT reconstruction, and (2) to investigate the effect of the number of rotation angles on the 3D R-mfEIT reconstruction. Finally, we describe the multimodal OPT-mfEIT reconstruction, where the structural information provided by OPT is included in R-mfEIT.

Both the conventional and the multimodal reconstructions are in principle absolute image reconstructions. This means that the data, from which the reconstructions are computed, are measured at a single time instant instead of using the difference of two data sets measured at different times or using different frequencies. Additionally, our reconstruction methods include an approximative correction for errors in the modelling of the EIT measurements, which is explained below.

The FE model and reconstruction algorithm were written for Matlab, with modifications to account for rotational data acquisition (Koskela *et al* 2018). For mesh creation, the open-source software Netgen v.4.9.11 was used. R-mfEIT and OPT-mfEIT 3D visualizations were done in Avizo.

### 2.6.1. Modeling of Rotational EIT Measurements

EIT measurements are modeled by the CEM, which consists of a partial differential equation (3) and three boundary conditions (4)–(6):

$$\nabla \cdot (\sigma \nabla u) = 0, \quad \vec{r} \in \Omega, \quad (3)$$

$$\sigma \frac{\partial u}{\partial \vec{n}} = 0, \quad \vec{r} \in \partial\Omega \setminus \bigcup_{l=1}^L e_l, \quad (4)$$



$$\int_{\{e_l\}} \sigma \frac{\partial u}{\partial \vec{n}} dS = I_l, \quad l = 1, \dots, L, \quad (5)$$

$$u + z_l \frac{\partial u}{\partial \vec{n}} = U_l, \quad \vec{r} \in e_l, \quad l = 1, \dots, L, \quad (6)$$

where  $\sigma$  is the electric conductivity,  $u$  is the electric potential inside the target  $\Omega$  with boundary  $\partial\Omega$ ,  $\vec{n}$  is the outward unit normal of the boundary,  $I_l$  is the current through electrode  $e_l$ ,  $z_l$  is the contact impedance between electrode  $e_l$  and the target,  $U_l$  is the potential on electrode  $e_l$ , and  $L$  is the number of electrodes. EIT measurements are modeled by approximating the CEM with the finite element method (FEM) for given values of  $\sigma$ ,  $z$ , and given current excitation (Vauhkonen *et al* 1999). In this study, tetrahedral elements are used, and both  $\sigma$  and  $u$  are represented by linear basis functions. In addition to (3)–(6), the reference level of electric potential is set, and charge conservation is fulfilled by requiring that

$$\sum_{l=1}^L U_l = 0, \quad (7)$$

$$\sum_{l=1}^L I_l = 0. \quad (8)$$

Approximating the CEM with FEM leads to a matrix equation  $A\theta = I$ , where  $A$  is the system matrix,  $\theta$  is a vector containing nodal values of  $u$  and electrode potentials  $U$ , and vector  $I$  depends on the current excitation.

In rotational EIT, the overriding idea is to improve EIT measurements' information content by rotating the specimen and carrying out the current excitations and potential measurements sequentially for various rotation angles. This approach significantly improves the EIT reconstructions compared to stationary limited angle EIT. In technical terms, the temporal changes of the conductivity distribution due to rotation are modeled by constructing mappings that deform the electrical conductivity of the initial state to each of the rotational positions and incorporating these mappings into the forward solver of EIT. Lehti-Polojärvi *et al* (2018)

We adopted a previously presented approach to constructing the rotation mappings (Koskela *et al* 2018) but extended it to 3D. In this so-called click method, a rotationally invariant inner boundary in the mesh limits the rotational domain. In the FE mesh, a rotating cylindrical body with a radius of 3.2 mm was modeled in the middle of the rectangular imaging chamber, as shown in figure 4. This radius was selected to be wider than the rotating tube in the experimental setup.

Nodes were placed on the modeled cylinder boundary with an angular spacing of  $4.5^\circ$ , corresponding to the measurements' angular spacing. Rotational measurements were modeled by rotating the cylinder  $4.5^\circ$  in the direction of rotation, thus rotating the conductivity distribution inside the cylinder without deforming the mesh. Performing the rotation in this way only requires re-indexing of the element connectivity table to connect elements inside the rotating cylinder to elements outside it. This index mapping is pre-computed for each rotation angle when the mesh is created. This click method was shown to be faster and resulted in more accurate reconstructions (Koskela *et al* 2018) than simpler approaches based on multiplying the nodal conductivity vector  $\sigma$  by a matrix that approximately computes the rotated conductivity distribution (Lehti-Polojärvi *et al* 2018).

Computing EIT reconstructions iteratively requires computing the Jacobian matrix, that is, derivatives of the electrode potentials with respect to nodal values of  $\sigma$  (Vilhunen *et al* 2002). In rotational EIT image reconstruction, the Jacobian is needed for each rotational position. This computation can be sped up by pre-computing and storing the derivatives  $dA/d\sigma$ , which appear in the Jacobian formula, for each rotational position when the mesh is created.

### 2.6.2. Conventional R-mfEIT reconstruction

The inverse problem of EIT is to reconstruct the electrical conductivity  $\sigma$  of the target based on the injected current and measured voltage data. Solving the inverse problem requires inverting the forward model of EIT described above. However, in conventional (R-mf)EIT, where structural constraints are not available, the inverse problem is mathematically ill-posed and its solution requires regularization or use of prior information about the conductivity. In this study, the inverse problem is formulated in the Bayesian framework. EIT measurements are modeled as  $V = U(\sigma, z) + e$ , where  $U(\sigma, z)$  is a FE approximation of the CEM in (3)–(8), and  $e$  is a noise vector assumed to be additive. In the Bayesian approach, the electric conductivity  $\sigma$  and measurement noise  $e$  are modeled as random variables (Kaipio and Somersalo 2006). The noise vector  $e$  is assumed to be Gaussian with zero mean. The covariance  $\Gamma_e(2)$  is estimated based on repeated measurements. Contact impedances are fixed to  $z = 1 \Omega$  for each electrode.

In the Bayesian framework, prior information about the unknown conductivity distribution  $\sigma$  is encoded into the prior probability density, which in this study is a multivariate Gaussian smoothness prior characterized by the mean  $\sigma^*$  and covariance matrix  $\Gamma_\sigma$ . The mean is chosen as the best homogeneous fit to reference data at a given frequency, namely

$$\sigma_*^f = \arg \min_{\sigma} \|L_e^f (V_{ref}^f - U(\sigma, z))\|^2, \quad (9)$$

where  $L_e^f$  is the Cholesky factor of the noise precision matrix  $(\Gamma_e^f)^{-1}$ , that is,  $(L_e^f)^T L_e^f = (\Gamma_e^f)^{-1}$ . The prior covariance  $\Gamma_{\sigma}$  used in this work has the form

$$\Gamma(i, j) = a \exp\left(-\frac{\|\vec{r}_i - \vec{r}_j\|^2}{2b^2}\right), \quad (10)$$

where  $\vec{r}_i$  is the position vector of the node  $i$ ,  $a = \left(\frac{\sigma_*}{3}\right)^2$ ,  $b = \frac{c}{\sqrt{2 \log 100}}$  and  $c = 1$  mm is called the correlation length, which controls the degree of spatial smoothness. Correlation length was chosen based on the approximate expected sizes of the inclusion(s). Details of the smoothness prior, including the interpretation and the choice of parameters, have been previously presented, where a similar prior model was used (Lipponen *et al* 2013).

Using the best-fit homogeneous conductivity  $\sigma_*$ , we also computed a model discrepancy term  $\varepsilon^f = U(\sigma_*, z) - V_{ref}^f$ , which is used for approximative model error correction in the image reconstruction (Hallaji *et al* 2014). In the present study, such modeling errors may result from the saline level's uncertainty in the imaging chamber, the saline surface's curvature, and possible uncertainty in the excitation current values.

With the above choices for the noise model and prior, the EIT reconstruction for each frequency was obtained as

$$\widehat{\sigma}^f = \arg \min_{\sigma} \|L_e^f (V^f - U(\sigma, z) + \varepsilon^f)\|^2 + \|L_{\sigma}(\sigma - \sigma_*)\|^2, \quad (11)$$

where  $L_{\sigma}$  is the Cholesky factor of the inverse prior covariance  $\Gamma_{\sigma}^{-1}$ .

For R-mfEIT image reconstruction, we applied an iterative Gauss–Newton method (Heikkinen *et al* 2002). The Gauss–Newton iteration has the form

$$\sigma_{k+1}^f = \sigma_k^f + d(J^T(\Gamma_e^f)^{-1}J + L_{\sigma}^T L_{\sigma})^{-1}(J^T(\Gamma_e^f)^{-1}(V^f - U(\sigma, z) + \varepsilon^f) - \Gamma_{\sigma}^{-1}(\sigma_k - \sigma_*)), \quad (12)$$

where the step length  $d$  was chosen by a line search method at each iteration (Karhunen *et al* 2010). As an initial point of iteration,  $\sigma_0^f$ , we use the best-fit homogeneous conductivity  $\sigma_*^f$ .

### 2.6.3. OPT-mfEIT reconstruction

In the OPT-informed mfEIT, the model for the electrical measurements is the same as in the conventional single-modality case: the dependence between electric conductivity and electrode potentials is described by CEM (3)–(8), and the model is approximated numerically using FEM. Also, the rotational setup is modeled as described above. The difference between the conventional R-mfEIT and the proposed OPT-mfEIT is that in the latter reconstruction, the segmentation obtained from OPT is used as a geometrical constraint for the electrical conductivity distribution  $\sigma$ . More specifically, the conductivity inside each segment is assumed to be homogeneous at any given frequency.

The benefit of utilizing the assumption of segmentally constant conductivity is that it dramatically decreases the number of unknown parameters in EIT imaging. In this study's experiments, the number of conductivity parameters at each frequency in OPT-mfEIT varies between 2 and 3. In contrast, in the conventional R-mfEIT, thousands of unknown conductivity parameters were reconstructed based on the electrode potential data at each frequency. This low order parameterization decreases the computational complexity and computation time from the conventional R-mfEIT case and—above all—stabilizes the originally ill-posed inverse problem of EIT and potentially leads to more reliable estimates of the tissue's conductivity spectrum. For this reason, a prior function is not required to compute the reconstructions, unlike in the conventional mfEIT reconstruction.

In the experiments performed in this study, the OPT reconstructions provided the following main segments: one or two inclusions, the FEP tube, and the background. The inclusion(s) and the background were considered as subvolumes, each having constant unknown conductivity at a given frequency. The FEP tube was modeled as a perfect insulator. Consequently, the tube segment's surface was modeled as a boundary of the computational domain in R-mfEIT; on this boundary, the zero-flux boundary condition (4) was assigned equivalently to all other electrode-free boundaries of the computational domain.

The segment conductivities at each frequency were computed by solving a minimization problem of the form

$$\widehat{\sigma}_s^f = \arg \min_{\sigma_s} \|L_e^f (V^f - U(F(\sigma_s), z) + \varepsilon^f)\|^2, \quad (13)$$

where  $\sigma_s = [\sigma_1, \dots, \sigma_{N_s}]^T$ ,  $N_s$  is the number of segments, and  $F$  maps the conductivity values  $\sigma_s$  to the nodal conductivity values in the mesh.

The Gauss–Newton method was also used for the segmentation-based OPT-mfEIT reconstruction with slight modifications. In this case, the iteration has the form

$$\sigma_{k+1}^f = \sigma_k^f + d(J_s^T (\Gamma_\epsilon^f)^{-1} J_s)^{-1} (J_s^T (\Gamma_\epsilon^f)^{-1} (V^f - U(\sigma, z) + \epsilon^f)), \quad (14)$$

where  $\sigma$  now denotes the conductivities of the segments, that is,  $\sigma = [\sigma_1, \dots, \sigma_{N_s}]^T$ , where  $N_s$  is the number of segments. Moreover,  $J_s$  is the Jacobian matrix of the measurements with respect to the segment conductivities, defined as  $J_s = JP$ , where  $P$  is a  $N_n \times N_s$  matrix, which maps the segment conductivity values to the  $N_n$  nodes in the mesh.

#### 2.6.4. Meshing

The imaging volume, excluding the tube segment, was first meshed with Netgen. The segmentation was then used to refine the mesh by increasing the mesh density at the tissue's location, as shown in figure 4. Since the FEP tube is a good electrical insulator, the boundary condition of zero normal current density (4) was imposed on the tube boundary, and the tube volume was not meshed. Each mesh used in this study had approximately 11 000 nodes. The center-of-rotation correction performed in the OPT reconstructions was not considered in the R-mfEIT reconstructions. The offset values were typically close to zero and a maximum of 44 pixels, which corresponded to 143  $\mu\text{m}$ . These offsets were not considered a significant source of error in the R-mfEIT reconstructions.

### 2.7. Materials and specimens

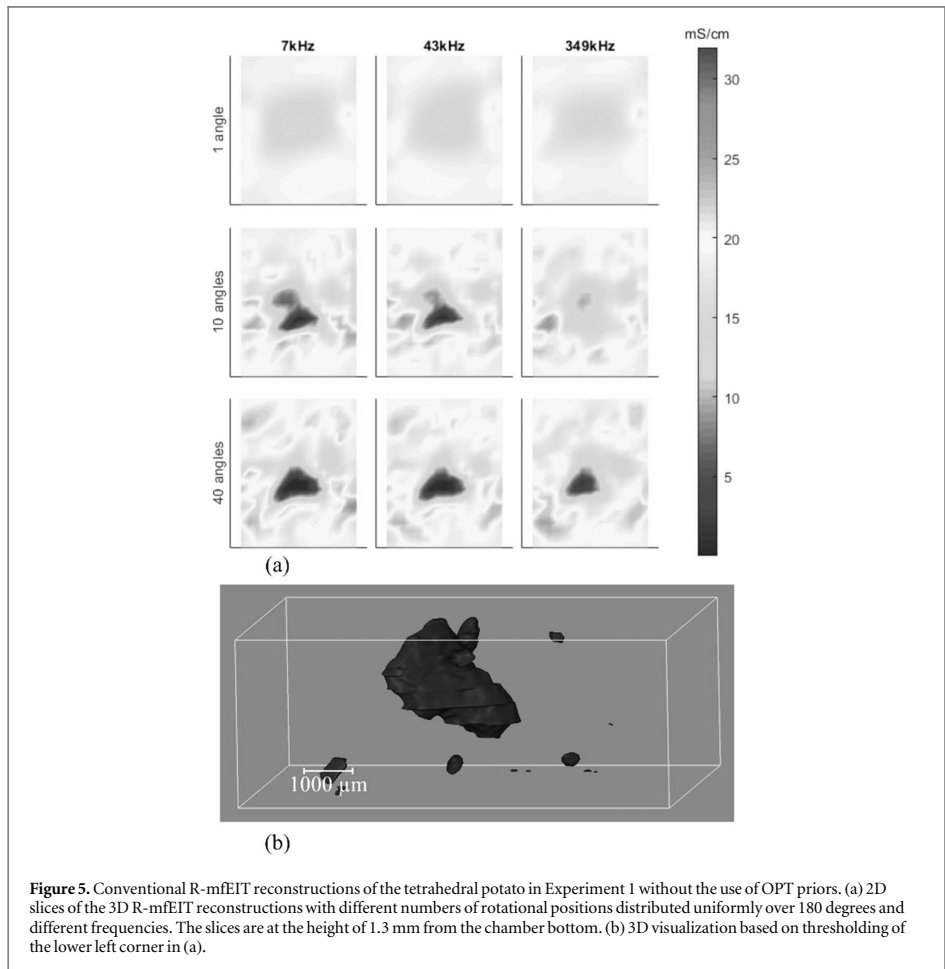
We performed four experiments with different specimen types to demonstrate the feasibility of the proposed technique. The imaging chamber was filled with phosphate buffered saline (PBS, Sigma-Aldrich PBS tablet in purified Milli-Q water, concentration 0.01 M phosphate buffer, 0.0027 M KCl and 0.137 M NaCl). All specimens were prepared into 5 mm inner diameter FEP tubes. Agarose gel 1.5% (w/w) (low gelling powder, Sigma Life Science) was prepared in PBS. Phantom and tissue inclusions were manually cut to approximately 1 mm  $\times$  1 mm  $\times$  1.5 mm sized pieces. One or two inclusions were placed at the bottom of the tube, and 200  $\mu\text{l}$  of agarose was pipetted on top. All specimens were left to gelate and stabilize at room temperature for at least 15 min before imaging. All measurements were acquired at room temperature.

In Experiment 1, a tetrahedral piece of fresh potato was embedded in agarose. The potato phantom was chosen due to its well-known electrical properties.

Experiment 2 was performed with fresh human subcutaneous adipose tissue (female donor with normal Body Mass Index) with written informed consent in accordance with the Regional Ethics Committee of the Expert Responsibility area of Tampere University Hospital, Tampere, Finland (ethical approval R15161). The aim was to investigate the OPT-mfEIT capability to differentiate viable and thermally killed tissues. The first specimen contained a viable piece of adipose tissue that was imaged within 24 h of cutting. To induce necrotic cell death, another specimen was prepared by placing a tissue piece on aluminum foil and kept on top of dry ice (approximately  $-79^\circ\text{C}$ ) for 55 min before embedding it in agarose.

To investigate the ability of OPT-mfEIT to distinguish between intact and broken cell membranes, we used fresh and chemically treated porcine liver tissue in Experiment 3. Porcine liver tissue was purchased from a local abattoir, and all measurements were performed within 14 h of extraction. Triton X-100 is commonly used to lyse cells in biological research. We prepared 2% (v/v) solution by diluting Triton X-100 (Sigma-Aldrich, Inc. USA) with PBS. Before embedding the inclusions in agarose, the treated tissue pieces were incubated in the solution for 1 h and then washed with PBS for 15 min to rinse the Triton X-100 residues from the tissue. We studied four specimens: liver 1 (one piece of fresh liver), liver 2 (one piece of treated liver), liver 3 and 4 (one piece of fresh and one piece of treated liver in each specimen).

In Experiment 4, iPSCs embedded in biomaterial spheroids were imaged to investigate the ability of OPT-mfEIT to detect tissue engineered inclusions. The iPSCs (cell line UTA.10211.EURCCs, ethical approval R12123) were cultured on Geltrex-coated plates in mTesR1 medium (Stemcell) at  $37^\circ\text{C}$  in 5%  $\text{CO}_2$ . The cells were collected from the cell culture plates by incubating them with Versene at  $37^\circ\text{C}$  for 4 min and collecting them into mTesR1 medium. Cell suspension was centrifuged with  $150 \times g$  for 5 min, washed with 10% sucrose twice, and finally resuspended in 10% sucrose. Then, the cell suspension was mixed with biomaterial (Puramatrix, Corning, USA) and Collagen I (Gibco) solution. iPSC spheroids were created by pipetting 5  $\mu\text{l}$  droplets of the cell-biomaterial mix into cell culture medium on a 48 well plate, and thereby creating spheroids with a diameter of approximately 1 mm. The spheroids were then immediately embedded in agarose and imaged within 7 h. To clarify the effect of the cells on specimen conductivity, we also imaged two biomaterial spheroids without cells. We studied four specimens: cells 1 (one biomaterial spheroid with cells), cells 2 (two biomaterial spheroids with cells), biomaterial 1 and 2 (one blank biomaterial spheroid).



### 3. Results

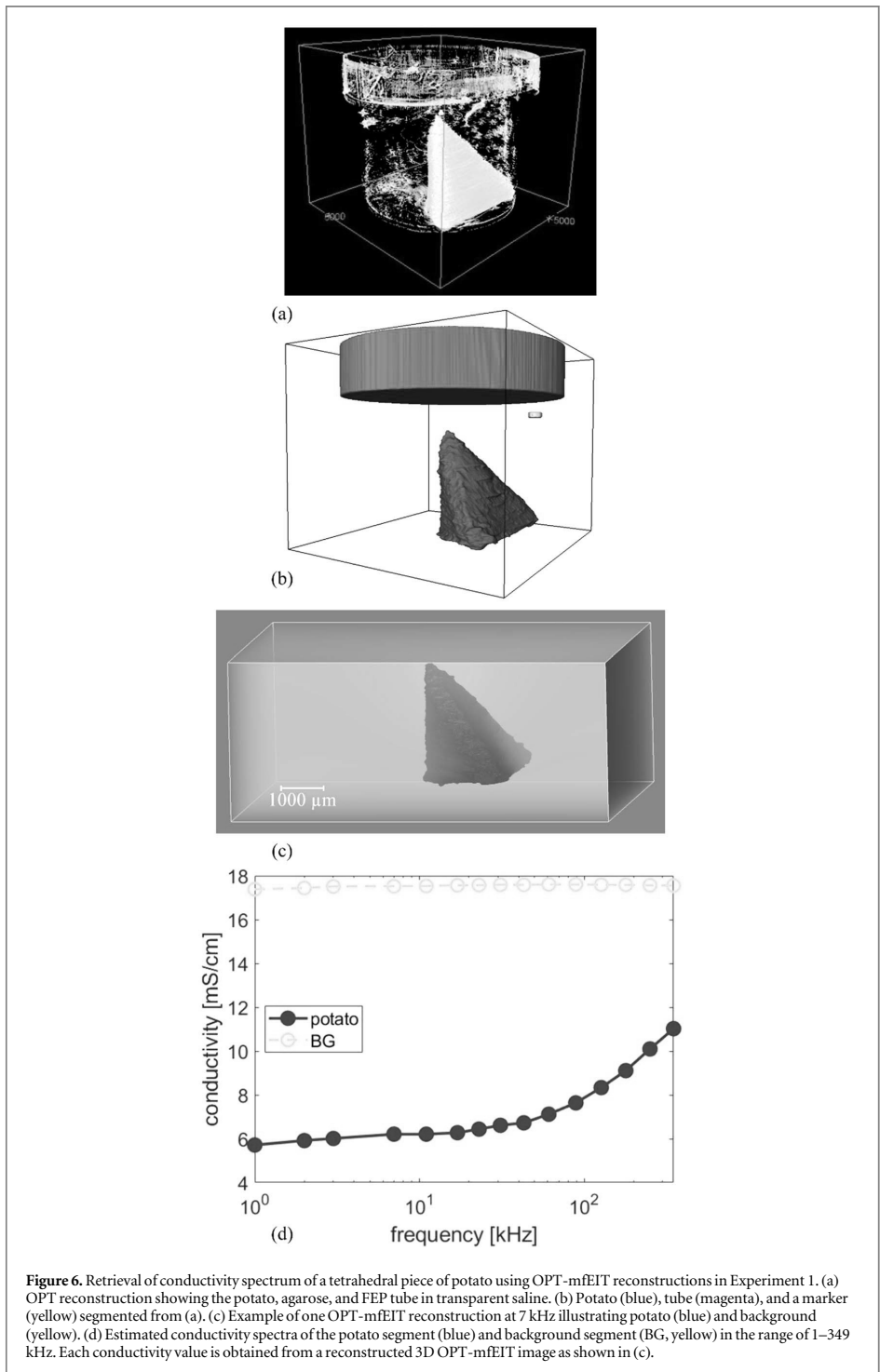
The results of Experiment 1 are presented in figures 5 and 6. These figures illustrate the reconstruction of conventional R-mfEIT (figure 5) and the OPT-mfEIT (figure 6), according to the steps described in the flowchart in figure 1. For Experiments 2–4, only the main results are shown in the figures: the tissue conductivity spectrum and one 3D visualization at 7 kHz, as in figures 6(c) and (d).

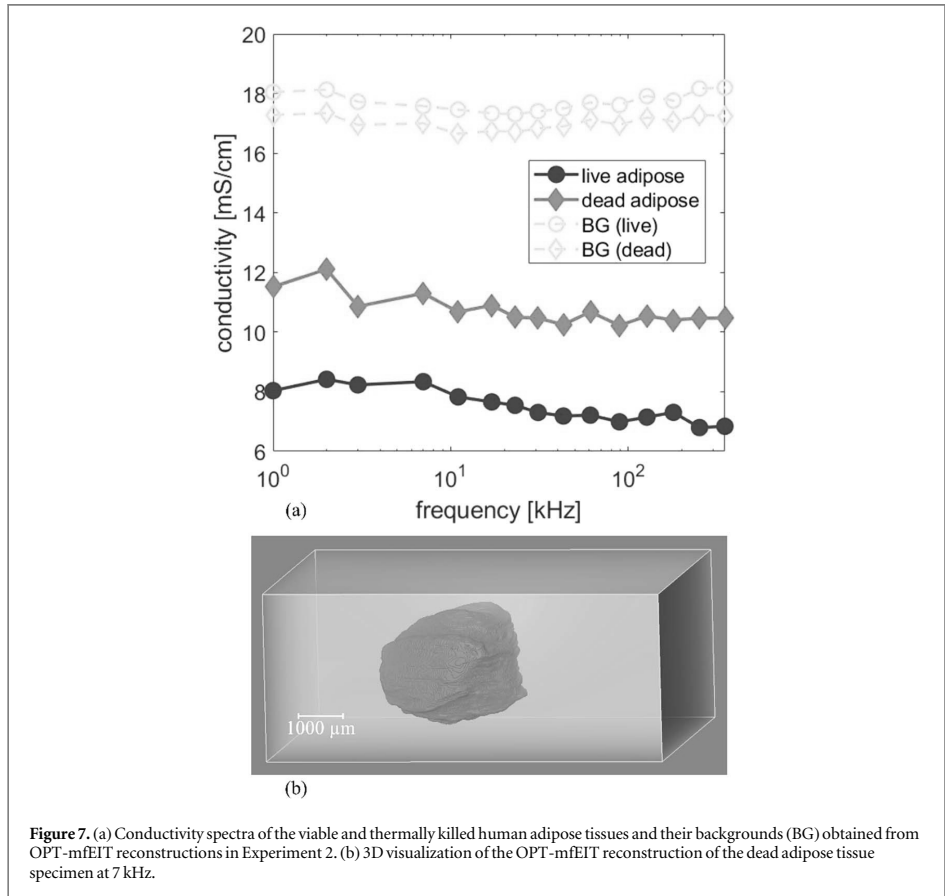
The 2D slices of the conventional 3D R-mfEIT reconstructions in figure 5(a) clearly show that the potato is less conductive than the background. The estimated conductivity of the potato increases with increasing AC frequency from 7 to 349 kHz. The background conductivity is not, however, affected by the frequency change.

Increasing the number of measurement angles enhances image quality, as the shape of the inclusion is detected more accurately with 40 angles than with 10 angles in 180° rotation in figure 5(a). One angle—one measurement set with the 16-electrode setup—is not enough to provide reasonable images in our limited angle R-mfEIT setup. We therefore chose to use 40 angles to compute all further results.

Figure 5(b) shows a 3D illustration of the conventional R-mfEIT at 7 kHz (thresholding  $8.5 \text{ mS cm}^{-1}$ ). Although some imaging artifacts are present, the R-mfEIT captures the shape of the potato relatively well. This result implies that R-mfEIT can provide valuable information on the spatially distributed conductivity within the imaging domain. This result is an encouraging observation, as in the multimodal OPT-mfEIT, the reconstruction quality is further enhanced.

The OPT-mfEIT results for the potato are shown in figure 6. The OPT reconstruction (figure 6(a)) was used to segment electrically relevant regions (figure 6(b)), where the potato specimen and the FEP tube are depicted with different colors, whereas the background is transparent. The OPT-mfEIT reconstruction at 7 kHz is





**Figure 7.** (a) Conductivity spectra of the viable and thermally killed human adipose tissues and their backgrounds (BG) obtained from OPT-mfEIT reconstructions in Experiment 2. (b) 3D visualization of the OPT-mfEIT reconstruction of the dead adipose tissue specimen at 7 kHz.

visualized in figure 6(c), and the conductivity spectra of the potato and the background in figure 6(d). As in conventional R-mfEIT, the background is more conductive than the potato inclusion. Also, the potato's conductivity increases as the applied frequency increases, whereas the background remains nearly constant.

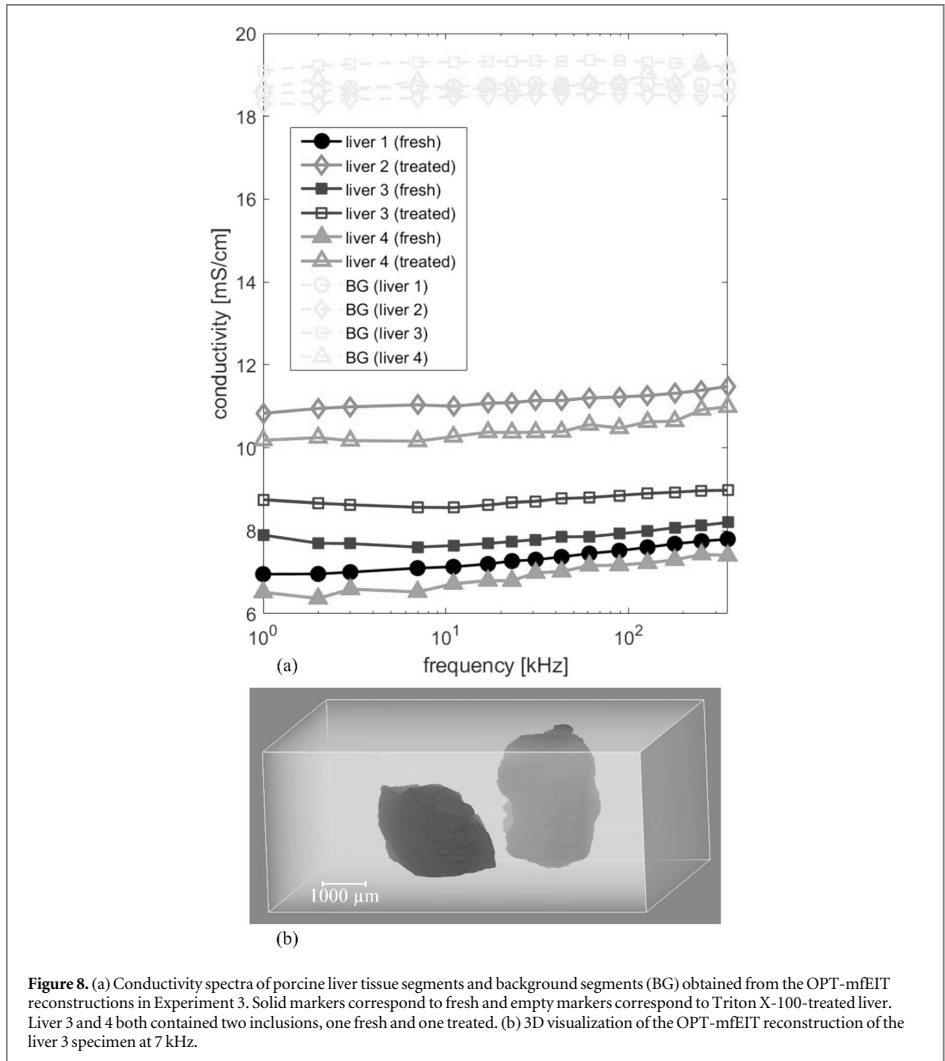
The OPT-mfEIT results of Experiment 2 on human adipose tissue are shown in figure 7. The dead tissue is more resistive than the background, and the viable tissue is more resistive than the dead tissue. The background conductivities are approximately the same as in Experiment 1.

The porcine liver tissues conductivity spectra of Experiment 3 are shown in figure 8. Regardless of the specimen containing one or two inclusions, the estimated conductivities of all Triton X-100-treated inclusions are higher than the conductivities of the fresh liver inclusions. All background conductivity values are close to those in Experiments 1 and 2.

The estimated conductivity spectra for iPSCs and the biomaterial spheroids in Experiment 4 are shown in figure 9. The blank biomaterial appears more conductive than the background and the iPSC-containing biomaterial spheroids. The background spectra are close to those in Experiments 1–3.

#### 4. Discussion and conclusions

The results of the experimental studies clearly show the power of multimodal tomography and the use of OPT as prior for R-mfEIT. The conventional, single-modality R-mfEIT reconstructions in Experiment 1 are of typical absolute EIT image quality, representing the shape, location, and conductivity of the inclusion relatively well (figure 5). The spatial resolution of OPT-mfEIT, however, is superior to the R-mfEIT reconstruction seen in figures 6–9. Furthermore, although the potato conductivity provided by the conventional R-mfEIT was in the same range as that provided by OPT-mfEIT (compare figures 5 and 6), the smoothness and image artifacts in conventional R-mfEIT make the quantitative analysis of conductivity spectra difficult from these EIT images. In



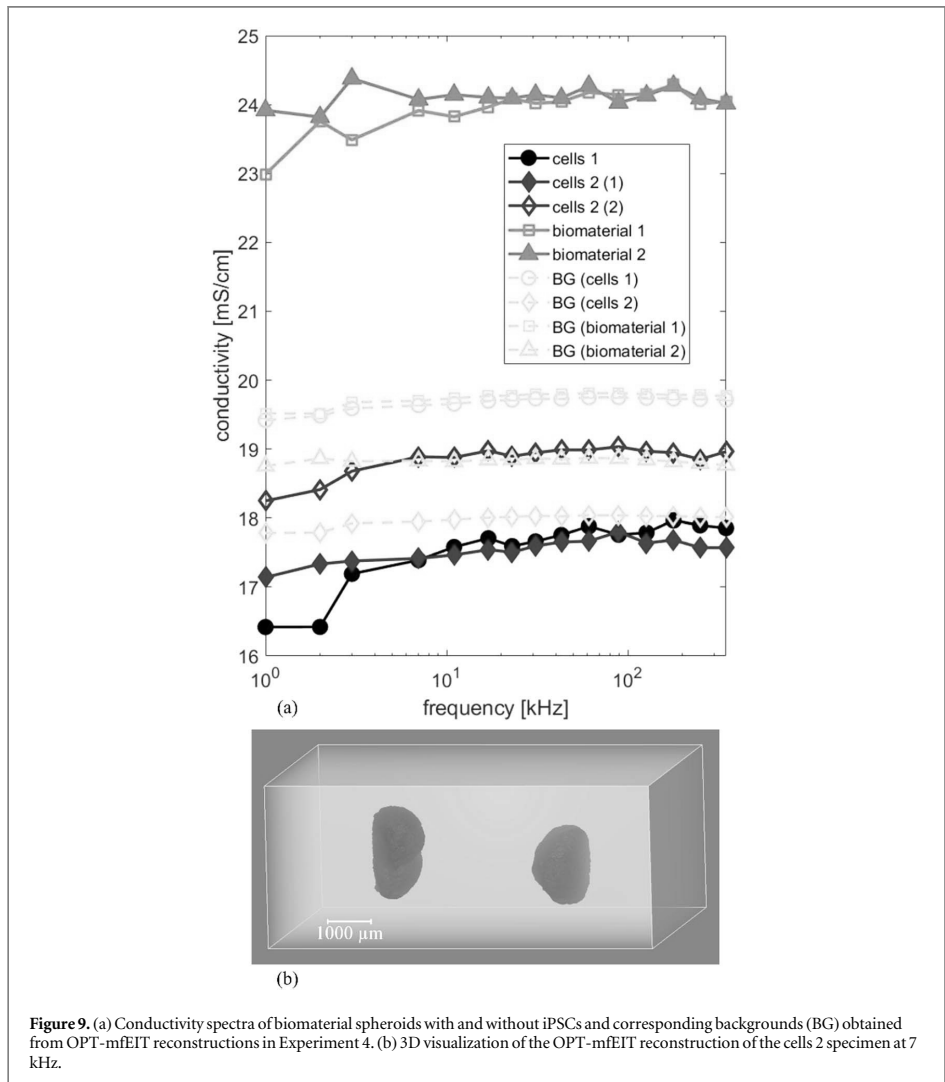
OPT-mfEIT, the conductivity spectra can be directly extracted from the reconstructed frequency-dependent (but inclusion-wise constant) conductivities.

Increasing the number of rotational positions in figure 5 (a) enhanced the image quality. This effect is due to the rotational measurement protocol increasing the number of independent measurements compared to stationary EIT. Similar results have been shown in 2D (Lehti-Polojärvi *et al* 2018).

The background segments' conductivity was assumed to be homogeneous in all OPT-mfEIT reconstructions. This segment consisted of the PBS solution and the agarose gel in all experiments. Since agarose was prepared in PBS, the assumption of background homogeneity was justified. The reconstructed background conductivities were close to  $18 \text{ mS cm}^{-1}$  in all experiments indicating stability of OPT-mfEIT. This value is somewhat higher than our directly measured values of  $12 \text{ mS cm}^{-1}$  for PBS and  $13 \text{ mS cm}^{-1}$  for agarose (conductivity meter, Hanna Instruments, HI-8733) at room temperature.

The potato results in Experiment 1 show a clear increase in conductivity at high frequencies (from  $6 \text{ mS cm}^{-1}$  to  $11 \text{ mS cm}^{-1}$ ), suggesting that the potato cell walls were intact, acting resistively at low frequencies and passing more current at higher frequencies. These results are in accordance with a previous study that show an increase of potato conductivity from  $0.25$  to  $4.5 \text{ mS cm}^{-1}$  at the same frequency range (Ahn *et al* 2010).

The adipose tissues in Experiment 2 (figure 7) showed relatively flat conductivity spectra at the used frequency range as was expected (Gabriel *et al* 1996). Killing the adipose tissue by freezing is expected to cause necrotic cell death that includes the breakdown of cell membranes, allowing the current to flow through the well



conducting cytoplasm. This effect caused the conductivity to increase after freezing, which is in accordance with a previous study on rat liver (Davalos and Rubinsky 2004).

The porcine liver inclusions in Experiment 3 (figure 8) show a modest but consistent increase of conductivity along with increasing frequency as was expected (Gabriel *et al* 1996). After treatment by Triton X-100 solution, liver tissues indicate an increase in conductivity due to the breakdown of cell membranes, allowing current to pass the well conducting cytoplasm. These results are in line with previous studies on, for example, the Triton X-100 treatment of breast cancer spheroids (Wu *et al* 2018).

The iPSCs and biomaterial spheroids were challenging specimens, as they only covered approximately 0.5% of the whole measured volume. Also, inside the spheroids, there was biomaterial between the iPSCs with no developed cell–cell junctions. However, our results show that we can detect the presence of iPSCs in the spheroids, as they decreased the conductivity compared to the blank biomaterial in Experiment 4 (figure 9). This was expected since the iPSCs can be assumed viable and thus resistive at the used frequency range. Also, iPSC spheroids showed flat conductivity spectra that were expected at the used frequency range and tetrapolar measurement scheme (Canali *et al* 2015).

The mEIT device used in this study did not provide the accurate excitation current values, and thus a nominal value of 1 mA was used in the forward model for each excitation. This approximation may be one reason for the estimated conductivities of potato, tissues, and background to be higher than reference values in



the literature (Gabriel *et al* 1996, Ahn *et al* 2010) and direct measurements. In general, EIT measurements and obtained conductivity values are dependent on the measurement system and the temperature and condition of the specimen. Thus, direct comparison of the conductivity values between different studies is difficult. Moreover, it is more meaningful to compare the changes occurring in the same specimen type and measurement conditions.

Overall, the conductivity values and the frequency responses obtained were in good agreement with previous knowledge considering the general difficulty of measuring the conductivity of very small soft objects. Typically, tissue conductivity would have to be estimated based on impedances measured within a chamber with known dimensions. In future studies, one interesting possibility is to compare the OPT-mfEIT conductivity spectra with impedance spectra obtained, for example, by bioimpedance-based needle providing a defined and known measurement volume (Halonen *et al* 2019).

The volume of the inclusions in our experiments only covered from 0.5% to 5.6% of the total measured volume, being highest for adipose tissues and smallest for the iPSC spheroids. Thus, OPT-mfEIT proved to be an effective technique even for low volume fraction specimens.

The data acquisition time induces a possible error source in our measurements because some of the saline typically evaporated during imaging. Also, due to the small size of the imaging chamber and the surface tension of the PBS, the saline surface had a significant curvature (seen in the OPT raw data videos in supplementary materials). These factors can cause geometric modeling errors in our R-mfEIT model, affecting the reconstructions' accuracy. An approximative method was used to correct for modeling errors using a reference R-mfEIT measurement. In future, the imaging system could be improved to reduce these uncertainties, or the reconstruction methods could be modified to take these modeling errors into account more accurately.

Our 3D reconstruction algorithms were relatively time-efficient since the conventional R-mfEIT took approximately 37 min and the OPT-mfEIT approximately 21 min for each frequency with 40 angles. Computations were performed on a desktop PC with i5-7500 3.4 GHz CPU and 16 GB RAM.

In the future, the image processing could be automatized to enable faster throughput. This would be feasible with, for example, cell spheroids that were straightforward to segment with simple thresholding operations. We also note that concave or hollow opaque samples are not optimal for OPT because some parts might be undetected in the OPT reconstruction.

As shown in this study, OPT-mfEIT imaging can be used to extract qualitative information about 3D cell and tissue cultures, such as the breakdown of cell membranes and cell death or the presence of stem cells in biomaterial scaffold. To achieve these results, we have built a novel imaging system and enhanced the rotational EIT image reconstruction via segmented OPT data, FEM rotational meshing and modeling, and a nonlinear Bayesian image reconstruction algorithm. Our tool provides a new avenue to study live cells in *in vitro* culturing for various specimen types and applications, ranging from following cell culture growth to cell-cell junctional development or disintegration. This tool will be of interest, for example, in drug development and disease modeling.


## Acknowledgments

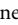
This work was supported in part by the Finnish Centre of Excellence in Inverse Modelling and Imaging (award 303801) and the Finnish Cultural Foundation (Pohjois-Savon Rahasto), and in part by the Centre of Excellence in Body-on-Chip (awards 326580, 336784) and Emil Aaltonen Foundation. The authors would like to thank the impedance group (Thomas Johann Seebeck Department of Electronics at Tallinn University of Technology) for collaborating on the mfEIT device and electrode fabrication. The corresponding author, M L-P would like to thank MSc Markus Hannula for guidance in image segmentation. We are thankful to MSc Olli Koskela for providing insights into the writing and MA Peter Heath for reviewing the spelling and grammar of this work.


## Conflicts of interest

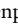
The authors report no conflicts of interest.


## ORCID iDs


M Lehti-Polojärvi  <https://orcid.org/0000-0001-9826-5741>


M J Räsänen  <https://orcid.org/0000-0002-4608-7901>

L E Viiri  <https://orcid.org/0000-0003-2279-0392>

H Vuorenpää  <https://orcid.org/0000-0002-6351-3044>

S Miettinen  <https://orcid.org/0000-0002-0647-9556>

A Seppänen  <https://orcid.org/0000-0002-4042-2254>

J Hyttinen  <https://orcid.org/0000-0003-1850-3055>

## References

- Ahn S, Jun S C, Seo J K, Lee J, Woo E J and Holder D 2010 Frequency-difference electrical impedance tomography: phantom imaging experiments *J. Phys.:Conf. Ser.* **224** 012152
- Belay B, Koivisto J T, Parraga J, Koskela O, Montonen T, Kellomäki M, Figueiras E and Hyttinen J 2021 Optical projection tomography as a quantitative tool for analysis of cell morphology and density in 3D hydrogels *Sci. Rep.* **11** 6538
- Borsic A, Halter R, Wan Y, Hartov A and Paulsen K D 2010 Electrical impedance tomography reconstruction for three-dimensional imaging of the prostate *Physiol. Meas.* **31** S1–16
- Canali C, Heiskanen A, Muhammad H B, Høyum P, Pettersen F J, Hemmingsen M, Wolff A, Dufva M, Martinsen Ø G and Emnéus J 2015 Bioimpedance monitoring of 3D cell culturing—complementary electrode configurations for enhanced spatial sensitivity *Biosens. Bioelectron.* **63** 72–9
- Davalos R and Rubinsky B 2004 Electrical impedance tomography of cell viability in tissue with application to cryosurgery *J. Biomech. Eng.* **126** 305–9
- Fang Y and Eglen R M 2017 Three-dimensional cell cultures in drug discovery and development *SLAS Discovery* **22** 456–72
- Figueiras E et al 2014 Optical projection tomography as a tool for 3D imaging of hydrogels *Biomed. Opt. Express* **5** 3443–9
- Gabriel S, Lau R W and Gabriel C 1996 The dielectric properties of biological tissues: II. Measurements in the frequency range 10 Hz–20 GHz *Phys. Med. Biol.* **41** 2251–69
- Geselowitz D B 1971 An application of electrocardiographic lead theory to impedance plethysmography *IEEE Trans. Bio-Med. Eng.* **18** 38–41
- Gomes M E, Rodrigues M T, Domingues R M A and Reis R L 2017 Tissue engineering and regenerative medicine: new trends and directions—a year in review *Tissue Eng. B* **23** 211–24
- Hallaji M, Seppänen A and Pour-Ghaz M 2014 Electrical impedance tomography-based sensing skin for quantitative imaging of damage in concrete *Smart Mater. Struct.* **23** 085001
- Halonen S, Kari J, Ahonen P, Kronström K and Hyttinen J 2019 Real-time bioimpedance-based biopsy needle can identify tissue type with high spatial accuracy *Ann. Biomed. Eng.* **47** 836–51
- Heikkinen L, Vilhunen T, West R and Vauhkonen M 2002 Simultaneous reconstruction of electrode contact impedances and internal electrical properties: II. Laboratory experiments *Meas. Sci. Technol.* **13** 1855–61
- Kaipio J, Kolehmainen V, Vauhkonen M and Somersalo E 1999 Inverse problems with structural prior information *Inverse Problems* **15** 713–29
- Kaipio J and Somersalo E 2006 *Statistical and Computational Inverse Problems* (Berlin: Springer Science & Business Media)
- Karhunen K, Seppänen A, Lehtikoinen A, Monteiro P and Kaipio J 2010 Electrical resistance tomography imaging of concrete *Cement Concr. Res.* **40** 137–45
- Klösgen B, Rümenapp C and Gleich B 2011 Bioimpedance spectroscopy *BetaSys, Systems Biology 2* ed B Boof-Bavnbek et al (Berlin: Springer) pp 241–71
- Koskela O, Chowdhury M T K, Montonen T, Belay B, Pursiainen S and Hyttinen J 2021 Optical projection tomography for particle counting and morphology analysis *8th European Medical and Biological Engineering Conf.* vol 80 (Berlin: Springer) pp 944–51 (IFMBE Proc.)
- Koskela O, Lehti-Polojärvi M, Seppänen A, Figueiras E and Hyttinen J 2018 Finite element mapping for efficient image reconstruction in rotational electrical impedance tomography *World Congress on Medical Physics and Biomedical Engineering 68/2* ed L Lhotska et al (Berlin: Springer) pp 901–4 (IFMBE Proceedings)
- Lehti-Polojärvi M, Koskela O and Hyttinen J 2021 Multifrequency electrical impedance tomography in biological applications: a multimodal perspective *Bioimpedance and Spectroscopy* ed P Annus and M Min (Elsevier Inc.: Academic press) pp 157–89
- Lehti-Polojärvi M, Koskela O, Seppänen A, Figueiras E and Hyttinen J 2018 Rotational electrical impedance tomography using electrodes with limited surface coverage provides window for multimodal sensing *Meas. Sci. Technol.* **29** 025401
- Lehti-Polojärvi M, Koskela O, Seppänen A, Rist M, Land R, Annus P, Min M, Figueiras E and Hyttinen J 2019 EIT in hybrid imaging setup for tissue engineering applications *Proc. 20th Int. Conf. on Biomedical Applications of Electrical Impedance Tomography (London)* ed A Boyle et al (London, UK) (<https://doi.org/10.5281/zenodo.2691705>)
- Lipponen A, Seppänen A and Kaipio J P 2013 Electrical impedance tomography imaging with reduced-order model based on proper orthogonal decomposition *J. Electron. Imaging* **22** 023008
- Liu Z, Kang X, Bagnaninchi P and Yang Y 2020 Impedance-optical dual-modal sensor and image reconstruction for cell spheroids imaging *2020 IEEE SENSORS* pp 1–4
- Min M, Lehti-Polojärvi M, Hyttinen J, Rist M, Land R and Annus P 2018 Bioimpedance spectro-tomography system using binary multifrequency excitation *Int. J. Bioelectromagn.* **20** (1) 76–9
- Natterer F 2001 *The mathematics of computerized tomography* (Philadelphia, PA: Society for Industrial and Applied Mathematics)
- Savolainen V, Juuti-Uusitalo K, Onnela N, Vaajasaari H, Narkilahti S, Suuronen R, Skottman H and Hyttinen J 2011 Impedance spectroscopy in monitoring the maturation of stem cell-derived retinal pigment epithelium *Ann. Biomed. Eng.* **39** 3055–69
- Sharpe J, Ahlgren U, Perry P, Hill B, Ross A, Hecksher-Sørensen J, Baldock R and Davidson D 2002 Optical projection tomography as a tool for 3D microscopy and gene expression studies *Science* **296** 541–5
- Soleimani M 2006 Electrical impedance tomography imaging using *a priori* ultrasound data *Biomed. Eng. Online* **5** 1–8
- Tamminen I, Lehto K, Hannula M, Ojansivu M, Johansson L, Kellomäki M, Miettinen S, Aula A, Ihalaainen T and Hyttinen J 2020 A tube-source x-ray microtomography approach for quantitative 3D microscopy of optically challenging cell-cultured samples *Commun. Biol.* **3** 1–13
- Vauhkonen P, Vauhkonen M, Savolainen T and Kaipio J 1999 Three-dimensional electrical impedance tomography based on the complete electrode model *IEEE Trans. Biomed. Eng.* **46** 1150–60
- Vilhunen T, Kaipio J, Vauhkonen P, Savolainen T and Vauhkonen M 2002 Simultaneous reconstruction of electrode contact impedances and internal electrical properties: I. Theory *Meas. Sci. Technol.* **13** 1848–54
- Winkler S, Lehti-Polojärvi M and Hyttinen J 2020 Hyperparameter algorithms in electrical impedance tomography for rotational data *Proc. EMBEC 2020* ed T Jarm (Berlin: Springer) pp 631–43
- Wu H, Yang Y, Bagnaninchi P O and Jia J 2018 Electrical impedance tomography for real-time and label-free cellular viability assays of 3D tumour spheroids *Analyst* **143** 4189–98
- Yuan Q 2020 A modular labview program for controlling multimodal microscope imaging platform *MS Thesis* Tampere University <http://urn.fi/URN:NBN:fi:tuni-202004284176>



